

**INVESTIGATION OF DIHYDROGEN
INTERACTIONS WITH ACTIVATED
GRAPHITIC NANOSTRUCTURES AND
NOVEL METAL-ORGANIC FRAMEWORKS**

IRVIN PETELO LOSE TELEPENI

**GEORGE GREEN LIBRARY OF
SCIENCE AND ENGINEERING**

Thesis submitted to The University of Nottingham
for the degree of Doctor of Philosophy

August 2009



The University of
Nottingham

Abstract

Hydrogen is an ideal energy carrier as it only produces water as a by-product. However, technical and social issues first need to be overcome in order to achieve such economy. In particular, this work focuses on solid state hydrogen storage as it is a key technological challenge. Herein, potential candidates currently investigated are porous materials that physisorb molecular hydrogen with fast kinetics and good reversibility in order to meet mobile transportation requirements. The goal is to be able to optimize the sorption properties of a compound by tuning critical parameters such as its pore size and/or its specific surface area. Carbon nanofibres were investigated as potentially cost-efficient materials. Engineering routes such as the integration of hetero-species by nitrogen doping and exfoliation / intercalation were performed on various carbon nanostructures affecting the surface topology of the engineered compounds compared to the as-prepared materials although the excess uptakes at 77 K and 20 bar remained low *ca.* 0.6 *wt. %*. Metal-organic frameworks are a promising class of porous materials and are currently strong competitors as hydrogen storage media thanks to their flexibility in structure design. A series of Cu (II) - frameworks have been found to have exceptional sorption properties at 77 K and 20 bar up to 7 *wt. %*. The successful combination of neutron techniques at NIST-CNR and ISIS-RAL enabled a clear insight of the adsorption site distribution of two Cu (II) - frameworks using para-H₂ and D₂ as probing gases. A common feature for the MOFs investigated was that dihydrogen preferentially coordinated to the exposed metal centres *ca.* 2.4 Å, followed by sorption at two discrete sites located within triangular windows connecting the MOF cavities. It revealed the co-existence of preferential site-specific with non-site specific adsorption within the pore structure which is different from the common concept of dihydrogen interacting with a homogeneous surface. It

was also possible to follow the dynamics of hydrogen molecules at different coverage of the surface through the rotational transitions of the para-H₂ molecule.

Acknowledgements

I thank first the research training network HyTRAIN part of the FP6 program for the fantastic opportunity. I thank Dr. Gavin Walker and Prof. David Grant for their full support and their guidance during these four years. I also thank the italian team in Sesto Fiorentino Dr. Marco Zoppi, Dr. Daniele Colognesi, Dr. Lorenzo Ulivi, Dr. Milva Celli, Dr. Francesco Grazzi, Dr. Alessandra Giannasi, Laura Innoncenti and Maria Petrone. The neutron work would not have been possible without Dr. Winfried Kockelman, Dr. A. J. Ramirez-cuesta, Chris Goodway and Mark Kibble at ISIS, Dr. Craig Brown and Dr. Jason Simmons at NIST-CNR. The samples were also kindly provided by Dr. Xiang Lin. I also thank Dr. Radovan Cerny and Dr. Konstantin Lokshin for helpful discussions. On a more personal note, I thank Dan and David in Salford for all the clubs we have never been to, Laura and Francesco in Prato for showing me the real Italian cooking. I address a big thank to Chris for helping me out during my first year and for taking me back to the gym and also Nathan and Ioannis for keeping me there... I thank my family, Cindy and Patrick for their full support when I was in France, Muko for being more than a brother and my grand dad who wished I had become a priest. Finally, I thank Uta for showing me love and giving me all I will ever deserve.

To Heneliko and Emmanuelle

Contents

Abstract	i
Acknowledgements	iii
List of Figures	ix
List of Tables	xviii
1 Introduction	1
1.1 Hydrogen Economy	1
1.2 Education	2
1.3 Production	3
1.4 Storage	4
1.5 Delivery	5
1.6 Conclusions	6
2 Literature Review	7
2.1 Fundamental Principles	7
2.1.1 Physisorption	7
2.1.2 Chemisorption	10
2.2 Metal-Hydrides	10
2.3 Kubas Complex	11
2.4 Carbon Materials	12
2.4.1 Activated Carbons	13
2.4.2 Fullerenes	14
2.4.3 Nanotubes	16
2.4.3.1 Single-Walled Carbon Nanotubes	16
2.4.3.2 Multi-Walled Carbon Nanotubes	17

CONTENTS

2.4.3.3	Graphitic Nanofibres	19
2.5	Nitrogen Doping	22
2.6	Exfoliation Via Intercalation	23
2.7	Metal-Organic Frameworks	26
2.7.1	Pore Structure	26
2.7.2	Metal Centres	28
2.8	Conclusions	31
3	Experimental	33
3.1	Synthesis	33
3.2	Exfoliation of Intercalated Compounds	35
3.3	Thermal Activation	35
3.4	Sorption Properties Characterisation	36
3.4.1	Gravimetric Method	36
3.4.1.1	Theory	36
3.4.1.2	Experimental	38
3.4.2	BET Method	38
3.4.2.1	Theory	38
3.4.2.2	Experimental	40
3.5	Structural Characterisation and Spectroscopy	41
3.5.1	Transmission Electron Microscopy	41
3.5.1.1	Theory	41
3.5.1.2	Experimental	41
3.5.2	X-Ray Powder Diffraction	42
3.5.2.1	Theory	42
3.5.2.2	Crystallite Size	44
3.5.2.3	Experimental	45
3.5.3	Neutron Scattering	46
3.5.3.1	Neutron Powder Diffraction	48
3.5.3.2	Inelastic Neutron Scattering	49
3.5.3.2.1	Quantum Rotor	49
3.5.3.2.2	Homonuclear Diatomic Molecule	50
3.5.3.2.3	Homonuclear Diatomic Molecular Gas	53
3.5.3.2.4	Molecular Vibrations	54
3.5.3.2.5	Solid Phase	56

3.5.3.2.6	Rotations of a Homonuclear Diatomic Molecule in a Hindering Potential .	57
3.5.3.2.7	Hydrogen Deuteride	58
3.5.3.2.8	Response Function	59
3.5.3.3	Neutron Powder Diffraction Experiments . .	59
3.5.3.4	Inelastic Neutron Scattering Experiments .	61
3.5.4	Rietveld Analysis	64
4	Carbon Nanostructures For Hydrogen Storage	67
4.1	Results	67
4.1.1	Activated Carbon	67
4.1.2	As-Prepared GNFs	68
4.1.3	Nitrogen Doped GNFs	71
4.1.4	Exfoliation of Intercalated GNFs	75
4.2	Discussion	77
4.3	Conclusions	82
5	Metal-Organic Frameworks	85
5.1	Introduction	85
5.2	Materials	86
5.3	Results	88
5.3.1	X-Ray Powder Diffraction	88
5.3.2	Neutron Powder Diffraction	89
5.3.3	Inelastic Neutron Scattering	94
5.4	Discussions	98
5.4.1	Neutron Powder Diffraction	98
5.4.2	Inelastic Neutron Scattering	100
5.5	Conclusions	114
6	Summary and Conclusions	115
6.1	Pore Size	115
6.2	Specific Surface Area	116
6.3	Adsorption Site Distribution	117
6.4	Conclusions	117
6.5	Future Work	119

CONTENTS

Bibliography	121
--------------	-----

List of Figures

1.1	Potential energy sources for generating H ₂ and potential end uses (U.S. Department of Energy, 2006).	2
1.2	Gravimetric and volumetric targets for 2010 and 2015. Status of current technologies relative to key system performance and cost targets (inset) (U.S. Department of Energy, 2009e).	5
1.3	Technical system targets: On-board hydrogen storage for light-duty vehicles (U.S. Department of Energy, 2009b).	6
2.1	Interaction potential curves for hydrogen molecular physisorption and atomic chemisorption (Attard and Barnes, 1998). . . .	8
2.2	Five types of van der Waals adsorption isotherms (Brunauer et al., 1940).	9
2.3	The vertical axis indicates the corresponding hydrogen pressure. From the slope of the van't Hoff plot, experimental values of the enthalpy of hydride formation H can be evaluated. The plateau pressure $p_{eq}(T)$ as a function of temperature is related to the changes H and S of enthalpy and entropy, respectively, by the van't Hoff equation: $\ln(p_{eq}/p_{eq}^0) = (-\Delta H/R)(1/T) + \Delta S/R$. Data were taken for LaNi ₅ (Schlapbach and Züttel, 2001).	11
2.4	W(CO) ₃ complexes and H-H stretch within complex (Kubas 2001).	12
2.5	Linear relationship between hydrogen storage capacity for different carbon samples and the specific surface area at 77 K and 70 bar (Hirscher and Panella, 2005).	13
2.6	Two dimensional representation of the pore structure of granular activated carbon (Rodriguez-Reinoso, 2002).	15
2.7	a) C ₆₀ fullerene. b) C ₆₀ doped with Ti atoms in dark blue (exohedral site) (Yildirim et al., 2005).	15

LIST OF FIGURES

2.8	a) Graphene sheet rolled up to form a SWCNT. b) SWCNT configuration: (a) Armchair, (b) Zigzag, and (c) Chiral with fullerene caps at each end. Reproduced from (Strobel et al., 2006).	16
2.9	Contour plot of excess density adsorbed as a function of SWCNT diameter and lattice spacing at 77 K and 1 atm (bundle of seven units), obtained using grand canonical Monte-Carlo simulations of adsorption of hydrogen on a SWCNT. The hydrogen-carbon interactions were modelled using standard Lennard-Jones potential (Benard and Chahine, 2007).	17
2.10	Adsorption site distribution within a bundle of CNTs (Pradhan et al., 2002).	18
2.11	Scheme of GNF types: A) Platelet and B) Herringbone (McCaldin et al., 2006).	19
2.12	(a) Schematic representation showing the key steps in the growth of a GNF. 1. Adsorption and decomposition of hydrocarbon gas at the particle-gas interface on the front face of the catalyst particle. 2. Diffusion of carbon through the catalyst particle. 3. Precipitation of carbon at the particle-nanofibre interface on the rear face of the catalyst particle (b) Schematic representation of a GNF that has ceased growth due to a carbon over layer, forming over the leading face (Rodriguez, 1993).	21
2.13	a) Possible intercalation stages of K intercalated GIC. b) X-ray powder diffraction patterns of different stage GICs (Dresselhaus and Dresselhaus, 2002).	24
2.14	TEM analysis of EGNF-1000. Dark and light regions are observed in the fibers (a and b) after exfoliation. Certain fiber regions (arrows) with large expansion indicate fiber rupture. (c) SAED pattern of the nanofiber in (b), (002), (100) and (110) diffraction features can be observed. The inset is a schematic model of the cup-stacked crystalline structure of the fiber after exfoliation; those segments of the fiber keeping the graphite spacing between cups ($\simeq 3.35 \text{ \AA}$) are responsible for the (002) diffraction spots observed in the SAED pattern (Lueking et al., 2007).	25

-
- 2.15 From the left MOF-505 (NOTT-100), NOTT-101, and NOTT-102 cage structures with elliptical (grey sphere) and spherical (yellow sphere) cages. Bond colour code: Blue: Copper, Grey: Carbon, Red: Oxygen. No hydrogen bonds shown for clarity (Lin et al., 2006a). 27
- 2.16 MIL-53(Al) pore structure obtained from neutron powder diffraction experiments collected at room temperature after heating to 450 K (a) and cooling to 77 K (b). MIL-53(Al) exists either as an open-pored (a) phase or a predominantly closed-pored phase (b), depending on the thermal history (Liu et al., 2008). 28
- 2.17 a) Schematic representation of the repeated unit. b) and d) Interpenetration of two identical catenated units allowing the reduction of the pore dimension by different pore configurations. c) Interweaving results in the total reduction of the pore size (Rowsell and Yaghi, 2005). 28
- 2.18 On the left: Dicopper (II) tetracarboxylate building block for HKUST-1 (Chui et al., 1999). On the right HKUST-1 cage structure with spherical (grey sphere) and secondary (khaki sphere) cages. Bond colour code: Blue: Cu, Red: O, Grey: C. No hydrogen bonds shown for clarity. 29
- 2.19 MOF-5 (A), IRMOF-6 (B), and IRMOF-8 (C) pore structure. On each of the corners is a cluster $[\text{OZn}_4(\text{CO}_2)_6]$ of an oxygen-centred Zn_4 tetrahedron that is bridged by six carboxylates of an organic linker (Zn, blue polyhedron; O, red spheres; C, black spheres). The large yellow spheres represent the largest sphere that would fit in the cavities without touching the van der Waals atoms of the frameworks. Hydrogen atoms have been omitted (Rosi et al., 2003). 30

LIST OF FIGURES

2.20	Dependence of the Langmuir surface area on the adsorbed H_2 amounts at 77 K and 45 bar (volumetric values) for the three MOFs under investigation. Values taken from the literature: MOF-5,3 HKUST-1,3 and CPO-27-Ni. The dependence of the H-H shift for the most energetic complexes on the hydrogen uptake is also shown (para- H_2 has been used as reference, gray squares). For CPO-27-Ni, the barycenter of the 4028 and 4035 cm^{-1} bands has been considered (Vitillo et al., 2008).	31
2.21	The H_2 surface packing density, SPD, as a function of N_2 BET surface. The horizontal dashed line shows the SPD for typical carbon material, where every 500 $m^2.g^{-1}$ of N_2 BET surface area can adsorb 1 <i>wt.%</i> of H_2 . Solid green (gray) curves show the lines for gravimetric uptake of 6 and 9 <i>wt.%</i> , which is the product of SPD and S. One-dimensional nanoscale tube like structure formed from adsorbed D_2 . D_2 molecules (large green (gray) balls) adsorbed in MOF-74 form a one-dimensional nanoscale tube like structure. (Only the first three adsorption sites are shown) (Liu et al., 2008).	31
3.1	Horizontal tube furnace used for undoped GNF growths and N-doping experiments.	34
3.2	CVD procedure with 4 different phases. For the N-doping experiments, different amines were added to the $C_2H_4:H_2$ gas mixture.	35
3.3	On the left: Paddle-wheel unit within the non-activated NOTT-100, NOTT-101, and NOTT-102 with two water molecules attached onto the copper sites. On the right: degassed sample with two exposed copper centres. Colour code: Blue: copper; Red: oxygen; Grey: carbon. No hydrogen bonds shown for clarity. Water molecules are removed from the copper sites after thermal treatment.	36
3.4	Representation of a TEM instrument (Edwards, 1989).	42
3.5	Simplified path geometry of an incident and a diffracted beam by two atoms M and N from two (hkl) lattice planes separated by a distance d_{hkl} . The scattering vector, Q , is defined by: $Q = k_f - k_i$	44

3.6	a) H ₂ molecule with the angular coordinates (θ, ϕ). b) Rotational energy diagram of para-H ₂ and ortho-D ₂ (Silvera et al., 1978, Silvera, 1980).	51
3.7	Solid para-H ₂ INS spectrum collected at 4 K on the neutron spectrometer TOSCA at ISIS-RAL (Mitchell et al., 2004). . . .	57
3.8	Solid HD INS spectra obtained on TOSCA (Colognesi et al., 2009). . . .	59
3.9	BT-1 instrument as viewed from above. For size reference, note that the diffractometer radius is approximately one meter (NIST). b) A schematic layout of the detector banks of the GEM detector array (Hannon, 2005).	61
3.10	A schematic layout of FANS and TOSCA reproduced from (NIST) and (ISIS-RAL)	62
3.11	a) Energy resolution of FANS. The pyrolytic graphite monochromator 002 with 20' horizontal collimation before and after the monochromator. b) FANS (Q, ω) trajectories (NIST, 2006). . . .	63
3.12	a) Energy resolution of TOSCA-II compared to earlier versions TOSCA-I and TXFA (ISC-CNR). b) (Q, ω) trajectories of the back (B) and forward (F) scattering banks on TOSCA (ISC-CNR). . . .	63
4.1	BET plot of activated carbon sample (Maxsorb) within the 0.04 – 0.28 $\frac{p}{p_0}$ linear region.	68
4.2	Hydrogen isotherm for activated carbon sample (Maxsorb) measured at 77 K and 20 bar.	68
4.3	TEM images of Ni-550 as prepared herringbone GNFs.	69
4.4	TEM images of as prepared platelet GNFs: a) Ni-550 and b) Co-550.	69
4.5	a) XRPD of Ni-500, Ni-550 and Ni-600. b) XRPD of Co-500, Co-550, Co-600. The data were collected at room temperature. Baselines were subtracted.	70
4.6	a) Hydrogen isotherm of Ni-600 and b) Hydrogen adsorption curve of Co-550 measured at 77 K and 20 bar.	71
4.7	BET plot of Ni-600 within the 0.08-0.32 $\frac{p}{p_0}$ linear region.	72
4.8	XRPD of the as prepared EA-(Ethene)-Co- samples. The data were collected at room temperature. Baselines were subtracted.	73

LIST OF FIGURES

4.9	XRPD of the as prepared EA-Ni- and EA-Ethene-Ni- samples. The data were collected at room temperature. Baselines were subtracted.	73
4.10	TEM images: a) Herringbone type EA-Ethene-Ni-500 and b) Platelet type EA-Ethene-Co-550. c) TEM image of herringbone type DEA-Ethene-Ni-550.	74
4.11	a) Hydrogen isotherm of EA-Ethene-Co-550 measured at 77 K and 20 bar. b) Hydrogen isotherm of DEA-Ethene-Ni-550 measured at 77 K and 20 bar.	74
4.12	TEM images: a) As prepared I-Ni and b) herringbone type E1000-Ni.	75
4.13	a) XRPD of E700-Ni, E800-Ni, E900-Ni, E1000-Ni and I-Ni. b) XRPD of I-Co and E1000-Co. The data were collected at room temperature. Baselines were subtracted.	76
4.14	XRPD of as-prepared, intercalated, and exfoliated graphite flakes. The data were collected at room temperature. The intensity for the raw graphite flakes was reduced by one order of magnitude for comparison. Baselines were subtracted.	76
4.15	Hydrogen adsorption curve of as prepared E1000-Co. The data were collected at 77 K and 20 bar.	77
5.1	From the left MOF-505 (NOTT-100), NOTT-101, and NOTT-102 cage structures with elliptical (grey sphere) and spherical (yellow sphere) cages. Bond colour code: Blue: Copper, Grey: Carbon, Red: Oxygen. No hydrogen for clarity. Crystal structures were obtained from (Lin et al., 2006b). Image generated using DIAMOND software.	87
5.2	On the right: HKUST-1 cage structure with spherical (grey sphere) and secondary (kaki sphere) cages. On the left: triangular windows common to HKUST-1 and NOTT-100 series. Bond colour code: Blue: Cu, Red: O, Grey: C. No hydrogen bonds for clarity. Crystal structure obtained from (Chui et al., 1999). Image generated using DIAMOND software.	87

5.3	Comparison of the simulated using Mercury 2.2 and the experimental XRPD patterns of the solvent free NOTT-100 degassed at 130 °C.	88
5.4	Comparison of the simulated using Mercury 2.2 and experimental XRPD patterns of the solvent free NOTT-101 (a) and NOTT-102 (b) degassed at 140 °C.	88
5.5	a) NPD patterns of the desolvated NOTT-101 with various D ₂ gas loadings per Cu site collected on BT1 at 4 K. No error bars. b) NPD patterns of the desolvated NOTT-102 with various D ₂ gas loadings per Cu site (forward scattering bank). The data were collected on GEM at 4 K. No error bars.	89
5.6	a) Bare NOTT-101 and b) NOTT-102 Rietveld refinement as implemented within GSAS-EXPGUI (forward scattering bank). The data were collected on BT1 at 4 K. No error bars.	90
5.7	Difference nuclear scattering density Fourier map (yellow) showing sites A and B within the triangular window common to NOTT-101 and NOTT-102. Colour code: Blue: Cu, Red: O, Grey: C. No hydrogen atoms shown for clarity. One copper-paddle wheel was removed. Image was obtained using the visualization program VESTA (Momma and Izumi, 2008).	90
5.8	NOTT-101 and NOTT-102 D ₂ adsorption sites identified in the elliptical (grey sphere) and spherical (yellow sphere) cages. Top right: view from the elliptical cage looking at the top of the spherical cage, site B _{1,2} is in the middle of the window between to the three phenyl rings. Site C _{1,2} is obscured by site B _{1,2} . Bottom right (one paddle-wheel was removed for clarity): site A _{1,2} is to the copper centre inside the spherical cage, site B _{1,2} is at the bottom of the elliptical cage close to the phenyl rings and site C _{1,2} is on the same 3-fold axis of site B ₁ within the spherical cage. There was an extra site D ₂ just above site A _{1,2} (top right one site D ₂ was removed to reveal site A _{1,2}). Bond colour code: Blue: Cu, Red: O, Grey: C. No hydrogen atoms shown for clarity.	91

LIST OF FIGURES

5.9	As collected INS spectra of NOTT-101 with various para-H ₂ loadings per Cu site. The data were collected on FANS at 4 K. Error bars are smaller than the symbols. The first loading was made with normal-H ₂ gas.	95
5.10	As collected $S(Q, \omega)_{back}$ and $S(Q, \omega)_{forward}$ for NOTT-102 with various para-H ₂ gas loadings per Cu site collected at 4 K on TOSCA Error bars are represented.	96
5.11	As collected $S(Q, \omega)_{forward}$ for NOTT-102 with various para-H ₂ gas loadings per Cu site collected at 4 K on TOSCA Error bars are represented.	96
5.12	As collected $S(Q, \omega)_{back}$ and $S(Q, \omega)_{forward}$ for NOTT-102 with various HD gas loadings per Cu site collected at 4 K on TOSCA Error bars are represented.	97
5.13	As collected $S(Q, \omega)_{forward}$ for NOTT-102 with various HD gas loadings per Cu site collected at 4 K on TOSCA Error bars are represented.	97
5.14	As collected $S(Q, \omega)_{back}$ of the gas free NOTT-102 before the para-H ₂ (black line) and the HD (red line) experiments. The intensity of the 1st sample has been normalized to the same amount as for the 2 nd sample. No error bars for clarity.	98
5.15	a) Equivalence of the sites A ₁ on both side of the paddle-wheel for NOTT-101. b) Triangular windows connecting a spherical and elliptical cage. Colour bond: Red O; Blue: Cu; Grey: Carbon. No hydrogen atoms shown for clarity.	100
5.16	Difference INS spectra for NOTT-101 between two subsequent para-H ₂ loadings; collected on FANS. The baselines were not subtracted. Error bars are smaller than the symbols.	101
5.17	a) Peak deconvolution of the difference NOTT-101 INS spectra obtained between 2.79-1.89 para-H ₂ per Cu collected on FANS at 4 K. The baseline was subtracted. Error bars are represented. b) Integrated areas of NOTT-101 INS peaks as function of para-H ₂ loadings from the difference NOTT-101 INS spectra.	102
5.18	$S(Q, \omega)_{back}$ of the difference INS spectra obtained for two subsequent para-H ₂ gas loadings per Cu site for NOTT-102 collected at 4 K on TOSCA Error bars are represented.	103

5.19	$S(Q, \omega)_{forward}$ of the difference INS spectra obtained for two subsequent para-H ₂ gas loadings per Cu site for NOTT-102 collected at 4 K on TOSCA. Error bars are represented.	104
5.20	Peak deconvolution for NOTT-102 spectrum from the $S(Q, \omega)_{back}$ of 0.5-0.0 and 3.0-2.0 para-H ₂ loadings collected on TOSCA at 4 K. Baseline was subtracted. Error bars are represented.	105
5.21	$S(Q, \omega)_{back}$ and $S(Q, \omega)_{forward}$ of the difference INS spectra between two subsequent HD gas loadings per Cu site for NOTT-102 collected at 4 K on TOSCA. Error bars also represented.	106
5.22	Peak deconvolution of NOTT-102 spectrum from the $S(Q, \omega)_{back}$ of 0.5-0.0 HD loadings collected on TOSCA at 4 K. Error bars are represented.	106
5.23	INS spectra for HKUST-1 on FANS with various amount of para-H ₂ gas. Data were collected at 4 K. The bare material spectrum was subtracted from each spectrum. Error bars are smaller than the symbols (Liu et al., 2007b).	107
5.24	a) NOTT-100, NOTT-101, NOTT-102 isotherms at 77 K using the IGA-003. Inset represents the lower pressure region of the isotherm ($p < 0.8$ bar). b) Conversion curves pressure / hydrogen weight uptake for NOTT-100, NOTT-101, and NOTT-102 within the low pressure region ($p < 0.8$ bar). HKUST-1 data reproduced from (Peterson et al., 2006). NOTT data reproduced from (Lin et al., 2006b).	112

List of Tables

4.1	Non-doped GNF growth parameters. BET surface area measurements and H ₂ uptakes at 77 K and 20 bar are reported. . .	71
4.2	N-doped GNF growth parameters using a mixture of ethylamine, ethene and hydrogen. BET surface area H ₂ weight uptakes and N level measurements are also reported.	74
4.3	Sorption and structural properties of as prepared, intercalated, and exfoliated carbon compounds.	77
4.4	Crystallite size analysis for undoped GNFs from XRPD data using gaussian profiles of the (002) reflection.	78
4.5	Crystallite size analysis for N-doped GNFs from XRPD data using Gaussian profiles.	79
4.6	Crystallite size analysis for exfoliated and intercalated GNFs from XRPD data using Gaussian profiles.	81
5.1	Unit cell parameters for NOTT-101 determined by Rietveld refinement for each D ₂ gas loading and goodness of fit.	92
5.2	Unit cell parameters for NOTT-102 determined by Rietveld refinement for each D ₂ gas loading and goodness of fit.	92
5.3	Fractional atomic positions and thermal parameters at 3.0 D ₂ per Cu within NOTT-101.	93
5.4	Fractional atomic positions and thermal parameters at 3.0 D ₂ per Cu within NOTT-102.	93
5.5	Fractional occupancies for NOTT-101 adsorption sites at 3.0 D ₂ per Cu within NOTT-101.	93
5.6	Fractional occupancies for NOTT-102 adsorption sites at 3.0 D ₂ per Cu within NOTT-102.	93
5.7	Shortest distance site-site within NOTT-101.	94

5.8 Shortest distance site-site within NOTT-102. 94

Chapter 1

Introduction

This chapter introduces the hydrogen economy. It will help to identify the needs and the main objectives for this alternative economy. In particular, technical aspects will be addressed from the point of view of the hydrogen production, storage, and delivery. At the same time, we will see that social issues generated by the potential integration of this new technology are also essential for the hydrogen economy to be achieved.

1.1 Hydrogen Economy

Hydrogen is a clean energy carrier and an attractive alternative for fossil fuels as its reaction with oxygen releases energy with the only by-product being water. The energy crisis in 1973 gave an early indication of the disadvantages of an oil based economy often subject to the geo-political climate although the oil market has formed a central part in the modern world. Recently more and more efforts are being invested towards alternative energies. In combination with other renewable resources, a hydrogen energy / economy has been proposed as a long-term solution which would secure the energy supply but also reduce carbon emissions especially from the growing transportation sector (U.S. Department of Energy, 2009a). A series of targets for transportation have been set by the US department of energy (DoE) in order to deliver a comparable performance and price to current vehicles (U.S. Department of Energy, 2009a). It is therefore essential to clearly identify the main technical, social and political challenges to achieve a sus-

1. INTRODUCTION

tainable hydrogen economy. Figure 1.1 depicts potential energy sources for generating H_2 and potential end uses. It also highlights that hydrogen is an energy carrier as opposed to an energy source.

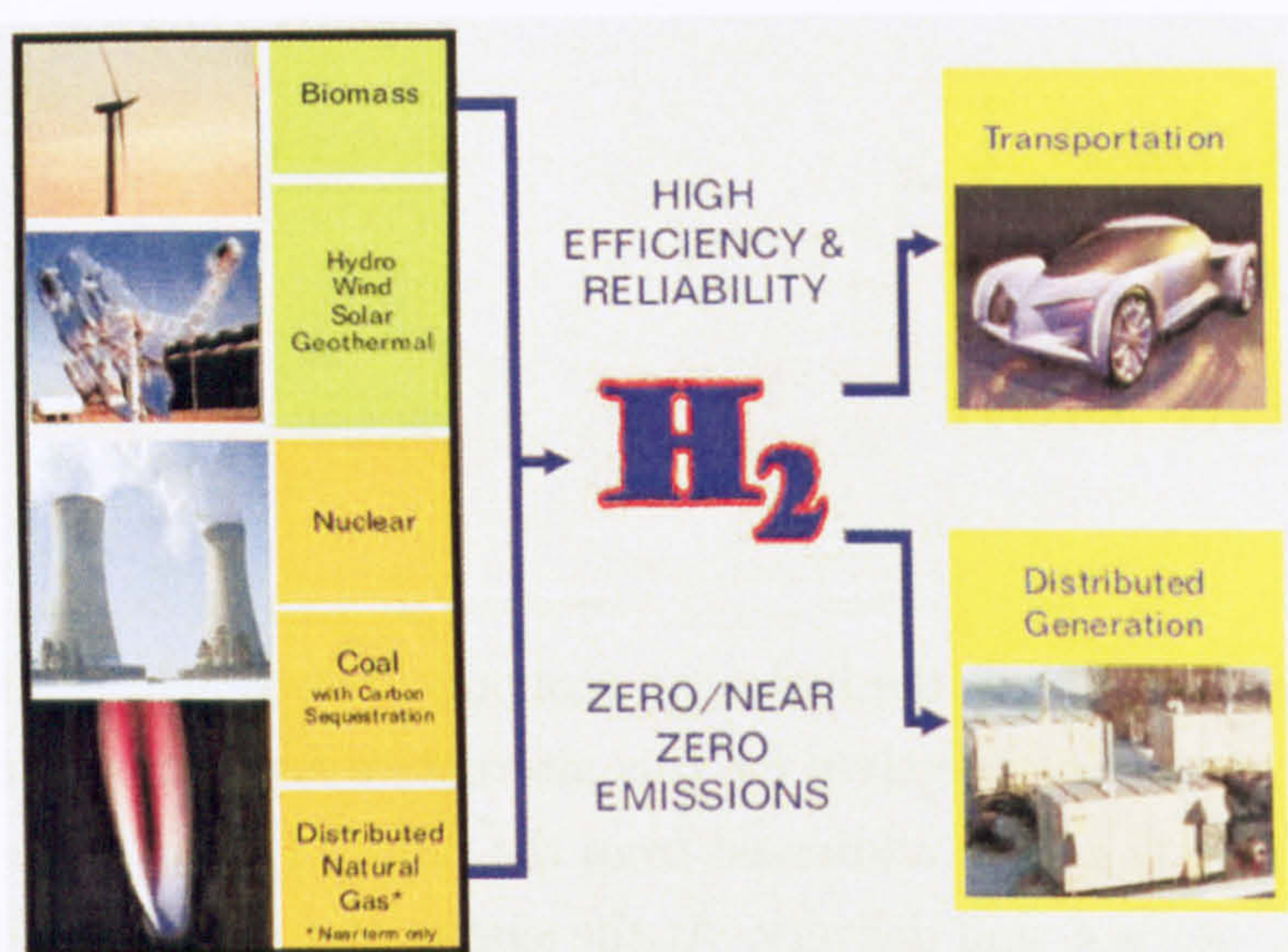


Figure 1.1: Potential energy sources for generating H_2 and potential end uses (U.S. Department of Energy, 2006).

1.2 Education

Exhibitions and small-scale projects are compulsory if one wants to facilitate the integration of new technologies. The European community funded clean urban transport for europe (CUTE) project ran 27 hydrogen-powered fuel cell regular service buses over a period of two years in 9 European inner city areas (HyFLEET:CUTE, 2004, CUTE, 2004). A range of similar innovative public-outreach demonstration programs are being initiated around the world aimed at demonstrating the feasibility of small-scale integrated hydrogen energy infrastructures and improving the public perception. These are field-tests with direct feedbacks to validate and integrate these new technologies. In higher education, fundamental and applied research programs were also created to develop the technology required for a sustainable hydrogen economy. For instance, UK scientists are currently looking at the socio-economic, political and scientific aspects of the hydrogen economy as part of the United Kingdom sustainable hydrogen energy

consortium (UKSHEC), funded by the British Government through the engineering and physical sciences research council (EPSRC) (UK-SHEC, 2007, EPSRC). European research training networks involving early stage and experienced researchers through the FP6 are dedicated to more specific targets such as the hydrogen storage issue within hydrogen storage research training network (HyTRAIN) and novel efficient solid storage for H_2 (NESSHY) projects (HyTRAIN, 2005, NESSHY, 2006). These examples illustrate the scientific community's commitment to promote hydrogen technologies and provide the skills training needed for a future hydrogen economy. They are also the platform where an easy and open access to accurate information is provided. In particular, this work is part of the HyTRAIN research training network (ESR6) involving the division of fuels and power technology research from the University of Nottingham and the istituto dei sistemi complessi - consiglio nazionale delle ricerche (ISC-CNR) in Italy.

1.3 Production

Although hydrogen is one of the most abundant elements on earth, it is always chemically bound to other elements to form stable compounds like water, biomass or hydrocarbons. It is therefore essential to find inexpensive and efficient routes to separate hydrogen from non-fossil natural resources. This step requires energy such as heat, light, or electricity to achieve the process (U.S. Department of Energy, 2009b). Hydrogen can be derived from non-renewable resources with nuclear energy or hydrocarbons however these are short-term solutions as it raises waste management issues (U.S. Department of Energy, 2009d). It is also possible to obtain hydrogen from hydrogen natural carriers such as water and biomass. Water electrolysis is the most common method to separate hydrogen from water (U.S. Department of Energy, 2009c). Solar energy can be used to produce electricity for electrolysis but also to generate H_2 directly either photo-catalytically or by thermochemical processes at high temperature *ca.* up to 2000 °C. However this method presents obvious practical limitations. Here the main challenge is to develop and expand low cost production technologies. In the long term it should be limited to production techniques from renewable resources.

1.4 Storage

The challenges depend on the hydrogen use: for large and medium-scale utilizations such as hydrogen tanks for industrial applications or refuelling station, hydrogen will be preferentially stored as a gas or liquid phase. For on-board applications vehicles require compact, light, safe and low cost containment. The DoE targets are by 2010 to develop and verify on-board hydrogen storage systems achieving 1.5 kWh.kg^{-1} (6 *wt. %*), 0.9 kWh.L^{-1} and $4 \text{ $.kWh}^{-1}$ (U.S. Department of Energy, 2009a). By 2015, targets are to develop and verify on-board hydrogen storage systems achieving 1.8 kWh.kg^{-1} (9 *wt. %*), 1.3 kWh.L^{-1} , and $2 \text{ $.kWh}^{-1}$. A combustion engine of an average vehicle requires 28 kg of petrol within a range of 400 km which is equivalent to 4 kg of hydrogen using current fuel cells (U.S. Department of Energy, 2009b). Figure 1.2 shows the gravimetric and volumetric hydrogen storage capacities for mobile application requirements and their costs (U.S. Department of Energy, 2009e). High pressure tanks and hydrogen liquification are obviously not favourable storage solutions and cannot meet the DoE targets because of overpressure issues and low condensation temperatures required.

Solid state hydrogen storage was proposed as the most promising and efficient path. It involves two different mechanisms: First, molecular hydrogen can be physically adsorbed on a surface at cryogenic temperatures and reasonable pressures (see section 2.1.1). Hydrogen molecules can be easily extracted from the surface thanks to the weak van der Waals interaction between the gas (adsorbate) and the surface (adsorbent). Other materials can also dissociate the hydrogen molecules and form a chemical bound with atomic hydrogen (see section 2.1.2). With such materials hydrogen can be retrieved only at high temperature. The challenge for mobile applications is to be able to fill and discharge hydrogen in a reasonable time. In essence, the material needs to have fast cycling kinetics, good reversibility with an excellent lifecycle under ambient conditions as shown in Figure 1.3 (U.S. Department of Energy, 2009b). Scientists have been investigating a wide range of materials such as metal-hydride and porous materials in order to match DoE targets.

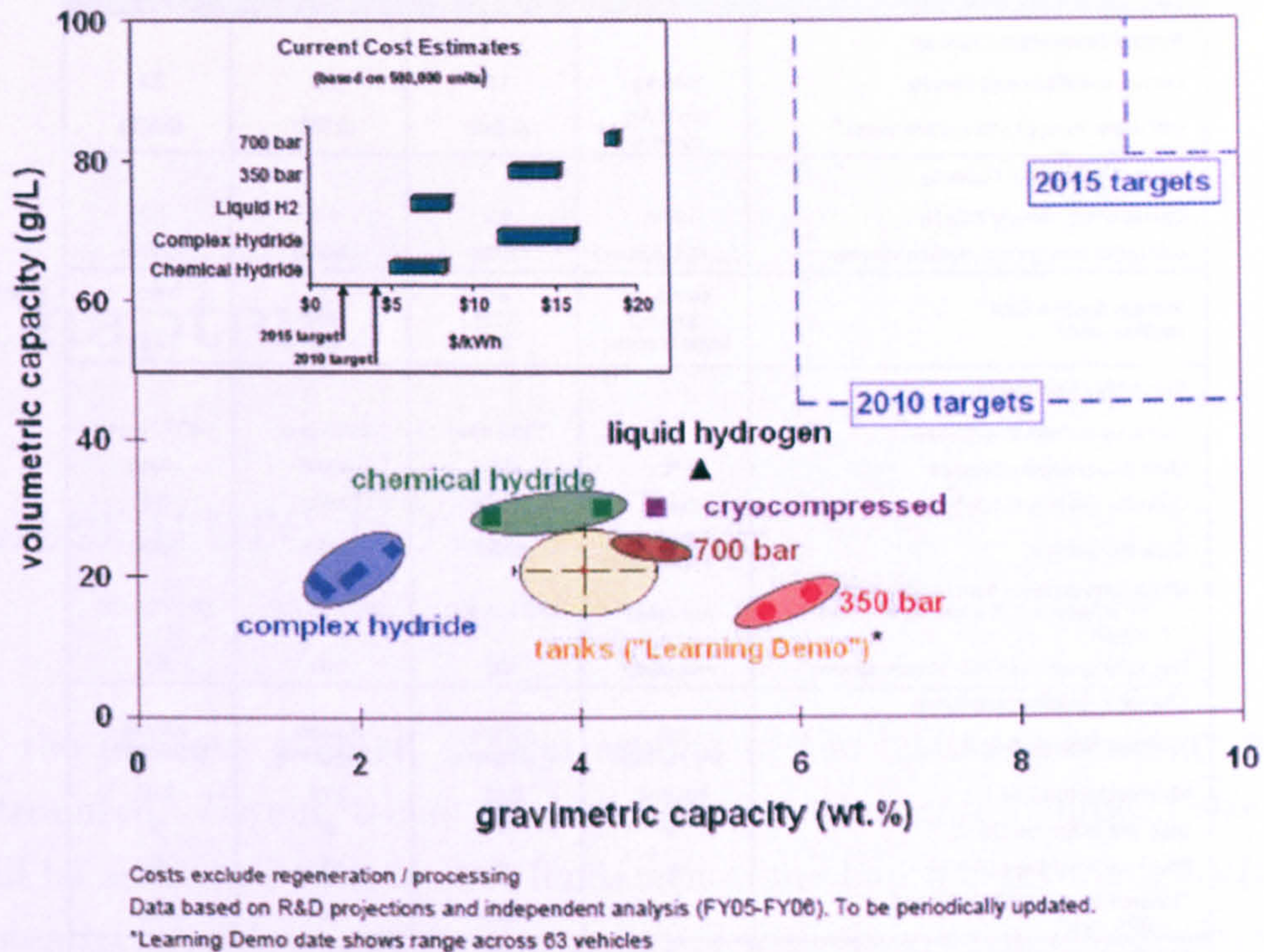


Figure 1.2: Gravimetric and volumetric targets for 2010 and 2015. Status of current technologies relative to key system performance and cost targets (inset) (U.S. Department of Energy, 2009e).

1.5 Delivery

Currently hydrogen is either used on-site where it is produced or supplied to industry for chemical uses. The challenge here is to lower the cost of delivery technologies from decentralized hydrogen production points to re-fuelling stations for hydrogen-powered applications and storage facilities. It is currently transported either as a gas or as a liquid using tanks and pipelines. Efficient compression and liquefaction technologies are to be developed for long distance delivery and stationary use (U.S. Department of Energy, 2009f). Hydrogen embrittlement issues are also of the great interest, therefore institutions will have to decide on the level of specific upgrades or completely change the existing delivery system in order to integrate hydrogen for a more common use. This will heavily influence the costs in terms of technology and safety.

1. INTRODUCTION

Storage Parameter	Units	2010	2015	Ultimate
System Gravimetric Capacity				
Usable, specific-energy from H ₂ (net useful energy / max system mass) ^a	kWh/kg (kg H ₂ /kg system)	1.5 (0.045)	1.8 (0.055)	2.5 (0.075)
System Volumetric Capacity				
Usable energy density from H ₂ (net useful energy / max system volume)	kWh/L (kg H ₂ /L system)	0.9 (0.028)	1.3 (0.040)	2.3 (0.070)
Storage System Cost ^b (and fuel cost) ^c	\$/kWh net (\$/kg H ₂) \$/gge at pump	4* (133) 2-3	2* (67) 2-3	TBD* 2-3
Durability / Operability				
Operating ambient temperature ^d	°C	-30/50 (sun)	-40/60 (sun)	-40/60 (sun)
Min/max delivery temperature	°C	-40/85	-40/85	-40/85
Cycle life (1/4 tank to full) ^e	Cycles	1000	1500	1500
Cycle life variation ^f	% of mean (min) at % confidence	90/90	99/90	99/90
Min delivery pressure from storage system; FC = fuel cell, ICE = internal combustion engine	Atm (abs)	4FC / 35 ICE	3FC / 35 ICE	3FC / 35 ICE
Max delivery pressure from storage system ^g	Atm (abs)	100	100	100
Charging / Discharging Rates				
System fill time (for 5 kg H ₂)	min (Kg H ₂ /min)	4.2 min (1.2 kg/min)	3.3 min (1.5 kg/min)	2.5 min (2.0 kg/min)
Minimum full flow rate	(g/s)/kW	0.02	0.02	0.02
Start time to full flow (20 °C) ^h	s	5	5	5
Start time to full flow (-20 °C) ^h	s	15	15	15
Transient response 10%-90% and 90% - 0% ⁱ	s	0.75	0.75	0.75
Fuel Purity (H ₂ from storage) ^j	% H ₂	99.99 (dry basis)		
Environmental Health & Safety		Meets or exceeds applicable standards		
Permeation and leakage ^k	Sec/h			
Toxicity	-			
Safety	-			
Loss of useable H ₂ ^l	(g/h)/kg H ₂ stored	0.1	0.05	0.05

^aThe storage system costs are currently under review and will be changed at a future date.
Useful constants: 0.2778kWh/MJ, ~33.3kWh/gal gasoline equivalent.

Figure 1.3: Technical system targets: On-board hydrogen storage for light-duty vehicles (U.S. Department of Energy, 2009b).

1.6 Conclusions

A large scale adoption of these novel energy technologies will undeniably change the face of our society. The scenarios and roadmaps will have to take into account technical and social hurdles mentioned earlier for a sustainable hydrogen economy. It will also have to meet market-based requirements for all the costs, transitions towards a new energy system, its maintenance, and overall performance. The focus of this work is the solid state hydrogen storage aspect of the problem using physisorbing materials. In the next chapters, we will try to identify and investigate the key parameters responsible for the sorption properties of a series of compounds potential candidate as hydrogen storage media.

Chapter 2

Literature Review

In the previous chapter, general aspects of the hydrogen economy were introduced. Herein, technical challenges for solid state hydrogen storage will be addressed with at first fundamental mechanisms involved. Current potential candidates will be also reviewed with their strengths, weaknesses and potential engineering routes to improve their sorption properties as reported in the literature.

2.1 Fundamental Principles

2.1.1 Physisorption

Physisorption is a non-dissociative physical adsorption of a molecule (adsorbate) on a solid surface (adsorbent). It is the direct result of resonant fluctuations of the charge distributions also called dispersive interactions or van der Waals' interaction. Molecules are physisorbed onto a surface. The simplest approximation for this interaction is the Lennard-Jones potential with no activation energy leading to a shallow well (Lennard-Jones and Devonshire, 1936) (Figure 2.1). The interaction potential strongly depends on rotational and vibrational energies of the adsorbate and the symmetry of the adsorption site and / or the surface (McClurg et al., 1997). The equilibrium distance, r_0 , is of the order of one molecular radius. As the surface-molecule distance, r , increases the interaction reduces to zero and the molecule is free of the surface. An adsorbed molecule is kept at a distance, r_0 , from the surface because of the repulsive contribution at low r .

2. LITERATURE REVIEW

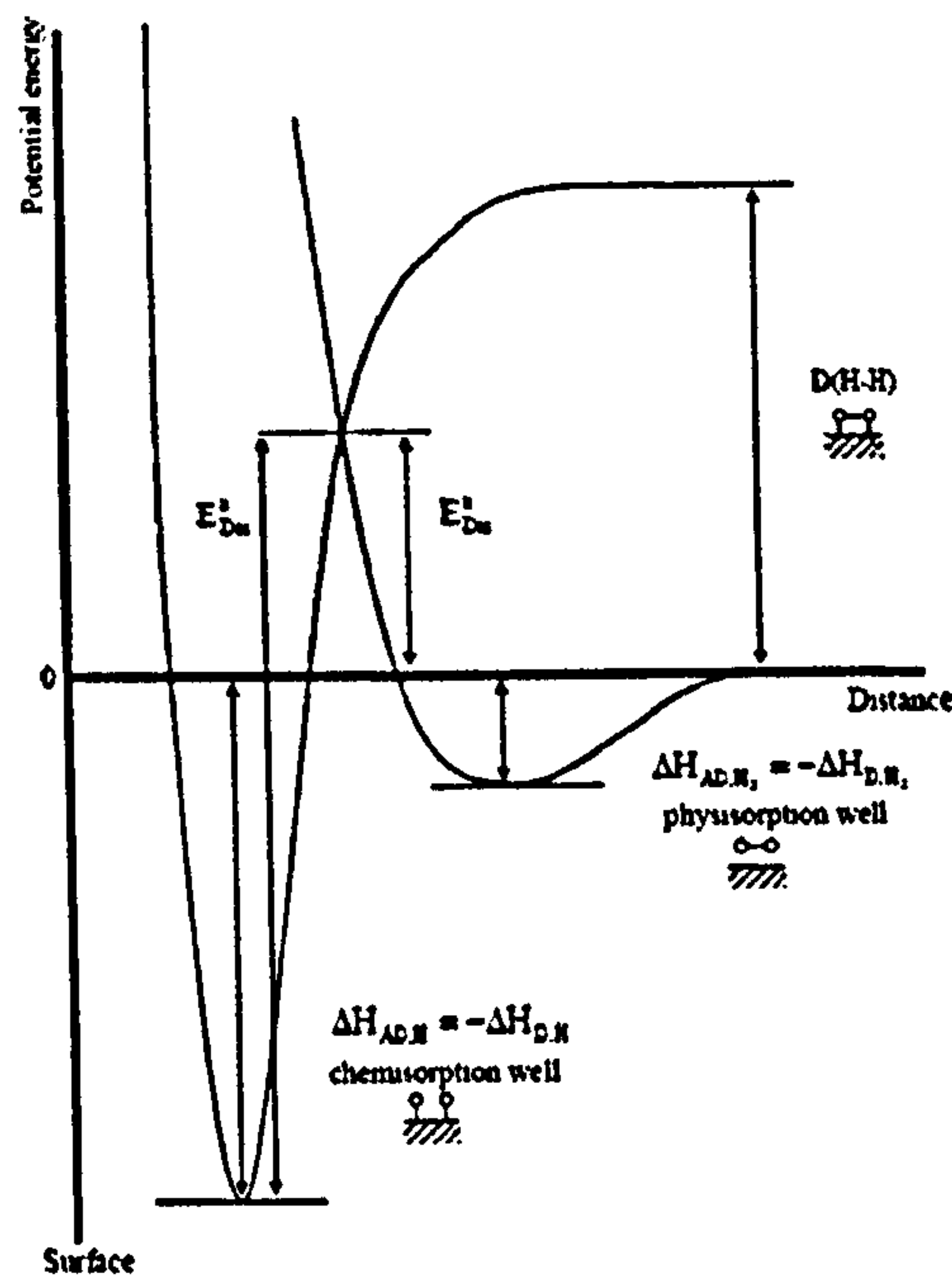


Figure 2.1: Interaction potential curves for hydrogen molecular physisorption and atomic chemisorption (Attard and Barnes, 1998).

The binding energy or adsorption energy is of the order of 0.01–0.1 eV (1–15 kJ.mol⁻¹). Due to this weak van der Waals interaction with no energy barrier, physisorption is in general fast but occurs only at cryogenic temperature. Only the first monolayer of adsorbate molecules experiences the surface potential, the second monolayer of gaseous molecules do not interact directly with the surface but with the first monolayer and so on. Therefore, the binding energy of the second layer of adsorbate molecules is similar to the latent heat of sublimation or vaporization of the adsorbate. Gas sorption studies at liquid nitrogen *ca.* 77 K are very common, consequently, in the case of H₂ gas the adsorption of the H₂ molecules at a temperature greater than the boiling point leads to the adsorption of up to one single monolayer while for N₂ adsorption multi-layers can occur (Brunauer et al., 1938). Typical materials physisorbing H₂ molecules are porous compounds such as carbon based materials (Dillon et al., 1997, Dillon and Heben, 2001, Schlappbach and Züttel, 2001, Walker, 2008), metal-organic frameworks (Blake et al., 1999, Lin et al., 2003, Yaghi et al., 2003, Jia et al., 2006, Yang et al., 2008), or zeolites (Yang et al., 2005a,b, 2006,

2007). For a uniform adsorption energy, the fractional coverage of the surface is usually defined by θ :

$$\theta(p) = \frac{\text{Number of adsorption sites occupied by the adsorbate}}{\text{Total number of surface adsorption sites}} \quad (2.1)$$

A complete monolayer is obtained for $\theta = 1$. The amount of adsorbate on a surface is determined at equilibrium over a range of pressures at constant temperature: the result $\theta(p)$ is an adsorption isotherm. It is possible to classify each material regarding their adsorption behaviour, their pore structure and the number of monolayers formed according to the Brunauer, Denning, Denning, Teller (BDDT) classification as shown on Figure 2.2 (Brunauer et al., 1940). A type I isotherm (Langmuir isotherm) is typical of microporous materials at low temperature starting with a linear fast adsorption (Henry's law) and at higher pressure a plateau corresponding to a complete monolayer. The coverage $\theta(p)$ can also be defined here by:

$$\theta(p) = \frac{Kp}{1 + Kp} \quad (2.2)$$

with K the equilibrium constant, and p the pressure.

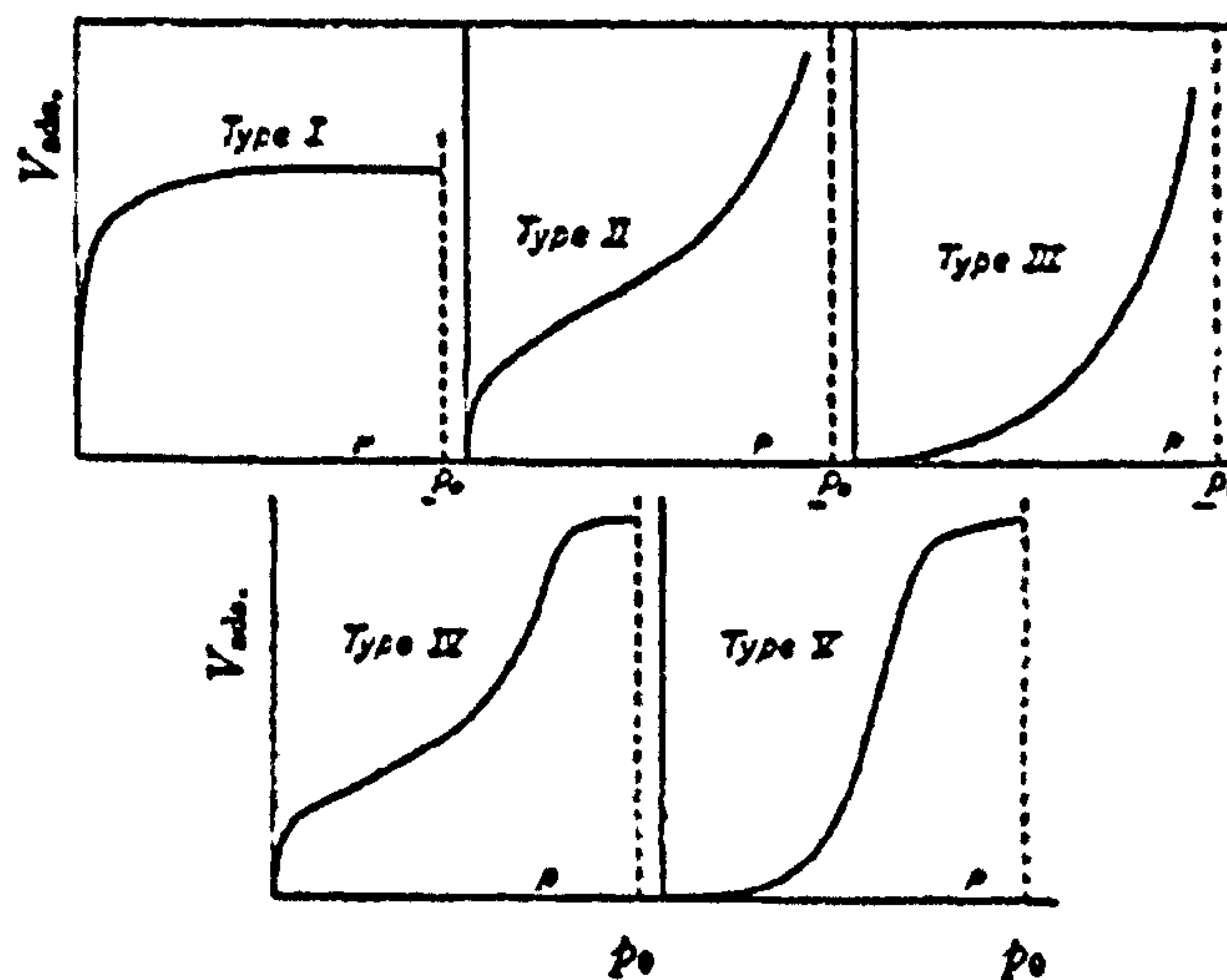


Figure 2.2: Five types of van der Waals adsorption isotherms (Brunauer et al., 1940).

However, as with all models, the Langmuir adsorption isotherm is based on

the severe approximation of a uniform adsorption site distribution with all the adsorption sites being equivalent. This is often not the case with for example the presence of specific adsorption sites to metal centres in metal-organic frameworks (Dinca et al., 2006). At low pressure both localized and non-localized physisorption are possible depending on the corresponding binding energies or heats of adsorption. The isosteric heat of adsorption of a gas on a solid surface is exothermic and is related to the type of bonding between a molecule and the surface. However, this also depends on the surface coverage $\theta(p)$ as intra-molecular interactions on the surface occur as adsorption sites are populated. Instead the isosteric enthalpy of adsorption ΔH_{AD}^0 is measured at similar coverage θ on two isotherms ($T_1 > T_2$). Therefore as the surface coverage increases (Attard and Barnes, 1998):

$$\log \left(\frac{p_1}{p_2} \right)_{\theta} = \frac{\Delta H_{AD}^0}{R} \left(\frac{1}{T_1} - \frac{1}{T_2} \right) \quad (2.3)$$

2.1.2 Chemisorption

Chemisorption is a dissociative mechanism and involves a chemical bond with a covalent character between the adsorbate and the adsorbent. It also differs from strong physisorption as the molecule is often dissociated before reacting with the surface. In Figure 2.1, considering the potential curve of a molecule approaching a solid surface, in order for the molecule to chemically react, it must overcome an activation energy barrier (or dissociation energy), E_{dis} , represented by the crossing of the two curves. The position of the crossing point determines whether the chemisorption is activated or not. In general for $E_{dis} > 0$ the mechanism is activated and requires energy to chemically adsorb and release H_2 with $LaNi_5$ and its alloys being an exception (Schlapbach and Züttel, 2001).

2.2 Metal-Hydrides

Metal, inter-metallic compounds and alloys react with hydrogen to form solid metal-hydrogen compounds also called metal-hydrides which involves a bulk reaction as opposed to a surface phenomenon. The thermodynamic of a metal-hydride formation from gaseous hydrogen is monitored using a

pressure - composition isotherm (Figure 2.3). The pressure increases with the C / H composition until a plateau region is reached corresponding to the amount of H₂ stored.

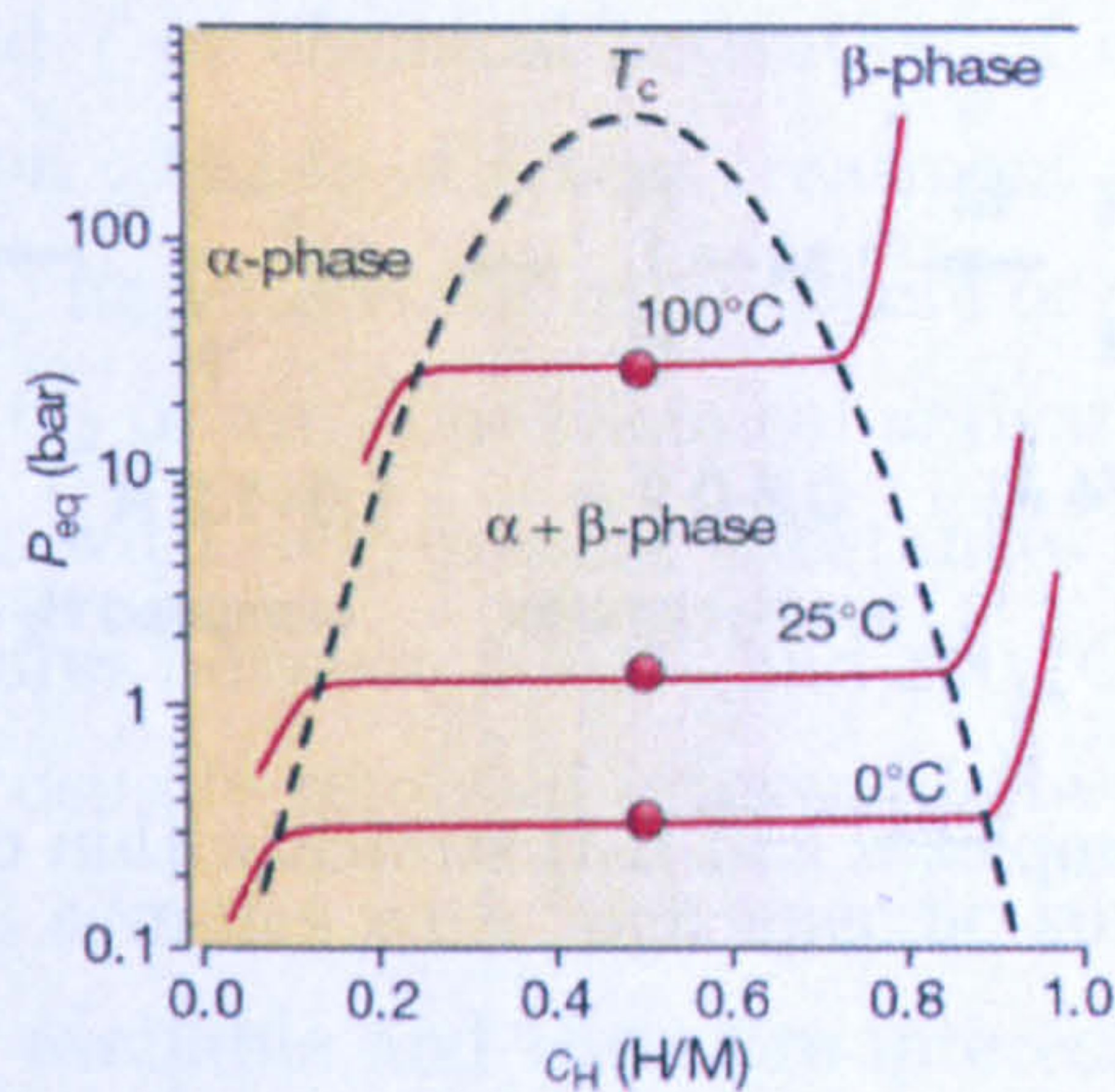


Figure 2.3: The vertical axis indicates the corresponding hydrogen pressure. From the slope of the van't Hoff plot, experimental values of the enthalpy of hydride formation H can be evaluated. The plateau pressure $p_{eq}(T)$ as a function of temperature is related to the changes H and S of enthalpy and entropy, respectively, by the van't Hoff equation: $\ln(p_{eq}/p_{eq}^0) = (-\Delta H/R)(1/T) + \Delta S/R$. Data were taken for LaNi₅ (Schlapbach and Züttel, 2001).

Metal-hydrides exhibit stronger hydrogen interactions (50-100 kJ.mol⁻¹) than molecular physisorption (4-10 kJ.mol⁻¹) but the activation (or dissociation) process limits their potential application for hydrogen storage because of a poor reversibility and slow kinetics although compounds such as LaNi₅ showed good hydrogen capacities *ca.* 2 wt. % at room temperature and 2 bar but are limited by the heavy elements such as La and Ni (Schlapbach and Züttel, 2001).

2.3 Kubas Complex

Kubas reported in 1984 a new type of chemical bonding with a stable H₂ molecule coordinated to a metal center within the complex M(CO)₃(PR₃)₂(H₂) identified by infrared spectroscopy where M = Mo, W; R = Cy, -*i*-Pr₃ which forms a phosphine (Kubas et al., 1984, Kubas, 2001). The molecular-hydrogen complex forms a sigma complex wherein a σ -bonding electron pair

2. LITERATURE REVIEW

(H-H) binds a ligand to a metal (Figure 2.4). This holds from the right balance between the back donation from a filled metal d orbital to the σ^* orbital of the H-H bond.

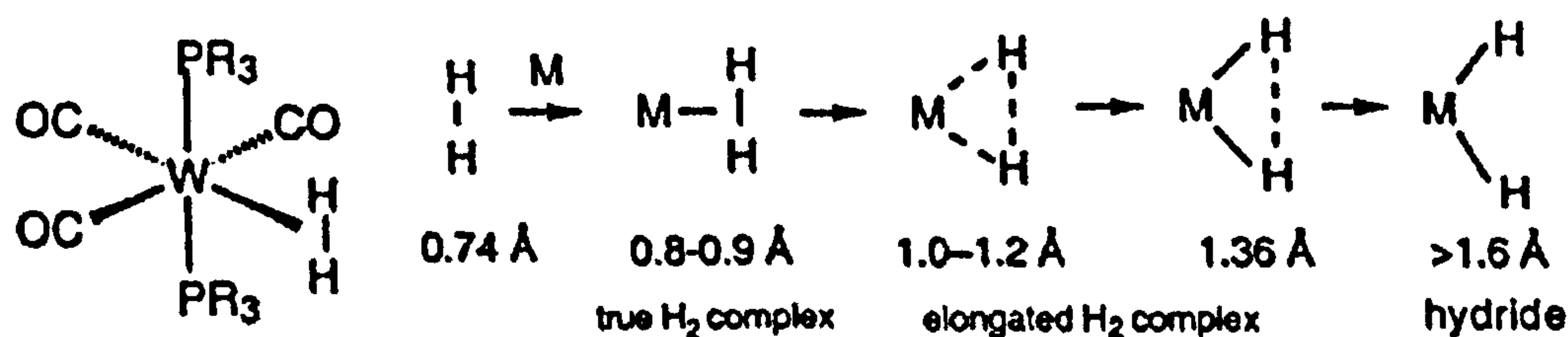


Figure 2.4: W(CO)₃ complexes and H-H stretch within complex (Kubas 2001).

H₂ is first stretched to about 20 % of its free value and reacts by oxidative addition with the metal center. H₂-complexes exhibit various H-H bond lengths ranging from 0.8 to 1.36 Å. Hydrogen can be store in its molecular form or split into two atoms. The binding energy range of interest, in order to meet the DOE 2015 targets, is between 10-50 kJ.mol⁻¹. In essence it represents an intermediate bonding type between the non-dissociative physisorption and the dissociative chemisorption, most likely maintaining the H₂ molecular form as found for Kubas complexes. Fundamental principles of sorption for solid state hydrogen storage were covered. Fast kinetics and low density compounds with good reversibility are targeted to meet the DoE requirements. Two important classes of materials physisorbing molecular hydrogen will be reviewed: carbon based materials and metal-organic frameworks.

2.4 Carbon Materials

Three types of carbon materials will be addressed: activated carbons (ACs), carbon nanotubes (CNTs) and graphitic nanofibres (GNFs). This section will review the structural parameters responsible for hydrogen sorption and the potential engineering routes to enhance hydrogen capacity as reported by the literature.

2.4.1 Activated Carbons

AC materials were amongst the first carbon adsorbents investigated. Back in 1966, Kidnay and Hiza were one of the first groups working on adsorption properties of ACs at low temperature (Kidnay and Hiza, 1966). ACs result from the thermal and / or chemical activation of carbon-rich precursors. The thermal activation consists of a heat treatment at a temperature range of 700 °C and 1000 °C under a static atmosphere or dynamic flow of oxidizing gas such as CO₂, O₂ or air. The chemical activation is essentially based on chemical reactions with dehydrating substances such as ZnCl₂, H₃PO₃ or KOH at temperatures between 500 °C and 800 °C (Strobel et al., 2006). Chemical agents are usually removed afterwards by evaporation or simply washed. Commercial samples with high specific surface areas up to 3000 m².g⁻¹ are currently available and therefore interesting for sorption applications (Chahine and Bose, 1994, Hirscher and Panella, 2005). In general a typical isotherm of an AC sample is that of a microporous type I, with hydrogen weight uptakes up to 6.7 wt.% at 77 K and 20 bar (Yang et al., 2005b).

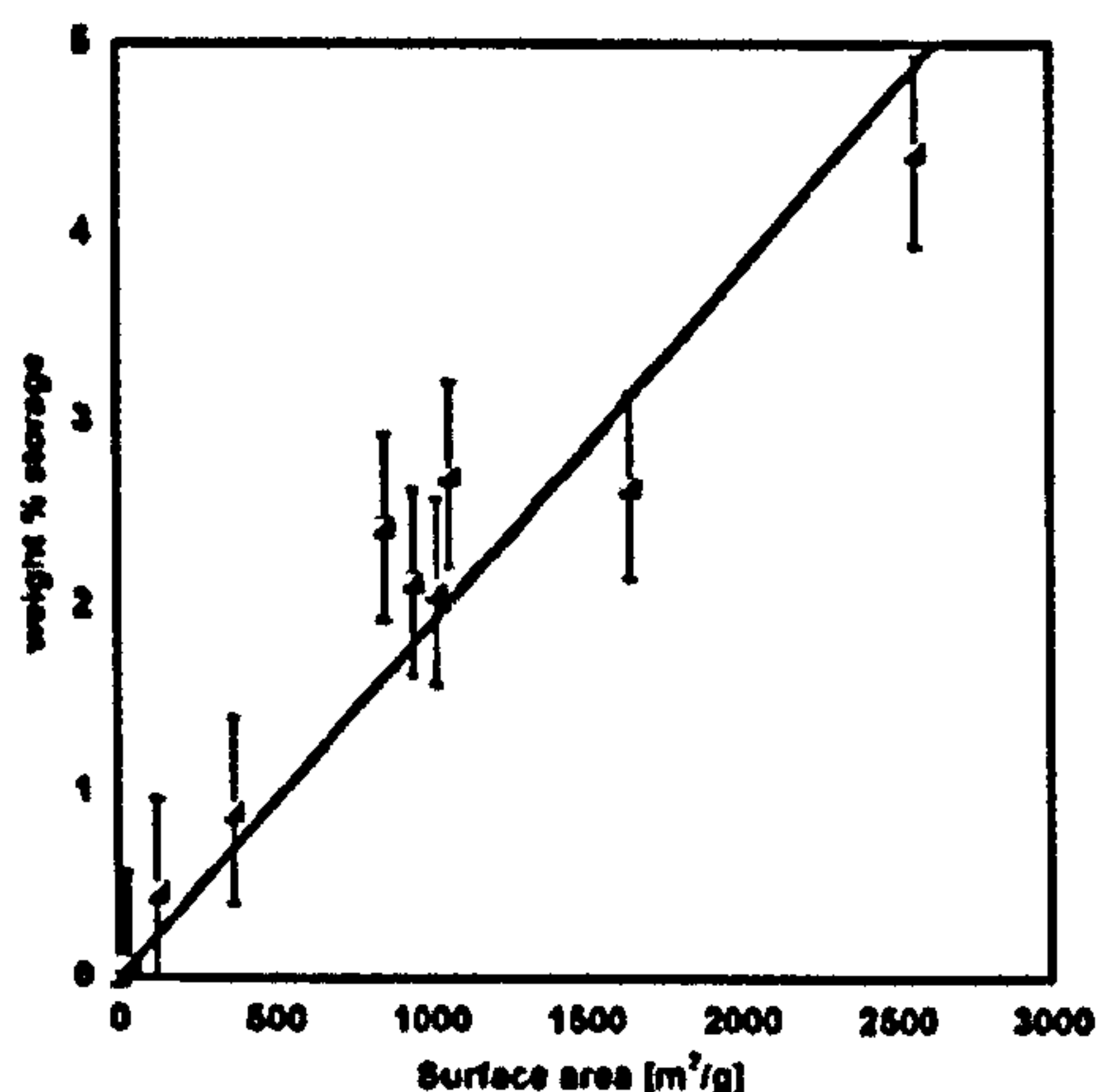


Figure 2.5: Linear relationship between hydrogen storage capacity for different carbon samples and the specific surface area at 77 K and 70 bar (Hirscher and Panella, 2005).

ACs can exhibit either a wide range of pores of different size with micropores (width < 2 nm), mesopores (width 2-50 nm), and macropores (width > 50 nm) (Figure 2.6) or just one type of pore with a narrow pore size

distribution (Purewal et al., 2009). The pore size is a critical parameter as micropores tend to be occupied first with H_2 molecules compared to bigger pores (Rouquerol et al., 1998). These pores are most beneficial because the surface potentials on the walls overlap and allow the creation of more favourable adsorption sites for H_2 molecules with an optimum diameter around 7 Å and a heat of adsorption up to 9 kJ.mol⁻¹ at low coverage of the surface (Dillon et al., 1997, Strobel et al., 1999, Dillon and Heben, 2001, Strobel et al., 2006, Wang and Johnson, 1999). Above cryogenic temperatures and under moderate pressure, pure ACs are not as efficient because of the weak van der Waals' interactions between the surface and H_2 molecules. In principle, the entire surface can interact with H_2 molecules but only micro-pores are strong enough to retain the H_2 molecules. However, up to now it is still difficult to combined high surface area and a narrow pore size distribution due to the sample preparation. In practice, physical / thermal treatments are used to achieve the optimum pore size distribution (Purewal et al., 2009). However, H_2 adsorption enthalpy is not necessarily the absolute key parameter. Purewall *et al.* showed that ACs with a low H_2 adsorption enthalpy, a broad pore size distribution and a high surface area had a higher H_2 adsorption capacity than those with a high adsorption enthalpy, a narrow pore size distribution and a low surface area. However, to our knowledge no systematic study regarding the effect of the pore size distribution and the surface area upon physisorption has been reported up to now.

ACs remain good candidates for solid hydrogen storage as they exhibit: high specific surface area, good reversibility and fast kinetics at cryogenic temperatures and pressures up to 30 MPa. Despite the van der Waals' interactions, these materials are relatively low-cost candidates. Here the challenge is to develop engineering routes that would allow ACs materials to combine an optimized pore size distribution and a high surface area.

2.4.2 Fullerenes

First it is important to distinguish graphene from graphite. Graphene is a single layer of carbon atoms within the graphite structure. It simply

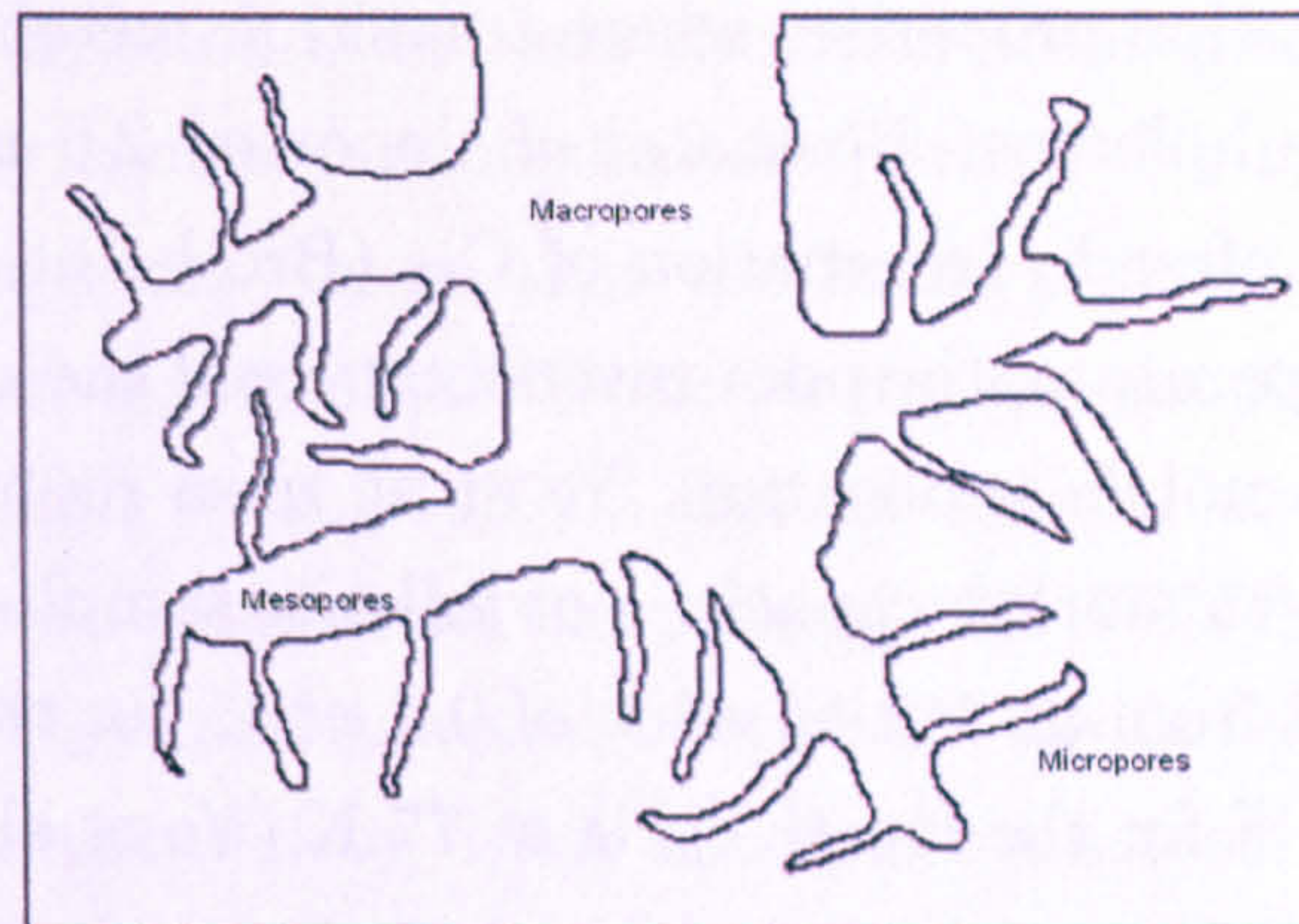


Figure 2.6: Two dimensional representation of the pore structure of granular activated carbon (Rodriguez-Reinoso, 2002).

represents the building unit for CNTs and fullerenes (Dresselhaus et al., 1992, 1995, 1998, Dresselhaus, 1999, Dresselhaus et al., 1999, Dresselhaus and Avouris, 2001, Dresselhaus and Endo, 2001, Dresselhaus, 2004). The first carbon nano-materials discovered was buckminsterfullerene (C_{60}) in 1985 and as the result of 12 pentagonal cells being added to hexagonal cells formed by a graphene sheet (Figure 2.7) (Kroto et al., 1985).

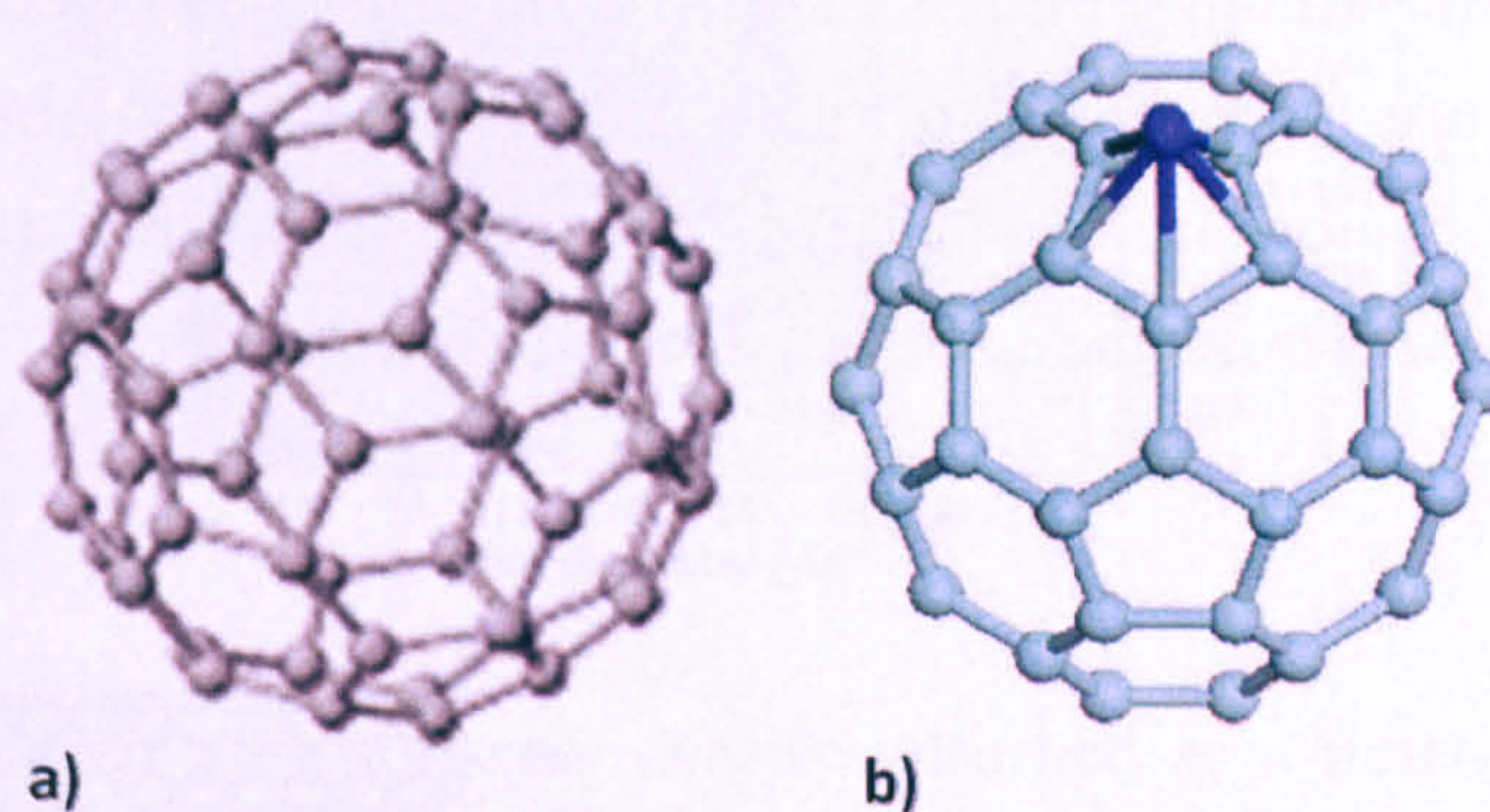


Figure 2.7: a) C_{60} fullerene. b) C_{60} doped with Ti atoms in dark blue (exohedral site) (Yildirim et al., 2005).

In general pure fullerenes are very poor surface area materials typically around 10 to $50 \text{ m}^2.\text{g}^{-1}$ with no open pores structure and very low hydrogen storage capacity. However, first-principle calculations reported by different groups on C_{60} (Yildirim et al., 2005) *ca.* 7 to $8 \text{ wt.}\%$ under ambient conditions and other buckyballs (Zhang et al., 2009), demonstrated

their potential sorption properties where transition metals such as Ti were coordinated to the fullerene. Brosha *et al.* reported 2.6 wt.% of hydrogen released at 673 K after hydrogenation of C₆₀ (Brosha *et al.*, 1999). However, the high temperature, the poor reversibility and the slow kinetics were not favourable for mobile application. Ye *et al.* even reported an improvement of the hydrogen storage capacities of fullerite samples (mixture of C₆₀ and C₇₀) increased from an initial value of 0.4 wt.% for the first cycle to a capacity of 4.4 wt.% for the fourth cycle at 77 K (Ye *et al.*, 2000).

2.4.3 Nanotubes

2.4.3.1 Single-Walled Carbon Nanotubes

Single-walled carbon nanotubes (SWCNTs) consist of a graphene sheet rolled cylindrically with nanometre size diameters typically from 1 to 15 nm and a fullerene-like cap at each end (Figure 2.8.a). The presence of dangling bonds corresponds to high energy states which favours the curvature of the graphene layer (Louie, 2001, Dresselhaus, 1999, Dresselhaus and Endo, 2001) combining planar sp^2 with some sp^3 bondings. Therefore SWCNTs with small diameter will have a more reactive surface than SWCNTs with infinite diameter equivalent to pure graphene layers (Cheng *et al.*, 2005). There are many ways to fold a graphene sheet to obtain a SWCNT depending on the orientation of the hexagonal network: armchair, zigzag, and chiral types (Dresselhaus *et al.*, 1995) (Figure 2.8.b).

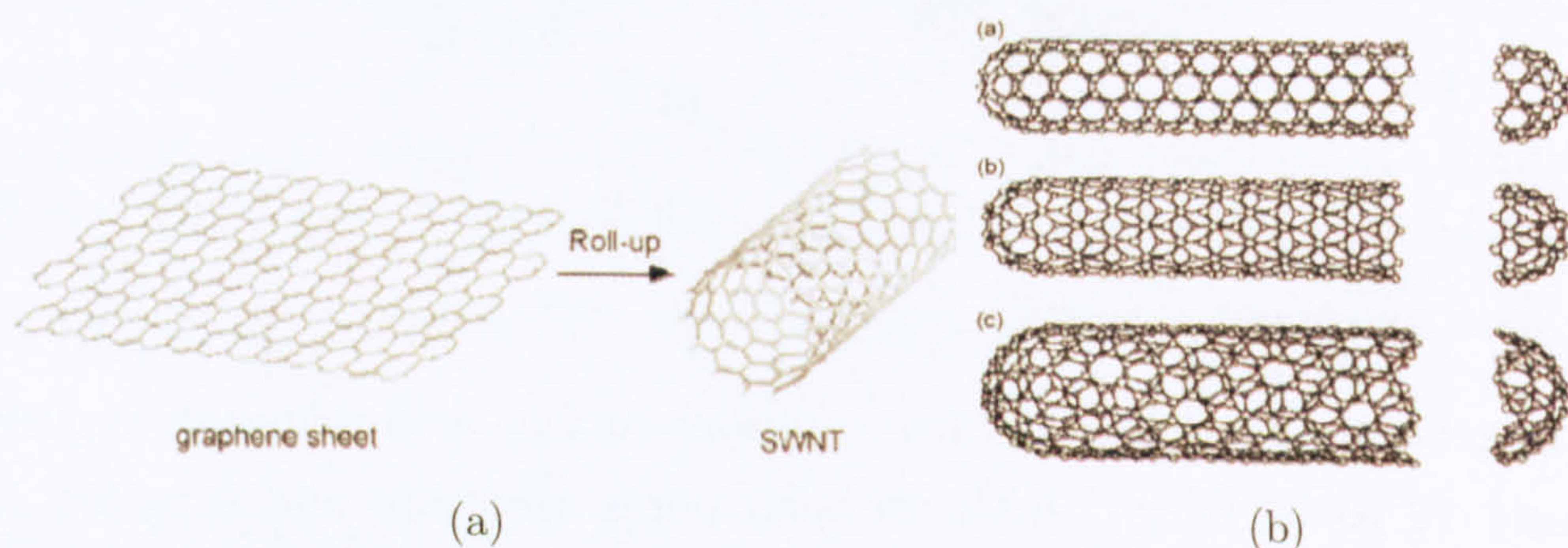


Figure 2.8: a) Graphene sheet rolled up to form a SWCNT. b) SWCNT configuration: (a) Armchair, (b) Zigzag, and (c) Chiral with fullerene caps at each end. Reproduced from (Strobel *et al.*, 2006).

Early work suggested radial and circumferential quantum confinements inside the hollow centre (endohedral site) where H_2 molecules would be adsorbed with a density close that the liquid density although this was extrapolated from a low SWCNT concentration sample measured at low temperature (Dillon et al., 1997). Instead Benard and Chahine showed that pores can be created from the packing of SWCNTs. They also found that the highest H_2 capacity would be with SWCNTs having tube diameter of 12-14 Å and separated by 6-7 Å which is consistent with a pore size of around 6-7 Å (Figure 2.9) (Benard and Chahine, 2007). Wang and Johnson also simulated the sorption properties of an isolated SWCNT, arrays of SWCNTs and an idealized carbon slit pore and found that the latter showed better sorption capacities at low temperature with a pore size around 7 Å characterised by the distance between two CNTs. SWCNTs have surface areas up to $1000 \text{ m}^2.\text{g}^{-1}$ as reported by Poirier *et al.* after heat treatment of commercial samples (CNI) (Poirier et al., 2006).

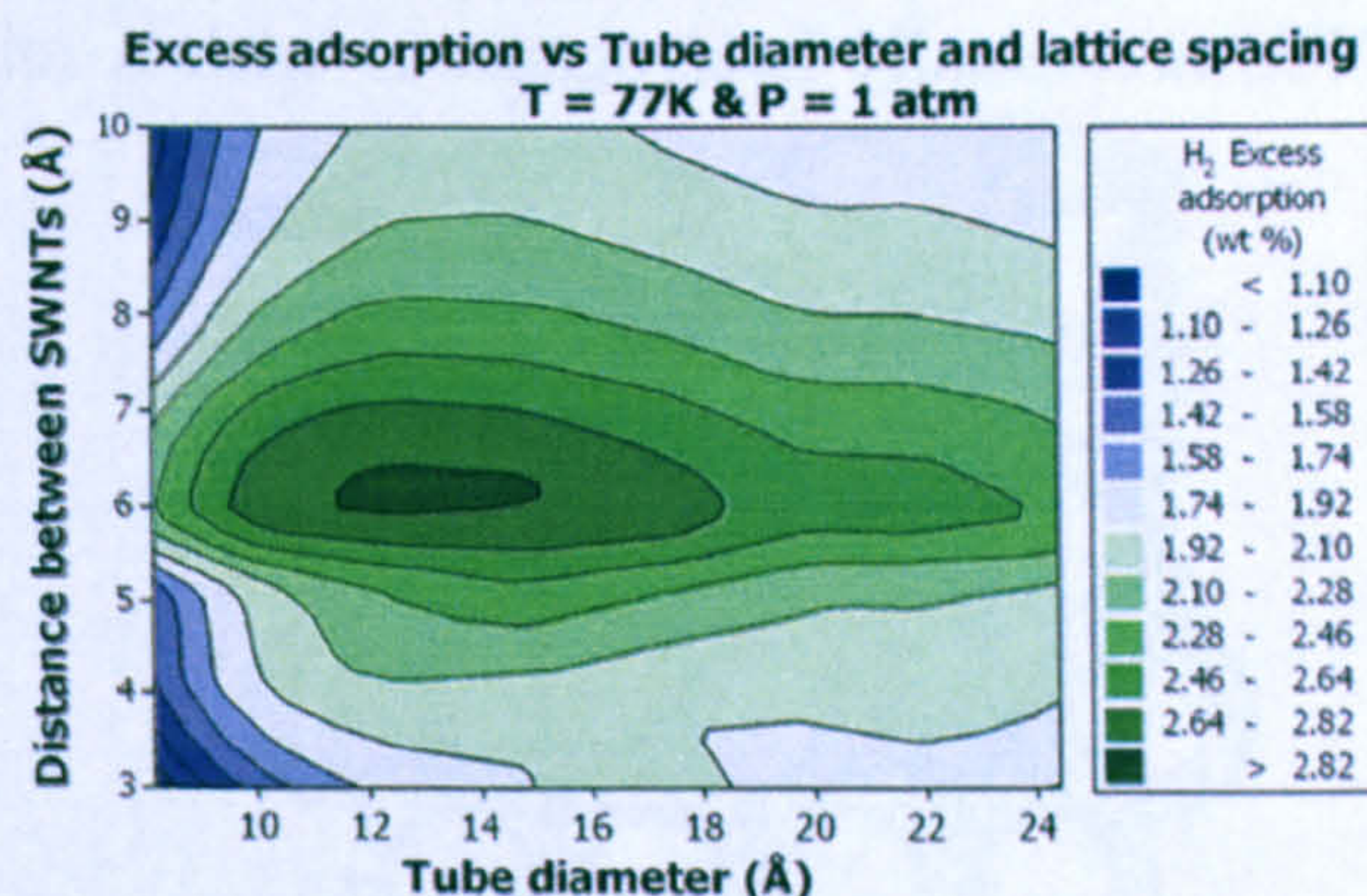


Figure 2.9: Contour plot of excess density adsorbed as a function of SWCNT diameter and lattice spacing at 77 K and 1 atm (bundle of seven units), obtained using grand canonical Monte-Carlo simulations of adsorption of hydrogen on a SWCNT. The hydrogen-carbon interactions were modelled using standard Lennard-Jones potential (Benard and Chahine, 2007).

2.4.3.2 Multi-Walled Carbon Nanotubes

Multi-walled carbon nanotubes (MWCNTs) are composed of layers of nested concentric cylinders of graphene with a hollow center terminated by a

2. LITERATURE REVIEW

fullerene-like cap at each end. They are usually microns in length. The concentric nanotubes which can vary from 2 to 50 are separated from one another by a distance of approximately 0.34 nm. The inner and outer diameters are typically 2-10 and 15-30 nm respectively. It was in fact the first type of carbon nanotubes discovered back in 1991 by Iijima while vaporizing carbon in an electric arc discharge (Iijima, 1991). Their synthesis has been improved with arc discharge process, laser ablation, and decomposition of hydrocarbons through chemical vapour deposition. Considering a bundle of MWCNTs, different adsorption sites were suggested by Pradhan *et al.* (Pradhan et al., 2002) and later by Melancon and Benard (Melancon and Benard, 2004) for physisorbed H_2 molecules (Figure 2.10): the groove, the channel, the surface and the core. While the first three are opened and accessible to H_2 molecules (exohedral sites), the latter is blocked by fullerene-like caps and is only accessible after removing (endohedral site). In essence, MWCNTs and SWCNTs have similar adsorption properties which depend more on their diameters and their packing arrangement than on their chirality. Here, the challenge is to optimize these two parameters.

As-prepared CNTs are usually heterogeneous with a mixture of SWC-

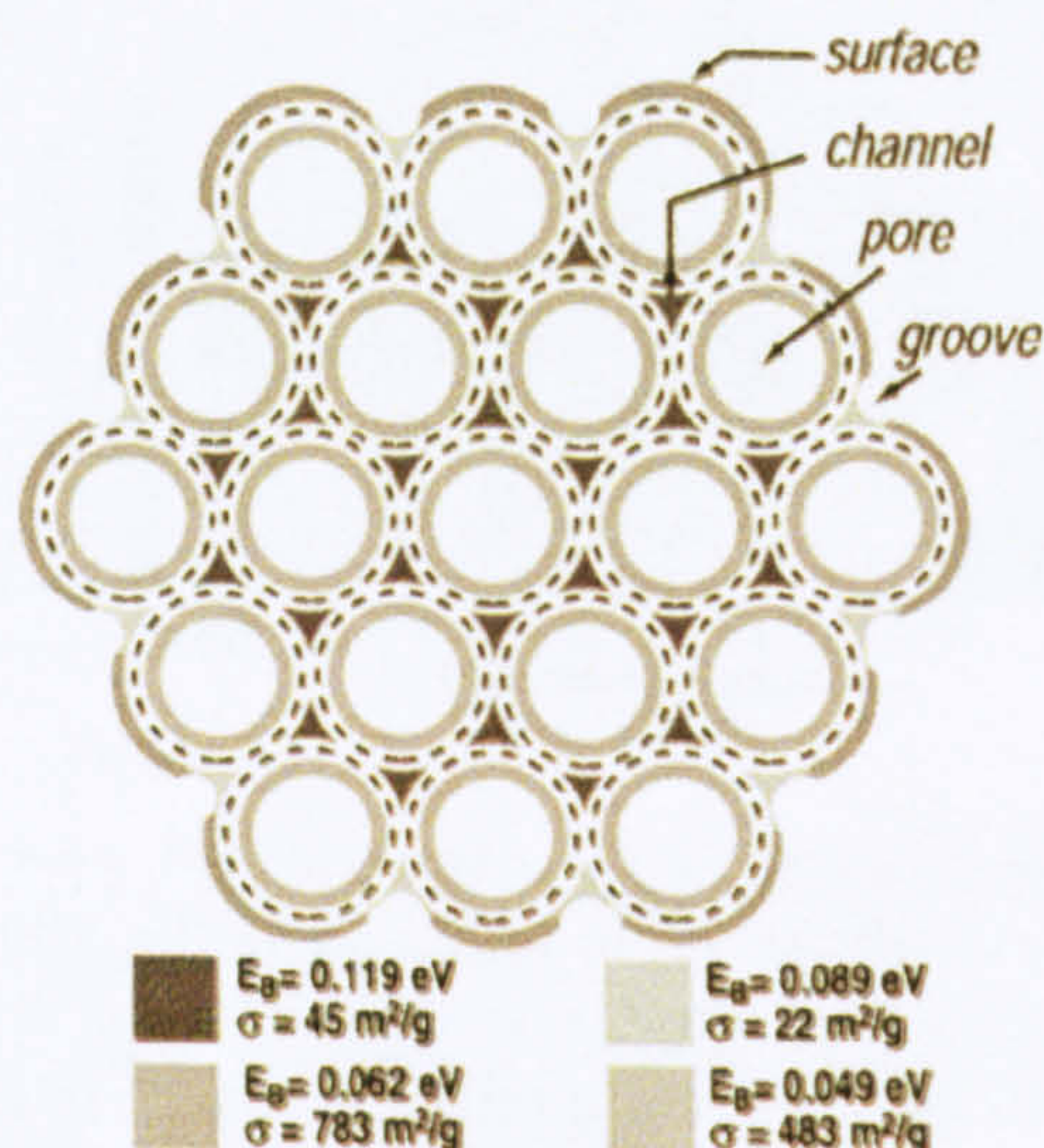


Figure 2.10: Adsorption site distribution within a bundle of CNTs (Pradhan et al., 2002).

NTs, MWCNTs of various diameters and with some amorphous phases (*e.g.*: soot). It is always necessary to purify the sample in order to remove any undesired species depending on the quality of the as-prepared sample. For

SWNCTs and MWCNTs, parameters such as structural defects, tube diameter, length, arrangements of tubes in bundles will determine the sorption properties of the nanotube (Rzepka et al., 1998). Theoretical calculations have shown that a graphene sheet with a specific surface area of $1.315 \text{ m}^2 \cdot \text{g}^{-1}$ would correspond to a hydrogen storage capacity of 2 wt.% or 0.4 H per carbon at 77 K (Schlapbach and Züttel, 2001).

2.4.3.3 Graphitic Nanofibres

The nomenclature gathers under the same terminology graphitic nanofibre and graphitic fibre. The former consist of fibres with nanometre size diameters typically 10 nm to 100 nm, while the latter is used for fibres of larger diameters. Whereas SWCNTs, MWCNTs and fullerenes are graphene structures with a hollow centre, GNFs consists of graphitic planes stacked with various angular orientations with respect to the fibre axis (Figure 2.12). Therefore the surface topology is totally different from that of SWCNTs and MWCNTs.

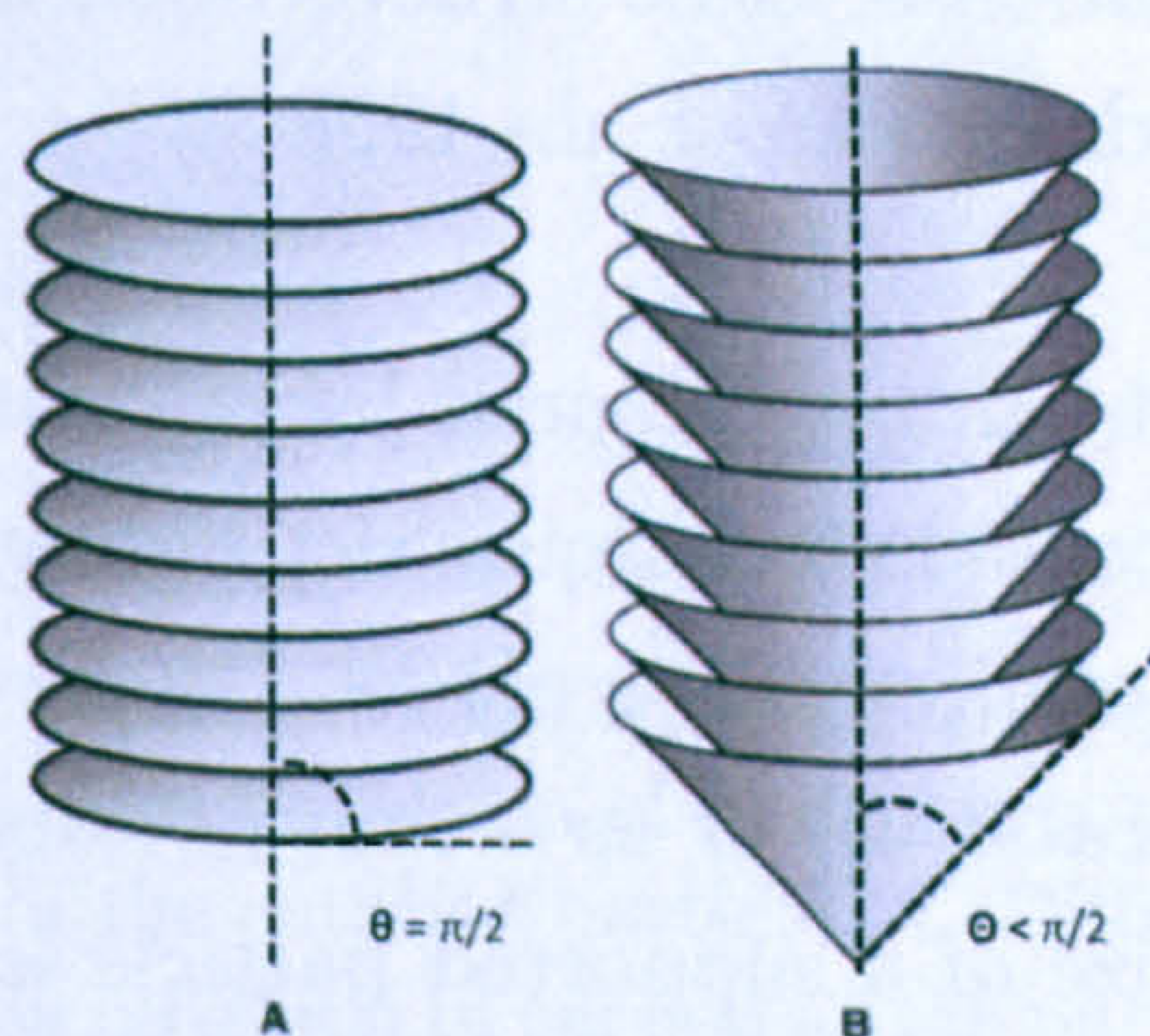


Figure 2.11: Scheme of GNF types: A) Platelet and B) Herringbone (McCaldin et al., 2006).

The graphitic planes are stacked at different angles with respect to the fibre axis leading to two types of GNFs: herringbone (with $0 < \theta < \frac{\pi}{2}$), and platelet (with $\theta = \frac{\pi}{2}$) GNFs as shown on Figure 2.11. Herringbone type GNFs can either have a hollow or filled core structure while platelet type GNFs do not exhibit any hollow core. The cheapest and most flexible way of producing GNFs is by chemical vapor deposition (CVD). An excellent review of the catalytic synthesis of carbon nanotubes and nanofibres can

be found in (De Jong and Geus, 2000). Both the thermodynamics of the steady-state growth and the nucleation phase of the CVD are now reasonably well understood as the thermal decomposition of a carbon containing gas over one side of a metal catalyst followed by the growth of graphitic planes on the other side. Hoogenraad proposed a good model for the nucleation and the growth phase (Hoogenraad, 1995). The choice of the metal catalyst is a primary parameter as it should be able to dissolve the carbon source to form a metal-carbide. Alstrup also reported that specific facets of the metal particle would favour either the feedstock decomposition and/or the nucleation of basal planes. For instance Ni (110) and Ni (100) surfaces are much more active for methane dissociation than is the Ni (111) surface to the growth of carbon fibres (Schouten et al., 1977, 1979, Alstrup, 1988). The carbon would then diffuse through the bulk and on the surface of the catalyst. The carbon source is generally a mixture of hydrocarbons and hydrogen gases flowing dynamically over the metal catalyst. Nolan *et al.* suggested that H_2 gas is a critical parameter for the GNF growth as H can terminate the large number of dangling bonds at the edges of graphite layers avoiding the formation of close structures such as fullerenes and CNTs with no dangling bonds (Nolan et al., 1998).

The metal catalyst can be prepared by wet catalysis, thin film, sol-gel, thick metal catalyst, colloids techniques depending on the application. It is usually a transition metal (or alloys of) Ni, Co, Fe which can be either on a substrate (supported catalyst) or as a thin powder (unsupported catalyst) (Figure 2.12). The size of a supported particle is typically 10-50 nm and around 100 nm for an unsupported catalyst. The CVD using the floating catalyst is the most promising, flexible and cheapest catalytic method to produce GNFs. Moreover GNFs generated by CVD can be used directly without further purification unless the metal catalyst and the amorphous carbon are to be removed. The catalytic decomposition of the feedstock gas occurs at temperatures varying typically from 500 °C to 1000 °C which is highly correlated to the specific catalyst activity (Teo et al., 2003).

GNFs are characterised by their diameter, length, graphitic basal planes, stacking angles, and surface texture. It is possible to synthesize GNFs

within a range of diameters and lengths by playing with the nature, the size of the catalyst, and the reaction temperature (Bououdina et al., 2005, 2006, McCaldin et al., 2006). The final size of the metal particle will determine the diameter of the fibre whereas the temperature will have a direct effect upon its purity/crystallinity. At high temperature the nucleation starts before the metal is entirely covered by the carbon. This leads to high growth rates which may be desirable for mass-production synthesis but with the disadvantage of having less crystalline carbon along the fibre axis. At lower temperature the metal catalyst/gas and metal catalyst/carbon interfaces are saturated as the diffusion and nucleation are rather slow which gives GNFs with hardly any amorphous phases in the centre. In theory the catalytic growth will always occur as long as the metal catalyst/phase interface exists. However, in almost all the cases the growth is stopped because of encapsulated metal particles or simply by the user.

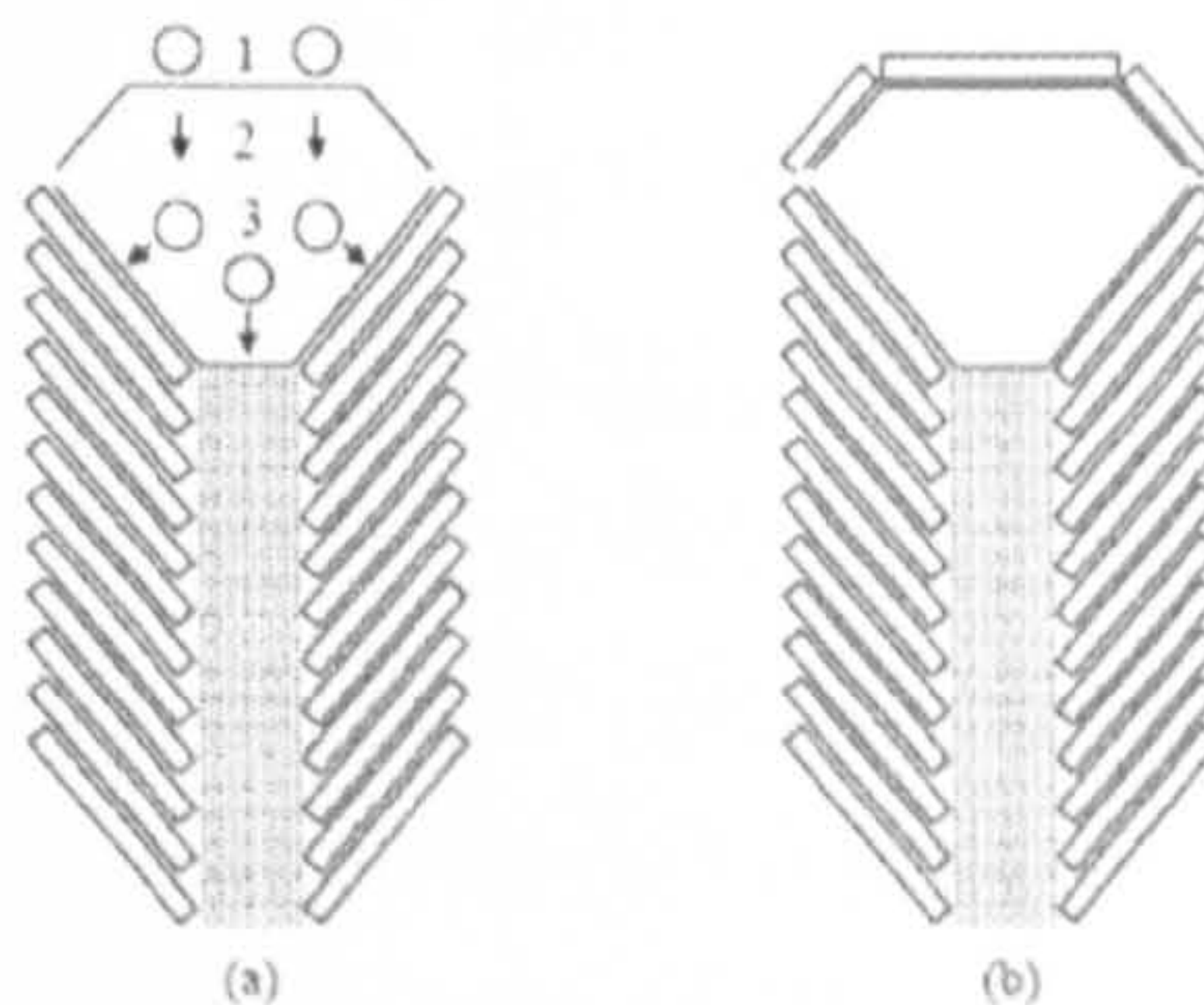


Figure 2.12: (a) Schematic representation showing the key steps in the growth of a GNF. 1. Adsorption and decomposition of hydrocarbon gas at the particle-gas interface on the front face of the catalyst particle. 2. Diffusion of carbon through the catalyst particle. 3. Precipitation of carbon at the particle-nanofibre interface on the rear face of the catalyst particle (b) Schematic representation of a GNF that has ceased growth due to a carbon over layer, forming over the leading face (Rodriguez, 1993).

GNFs produced by CVD are generally purified in order to remove the metal catalyst and the amorphous phase on the surface depending on its utilization (McCaldin et al., 2006). In general GNFs are low specific surface area (SSA) materials typically around $100 \text{ m}^2.\text{g}^{-1}$ and show rather low hydrogen storage capacities less than 1 *wt.%* (at 77 K and 105 bar) although early studies reported their exceptional properties leading to an outburst of interest for GNFs compounds (Chambers et al., 1998). Typical

2. LITERATURE REVIEW

GNF isotherms reveal a micro-porous behaviour similar to CNTs. The adsorption site distribution on GNFs is slightly different from that for carbon nanotubes since GNFs often do not have a hollow centre. The adsorption occurs essentially on the external surface of the graphitic fibre (exohedral sites). The only way to enhance the physisorption is either to increase the low specific surface area (more delocalized adsorption sites) or to add specific hetero-atoms onto the surface (more specific adsorption sites) in order to affect locally change the electronic structure of the carbon atoms. The graphitic interlayer distance *ca.* 3.354 Å does not take into account the electron cloud around each carbon which makes it too small for the spontaneous intercalation of “free” H₂ molecules *ca.* 2.9 Å. Therefore, the expansion within the graphitic plates surely will be essential for any significant uptake in graphite structures. The next paragraphs will introduce two engineering options.

2.5 Nitrogen Doping

The creation of more adsorption sites for hydrogen molecules could be an alternative for low surface area materials. Up to now the direct effect of hetero-species regarding their position within the carbon network, and their doping level upon the hydrogen interactions are not fully understood. In layered *sp*² carbon systems, hetero-atomic species doping could locally change the electronic structure. For instance, if B (one electron less than C) replaces some atoms C in a graphene layer, the electronic structure lacks one electron, which leads to a p-type character. From the chemical point of view, the resulting structure is more likely to react with donor-type molecules. In the case N doping (one electron more than C) the electronic structure exceeds with one electron which either gives a *p*- or *n*-type character depending on the N-doping level and the number of C removed (via substitution) (Terrones 2004). Density functional theory (DFT) calculations on B / N-doped SWCNTs showed in case of H₂ molecular physisorption, both B- and N-doping would decrease the adsorption energies in SWCNTs. Sankaran *et al.* suggested atomic hydrogen chemisorbed onto the surface of carbon nanotubes with an elongated H-H bond length *ca.* 0.825 Å but with unphysical dissociation energies *ca.* 0.22 eV (Sankaran and Viswanathan,

2008, Sankaran et al., 2008). Extensive work was carried out on BN-doped fullerenes and other carbon nanostructures suggesting it would enhance hydrogen interactions (Oku et al., 2001a,b, 2006) but little work was reported on N-doping of graphite-like structures for hydrogen storage. Instead N incorporation onto carbon compounds was studied because it would enhance their conduction properties (Terrones et al., 2004) or for their catalytic growth (He et al., 2006, Zheng et al., 2006). In the first attempts to integrate N species within the carbon network, substitution reactions such as the pyrolysis of N containing source with SWCNs were commonly used. Terrones *et al.* proposed an efficient route to produce large arrays of CN_x nanofibres by pyrolysis of ferrocene / melamine mixtures at high temperature (Terrones et al., 1999). The nanostructures exhibited 2 % N-doping level. More recently, Glerup *et al.* reported on N-doped carbon nanostructures using directly aerosol method initially developed for pristine CNTs with N doping level upto 20 atom % (Glerup et al., 2003). However, no sorption investigation was carried out on both studies. Badzian *et al.* synthesized N-doped carbon nanotubes by CVD diamond synthesis and addition of nitrogen gas to the CH_4 / H_2 gas mixture. The resulting compounds showed 0.7 *wt. %* gravimetrically at room temperature and 6 MPa (Badzian et al., 2001). Low cost and efficient production methods are essential for potential hydrogen storage media. More recently, Yang *et al.* successfully reported on the N-doping synthesis of microporous carbon using zeolites template and an organic precursor as carbon-nitrogen source (Yang et al., 2005a).

2.6 Exfoliation Via Intercalation

The location of hetero-atomic species within the carbon network is not limited to its apparent surface. It is possible to obtain graphite intercalated compounds (GICs) and expand the graphitic inter-layers because of the weak van der Waals interaction between layers associated with the sp^2 bonding in graphite (Schaffautl, 1841). The intercalation phenomenon occurs in general with highly anisotropic layered structures with very weak interlayer forces compared to intra-layer bonding using the chemical integration of atomic or molecular species between graphitic layers. A large

2. LITERATURE REVIEW

number of reagents can be intercalated into graphitic materials. The periodicity regarding the graphitic layers is also known as the intercalation stage n (Figure 2.13.a). It simply represents the number of graphitic layers between adjacent intercalate layers and can be easily identified by x-ray diffraction (XRD) technique (Figure 2.13.b). For instance GICs compounds prepared by chemical oxidation are usually stage 1 to 4.

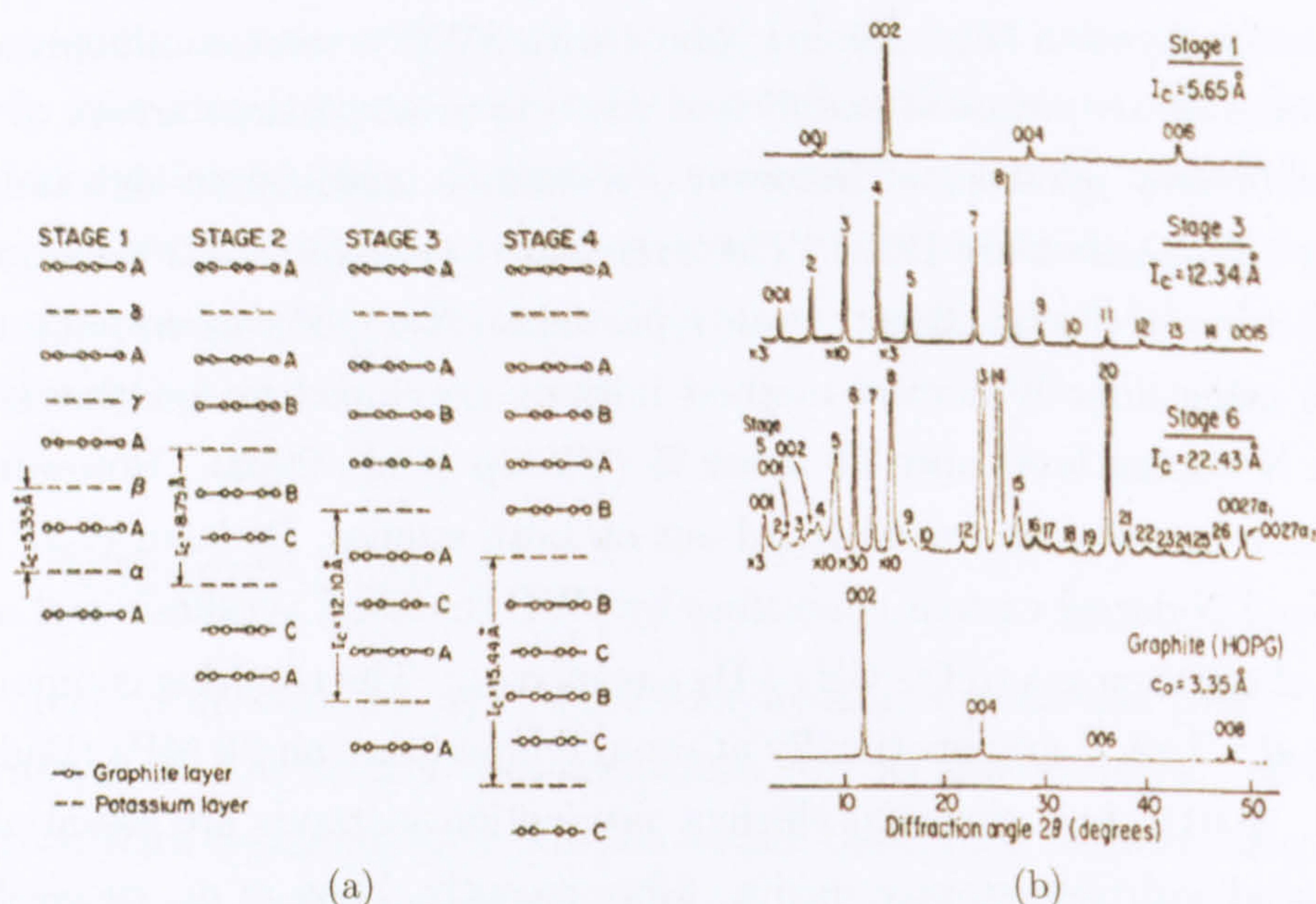


Figure 2.13: a) Possible intercalation stages of K intercalated GIC. b) X-ray powder diffraction patterns of different stage GICs (Dresselhaus and Dresselhaus, 2002).

GICs were mainly studied for their electrical properties as they are determined by the donor / acceptor character of the intercalate. In general donor GICs are formed with alkali metal K, Rb, Cs, and Li, or other alkali earth metals and metal alloys. For acceptor GICs, Lewis acid intercalants such as Br_2 or strong Brönsted acids such as H_2SO_4 and HNO_3 can also be used. The size and chemical affinity of a molecule determines whether or not the intercalation is possible. K and Li intercalated GICs have been already investigated for solid hydrogen storage purposes. Chen *et al.* reported on Li- K- intercalated carbon nanotubes with exceptional sorption capacity *ca.* 20 wt.% at room temperature although it was later explained that the measured change was due to moisture contamination (Chen *et al.*,

1999). Toyoda *et al.* exfoliated intercalated graphite flakes by thermal shock at high temperature *ca.* 1000 °C (Toyoda *et al.*, 2001b). Exfoliated graphitic compounds were widely investigated as thermal insulators and recent studies reported on good sorption properties of heavy oil. The idea is to use intercalent agents and a thermal shock in order to rapidly increase the graphitic interlayer space. Lueking *et al.* successfully exfoliated GNFs following the same experimental procedure as Toyoda and managed to create small pockets of 50-100 Å (Figure 2.14). Although no XRD experiment was made, nitrogen adsorption experiments revealed an exceptional increase of the surface area *ca.* 47 to 550 m².g⁻¹. However the pore size achieved remains too large compared to a 5-10 Å micro-pore (Lueking *et al.*, 2007).

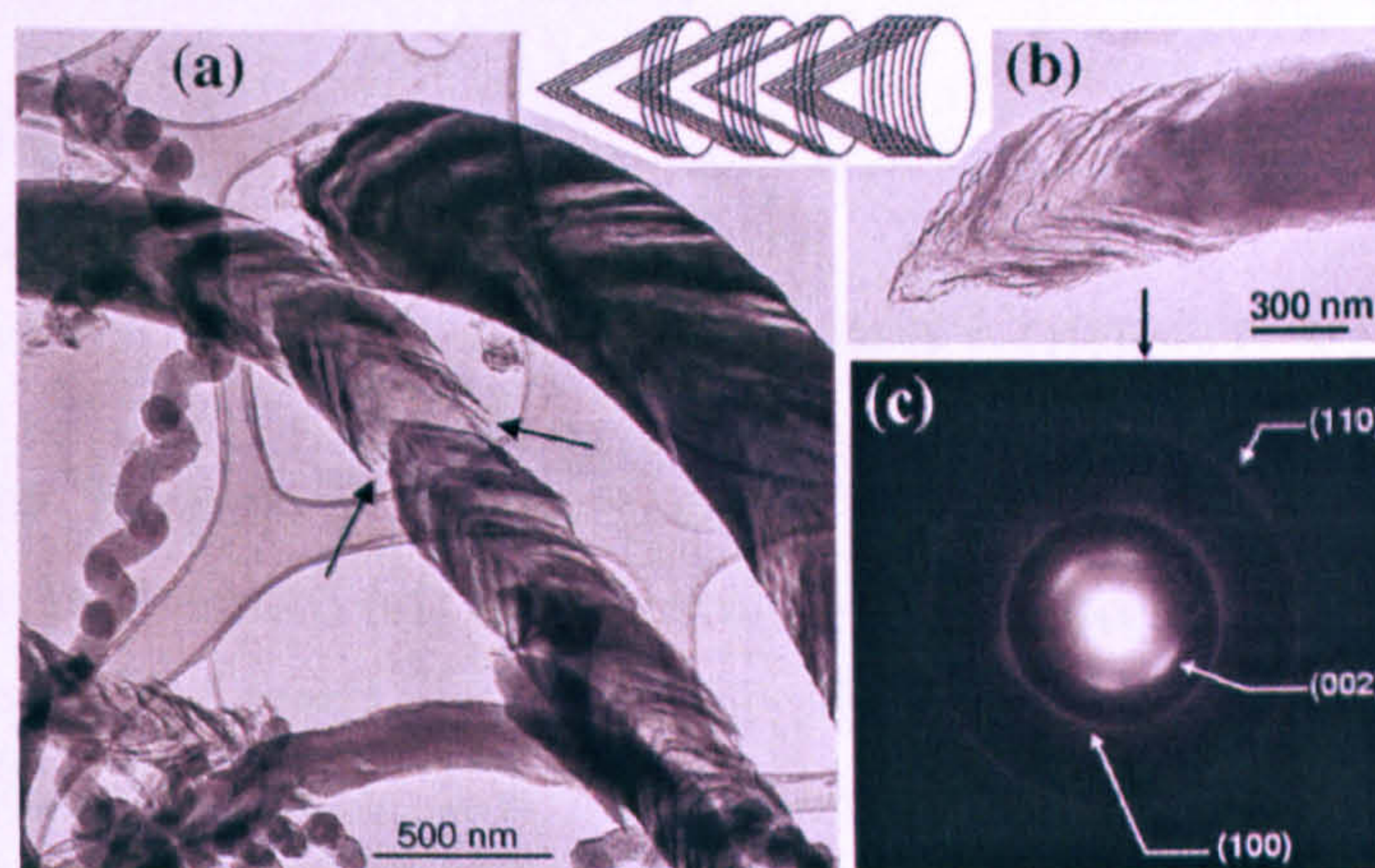


Figure 2.14: TEM analysis of EGNF-1000. Dark and light regions are observed in the fibers (a and b) after exfoliation. Certain fiber regions (arrows) with large expansion indicate fiber rupture. (c) SAED pattern of the nanofiber in (b), (002), (100) and (110) diffraction features can be observed. The inset is a schematic model of the cup-stacked crystalline structure of the fiber after exfoliation; those segments of the fiber keeping the graphite spacing between cups ($\simeq 3.35$ Å) are responsible for the (002) diffraction spots observed in the SAED pattern (Lueking *et al.*, 2007).

A wide range of carbon materials have been extensively studied for solid hydrogen storage. However these are only operational at cryogenic temperatures and moderate pressures. Many improvements remain to be done but some pathways are being investigated depending on the topology of the compound. For open pore materials with high surface areas such ACs,

the pore size is essential as 5-10 Å micro-pores tend to be first occupied and interact more strongly with H₂ molecules than macro-pores. Quantum effects and overlapping potentials are possible on curved surfaces and low temperature. Therefore, it is crucial to target compounds with uniform micropores and high surface areas. Low surface area carbon nanostructures such as SWCNTs, MWCNTs, and GNFs cannot follow the same functionalizing path as ACs. Some groups have been trying to increase the number of adsorption sites, with heterogeneous atomic doping (Terrones et al., 2004), intercalation (Dresselhaus and Dresselhaus, 2002), and / or exfoliation with thermal shock of intercalated compounds (Toyoda et al., 2001a, 2002b,a, 2003). The goal of this chapter was to present and compare standard carbon nanostructures which would physisorb molecular hydrogen. However, it has also highlighted that these as-prepared materials are not ready to meet the DOE targets.

2.7 Metal-Organic Frameworks

Metal-organic framework (MOF) materials are a class of very versatile porous and highly crystalline solids formed via the connection of metal ions or clusters with exodentate ligand bridges. Lately there has been an increasing interest for these open structures MOF compounds (Blake et al., 1999, Yaghi et al., 2003, Lin, 2008) and their potential application for catalysis (Chang et al., 2004), gas storage (Rowsell et al., 2005), and gas separation (Ferey, 2000, 2001, Chen et al., 2005, Kitaura et al., 2003). For the hydrogen economy to be achieved, MOF compounds offer the compositional flexibility at the molecular level required to obtain high surface area (typically from 800 m².g⁻¹ to 5000 m².g⁻¹) and crystalline compounds with specific pore metrics and chemical properties (Dillon et al., 1997, Schlögl and Züttel, 2001). Here current strategies to enhance hydrogen interactions will be addressed.

2.7.1 Pore Structure

It is essential for a porous material to exhibit a pore size distribution centred on 7 Å and combined with a high surface area (Dillon and Heben, 2001).

In general, the pore structure is ruled by the nature of the organic ligand and its connectivity with the metal nodes. For instance the NOTT-100 series is a family of Cu (II) - frameworks based on copper paddle-wheel units with different organic ligands. The geometry of the pores changes with the length of the organic linkers (Figure 2.15) (Lin et al., 2006a).

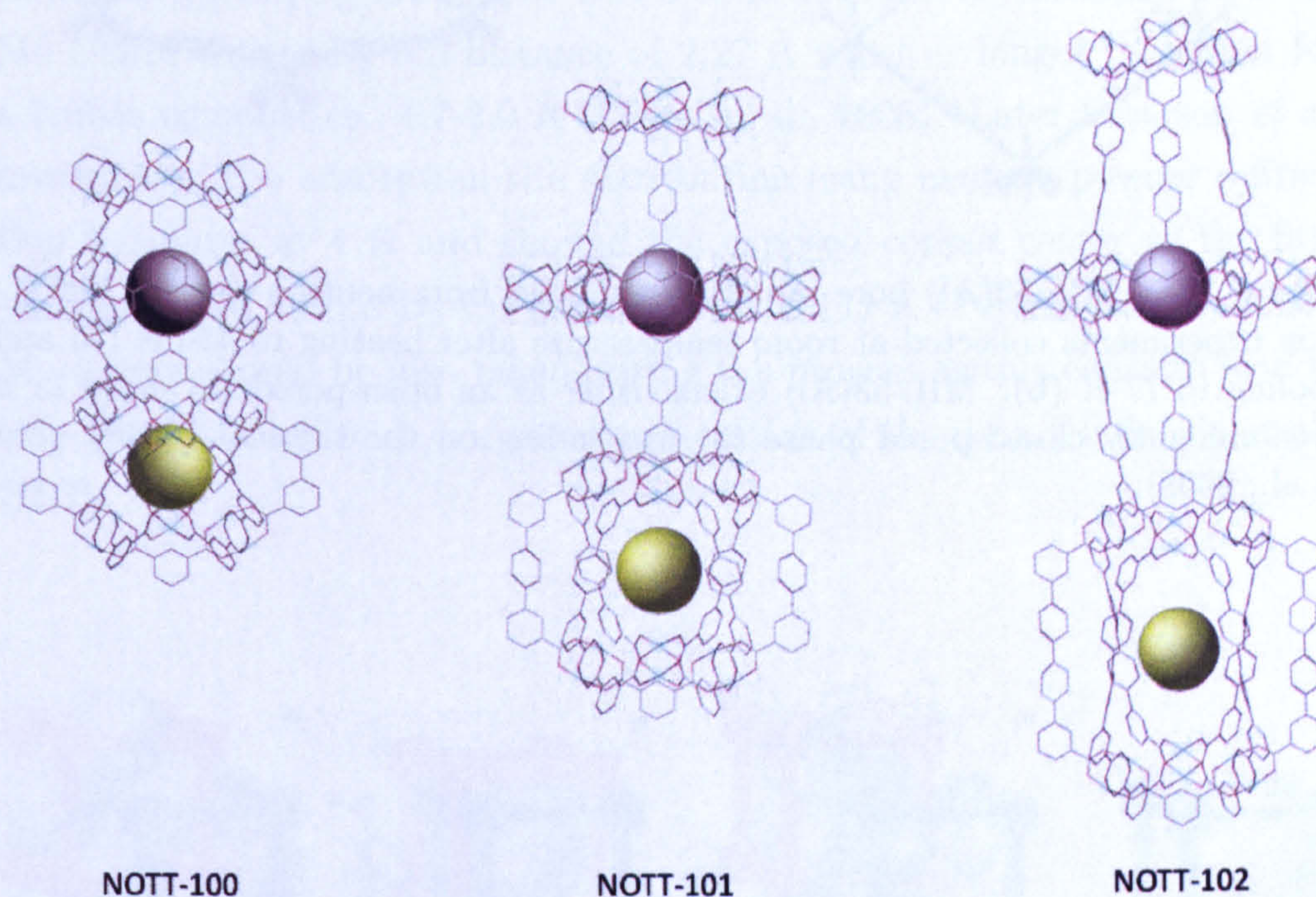


Figure 2.15: From the left MOF-505 (NOTT-100), NOTT-101, and NOTT-102 cage structures with elliptical (grey sphere) and spherical (yellow sphere) cages. Bond colour code: Blue: Copper, Grey: Carbon, Red: Oxygen. No hydrogen bonds shown for clarity (Lin et al., 2006a).

Some MOFs such as MIL-53 reveal structural transitions in temperature leading to a breathing effect from an open (close) - pore to a close (open) - pore structure by adsorbing different guest molecules (Serre et al., 2002, Loiseau et al., 2004) (Figure 2.16). Later neutron investigations confirmed the thermal hysteresis behaviour between the two configurations (Liu et al., 2008). Such effect would allow a pore wall to hold and release H_2 molecules at specific temperatures. The interpenetration and interweaving of catenated networks are also two possible alternatives to obtain various pore configurations as reported by Yaghi and his co-workers (Yaghi et al., 2003).

2. LITERATURE REVIEW

The interpenetration represents all the pore configurations allowing the reduction of the pore size while the interweaving results in the reinforcement of mutual networks by reducing the space voids (Figure 2.17).

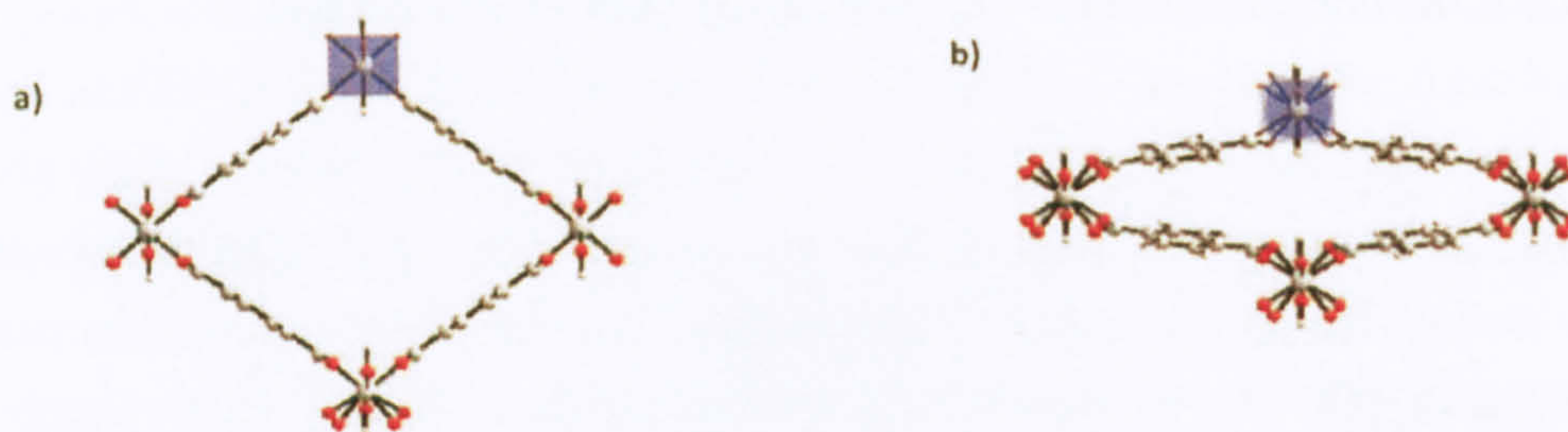


Figure 2.16: MIL-53(Al) pore structure obtained from neutron powder diffraction experiments collected at room temperature after heating to 450 K (a) and cooling to 77 K (b). MIL-53(Al) exists either as an open-pored (a) phase or a predominantly closed-pored phase (b), depending on the thermal history (Liu et al., 2008).

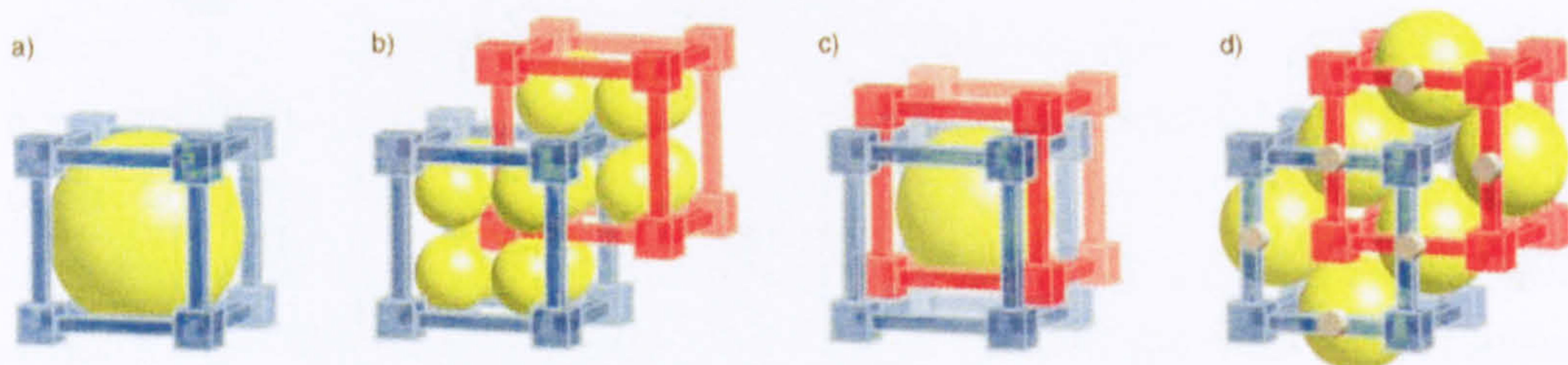


Figure 2.17: a) Schematic representation of the repeated unit. b) and d) Interpenetration of two identical catenated units allowing the reduction of the pore dimension by different pore configurations. c) Interweaving results in the total reduction of the pore size (Rowsell and Yaghi, 2005).

2.7.2 Metal Centres

In essence, metal-nodes are based on the d-block transition elements. These are connected to the organic linkers via bridging linkers such as carboxylate groups. In some cases, it is possible to remove the solvent molecule coordinated from the metal-node by thermal treatment and leading to a coordinatively unsaturated metal centre. The presence of such species has

proved to increase hydrogen binding strength in MOF compounds. This was undeniably inspired by Kubas complexes discovery in 1984 (Kubas *et al.*, 1984, Kubas, 2001). Early infra-red studies Prestipino *et al.* reported for the first time on hydrogen interactions with an open metal site within a $\text{Cu}_3\text{-(BTC)}_2$ (BTC = 1,3,5-benzenetricarboxylate) MOF, HKUST-1 (Prestipino *et al.*, 2006) (Figure 2.18). Neutron powder diffraction studies of $[\text{Mn}]_3[(\text{Mn}_4\text{Cl})(\text{BTT})_8]$ by Dinca *et al.* revealed D_2 adsorbed onto the Mn centre with a $\text{D}_2\text{-Mn}$ distance of 2.27 Å which is longer than that for a Kubas complex *ca.* 1.7-2.0 Å (Dinca *et al.*, 2006). Later Peterson *et al.* investigated the adsorption site distribution using neutron powder diffraction technique at 4 K and showed the exposed copper center as the first site populated with a $\text{D}_2\text{-Cu}$ distance of 2.39 (1) Å (Peterson *et al.*, 2006). Much care should be also taken during the process as this can also lead to structural damage and / or misinterpretation of the data (Hafizovic *et al.*, 2007).

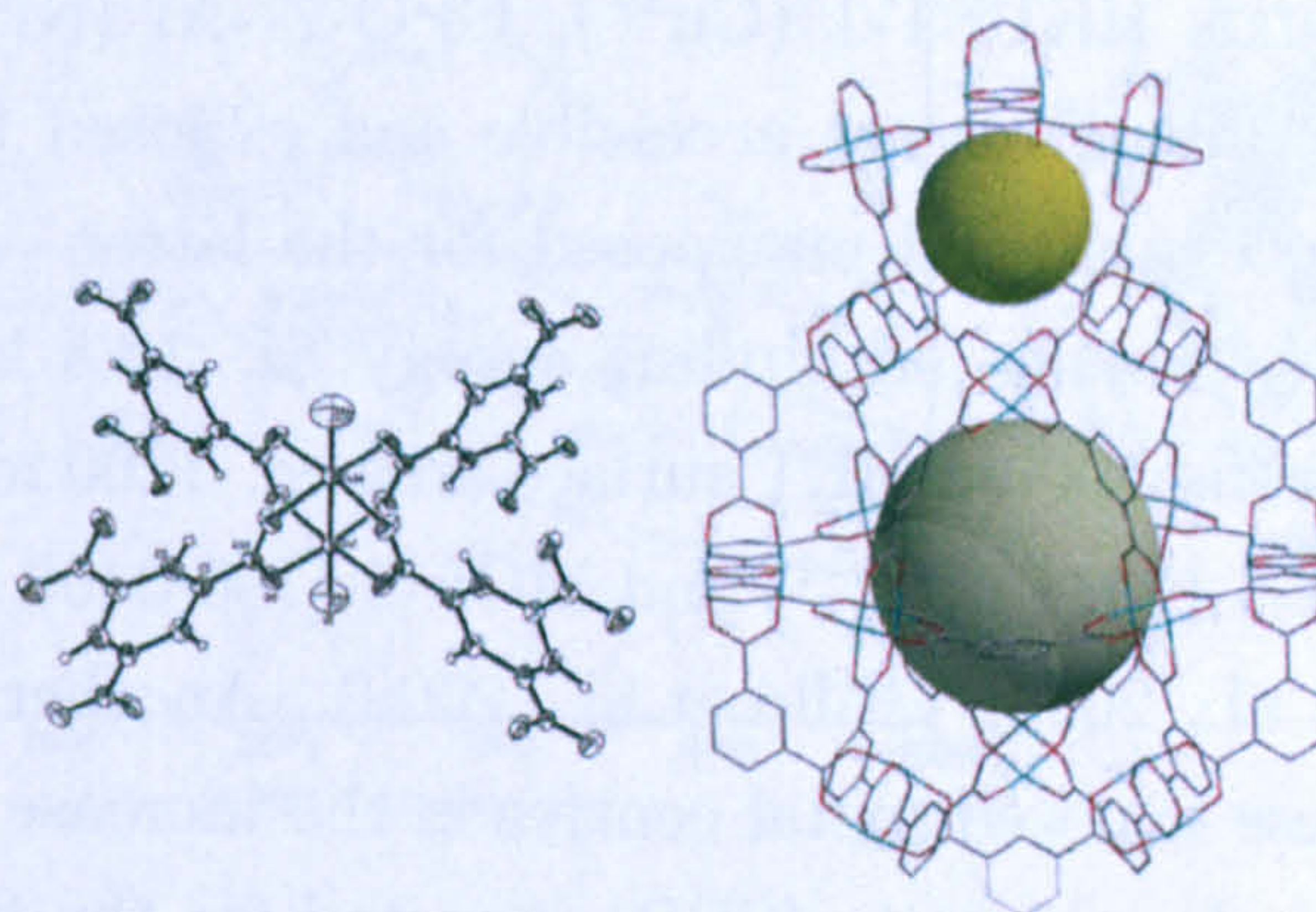


Figure 2.18: On the left: Dicopper (II) tetracarboxylate building block for HKUST-1 (Chui *et al.*, 1999). On the right HKUST-1 cage structure with spherical (grey sphere) and secondary (khaki sphere) cages. Bond colour code: Blue: Cu, Red: O, Grey: C. No hydrogen bonds shown for clarity.

Not all MOF materials exhibit a coordinatively unsaturated metal centre. Isoreticular metal-organic framework (IRMOF) series is a family of Zn-based clusters (Zn_4O) connected by various organic linkers (Figure 2.19). The most famous example is MOF-5 of composition $\text{Zn}_4\text{O}(\text{BDC})_3$ (BDC = 1,4-benzenedicarboxylate). Inelastic neutron scattering experiments on IRMOFs showed the Zn_4O environment as a less favourable adsorption site

2. LITERATURE REVIEW

compared to the carboxylate group.

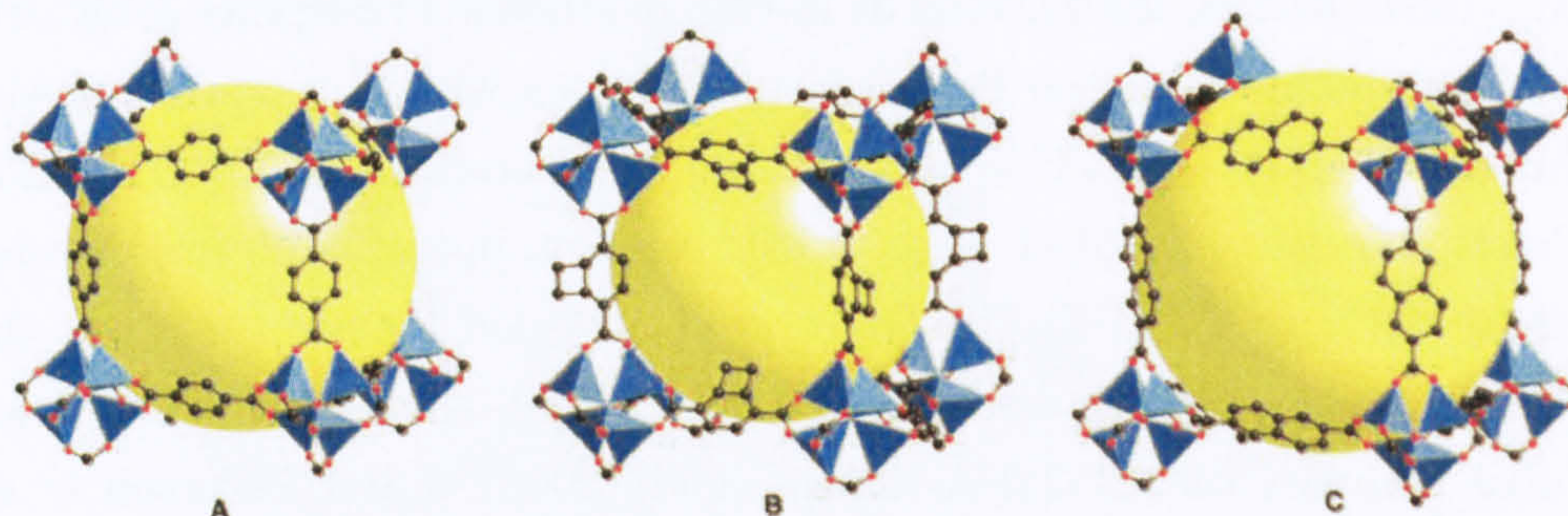


Figure 2.19: MOF-5 (A), IRMOF-6 (B), and IRMOF-8 (C) pore structure. On each of the corners is a cluster $[\text{OZn}_4(\text{CO}_2)_6]$ of an oxygen-centred Zn_4 tetrahedron that is bridged by six carboxylates of an organic linker (Zn, blue polyhedron; O, red spheres; C, black spheres). The large yellow spheres represent the largest sphere that would fit in the cavities without touching the van der Waals atoms of the frameworks. Hydrogen atoms have been omitted (Rosi et al., 2003).

Vitillo *et al.* showed the important role of the metal centres on three solvent free MOF compounds HKUST-1 (Cu^{2+}), CPO-27-Ni (Ni^{2+}) and MOF-5 (Zn) where the metal centres are accessible and exposed for the first two materials, and inaccessible and unexposed for the latter. Although CPO-27-Ni had the highest hydrogen binding energy *ca.* 13.5 kJ.mol^{-1} , it was not enough to overcome its low BET surface area *ca.* $1200 \text{ m}^2.\text{g}^{-1}$ compared to that for HKUST-1 ($1532 \text{ m}^2.\text{g}^{-1}$) and MOF-5 ($700\text{-}3400 \text{ m}^2.\text{g}^{-1}$) (Figure 2.20) (Hafizovic et al., 2007, Vitillo et al., 2008). Another consequence of the presence of these exposed metal centres is the increase of the so-called hydrogen surface packing density (SPD) reported for the first time by Liu and his co-workers with MOF-74 *ca.* $3.5.10^{-5} \text{ g.m}^2$ compared to that for solid H_2 phase *ca.* $2.8.10^{-5} \text{ g.m}^2$ (Figure 2.23). This was also correlated with a shorter $\text{D}_2\text{-D}_2$ distance *ca.* 2.85 \AA at 4 K and 0 Pa (Liu et al., 2008) instead of 3.6 \AA for solid D_2 (Figure 2.21).

In essence potential MOF candidates would combine high surface area, with an optimized pore size and the presence of coordinated unsaturated metal centres. The role of the metal center and of the organic ligand upon the adsorption properties will be addressed later in this work using neutron techniques.

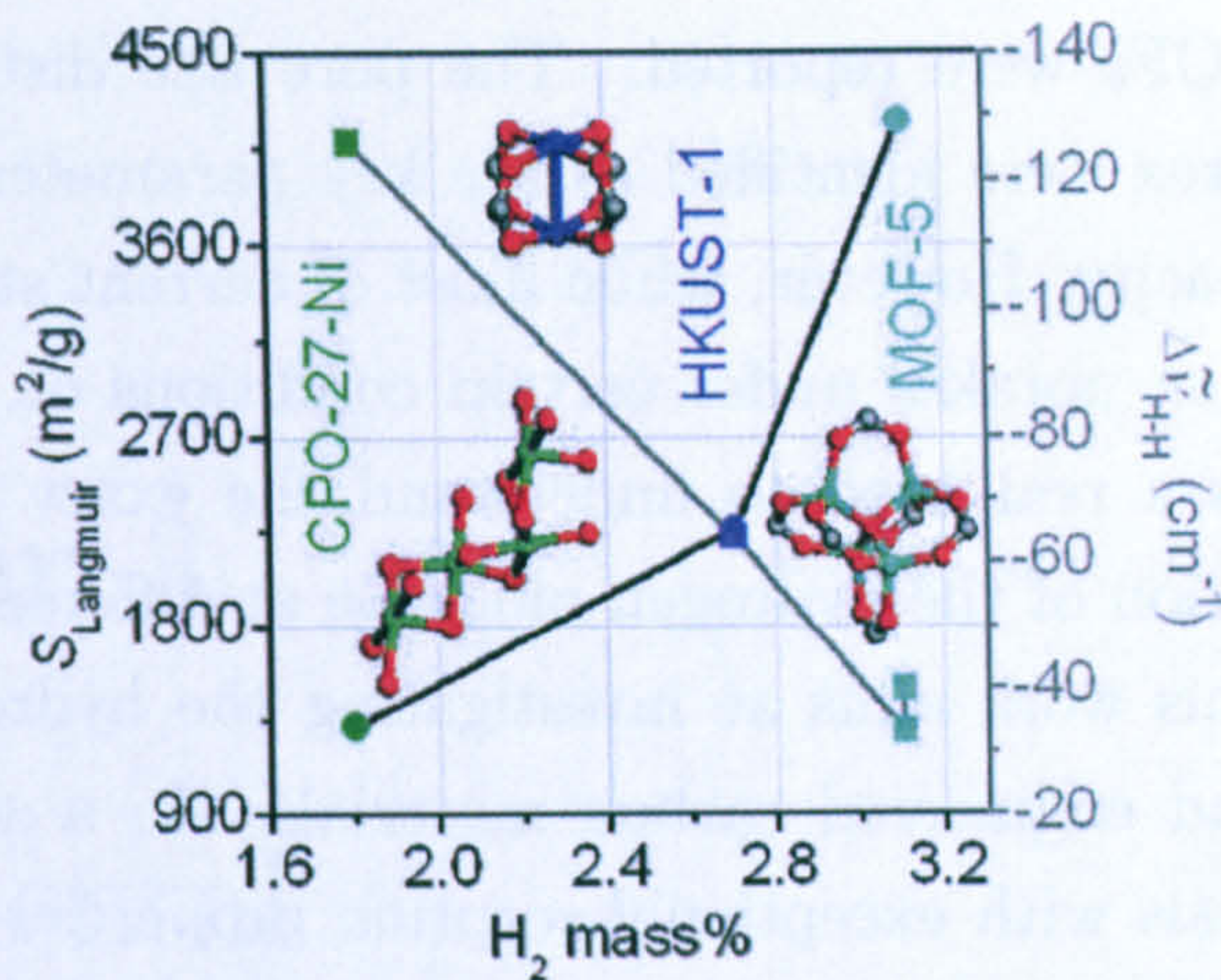


Figure 2.20: Dependence of the Langmuir surface area on the adsorbed H_2 amounts at 77 K and 45 bar (volumetric values) for the three MOFs under investigation. Values taken from the literature: MOF-5,3 HKUST-1,3 and CPO-27-Ni. The dependence of the H-H shift for the most energetic complexes on the hydrogen uptake is also shown (para- H_2 has been used as reference, gray squares). For CPO-27-Ni, the barycenter of the 4028 and 4035 cm^{-1} bands has been considered (Vitillo et al., 2008).

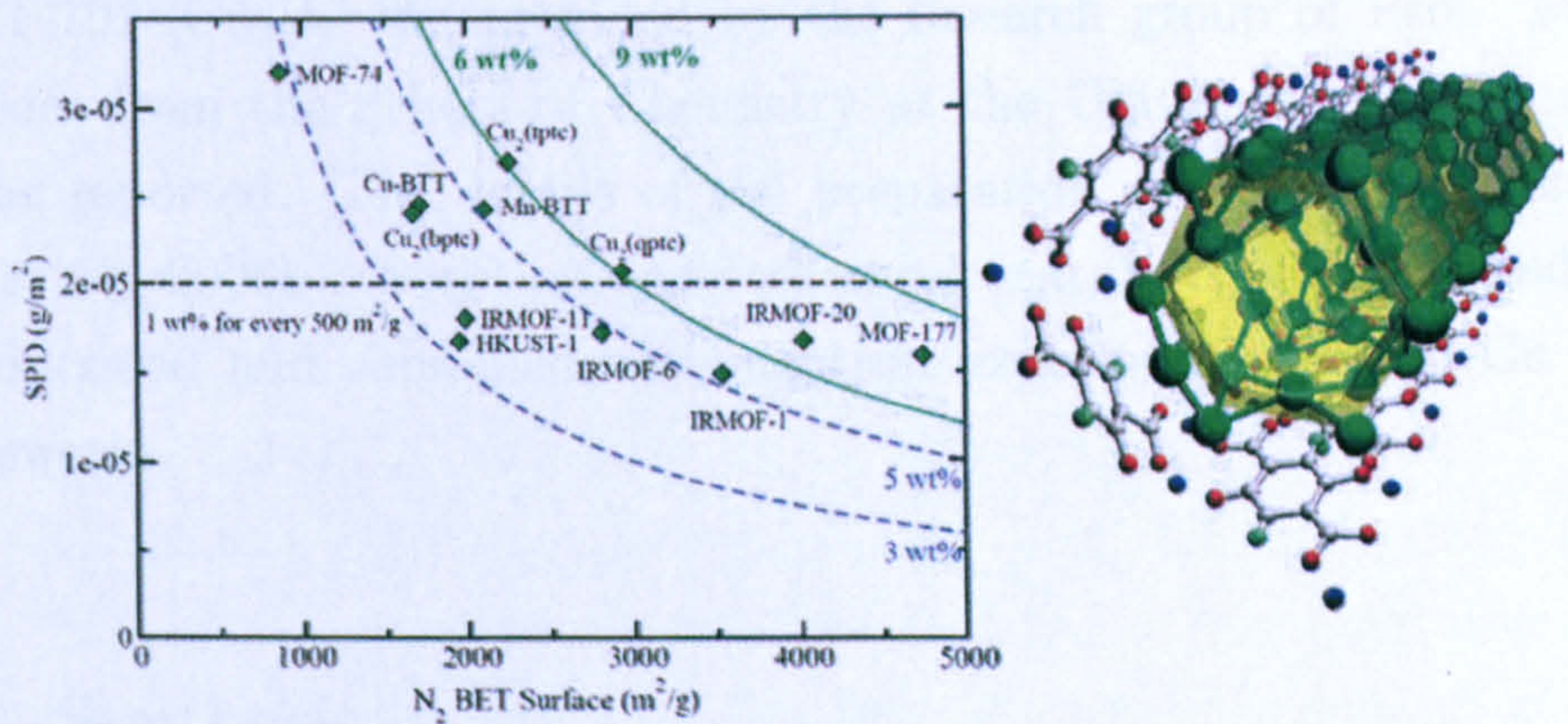


Figure 2.21: The H_2 surface packing density, SPD, as a function of N_2 BET surface. The horizontal dashed line shows the SPD for typical carbon material, where every 500 $\text{m}^2.\text{g}^{-1}$ of N_2 BET surface area can adsorb 1 *wt.%* of H_2 . Solid green (gray) curves show the lines for gravimetric uptake of 6 and 9 *wt.%*, which is the product of SPD and S . One-dimensional nanoscale tube like structure formed from adsorbed D_2 . D_2 molecules (large green (gray) balls) adsorbed in MOF-74 form a one-dimensional nanoscale tube like structure. (Only the first three adsorption sites are shown) (Liu et al., 2008).

2.8 Conclusions

Fundamental principles were introduced in order to understand the hydrogen interactions with physisorbing materials. In particular, carbon nanos-

2. LITERATURE REVIEW

structures and MOFs were reported. The pore size distribution and the specific surface area were identified as the key parameters responsible for the hydrogen capacity. However, while most of current studies extensively report on hydrogen uptakes under certain conditions of temperature and pressure, there is a real need to understand the exact position and behaviour / orientation of the hydrogen molecule at different coverage of the surface. First, this work aims at investigating the hydrogen interactions of as-prepared and engineered carbon materials. In a second part, high crystalline materials with exceptional sorption properties will be reported combining state-of-the-art techniques.

Chapter 3

Experimental

First, synthesis of graphitic nanofibres (GNFs) will be addressed in this chapter. Two engineering options for GNFs were proposed in order to test their flexibility in design and improve their sorption properties. In a second part, highly crystalline Cu (II) - frameworks NOTT-100, NOTT-101 and NOTT-102 $[\text{Cu}_2(\text{L}^{1,2,3})]$ provided by the research group of Prof. Martin Schröder from the School of Chemistry at the University of Nottingham will be reported. The details of the preparation can be found elsewhere (Lin et al., 2006b). Sorption and structural characterisation methods will be addressed and combined with neutron experiments for the Cu (II) - frameworks.

3.1 Synthesis

Undoped and N-doped GNFs were prepared by thermal decomposition of C_2H_4 gas and a mixture of C_2H_4 with various amines respectively over different metal catalysts (Bououdina et al., 2005). Three catalysts precursors were investigated NiO, Fe_2O_3 and Co_3O_4 and respectively prepared from the precipitation reaction of nickel (II) nitrate (*Fisher*), iron (III) nitrate (*Fisher*), and cobalt (II) nitrate (*Fisher*) mixed with 2 M ammonia solution (*Fisher*). The dried precipitates were subsequently calcined at 300 °C for 3 h to yield the oxide precursor. The amount of catalyst, the reaction time, and the total gas flow were kept constant, at 0.05 g, 2 h, and 100 $\text{cm}^3\cdot\text{min}^{-1}$ respectively. The catalyst precursor was heated up to the set-point temper-

3. EXPERIMENTAL

ature under a dynamic flow of argon gas at $100 \text{ cm}^3.\text{min}^{-1}$ and with a ramp rate of $10 \text{ }^\circ\text{C}.\text{min}^{-1}$ in a temperature controlled horizontal tube furnace (Figure 3.1). Hydrogen gas was first flowed in to reduce the precursor for at least two hours and evacuated prior to flowing the feedstock gas.

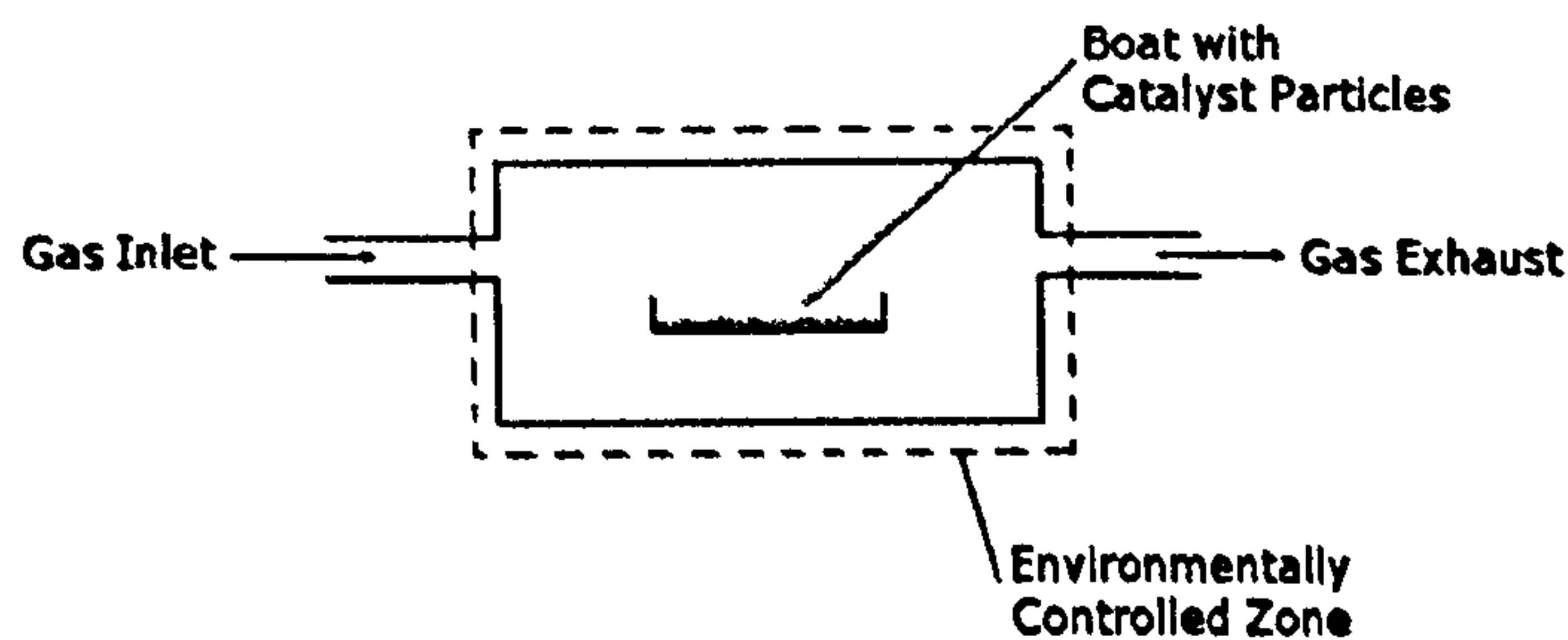


Figure 3.1: Horizontal tube furnace used for undoped GNF growths and N-doping experiments.

The temperature of the reaction was set between 500 and 700°C . For the undoped GNF, the carbon source was composed of ethene, C_2H_4 (*BOC*, 99.999%) and hydrogen, H_2 (*BOC*, 99.99%), using mass flow controllers (*MKS Ltd.*) to provide $\text{C}_2\text{H}_4/\text{H}_2$ gas mixture of 100/0, 80/20, 50/50, 20/80 and 5/95, while maintaining a total flow of $100 \text{ cm}^3.\text{min}^{-1}$. For the N-doping growths, the feedstock gas was bubbled through a Dreschel bottle containing either ethylamine ($\text{CH}_3\text{CH}_2\text{NH}_2$), diethylamine ($\text{CH}_3\text{CH}_2\text{NHCH}_2\text{CH}_3$), or triethylamine ($\text{N}(\text{CH}_2\text{CH}_3)_3$), leading to different C-H-N containing gases in the tube furnace. A gas bottle would have been much easier to implement to the original tube furnace, however all the bottles available are a mixture of Ar and amines with a 4:1 molar ratio. At the end of each experiment, all reacting gases present in the tube furnace were evacuated before allowing the samples to cool down to room temperature under Ar atmosphere in order to stop the growth and avoid any undesired structure at lower temperature. All preparations were repeated to ensure reproducibility. The CVD procedure for the two types of GNFs was similar and is summarized on the Figure 3.2. CHN analysis were also performed at the School of Chemistry (*University of Nottingham*) using the elemental analyzer CE-440 (*Exeter Analytical, Inc.*) in order to quantify the C, H, and N contents within each N-doped sample.

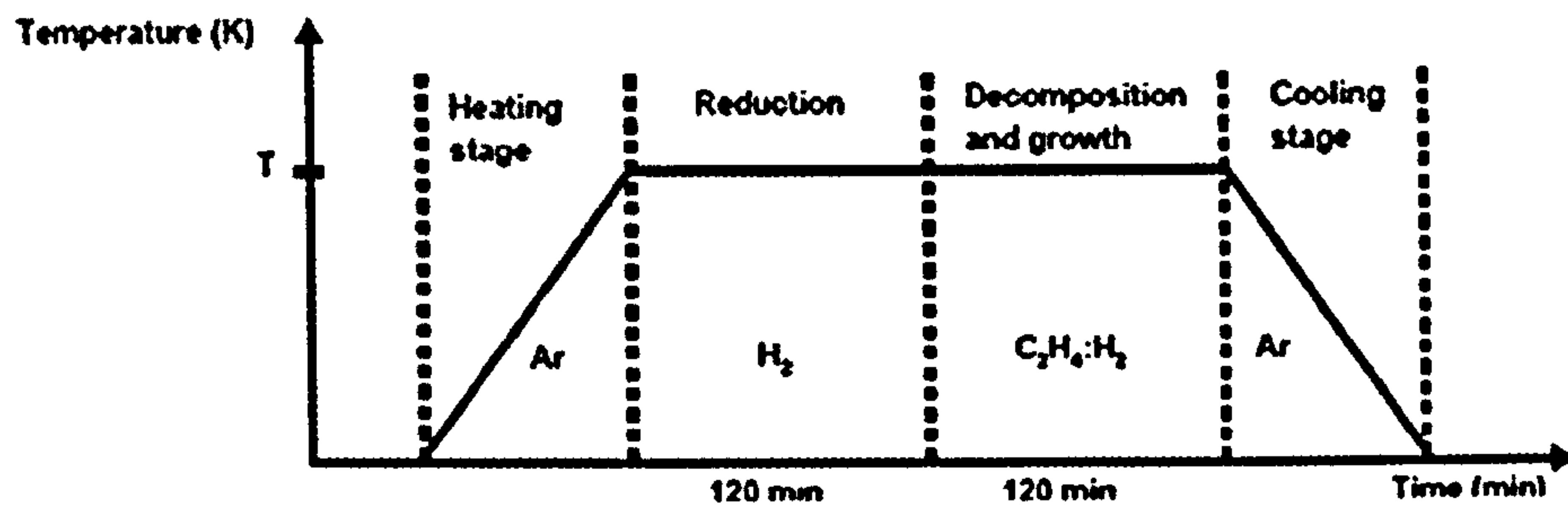


Figure 3.2: CVD procedure with 4 different phases. For the N-doping experiments, different amines were added to the $\text{C}_2\text{H}_4:\text{H}_2$ gas mixture.

3.2 Exfoliation of Intercalated Compounds

Exfoliation of graphite flakes (*University of Salford*) and undoped GNFs were investigated using methods described in the literature (Toyoda et al., 2001a, 2003, Lueking et al., 2007). Approximately 1 g of carbon material was stirred with a total mixture of 100 mL concentrated sulfuric and nitric acid with acid ratios of 4:1 and 1:1 at room temperature for 4 h. The acid treated compounds were then rinsed with water until neutralized, filtered and dried at 200 °C. The dried yield was then exposed to a thermal shock at either 800 °C, 900 °C, and 1000 °C under air.

3.3 Thermal Activation

For porous compounds, prior to any sorption, structural, and spectroscopic investigations, carbon materials and Cu (II) - frameworks were degassed at specific temperatures under dynamic vacuum in order to safely remove solvents and / or moisture from the micropores avoiding any structural damage. The carbon materials were degassed at 300 °C under dynamic vacuum for 4 h while the Cu (II) - frameworks NOTT-100 (MOF-505), NOTT-101, and NOTT-102 were thermally activated at lower temperatures, 130 °C for NOTT-100 and 140 °C for the other two samples, under dynamic vacuum for 12 h (Lin et al., 2006a). This removed the solvent from the micropores as well as the water molecules coordinated to the Cu (II) sites, leading to stable unsaturated metal centres (Figure 3.3). The formula unit of each desolvated sample is $[\text{Cu}_2\text{O}_8\text{H}_6\text{C}_{16}]$, $[\text{Cu}_2\text{O}_8\text{H}_{10}\text{C}_{22}]$, and $[\text{Cu}_2\text{O}_8\text{H}_{14}\text{C}_{28}]$.

3. EXPERIMENTAL

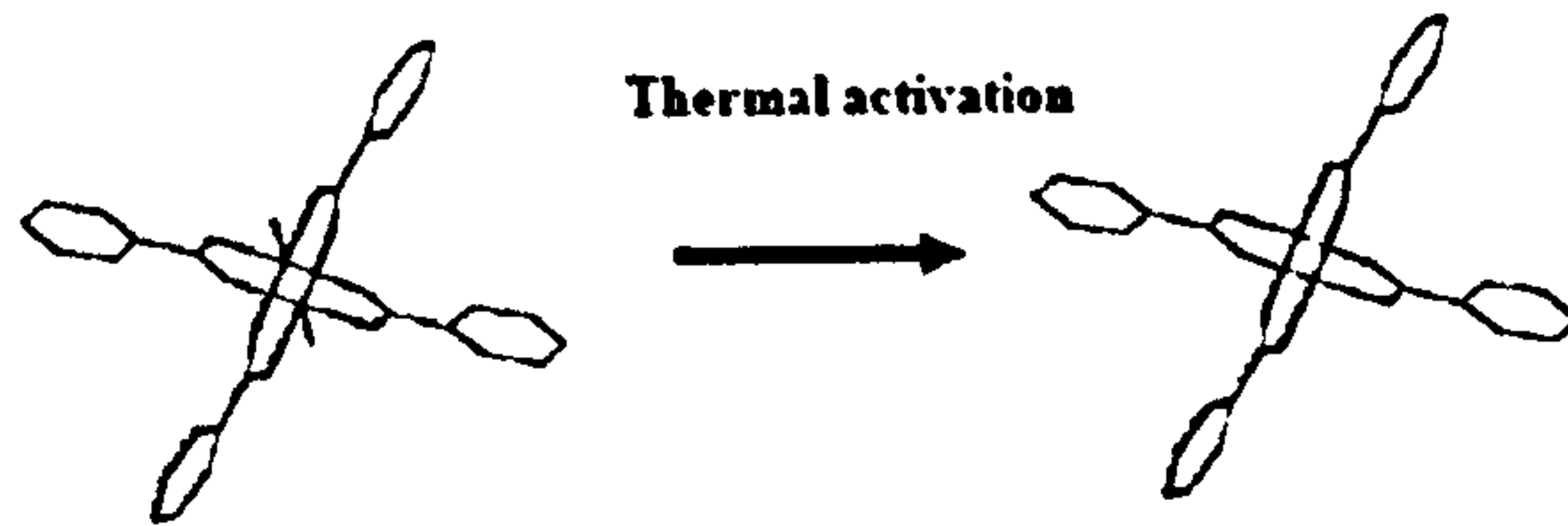


Figure 3.3: On the left: Paddle-wheel unit within the non-activated NOTT-100, NOTT-101, and NOTT-102 with two water molecules attached onto the copper sites. On the right: degassed sample with two exposed copper centres. Colour code: Blue: copper; Red: oxygen; Grey: carbon. No hydrogen bonds shown for clarity. Water molecules are removed from the copper sites after thermal treatment.

3.4 Sorption Properties Characterisation

3.4.1 Gravimetric Method

3.4.1.1 Theory

It is essential to be able to determine accurately the amount of hydrogen adsorbed / released by a sample under certain condition of temperature and pressure. The gravimetric method is commonly used for the determination of equilibrium sorption isotherms (Benham and Ross, 1989, Broom and Moretto, 2007). It provides a direct measurement of the hydrogen uptake capacity by measuring the mass of hydrogen adsorbed. The ratio of the adsorbate mass over that of the adsorbent-adsorbate system determines the hydrogen uptake capacity at a fixed temperature and pressure:

$$wt.\%(T, p) = \frac{m_{H_2}}{m_{H_2} + m_s} \quad (3.1)$$

For porous materials, the adsorption phase of an isotherm occurs when the hydrogen gas is introduced into the sample cell, whereas the desorption phase is obtained as the hydrogen gas is gradually removed from the sample cell at fixed temperature. Each point of the isotherm is collected isobarically until the thermodynamic equilibrium is reached. A series of isotherms at different temperatures can also lead to thermodynamic properties such as the isosteric enthalpy of adsorption for porous compounds or in the case of hydrides the heat of hydride formation or decomposition (see

section 2.1) (Rouquerol et al., 1980, Attard and Barnes, 1998). In general an isotherm determines the reversibility of the hydrogen sorption / desorption mechanism. Hysteresis behaviour can be related to the pore structure of the sample (see section 2.1.1) or simply to slow kinetics. Typical sources of errors mainly come from the high sensitivity of the measurement to environmental conditions:

- This method is highly sensitive to the sample temperature stability. A common problem for an isotherm at low temperature is the temperature difference between the sample (usually at 77 K) and the flowing gas introduced (usually at room temperature) which leads to convection phenomena and mass fluctuations. This increases the acquisition time for each data point.
- Purity of the hydrogen gas is also important since any moisture contamination would lead to an overestimation of the real H₂ uptakes.
- Low density materials such as activated carbon or GNFs are more affected by the buoyancy effect which increases with the pressure. This is easily corrected if the sample's skeletal density is known.

At each pressure point, the mass of the sample must be corrected from the buoyancy contribution following Archimedes's principal. The upthrust due to buoyancy, C_b , for a solid of density ρ_s , and mass m_s , in a gas of density ρ_g , is determined by:

$$C_b = m_s \cdot \frac{\rho_g}{\rho_s} \quad (3.2)$$

In our case, at each pressure step, the sample adsorbed a certain amount of H₂ gas while being in equilibrium with the remaining H₂ gas phase. Including the contribution of the adsorbed gas phase, Eq. (3.2) can be written as:

$$C_b = m_{ref} \cdot \frac{\rho_{H_2}}{\rho_s} + m_{adsorbed} \cdot \frac{\rho_{H_2}}{\rho_{adsorbed}} + A \quad (3.3)$$

where m_{ref} is the mass of the sample with nothing adsorbed, $m_{adsorbed}$ is the mass of the gas adsorbed, and A is the instrumental function. The H₂

3. EXPERIMENTAL

gas density, ρ_{H_2} , is defined by its gas molar mass, M , the pressure, p , and gas compressibility $Z(p, T)$:

$$\rho_{H_2} = \frac{M.p}{Z(p, T).R.T} \quad (3.4)$$

where R is the typical gas constant. The sample mass, $m(p)$, during the experiment is determined at each pressure step, p , by:

$$m(p) = m_{ref} + m_{adsorbed}(p) \quad (3.5)$$

It is therefore easy to retrieve the expression of the hydrogen weight uptake as in Eq. (3.1).

3.4.1.2 Experimental

Hydrogen isotherms were measured on an intelligence gravimetric analyzer (IGA) (IGA-003 *Hidenanalytical*). Prior to the sorption characterisation, carbon materials and Cu (II) - frameworks were degassed (see section 3.3). After the degas, the desolvated sample was weighed in order to fix the reference mass. Hydrogen gas (*BOC*, 99.999% purity) was passed through a nitrogen cold trap to eliminate any moisture in the gas. Experiments were run in static mode. During the adsorption phase, pressure steps of 10 mbar per measurement were used for the first 500 mbar, followed by 1000 mbar steps up to a maximum pressure of 20 bar. The pressure increases were controlled at a rate of 10 mbar.min⁻¹. The desorption cycle followed a similar series of pressure steps. The equilibrium time was fixed to 30 min for each pressure point to ensure thermal and pressure stability before acquisition *ca.* ± 0.1 °C and ± 0.1 mbar.

3.4.2 BET Method

3.4.2.1 Theory

The surface area measurements are discussed in this section. The most widely used method to determine the surface area of a material involves the Brunauer Emmett Teller (BET) equation (Brunauer et al., 1938):

$$\frac{1}{W \cdot \left(\frac{p}{p_0} - 1 \right)} = \frac{1}{W_m \cdot C} + \frac{C - 1}{W_m C} \cdot \frac{p}{p_0} \quad (3.6)$$

W is the weight of the gas adsorbed at a relative pressure, $\left(\frac{p}{p_0} \right)$ and W_m is the weight of the adsorbate used. C is the BET constant and is related to the energy of adsorption in the first monolayer. A BET measurement consists in measuring a nitrogen adsorption / desorption isotherm at low temperature as W the amount of N gas adsorbed as a function of the relative pressure $\frac{p}{p_0}$. In general only the low $\left(\frac{p}{p_0} \right)$ region *ca.* 0.05 to 0.35 of a BET plot leads to a linear behaviour $\frac{1}{W(1-\frac{p}{p_0})}$ and $\frac{p}{p_0}$. The multi-point BET method requires at least three points within this region. The slope, s , and the intercept, i , are determined graphically and defined as:

$$s = \frac{C - 1}{W_m \cdot C} \quad (3.7)$$

$$i = \frac{1}{W_m \cdot C} \quad (3.8)$$

This leads to W_m , the weight of the first monolayer adsorbed onto the surface:

$$W_m = \frac{1}{s + i} \quad (3.9)$$

The total surface area of the sample is written as:

$$S_t = \frac{W_m \cdot N_A \cdot A_{CS}}{M} \quad (3.10)$$

with A_{cs} the cross-sectional area, N_A the Avogadro's number, and M the molecular weight. The specific surface area of the sample, S , is the quantity of most interest:

$$S = \frac{S_t}{W} \quad (3.11)$$

It is also possible to determine quickly the BET surface area of a sample

3. EXPERIMENTAL

by limiting the number of points within the linear region. The single point method implies that the intercept, i , in the BET equation is close enough to zero. Therefore Eq. (3.6) is simplified and becomes:

$$\frac{1}{W \cdot \left(\frac{p}{p_0} - 1 \right)} = \frac{C - 1}{W_m \cdot C} \cdot \frac{p}{p_0} \quad (3.12)$$

In the low pressure region, the ideal gas equation is a good approximation and thus:

$$W_m = W \cdot \left(1 - \frac{p}{p_0} \right) = \frac{p \cdot V \cdot M}{R \cdot T} \cdot \left(1 - \frac{p}{p_0} \right) \quad (3.13)$$

which leads to S_t the total surface area:

$$S_t = \frac{p \cdot V \cdot N \cdot A_{cs}}{R \cdot T} \left(1 - \frac{p}{p_0} \right) \quad (3.14)$$

Different adsorbates can be used depending on the C BET constant. N_2 is the most widely used adsorbate since in general its C constant (50-250) allows a good cross sectional area A_{cs} . However, given the kinetic diameter of N_2 ca. 3.6 Å, the smallest pores a N_2 molecule can infiltrate is 7 Å which underestimates the available surface area for H_2 molecules which have a kinetic diameter of 2.9 Å. Smaller molecule such as CO_2 (ca. 3.3 Å) could be more appropriate for probing smaller pores.

3.4.2.2 Experimental

The surface area measurements of carbon materials were done using the Autosorb-1 (*Quantachrome*). Approximately 1 g of carbon material was loaded and degassed at 300 °C for 5 h under dynamic vacuum. The solvent free sample was then weighed and loaded into the nitrogen cell. Typically multi-points BET analysis was used in order to cover the linear $\frac{p}{p_0}$ pressure region ca. 0.1-0.3 $\frac{p}{p_0}$. The pressure steps were fixed to 0.03 units of $\frac{p}{p_0}$ with an equilibrium time equal to 10 min per pressure point. The BET measurements on Cu (II) - frameworks were run on the IGA-003 (*Hiddenanalytical*) using N_2 gas prior to undertaking the hydrogen uptake measurements in order not to waste any sample. Approximately 33 mg of as prepared sample

were loaded onto the micro-scale pan. 5 - points BET measurements were used within the linear 0.1-0.3 $\frac{p}{p_0}$ pressure region.

3.5 Structural Characterisation and Spectroscopy

3.5.1 Transmission Electron Microscopy

3.5.1.1 Theory

Transmission electron microscopy (TEM) technique was used to investigate the surface topology, morphology, composition, and crystallographic structure of the undoped, N-doped, and exfoliated GNFs produced. This technique is a powerful tool which allows a resolution up to 0.1-0.5 nm which is significantly higher than a typical optical microscope *ca.* 0.2 μm . The electrons are guided along an evacuated column through a series of condenser lenses and apertures before they hit the sample and go through another set of lenses and apertures and create an image of the target zone (Figure 3.4). The carbon nanostructure within a sample can be identified using selected area diffraction (SAD): for instance a platelet nanofibre would produce two arcs (one pair of diffraction arcs from the basal plane, $d_{(002)}$ which would be superimposed along the fibre axis; a herringbone nanofibre would produce four arcs (two pairs) at an angle to the fibre axis; and a MWCNT would produce two arcs (one pair) which would be superimposed on either side of the fibre axis (Edwards, 1989, Bououdina et al., 2006, McCaldin et al., 2006).

3.5.1.2 Experimental

TEM and SAD were used to characterise the carbon samples produced by CVD. Samples were prepared by placing drops of a sonicated propan-2-ol suspension onto a holey carbon TEM grid (*Agar*). Two electron microscopes were used, (1) a JEOL JEM-2000FX II microscope operating at 200 keV and (2) a JEOL JEM-4000FX microscope operating at 400 keV.

3. EXPERIMENTAL

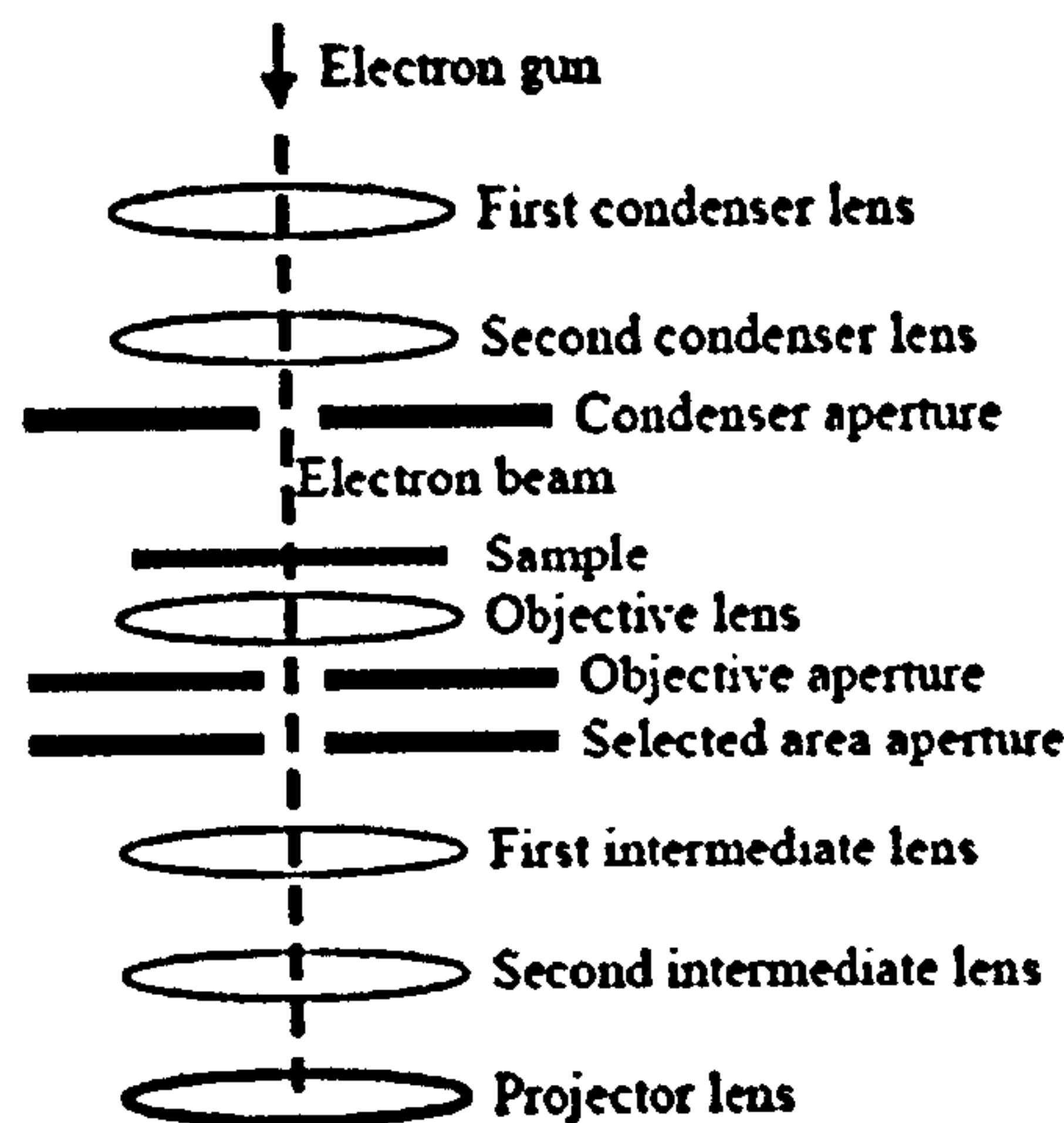


Figure 3.4: Representation of a TEM instrument (Edwards, 1989).

3.5.2 X-Ray Powder Diffraction

3.5.2.1 Theory

X-rays are electromagnetic waves with a much shorter wavelength than visible light, typically in the range of 0.1-100 Å. XRD techniques measure the intensity of X-rays scattered from electrons bound to atoms yielding information at the atomic level. It is a bulk technique with a limited depth of penetration typically few microns. The beam is generated by the bombardment of high energy electrons *ca.* 10-100 keV coming from an X-ray tube onto a target leading to the electron core emission. An outer shell electron immediately fills the vacant position and an X-ray photon is emitted according to the energy conservation principle. For a perfect crystal, a reciprocal vector in the reciprocal space, $\tau_{(h,k,l)}$, is defined by:

$$\tau_{h,k,l} = ha^* + kb^* + lc^* \quad (3.15)$$

where h, k, l are integers, a^* , b^* , and c^* define the reciprocal unit cell vectors and $(2\pi)^3/v_0$ represents the volume of a reciprocal unit cell:

$$\mathbf{a}^* = \frac{2\pi}{v_0} \mathbf{b} \times \mathbf{c} \quad (3.16)$$

$$\mathbf{b}^* = \frac{2\pi}{v_0} \mathbf{c} \times \mathbf{a} \quad (3.17)$$

$$\mathbf{c}^* = \frac{2\pi}{v_0} \mathbf{a} \times \mathbf{b} \quad (3.18)$$

where \mathbf{a} , \mathbf{b} , \mathbf{c} define the unit cell vectors in the real space. Each vector $\tau_{(h,k,l)}$ of the reciprocal space corresponds to a series of parallel lattice planes in the real space separated by a distance $d_{(h,k,l)}$ defined by:

$$d_{h,k,l} = \frac{1}{|\tau_{h,k,l}|} \quad (3.19)$$

During an XRD experiment, for a given reflection h,k,l the quantity measured is the intensity, $I_{(h,k,l)}$, which is proportional to the module of the structure factor $F_{(h,k,l)}$:

$$I_{h,k,l} \propto |F_{h,k,l}|^2 = \left| \sum_l f_l \cdot \exp(i\mathbf{Q} \cdot \mathbf{R}_l) \cdot \exp(-8\pi^2 \mathbf{Q}^2 \cdot \langle \mathbf{u}_l \rangle^2) \right|^2 \quad (3.20)$$

where f_l is the form factor of the element l at the position $\mathbf{R}_l = x\mathbf{a} + y\mathbf{b} + z\mathbf{c}$ and corrected by its thermal mean square displacement $\langle \mathbf{u}_l \rangle^2$. The scattering vector, \mathbf{Q} , is the difference between the diffracted wavevector, \mathbf{k}_f , and the incident wavevector \mathbf{k}_i :

$$\mathbf{Q} = \mathbf{k}_f - \mathbf{k}_i \quad (3.21)$$

Only elastic events will be considered which means that there is no exchange of energy. The intensity collected (Eq. (3.20)) will be strong in some directions (constructive interference) if the scattering vector, \mathbf{Q} , is a reciprocal vector (*i.e.*: $\mathbf{Q} = \tau_{hkl}$) and rather weak in other directions (destructive interference). This was first formulated by Bragg (Eq. (3.22)). For a given h, k, l , constructive interferences only occur if the difference path, δ , between two waves with an incident angle, θ_B , on two parallel lattice planes (Figure 3.5) is a multiple $n = 0, \pm 1, \pm 2, \dots$ of the wavelength λ . A more

3. EXPERIMENTAL

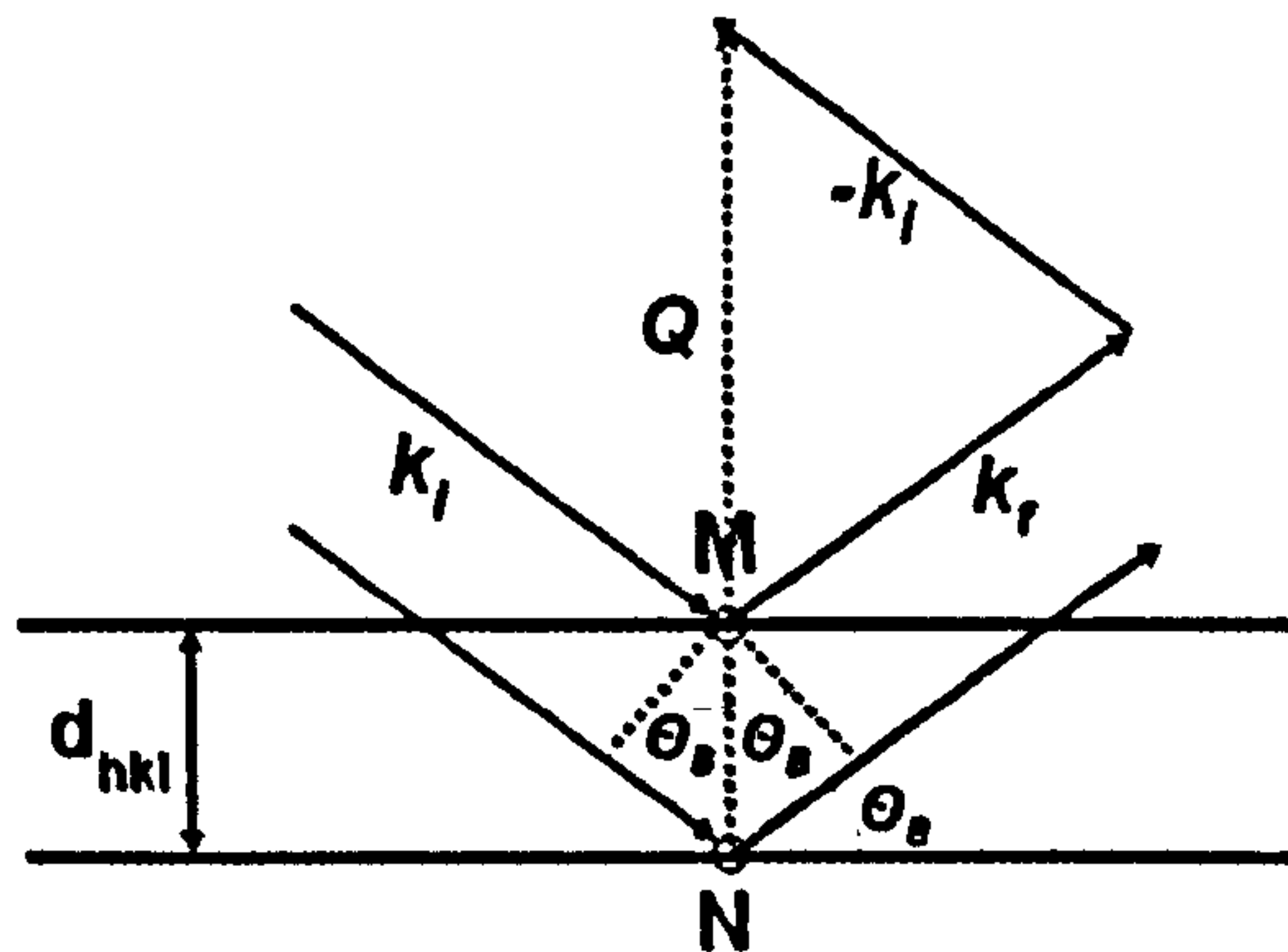


Figure 3.5: Simplified path geometry of an incident and a diffracted beam by two atoms M and N from two (hkl) lattice planes separated by a distance d_{hkl} . The scattering vector, Q , is defined by: $Q = k_f - k_i$

realistic picture was proposed by Bloss with two atoms shifted from their equilibrium position (Bloss, 1971).

$$\delta = n\lambda = 2|d_{h,k,l}| \cdot \sin \theta_B \quad (3.22)$$

In the case of a powder sample, the orientation condition, $Q = \tau_{(hkl)}$, is always satisfied. X-ray powder diffraction (XRPD) technique is one of the most common structural characterisation methods available. It provides a quick structural analysis of a sample. However, X-rays are sensitive to the electron cloud (as a function of the Z) and therefore it is difficult to gain information on light elements in the presence of heavier elements. More details can be found in elsewhere (Dinnebier and Billinge, 2008).

3.5.2.2 Crystallite Size

The mean crystallite size can be deduced from several parameters such as: the half width, ω , of a peak as introduced by Scherrer also defined as the full width at half maximum (FWHM) (Scherrer, 1918). The relevant size parameter, ϵ_ω , is related to the FWHM by:

$$\epsilon_\omega = \frac{K_\omega \cdot \lambda}{FWHM \cdot \cos \theta_B} \quad (3.23)$$

where K_ω is the Scherrer's constant and λ is the wavelength. K_ω is often approximated to 1 in the case of spherical crystallite distribution which does not necessary apply to every sample.

The integral breadth, β , as introduced by Laue *et al.* is defined as the integrated area of the peak over its maximum intensity f_m (Laue et al., 1926):

$$\beta = \int \frac{f(2\theta)d2\theta}{f_m} \quad (3.24)$$

The crystallite size ϵ_β is related to β by:

$$\epsilon_\beta = \frac{\lambda}{\beta} \cos \theta_B \quad (3.25)$$

The Scherrer's equation is commonly used to determine a rough approximation of the domain size and using the FWHM as a starting point. However, this approach does not take the size distribution into account since all the crystallites are not of the same size. It is therefore more sensible to use ϵ_β as an estimate of the crystallite domains or layers depending on the materials (Dinnebier and Billinge, 2008).

3.5.2.3 Experimental

Carbon materials and Cu (II) - framework compounds were investigated on the D8 advance X-ray instrument (*Bruker*) with a Cu K_α X-ray source, a Gobbel mirror to correct for sample height fluctuations and a sol-X detector. Each carbon material was loaded onto a silicon wafer. The instrument was set with a 2θ angular range from 5 to 100 ° and an angular step of 0.1 ° per minute for a total time of 2 h per sample. The Cu (II) - frameworks were degassed under specific conditions (see section 3.3). Each solvent free MOF sample was then transferred into a glove-box and loaded onto a silicon wafer covered by amorphous tape to avoid any moisture contamination. The XRPD data of desolvated samples were collected at room temperature for 2 h within a 2θ angular range of 5 °-35 °.

3. EXPERIMENTAL

3.5.3 Neutron Scattering

Neutron scattering techniques are a powerful tool to investigate bulk properties of materials with no structural damage. This is essentially due to the neutral charge of the neutron and the rather weak neutron-matter interaction. The neutron is also a sensitive probe of the nuclear and magnetic structure and not the electronic cloud which allows neutron techniques to detect light elements in the presence of heavier elements such as atomic / molecular hydrogen as opposed to X-ray techniques. The use of neutron to probe magnetic properties, is not relevant to the work reported here and is therefore not covered in this chapter. After some intrinsic neutron properties are described, neutron powder diffraction (NPD) and inelastic neutron scattering (INS) principles will be addressed. The energy, E , of a neutron with a mass, m_n , and a wave vector, k , is commonly defined by:

$$E = \frac{\hbar^2 k^2}{2m_n} \quad (3.26)$$

where $\hbar = \frac{h}{2\pi}$ with, h , the Planck's constant. Neutrons are usually classified according to their incident energy as cold (0.1-10 meV), thermal (10-100 meV), hot (100-500meV) or epithermal (> 500 meV) neutrons. The key variables are the amounts of energy, ω , and the momentum, Q , transferred from the incident neutron as determined by:

$$\hbar\omega = E_i - E_f \quad (3.27)$$

$$Q = k_i - k_f \quad (3.28)$$

where ω is the angular frequency, E_i , is the energy corresponding to the initial wave vector, k_i , of the incident neutron and E_f , is the energy corresponding to the final wave vector, k_f , of the scattered neutron. The quantity measured during a neutron scattering experiment is the double differential scattering cross section (DDSCS) ($d^2\sigma/d\Omega dE'$), which represents the amount of neutrons of incident energy, E_i , and a wave vector, k_i , scattered into an element of solid angle, $d\Omega$, in the direction $(2\theta, \phi)$ with an energy comprised between E' and $E'+dE'$ and the wave vector comprised between

k' and $k'+dk'$ (Foderaro, 1971). The differential scattering cross section for any molecular system is:

$$\left(\frac{d\sigma}{d\Omega}\right)_{\Psi_i}^{\Psi_f} = \frac{k_f}{k_i} |\langle \mathbf{k}_f, \Psi_f | \hat{V}_r | \mathbf{k}_i, \Psi_i \rangle|^2 \quad (3.29)$$

$|\Psi_i\rangle$ and $|\Psi_f\rangle$, are the initial and final *sample, neutron spin* states. \hat{V}_r represents the neutron-matter interaction and can be in general be described by the Fermi pseudo-potential:

$$\hat{V}_r = \frac{2\pi\hbar^2}{m_n} \sum_l \hat{b}_l \delta(\mathbf{r} - \mathbf{R}_l) \quad (3.30)$$

where \hat{b}_l represents the scattering length operator of the l^{th} element. The DDSCS is:

$$\left(\frac{d^2\sigma}{d\Omega dE'}\right)_{\Psi_i}^{\Psi_f} = \frac{k_f}{k_i} \frac{\sum_{\Psi_f, \Psi_i} p_{\Psi_i} \cdot \left| \sum_l \langle \Psi_f | \hat{b}_l \cdot \exp(i\mathbf{Q} \cdot \mathbf{R}_l) | \Psi_i \rangle \right|^2 \cdot \delta(\hbar\omega + E_{\Psi_i} - E_{\Psi_f})}{\sum_{\Psi_f, \Psi_i} p_{\Psi_i} \cdot \left| \sum_l \langle \Psi_f | \hat{b}_l \cdot \exp(i\mathbf{Q} \cdot \mathbf{R}_l) | \Psi_i \rangle \right|^2 \cdot \delta(\hbar\omega + E_{\Psi_i} - E_{\Psi_f})} \quad (3.31)$$

The sum is averaged over the isotope distributions, the nuclear spin orientations and positions. p_{Ψ_i} is the probability for the system (sample-neutron) to be in the Ψ_i initial state. E_{Ψ_i} and E_{Ψ_f} are the energies corresponding to Ψ_i and Ψ_f states. A different way of writing the δ function in Eq. (3.31) is:

$$\delta(\hbar\omega + E_{\Psi_i} - E_{\Psi_f}) = \frac{1}{2\pi\hbar} \int_{-\infty}^{+\infty} dt \exp(-it(\hbar\omega + E_{\Psi_i} - E_{\Psi_f}) \frac{1}{\hbar}) \quad (3.32)$$

For any molecular system in an initial state described by the wave function Ψ_i , the DDSCS is:

$$\left(\frac{d^2\sigma}{d\Omega dE'}\right)_{total} = \frac{1}{2\pi\hbar} \frac{k_f}{k_i} \sum_f \int_{-\infty}^{+\infty} dt \exp(-i\omega t) \left[\exp \frac{-it(E_i - E_f)}{\hbar} |\langle \Psi_f | \sum_l \hat{b}_l \cdot \exp(i\mathbf{Q} \cdot \mathbf{R}_l) | \Psi_i \rangle| \right]^2 \quad (3.33)$$

3. EXPERIMENTAL

3.5.3.1 Neutron Powder Diffraction

During a total diffraction experiment all scattered neutrons are detected regardless of their final energy E_f . Therefore, the relevant quantity measured is the differential scattering cross section $(d\sigma/d\Omega)_{total}^{elastic}$. In the case of an elastic neutron diffraction experiment only neutrons elastically scattered are detected and therefore:

$$\left(\frac{d\sigma}{d\Omega}\right)_{total}^{elastic} = I(Q) = \left|\sum_l \bar{b}_l \exp(i\mathbf{Q} \cdot \mathbf{R}_l)\right|^2 = \sum_{l,l'} \overline{b_l b_{l'}^*} \exp(i\mathbf{Q} \cdot (\mathbf{R}_l - \mathbf{R}_{l'})) \quad (3.34)$$

where each element l of the sample is characterized by its scattering length, \hat{b}_l , averaged over nuclear spin orientations and isotope distributions.

$$\overline{b_l b_{l'}^*} = \bar{b}^2 + \delta_{l,l'}(\bar{b}^2 - \bar{b}^2) \quad (3.35)$$

where δ is the Kröneckers symbol. Using Eq. (3.35), it is possible to separate Eq. (3.34) into a coherent and incoherent contribution:

$$\left(\frac{d\sigma}{d\Omega}\right)_{total}^{elastic} = \left(\frac{d\sigma}{d\Omega}\right)_{coh}^{elastic} + \left(\frac{d\sigma}{d\Omega}\right)_{inc}^{elastic} \quad (3.36)$$

with:

$$\left(\frac{d\sigma}{d\Omega}\right)_{coh}^{elastic} = \sum_{l,l'} \bar{b}_l \bar{b}_{l'} \exp(i\mathbf{Q} \cdot (\mathbf{R}_l - \mathbf{R}_{l'})) \quad (3.37)$$

and:

$$\left(\frac{d\sigma}{d\Omega}\right)_{inc}^{elastic} = \sum_l \bar{b}_l^2 - \bar{b}^2 = \frac{\sigma_{inc}}{4\pi} \quad (3.38)$$

where σ_{inc} is the incoherent cross section. As we can see in Eq. (3.38), the incoherent part does not contain any structural information, and only the coherent part (Eq. (3.37)) is relevant for an elastic process. For a large crystal one can show that (Lovesey, 1984):

$$|\sum_l \exp(i\mathbf{Q} \cdot \mathbf{R}_l)|^2 = N \cdot \frac{(2\pi)^3}{v_0} \cdot \sum_{\tau_{(h,k,l)}} \delta(\mathbf{Q} - \tau_{h,k,l}) \quad (3.39)$$

This shows that there is no Bragg scattering unless the momentum transfer, \mathbf{Q} , is a reciprocal vector $\tau_{(h,k,l)}$. In the case of more than one atom per unit cell, Eq. (3.37) can be generalized introducing the $F_N(\tau_{(h,k,l)})$ nuclear unit cell structure factor:

$$F_N(\tau_{h,k,l}) = \sum_l \bar{b}_l \cdot \exp(i\tau_{h,k,l} \cdot \mathbf{R}_l) \cdot \exp(-W_l) \quad (3.40)$$

$$\left(\frac{d\sigma}{d\Omega}\right)_{coh}^{elastic} = N \cdot \frac{(2\pi)^3}{v_0} \cdot \sum_{\tau_{(h,k,l)}} \delta(\mathbf{Q} - \tau_{(h,k,l)}) \cdot |F_N(\tau_{h,k,l})|^2 \quad (3.41)$$

where $\exp(-W_l)$ is the Debye-Waller factor and represents the thermal atomic displacement of the l^{th} element. The static approximation assumes that the incident energy, E_i , is large compared with the internal excitation energies of the sample. In this case, $\mathbf{k}_f \approx \mathbf{k}_i$, the initial and final scattering wavevectors are taken close to their elastic value so that:

$$|\mathbf{Q}| = |\mathbf{k}_f - \mathbf{k}_i| = 2k_i \sin \theta_B = 4\pi \frac{\sin \theta_B}{\lambda} \quad (3.42)$$

3.5.3.2 Inelastic Neutron Scattering

In the case of energy exchange between the incident neutrons and the sample, the spectrum collected is a function of the energy, $\hbar\omega$, and momentum, \mathbf{Q} , transfer and not of \mathbf{k}_i or \mathbf{k}_f . One can infer information about the dynamic of individual atoms and their spatial correlations through transitions between internal atomic (or molecular) energy levels (Newton, 1982).

3.5.3.2.1 Quantum Rotor

In the Born-Oppenheimer approximation and if the coupling effects are neglected, degrees of freedom can be treated separately. At low temperatures,

3. EXPERIMENTAL

ca. 4 K, the diatomic molecule is considered as a rigid body in its vibrational ground state where only molecular rotations are considered. An initial state for a free molecule is described by its rotational and nuclear spin states *i.e.*: $| -J \rangle | -s \rangle$ (Cohen-Tannoudji et al., 1977). Therefore, Eq. (3.31) can be written as:

$$\left(\frac{d^2\sigma}{d\Omega dE'} \right)_J^{J'} = \frac{k_f}{k_i} \frac{\sum_{J,s,J',s'} p_{J,s} \left| \sum_n \langle s'J' | \hat{b}_n \exp(i\mathbf{Q} \cdot \mathbf{R}_n) | sJ \rangle \right|^2 \delta(\hbar\omega + E_J - E_{J'})}{\sum_{J,s,J',s'} p_{J,s} \left| \sum_n \langle s'J' | \hat{b}_n \exp(i\mathbf{Q} \cdot \mathbf{R}_n) | sJ \rangle \right|^2 \delta(\hbar\omega + E_J - E_{J'})} \quad (3.43)$$

3.5.3.2.2 Homonuclear Diatomic Molecule

For a free rotating H₂ molecule as represented in Figure 3.6.a, under the Born Oppenheimer approximation the rotational wavefunctions $| J \rangle$ are the well known spherical harmonics, $Y_M^J(\theta, \phi)$ with no radial components. $J = 0, 1, 2, \dots$ and $M = 0, \pm 1, \pm 2, \pm J, \dots$ are the angular momentum quantum numbers. Each hydrogen atom is a half-integer spin particle and therefore H₂ has to obey Fermi's statistics, which is expressed through the Pauli's principle. The exchange operator $P_{1,2}$ applied to the total wavefunction $| J \rangle | s \rangle = (\pm 1) Y_M^J(\theta, \phi) | s \rangle$ leads to:

$$P_{1,2} | J \rangle | s \rangle = (\pm 1) Y_M^J(\theta, \phi) | s \rangle \quad (3.44)$$

The operator $P_{1,2}$ exchanges the nuclei position of two indistinguishable particles by applying $r \rightarrow -r$. Therefore Eq. (3.44) is also equivalent to:

$$Y_M^J(\pi - \theta, \phi + \pi) = (-1)^J Y_M^J(\theta, \phi) \quad (3.45)$$

In order to satisfy Eq. (3.45), the even numbered rotational states ($J = 0, 2, \dots$) are to be combined with anti-symmetric nuclear spin states and the odd rotational states ($J = 1, 3, \dots$) with symmetric nuclear spin states, leading respectively to two important species para-H₂ and ortho-H₂. In normal

H_2 gas, the ortho- H_2 / para- H_2 ratio is 3:1. For H_2 the molecular ground state is $J = 0$ which corresponds to para- H_2 whereas for D_2 it is ortho- D_2 $J = 1$ as shown below in Figure 3.6.b (Silvera et al., 1978, Silvera, 1980).

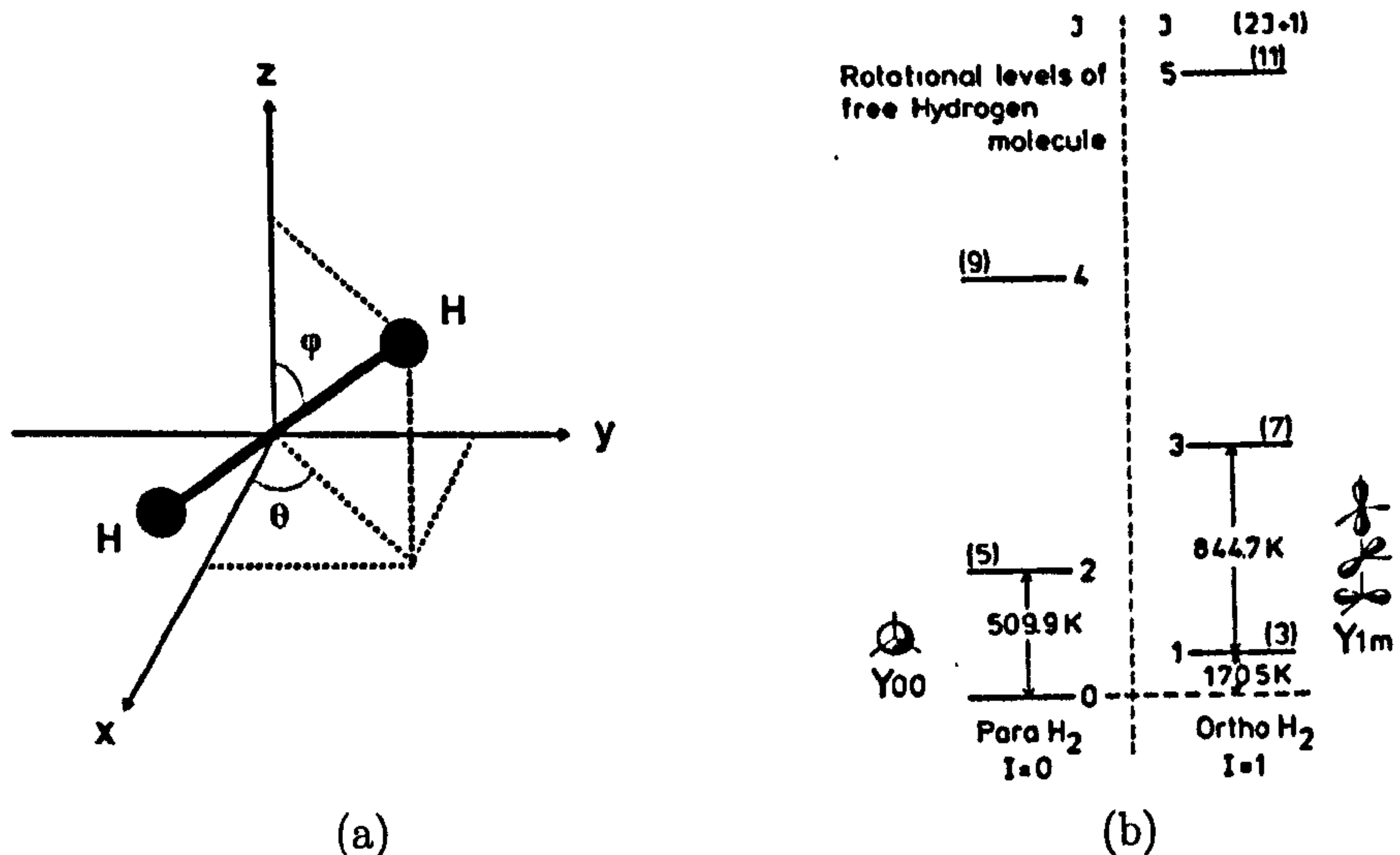


Figure 3.6: a) H_2 molecule with the angular coordinates (θ, ϕ) . b) Rotational energy diagram of para- H_2 and ortho- D_2 (Silvera et al., 1978, Silvera, 1980).

For a free H_2 molecule initially in a $|J \text{ even}, s \text{ even}\rangle$ state (*i.e.*: para- H_2 molecule) and its vibrational ground state, the double differential scattering cross section is:

$$\begin{aligned} \left(\frac{d^2\sigma}{d\Omega dE'} \right)_{\text{rotation}}^{\text{inc}} &= \frac{1}{4} \frac{k_f}{k_i} \sqrt{\frac{\beta M}{\pi \hbar^2 Q^2}} \sum_{J \text{ even}} p_J \\ &\left[\sigma_{\text{coh}} \sum_{J' \text{ even}} (2J' + 1) \exp \left(-\frac{\beta M}{\hbar^2 Q^2} (E_{J'} - E_J + E_r - \hbar\omega)^2 \right) F_{J \text{ even} \rightarrow J' \text{ even}} \right. \\ &\left. + \sigma_{\text{inc}} \sum_{J' \text{ odd}} (2J' + 1) \exp \left(-\frac{\beta M}{\hbar^2 Q^2} (E_{J'} - E_J + E_r - \hbar\omega)^2 \right) F_{J \text{ even} \rightarrow J' \text{ odd}} \right] \end{aligned} \quad (3.46)$$

where σ_{coh} and σ_{inc} are the coherent and incoherent cross section of atomic hydrogen and $\beta = \frac{1}{kT}$. m_{H_2} represents the mass of the dihydrogen molecule. E_r is the molecular recoil energy and is equal to:

3. EXPERIMENTAL

$$E_r = \frac{\hbar^2 Q^2}{4m_{H_2}} \quad (3.47)$$

The exponential term describes a free centre of mass (CoM) which is a good approximation for a gas. The molecular structure factors, $F_{J_{even} \rightarrow J'_{even}}$, and, $F_{J_{even} \rightarrow J'_{odd}}$, were introduced and represent the contribution from the ($J_{even} \rightarrow J'_{even}$) and ($J_{even} \rightarrow J'_{odd}$) rotational transitions:

$$F_{J_{even} \rightarrow J'_{even}} = \sum_{m=|J'-J|}^{J'+J} (2m+1) \begin{pmatrix} J' & J & m \\ 0 & 0 & 0 \end{pmatrix}^2 j_m^2 \left(\frac{\mathbf{Q} \cdot \mathbf{r}_e}{2} \right) \quad (3.48)$$

$$F_{J_{even} \rightarrow J'_{odd}} = \sum_{m=|J'-J|}^{J'+J} (2m+1) \begin{pmatrix} J' & J & m \\ 0 & 0 & 0 \end{pmatrix}^2 j_m^2 \left(\frac{\mathbf{Q} \cdot \mathbf{r}_e}{2} \right) \quad (3.49)$$

$\begin{pmatrix} J' & J & m \\ 0 & 0 & 0 \end{pmatrix}$ corresponds to the 3j symbols. $j_m^2 \left(\frac{\mathbf{Q} \cdot \mathbf{r}_e}{2} \right)$ represents the Bessel function of order m . r_e is the equilibrium distance between two hydrogen atoms. For solid para- H_2 , only the ($J = 0$) state is populated, the rotational transitions allowed by neutron spin exchange are limited to ($J = 1 \leftarrow 0$), ($J = 0 \leftarrow 0$) and ($J = 2 \leftarrow 0$). Therefore, Eq. (3.46) can be simplified and becomes:

$$\begin{aligned} \left(\frac{d^2 \sigma}{d\Omega dE'} \right)_{rotation}^{inc} &= \frac{1}{4} \cdot \left| \frac{\mathbf{k}_f}{\mathbf{k}_i} \right| \cdot \sqrt{\frac{\beta M}{\pi \hbar^2 Q^2}} \\ &\left[\sigma_{coh} \left(F_{0 \rightarrow 0} \exp \left(-\frac{\beta M}{\hbar^2 Q^2} (E_{J'} - E_J + E_r - \hbar \omega)^2 \right) \right. \right. \\ &\quad \left. \left. + 5 F_{0 \rightarrow 2} \exp \left(-\frac{\beta M}{\hbar^2 Q^2} (E_{J'} - E_J + E_r - \hbar \omega)^2 \right) \right) \right. \\ &\quad \left. + 3 \sigma_{inc} F_{0 \rightarrow 1} \exp \left(-\frac{\beta M}{\hbar^2 Q^2} (E_{J'} - E_J + E_r - \hbar \omega)^2 \right) \right] \quad (3.50) \end{aligned}$$

Where $F_{0 \rightarrow 0}$, $F_{0 \rightarrow 1}$, and $F_{0 \rightarrow 2}$ are defined by:

$$F_{0 \rightarrow 0} = \begin{pmatrix} 0 & 0 & 0 \\ 0 & 0 & 0 \end{pmatrix}^2 j_0^2 \left(\frac{\mathbf{Q} \cdot \mathbf{r}_e}{2} \right) \quad (3.51)$$

$$F_{0 \rightarrow 1} = 3 \begin{pmatrix} 1 & 0 & 1 \\ 0 & 0 & 0 \end{pmatrix}^2 j_1^2 \left(\frac{\mathbf{Q} \cdot \mathbf{r}_e}{2} \right) \quad (3.52)$$

$$F_{0 \rightarrow 2} = 5 \begin{pmatrix} 2 & 0 & 2 \\ 0 & 0 & 0 \end{pmatrix}^2 j_2^2 \left(\frac{\mathbf{Q} \cdot \mathbf{r}_e}{2} \right) \quad (3.53)$$

The energy associated with the rotational state $|J \text{ even}\rangle$ is $E_J = J(J + 1) \cdot B_{rot}$ with, B_{rot} , the rotational constant defined by:

$$B_{rot}(H_2) = \frac{\hbar^2}{2I} \quad (3.54)$$

I is the moment of inertia of the H_2 molecule and is determined by:

$$I = m_{H_2} \cdot r_{H-H}^2 \quad (3.55)$$

Therefore the first rotational transitions for a para- H_2 molecule in the ground state are:

$$E_1 - E_0 = 2B_{rot} = 14.7 \text{ meV} = 118 \text{ cm}^{-1} \text{ corresponding to } (J=1 \leftarrow 0)$$

$$E_2 - E_0 = 6B_{rot} = 44.1 \text{ meV} = 354 \text{ cm}^{-1} \text{ corresponding to } (J=2 \leftarrow 0)$$

3.5.3.2.3 Homonuclear Diatomic Molecular Gas

Eq. (3.50) showed the DDSCS for an isolated molecule in its vibrational ground state. For any diatomic molecular system in its vibrational ground state and an initial rotational state described by an initial wave function, Ψ_i , it is possible to write the DDSCS (Eq. (3.31)) as the sum of two contributions (Young and Koppel, 1964):

3. EXPERIMENTAL

$$\left(\frac{d^2\sigma}{d\Omega dE'}\right)_{total}^{inc} = \frac{1}{2\pi\hbar} \frac{k_f}{k_i} \sum_f \int_{-\infty}^{+\infty} dt. \exp\left(it \frac{\hbar\omega - E_i + E_f}{\hbar}\right) [G(t)_{self} + G(t)_{ms}] \quad (3.56)$$

We introduced the self and multi-scattering functions $G(t)_{self}$ and $G(t)_{ms}$ respectively referring to the scattering from two particles of a single molecule and from two particles of two different molecules:

$$G(t)_{self} = \sum_i \left| \langle \Psi_f | \sum_l \hat{b}_l. \exp(i\mathbf{Q} \cdot \mathbf{R}_l) | \Psi_i \rangle \right|^2 \quad (3.57)$$

and:

$$G(t)_{ms} = \sum_{i \neq j} \langle \Psi_i | \sum_j \exp(-i\mathbf{Q} \cdot \mathbf{R}_j) \hat{b}_l^+ | \Psi_f \rangle. \quad \langle \Psi_f | \sum_l \hat{b}_l. \exp(-i\mathbf{Q} \cdot \mathbf{R}_l) | \Psi_i \rangle \quad (3.58)$$

The DDSCS in Eq. (3.56) can be written as:

$$\left(\frac{d^2\sigma}{d\Omega dE'}\right)_{total}^{inc} = \left(\frac{d^2\sigma}{d\Omega dE'}\right)_{self}^{inc} + \left(\frac{d^2\sigma}{d\Omega dE'}\right)_{ms}^{inc} \quad (3.59)$$

The relevant DDSCS for the self scattering term, $(d^2\sigma/d\Omega dE')_{self}^{inc}$, is the same as that for the isolated molecule Eq. (3.50).

3.5.3.2.4 Molecular Vibrations

It is possible to write the time dependent atomic position, $\mathbf{R}_l(t)$, as the sum of internal, $\mathbf{u}_l(t)$, (intramolecular) and external, $\mathbf{r}_l(t)$, (intermolecular or phonons) vibrations. $\mathbf{r}_l(t)$ describes the CoM motion also known as the translational motion while $\mathbf{u}_l(t)$ represents the atomic positions with the CoM as the origin so that:

$$\mathbf{R}_l(\mathbf{t}) = \mathbf{r}_l(\mathbf{t}) + (-1)^n \cdot \frac{\mathbf{u}_l(\mathbf{t})}{2}, n=1,2 \quad (3.60)$$

The self and multi scattering terms introduced earlier in Eq. (3.56) can be written as:

$$G(t)_{self} = \sum_l \sum_{n=1}^2 \left| \langle \Psi_f | \sum_l \hat{b}_l \cdot \exp(i\mathbf{Q} \cdot \mathbf{r}_l + (-1)^n \frac{\mathbf{Q} \cdot \mathbf{u}_l}{2}) | \Psi_i \rangle \right|^2 \quad (3.61)$$

$$G(t)_{ms} = \sum_{l \neq j} \sum_{n,p=1}^2 \langle \Psi_i | \sum_l \exp(-i\mathbf{Q} \cdot \mathbf{r}_l - i(-1)^p \frac{\mathbf{Q} \cdot \mathbf{u}_l}{2}) \hat{b}_{lp}^+ | \Psi_f \rangle \langle \Psi_f | \sum_l \hat{b}_{ln} \cdot \exp(i\mathbf{Q} \cdot \mathbf{r}_l + i(-1)^n \mathbf{u}_l \cdot \frac{\mathbf{Q}}{2}) | \Psi_i \rangle \quad (3.62)$$

Only the intramolecular motion term in $G(t)_{self}$ Eq. (3.56) is relevant. At low temperature (*ca.* 4 K in our case), the expression for the v^{th} mode of an harmonic oscillator of amplitude $\mathbf{u}(\mathbf{t})$ and incoherent scattering cross section σ_{inc} is (Mitchell et al., 2004):

$$\left(\frac{d^2\sigma}{d\Omega dE'} \right)_{self,intra}^{inc} = \frac{\sigma_{inc}}{4\pi} \frac{k_f}{k_i} \frac{(\mathbf{Q} \cdot \mathbf{u})^{2n}}{n!} \cdot \exp\left(-\frac{(\mathbf{Q} \cdot \mathbf{u})^2}{3}\right) \quad (3.63)$$

$n=0$ represents the elastic line:

$$\left(\frac{d^2\sigma}{d\Omega dE'} \right)_{self,intra}^{inc} = \frac{\sigma_{inc}}{4\pi} \frac{k_f}{k_i} \cdot \exp\left(-\frac{(\mathbf{Q} \cdot \mathbf{u})^2}{3}\right) \quad (3.64)$$

$n=1$ represents the fundamental:

$$\left(\frac{d^2\sigma}{d\Omega dE'} \right)_{self,intra}^{inc} = \frac{\sigma_{inc}}{4\pi} \frac{k_f}{k_i} (\mathbf{Q} \cdot \mathbf{u})^2 \cdot \exp\left(-\frac{(\mathbf{Q} \cdot \mathbf{u})^2}{3}\right) \quad (3.65)$$

$n=2$ represents the 1st overtone:

$$\left(\frac{d^2\sigma}{d\Omega dE'} \right)_{self,intra}^{inc} = \frac{\sigma_{inc}}{4\pi} \frac{k_f}{k_i} \frac{(\mathbf{Q} \cdot \mathbf{u})^4}{2} \cdot \exp\left(-\frac{(\mathbf{Q} \cdot \mathbf{u})^2}{3}\right) \quad (3.66)$$

3. EXPERIMENTAL

where the Debye-Waller factor, $\exp(-(Q.u)^2/3)$, was introduced and represents the atomic thermal displacements. In general, in combining the rotational and vibrational part, the self scattering DDSCS per unit of solid angle and energy transfer measured during an inelastic neutron scattering experiment can be written as:

$$\left(\frac{d^2\sigma}{d\Omega dE'}\right)_{self}^{inc} = \left(\frac{d^2\sigma}{d\Omega dE'}\right)_{self,intra}^{inc} \times \left(\frac{d^2\sigma}{d\Omega dE'}\right)_{rotation}^{inc} \otimes \left(\frac{d^2\sigma}{d\Omega dE'}\right)_{self,CoM}^{inc} \otimes F_{instrument} \quad (3.67)$$

where the instrument resolution function, $F_{instrument}$, and the DDSCS describing the CoM motion in $G(t)_{self}$ are convoluted for a complete expression.

3.5.3.2.5 Solid Phase

The DDSCS for solid para-hydrogen is different from that for the para-hydrogen in the gas phase (Eq. (3.46)). In fact, while the rotational levels remain unchanged, the CoM is not free any longer. The DDSCS is now:

$$\left(\frac{d^2\sigma}{d\Omega dE'}\right)_{rotation}^{inc} = \frac{1}{4} \frac{k_f}{k_i} \sum_{J_{even}} p_J \exp(-2W(Q)) \left[\sigma_{coh} \sum_{J'_{even}} (2J' + 1) F_{J_{even} \rightarrow J'_{even}} \delta(\hbar\omega + E_{J'} - E_J + E_r) + \sigma_{inc} \sum_{J'_{odd}} (2J' + 1) F_{J_{even} \rightarrow J'_{odd}} \delta(\hbar\omega + E_{J'} - E_J + E_r) \right] \quad (3.68)$$

The Debye-Waller factor was kept, representing the mean atomic thermal displacements. The INS spectrum of solid para-H₂ is mainly composed of one sharp peak at 14.7 meV (or 118 cm⁻¹) which corresponds to the ($J=1 \leftarrow 0$) rotational transition and a Gaussian hump centred at meV (Lovesey, 1984, Mitchell et al., 2004). The rotational transition ($J=2 \leftarrow 0$) can also

be observed at 44.1 meV (354 cm^{-1}) (Figure 3.7).

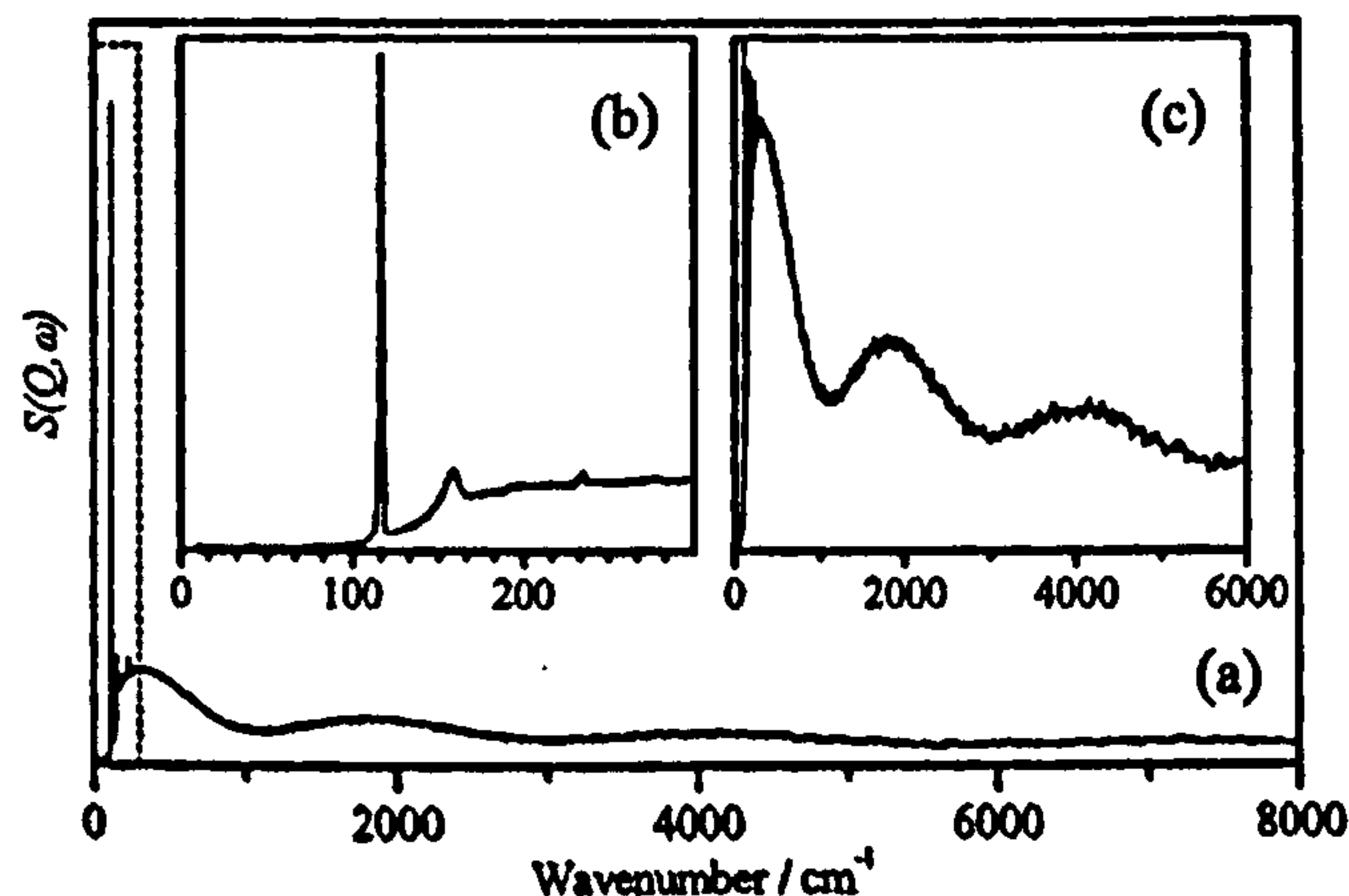


Figure 3.7: Solid para- H_2 INS spectrum collected at 4 K on the neutron spectrometer TOSCA at ISIS-RAL (Mitchell et al., 2004).

3.5.3.2.6 Rotations of a Homonuclear Diatomic Molecule in a Hindering Potential

In this work molecular hydrogen was used as a probe of its local environment through the study of its rotational transitions which can be either strongly or weakly perturbed by the interaction with the adsorption sites. Close to an adsorption site, para- H_2 molecules are not free to rotate any longer and start to experience the adsorption potential $\hat{V}(z, \theta, \phi)$ which depends on the z the distance of approach, and orientations of the molecule (Figure 3.6a). Therefore the spherical harmonics $Y_M^J = |J, M\rangle$ are no longer good eigenfunctions and the new Hamiltonian is:

$$\hat{\mathcal{H}} = \hat{\mathcal{H}}_{\text{freeH}_2} + \hat{V}(z, \theta, \phi) \quad (3.69)$$

Using the perturbation theory the element of the diagonal is:

$$\begin{aligned} \hat{\mathcal{H}}(J, J', M, M') = \\ J(J+1)B_{\text{rot}}\delta_{J,J'}\delta_{M,M'} + \langle Y_{J',M'} | \hat{V}(z, \theta, \phi) | Y_{J,M} \rangle \end{aligned} \quad (3.70)$$

3. EXPERIMENTAL

The goal is to find the right potential $\hat{V}(z, \theta, \phi)$ for a given adsorption site in order to match the INS spectrum with adsorbed para-H₂ (White and Lassettre, 1960).

3.5.3.2.7 Hydrogen Deuteride

It is also possible to derive similar DDSCS for a homonuclear diatomic molecule initially in a $|J_{odd}\rangle$ state (*i.e.*: ortho-H₂ and ortho-D₂) (Lovesey, 1984). Another type of molecular hydrogen of interest is hydrogen deuteride molecule which is not subject to the same selection rules as para-H₂ (D₂) or ortho-H₂ (D₂) since H and D are two distinguishable particles. In this case there is no quantum nuclear spin and spatial correlation. The self scattering DDSCS for solid HD in its rotational and vibrational ground state is similar to Eq. (3.56) (Colognesi et al., 2009):

$$\left(\frac{d^2\sigma}{d\Omega dE'}\right)_{rotation}^{inc} = \frac{\sigma_{inc}}{4\pi} \frac{k_f}{k_i} \sum_{J_{even}} p_J \exp(-2W(Q)) \cdot \sum_{J'} (2J' + 1) \cdot j_{J'}^2(Q \cdot |r - R|) \delta(\hbar\omega + E_J - E_{J'} + E_r) \quad (3.71)$$

The rotational transitions allowed are ($J = 1 \leftarrow 0$), ($J = 0 \leftarrow 0$) and ($J = 2 \leftarrow 0$). The ($J = 1 \leftarrow 0$) rotational transition remains the most intense INS feature at 10.9 meV (Figure 3.8). Features at 5.1 meV, 16.0 meV are replica of the density of phonon states while the small peak at 14.4 meV has not been assigned yet. At higher energy transfer *ca.* 32.9 meV it is possible to witness ($J = 2 \leftarrow 0$) rotational transition.

The use of HD gas compared to para-H₂ gas as a molecular probe allows the separation of the rotational lines from the vibrational lines as the respective rotational constants B_{HD} and B_{H_2} can be related. If the centre of the HD molecule coincides with the centre of the bond:

$$B_{rot}(HD) = \frac{3}{4} \cdot B_{rot}(H_2) \quad (3.72)$$

If the centre of the HD molecule is taken as the centre of gravity:

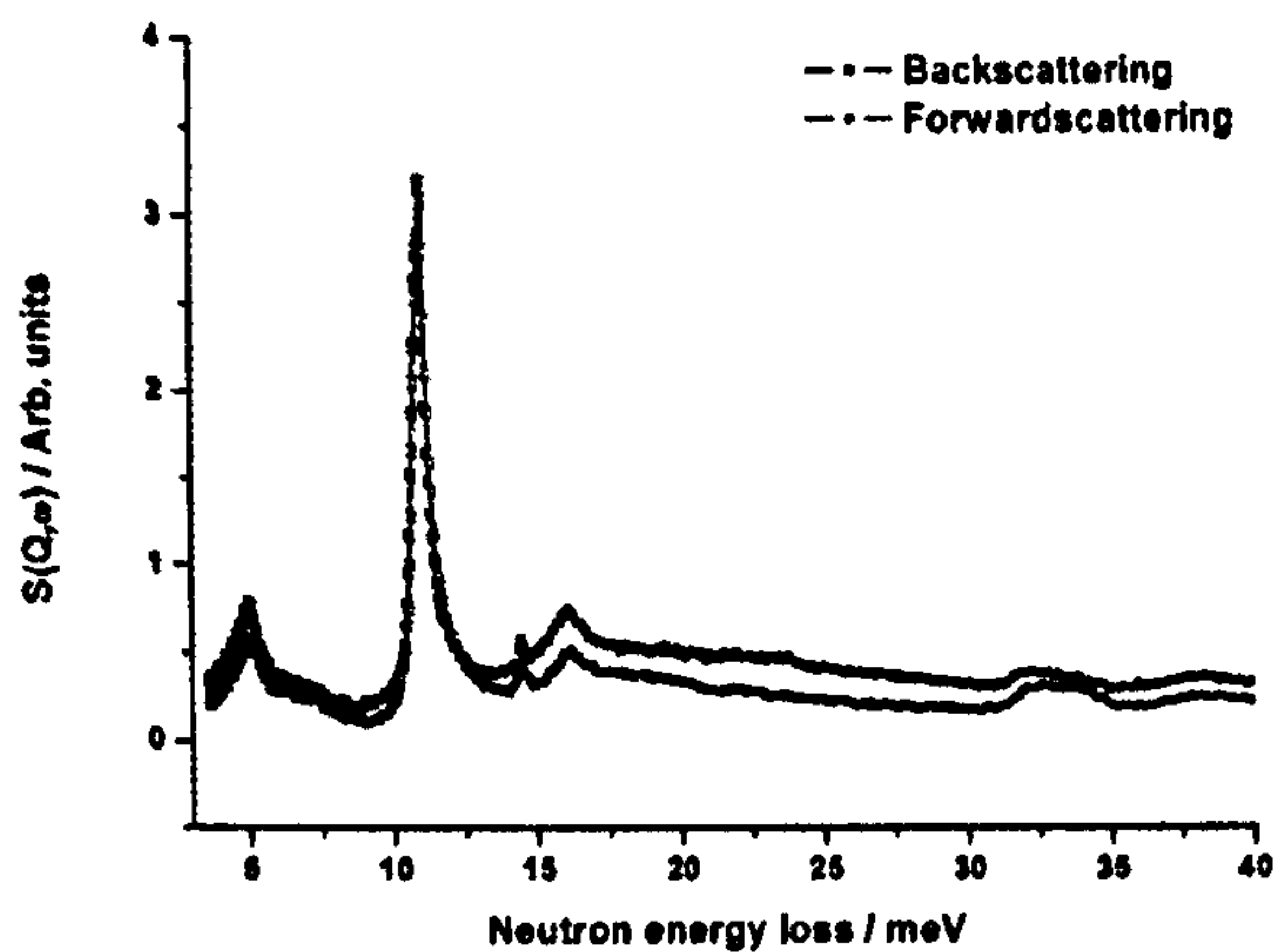


Figure 3.8: Solid HD INS spectra obtained on TOSCA (Colognesi et al., 2009).

$$B_{rot}(HD) = \frac{2}{3} \cdot B_{rot}(H_2) \quad (3.73)$$

Therefore, one would expect a shift of a pure rotational line.

3.5.3.2.8 Response Function

The response function or scattering law for N particles is defined as:

$$S(Q, \omega) = \frac{1}{2\pi\hbar N} \int_{-\infty}^{+\infty} dt \exp(-i\omega t) \sum_{l,l'} \langle \exp(-\mathbf{Q} \cdot \mathbf{R}_l) \cdot \exp(i\mathbf{Q} \cdot \mathbf{R}_{l'}(t)) \rangle \quad (3.74)$$

The term $\langle \exp(-\mathbf{Q} \cdot \mathbf{R}_l) \cdot \exp(i\mathbf{Q} \cdot \mathbf{R}_{l'}(t)) \rangle$ represents the thermal average. Therefore, it is possible to obtain the scattering law from the DDSCS using:

$$\left(\frac{d^2\sigma}{d\Omega dE'} \right)_{inelastic}^{incoherent} = \frac{\sigma_{inc}}{4\pi} \frac{k_f}{k_i} S(Q, \omega) \quad (3.75)$$

3.5.3.3 Neutron Powder Diffraction Experiments

The neutron powder diffraction (NPD) data were collected at the National Institute of Standards and Technology - Center for Neutron Research

3. EXPERIMENTAL

(NIST-CNR) (Gaithersburg, US) using the constant wavelength high - resolution powder diffractometer BT1 NIST (2006) and at the pulsed neutron source, Rutherford Appleton Laboratory, ISIS-RAL (Oxford, UK) using the time of flight General Material powder diffractometer GEM (Hannon, 2005). Only the Cu (II) - frameworks were investigated by neutron techniques. Prior to the neutron experiments, NOTT-101, and NOTT-102 were thermally activated following the same procedure (section thermal activation) and yielding solvent free sample masses of 1.7 g, and 1.9 g. XRPD experiments prior to loading-up the samples confirmed the quality and integrity of the desolvated samples for the neutron experiments.

A sample with all C-H bonds deuterated would require less time for acquisition in NPD, because of the large incoherent cross section of H which is one order of magnitude higher than that of any other element $\sigma_{inc}(D) = 2.05$ barn, $\sigma_{inc}(H) = 80.3$ barn. However, this is synthetically unrealistic and, as shown by Peterson *et al.*, acceptable data can be collected from native samples (Peterson *et al.*, 2006). D₂ gas was used instead of H₂ gas as deuterium has a more favourable scattering ratio with a smaller incoherent scattering cross section more suitable for NPD experiments. All the samples were loaded in a vanadium sample vessel. Vanadium has no coherent cross section, which means that the vanadium can be nearly invisible to neutrons. All the data were collected at 4 K in order to minimize any broadening effect from the Debye-Waller factor. NPD experiments followed the same experimental procedure starting with the collection of the bare material signal under vacuum for 12 h in the case of BT1 and approximately 1000 μA on GEM. In order to identify adsorption sites, known amounts of normal D₂ gas were introduced to the sample from a calibrated volume at room temperature. These samples were calculated to be 0.5, 1.0, 1.5, 2.0, and 3.0 molecules of D₂ per Cu site. After collection of the bare material signal, the sample was heated up to 50 K, dosed with the desired D₂ amount and cooled back down to 4 K for another data acquisition, having allowed enough time for the sample to reach thermal and pressure equilibria. These steps were repeated for each aliquot of D₂. As the baratron connected to the sample cell indicated zero pressure before cooling to 4 K, it was assumed that all the D₂ gas was adsorbed onto the Cu (II) - framework.

The high resolution constant wavelength neutron powder diffractometer BT1 was configured using a Ge (311) monochromator with a 75° take-off angle, $\lambda = 2.0787(2) \text{ \AA}$, and in-pile collimation of 7 minutes of arc were used. Data were collected over a 2θ range of $1.3\text{--}166.3^\circ$ with a step size of 0.05° (Figure 3.9a). Time of flight neutron diffraction measurements were also carried out on the GEM diffractometer. An orange-type cryostat was used to cool the sample. A gas handling system connected to a turbo pump was used for the gas loading. Diffraction data as a function of neutron time-of-flight were collected from the sample in three of the GEM detector banks centred at $2\theta = 9.1, 18.0, 35.1, 63.9$ and 94.4° with a constant beam current *ca.* $1000 \mu\text{A}$ (Figure 3.9b). This corresponds to a d-space range from 0.3 \AA to 20 \AA with a best resolution of $\Delta Q/Q = 0.34\%$ for the backward angle. The data were normalized to the wavelength distribution of the incident neutron beam, and focused into 5 separate histograms, one for each GEM detector bank.

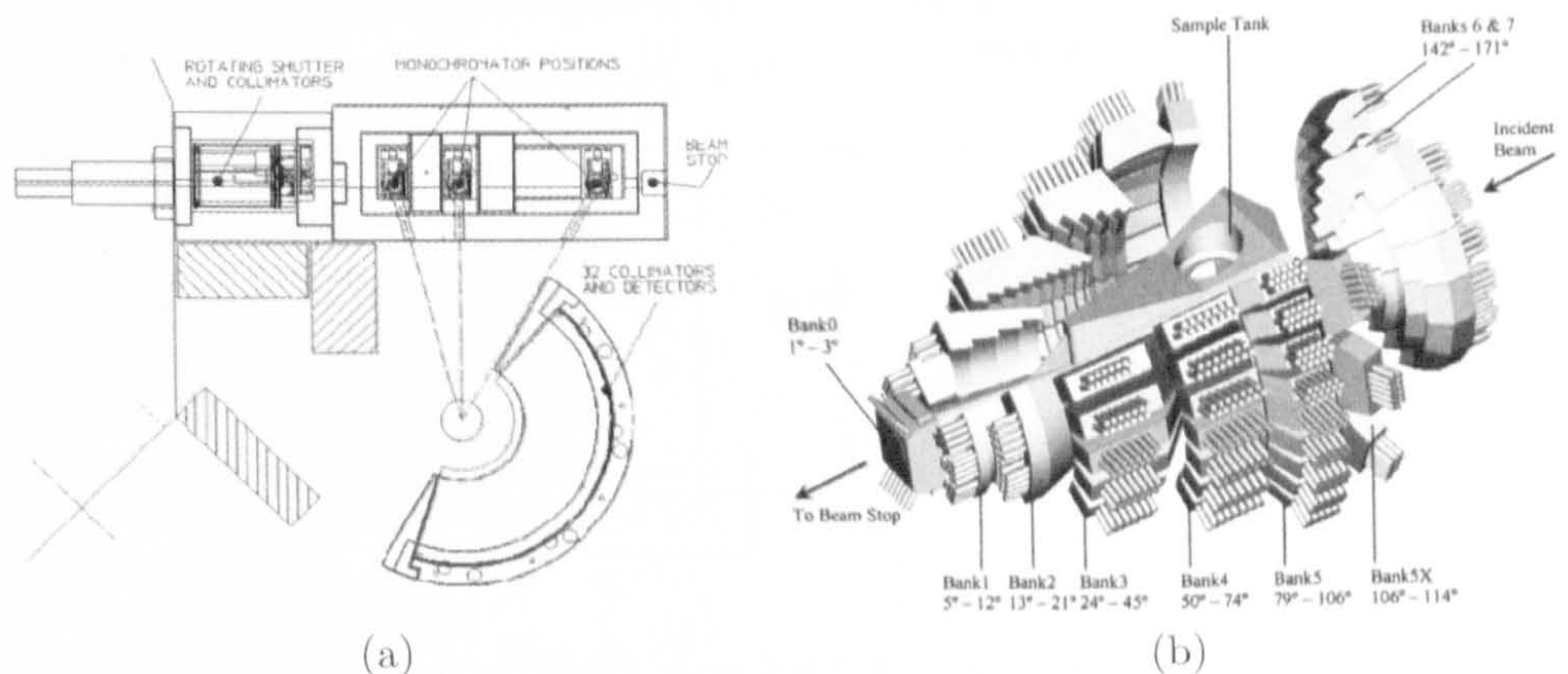


Figure 3.9: BT-1 instrument as viewed from above. For size reference, note that the diffractometer radius is approximately one meter (NIST). b) A schematic layout of the detector banks of the GEM detector array (Hannon, 2005).

3.5.3.4 Inelastic Neutron Scattering Experiments

INS experiments on Cu (II) - frameworks were carried out on the Filter Analyzer Neutron Spectrometer FANS (Udovic et al., 2004) at NIST-CNR and on TOSCA (Colognesi et al., 2002) at ISIS-RAL to complement the NPD studies. In order to compare the two neutron studies, a similar experimen-

3. EXPERIMENTAL

tal procedure as for the NPD work was applied with equivalent amounts of para-H₂ dosed onto the sample *ca.* 0.5, 1.0, 1.5, 2.0 and 3.0 para-H₂ molecules per Cu site. A converting cell was used to change normal-H₂ into a para-H₂ manifold in the presence of a paramagnetic catalyst at low temperature. The INS data were collected at 4 K, while each para-H₂ loading was made at 50 K.

FANS is an indirect neutron spectrometer using the beryllium filter to fix the neutron final energy, E_f , of the neutron detected to 5 meV. It was configured for use with a pyrolytic graphite monochromator 002 Bragg reflection and 20' horizontal collimation before and after the monochromator (Figures 3.10a, 3.11a, and 3.11b).

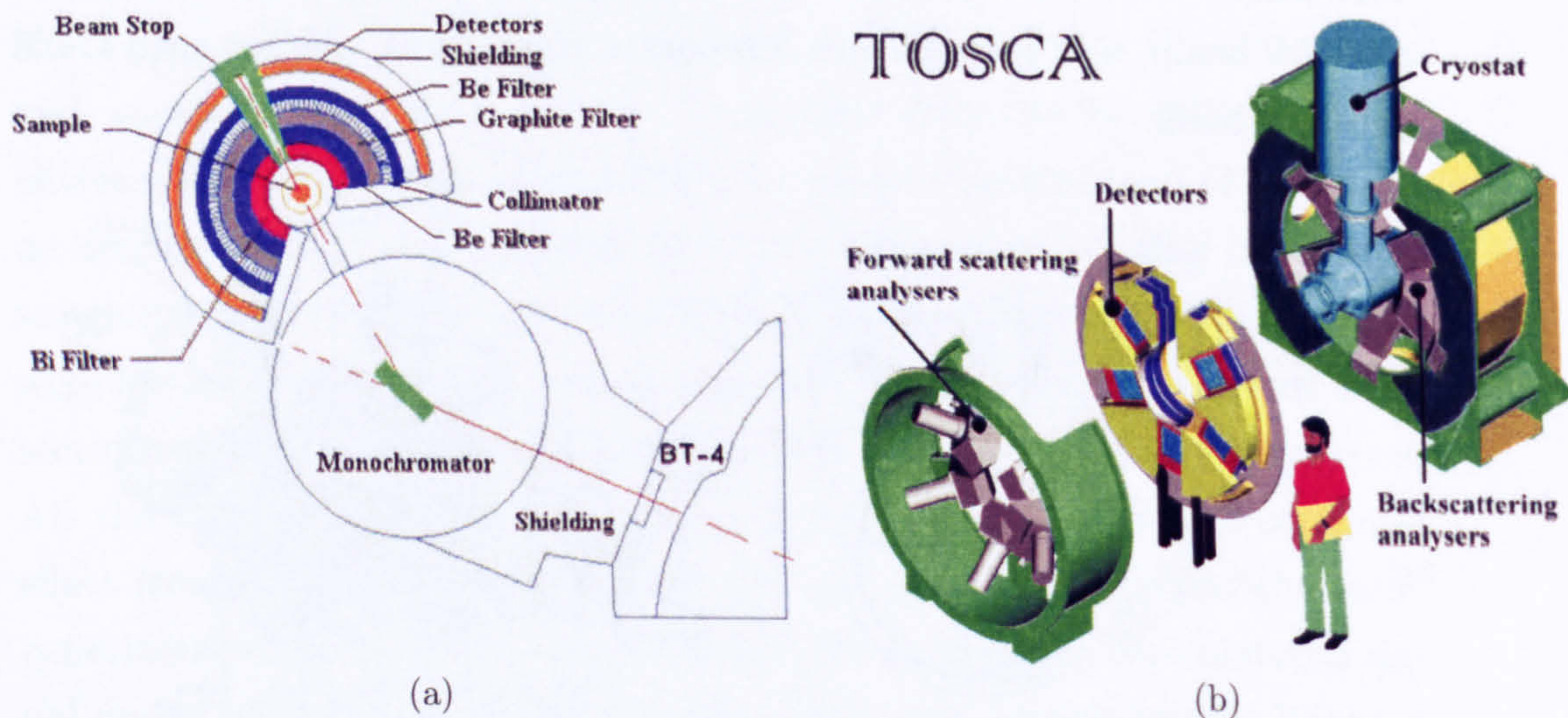


Figure 3.10: A schematic layout of FANS and TOSCA reproduced from (NIST) and (ISIS-RAL)

TOSCA is also an indirect geometry spectrometer with the neutron final energy, E_f , fixed to 3.5 meV (Figure 3.10b). It is up to now the world's best crystal analyzer neutron spectrometer including analyzer-detectors modules in both backward and forward scattering. The excellent resolution in Figure 3.12a limits the instrument to two trajectories along the (Q, ω) space as seen in Figure 3.12b. A gas handling system was connected to a turbo pump in order to dose para-H₂ and HD gases. The INS data were also collected at 4 K with a constant beam current of 1000 μA per acquisition. All the

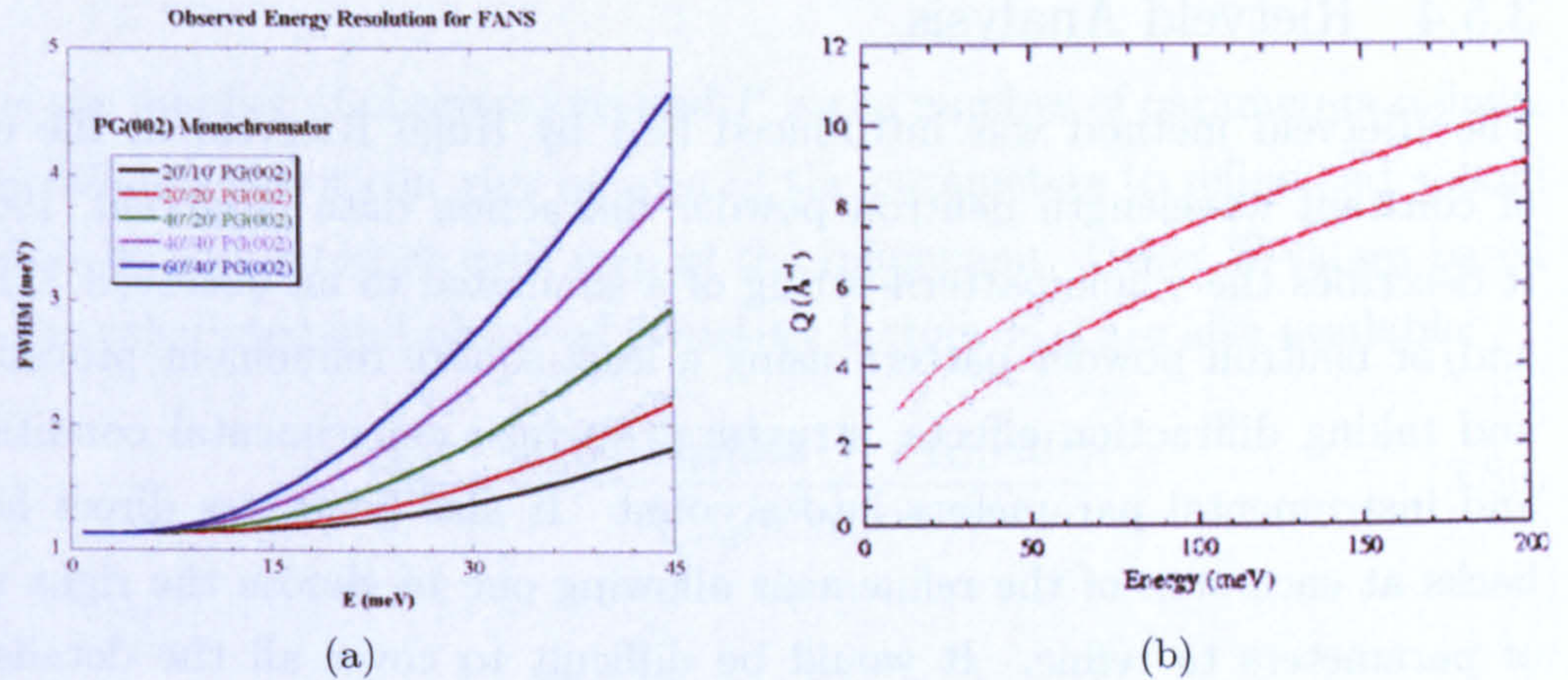


Figure 3.11: a) Energy resolution of FANS. The pyrolytic graphite monochromator 002 with 20' horizontal collimation before and after the monochromator. b) FANS (Q, ω) trajectories (NIST, 2006).

intensities $S(Q, \omega)$ will be reported separately for the back and the forward scattering banks since the corresponding (Q, ω) trajectory depends on the angular position of the detector (Figure 3.12b). This has its importance in the case of peak fitting analysis especially at low energy transfer. However for a qualitative description often only the total signal collected $S(Q, \omega)_{total} = S(Q, \omega)_{back} + S(Q, \omega)_{forward}$ is provided.

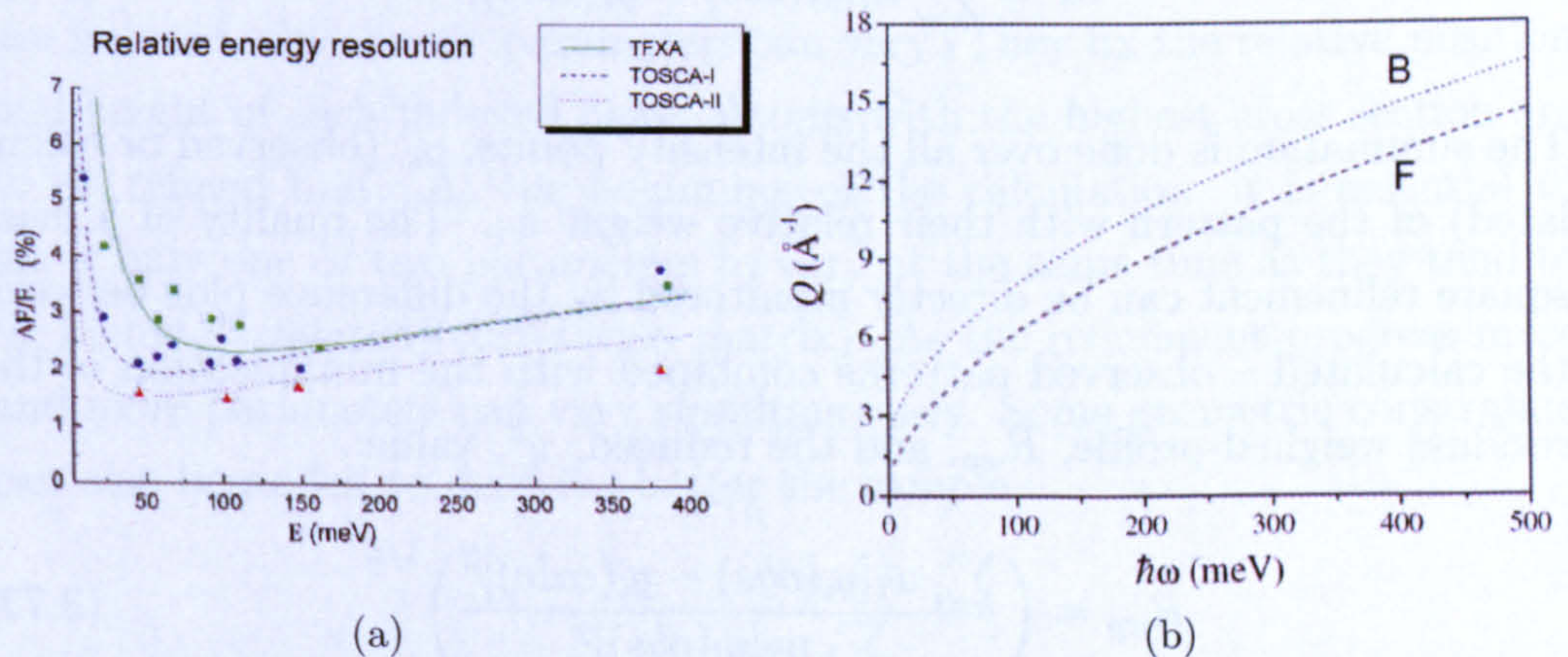


Figure 3.12: a) Energy resolution of TOSCA-II compared to earlier versions TOSCA-I and TFXA (ISC-CNR). b) (Q, ω) trajectories of the back (B) and forward (F) scattering banks on TOSCA (ISC-CNR).

3. EXPERIMENTAL

3.5.4 Rietveld Analysis

The Rietveld method was introduced first by Hugo Rietveld in the case of constant wavelength neutron powder diffraction data (Rietveld, 1969). It describes the whole-pattern-fitting of a simulated to an observed X-Ray and/or neutron powder pattern using a least-square refinement procedure and taking diffraction effects, structural models, experimental conditions and instrumental parameters into account. It also generates direct feedbacks at each step of the refinement allowing one to choose the right sets of parameters to refine. It would be difficult to cover all the details of a full refinement instead this section proposes a general strategy for the refinement of constant wavelength and time of flight NPD data from a non-magnetic sample. Guidelines of a Rietveld refinement for XRD data can be found in (Von Dreele et al., 1982, Toby, 2001, Dinnebier and Billinge, 2008, Walker, 2008). In general for each phase two sets of parameters are to be considered: profile and structural parameters. Profile parameters are instrumental parameters such as the zero position of the detectors, the background, and the peak shape functions, but also the sample geometry and unit cell parameters while structural parameters consists of atomic positions, fractional occupancies and thermal parameters. The least-square refinement is achieved by minimizing the function M :

$$M = \sum_i w_i [y_i(obs) - y_i(calc)]^2 \quad (3.76)$$

The summation is done over all the intensity points, y_i , (observed or calculated) of the pattern with their relative weight w_i . The quality of a least square refinement can be directly monitored by the difference plot between the calculated – observed patterns combined with the minimization of the residual weighed-profile, R_{wp} , and the reduced, χ^2 , value:

$$R_{wp} = \left(\frac{\sum_i w_i [y_i(obs) - y_i(calc)]^2}{\sum_i w_i [y_i(obs)]^2} \right)^{1/2} \quad (3.77)$$

$$R_{exp} = \left(\frac{N - P}{\sum_i^N w_i [y_i(obs)]^2} \right)^{1/2} \quad (3.78)$$

$$\chi^2 = \frac{R_{wp}}{R_{exp}} \quad (3.79)$$

N is the number of observations and P is the number of parameters refined. The difference plot can give an idea of the parameters to refine and should always be computed at each step of the refinement. Other R values based on the calculated and observed structure factors F_{hkl} are also available:

$$R_F = \frac{\sum_{hkl} |F_{hkl}(obs) - F_{hkl}(calc)|}{\sum_{hkl} |F_{hkl}(obs)|} \quad (3.80)$$

$$R_B = \frac{\sum_{hkl} |I_{hkl}(obs) - I_{hkl}(calc)|}{\sum_{hkl} |I_{hkl}(obs)|} \quad (3.81)$$

With:

$$I_{h,k,l} = mF_{h,k,l}^2 \quad (3.82)$$

m = multiplicity (Cox and Papoular, 1996).

In general, a good refinement starts with a good quality sample and data appropriately collected. Profile parameters such as instrumental parameters are usually obtained from a standard sample under the same experimental conditions. Unit cell, background, detector positions, scale factor and profile function parameters are first to be refined. Then once all the observations are indexed, the atomic parameters can vary. They fix the relative position and height of each indexed peak. Atoms with the highest cross section are to be refined first. At the beginning of the calculation, it is essential to allow only one or two parameters to vary at the same time as they tend to be highly correlated (correlation matrix). As the refinement progress more and more parameters can vary simultaneously. Some geometric constraints can also be added to describe better the sample.

Chapter 4

Carbon Nanostructures For Hydrogen Storage

Herein results from a series of experiments on carbon materials will be reported and discussed. The aim was to synthesize GNF samples and to investigate potential engineering routes to enhance hydrogen interactions with graphitic nanofibres either by adding hetero-atomic species within the carbon network or by increasing the specific surface area available. The advantages and inconvenients of such methods will be discussed regarding their flexibility in design and their application for possible scaling-up. First results of a commercial activated carbon will be given for comparison purposes.

4.1 Results

4.1.1 Activated Carbon

A Maxsorb activated carbon sample with a high BET SSA of $3182 \text{ m}^2\cdot\text{g}^{-1}$, was measured using 7 points within the $0.04\text{-}0.28 \frac{p}{p_0}$ linear region (Figure 4.1). The pore size was found to be less than 25.7 \AA . Excess hydrogen gravimetric uptakes up to $5.1 \text{ wt.}\%$ of a commercial activated carbon sample (Maxsorb) are reported on Figure 4.2. This is typical isotherm type I for microporous materials showing reversibility regarding adsorption/desorption phases and no hysteresis.

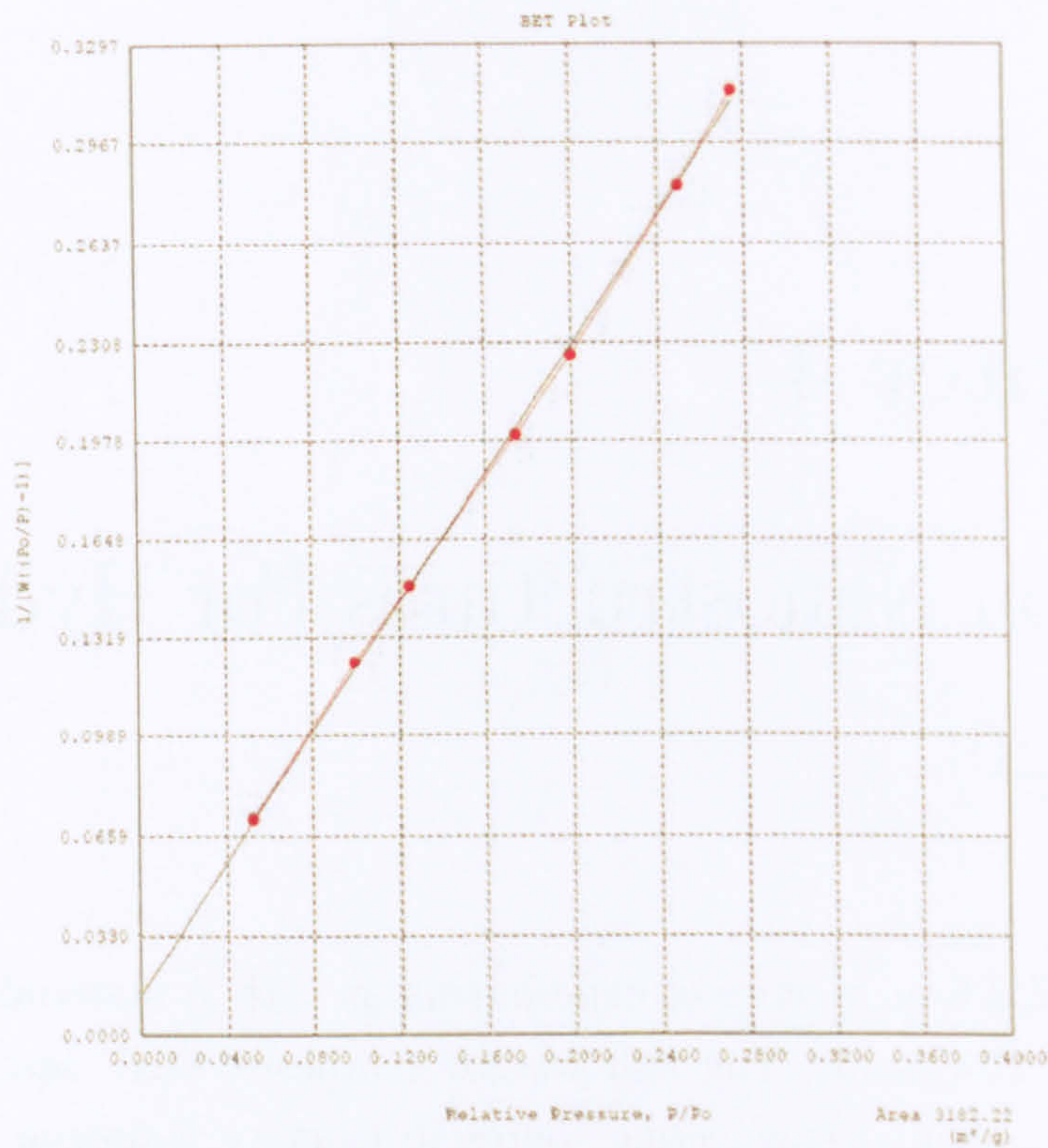


Figure 4.1: BET plot of activated carbon sample (Maxsorb) within the 0.04 – 0.28 $\frac{p}{p_0}$ linear region.

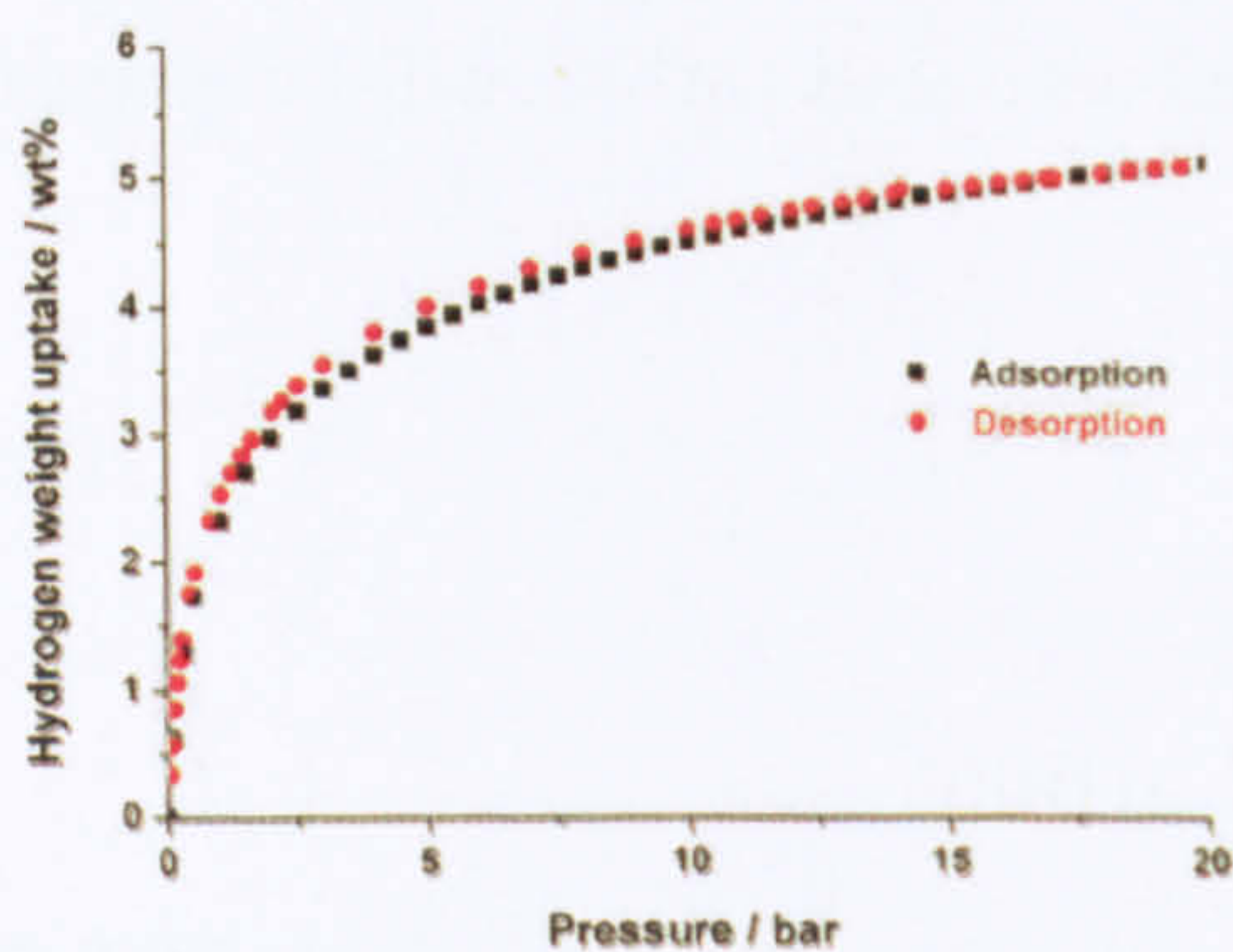


Figure 4.2: Hydrogen isotherm for activated carbon sample (Maxsorb) measured at 77 K and 20 bar.

4.1.2 As-Prepared GNFs

A series of non-doped GNFs were synthesized by CVD using a mixture of ethene and hydrogen at a constant molar ratio of 80:20 and various

temperatures. Two metal catalyst precursors, NiO and Co_3O_4 , were used. TEM images of as prepared Ni-550 and Co-550 are shown in Figures 4.3 and 4.4 revealed in both cases a higher content of herringbone type GNFs. The surface topology of the herringbone fibres within Ni-550 was serrated. These were used for the exfoliation experiments (see section 4.1.4).

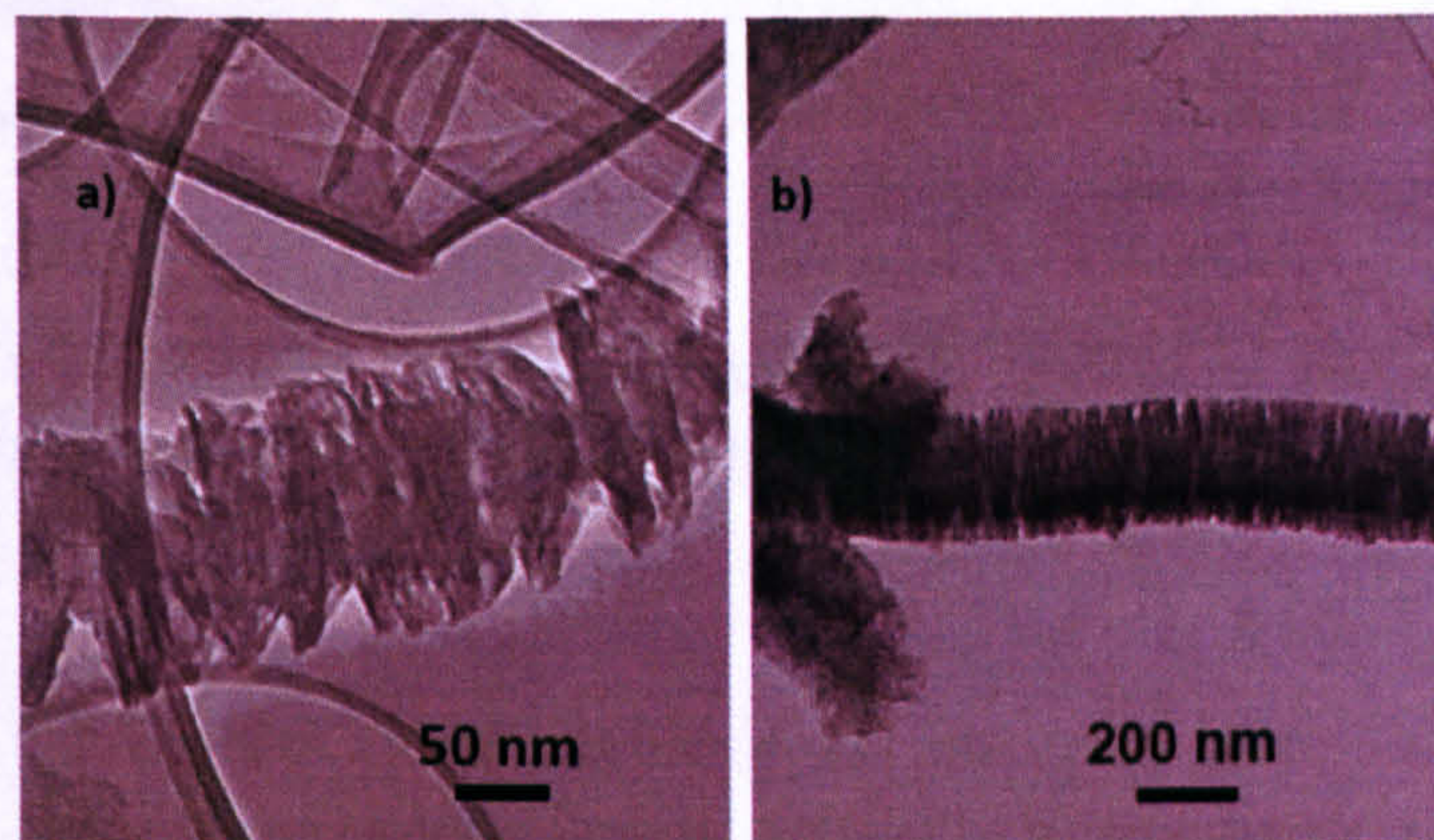


Figure 4.3: TEM images of Ni-550 as prepared herringbone GNFs.

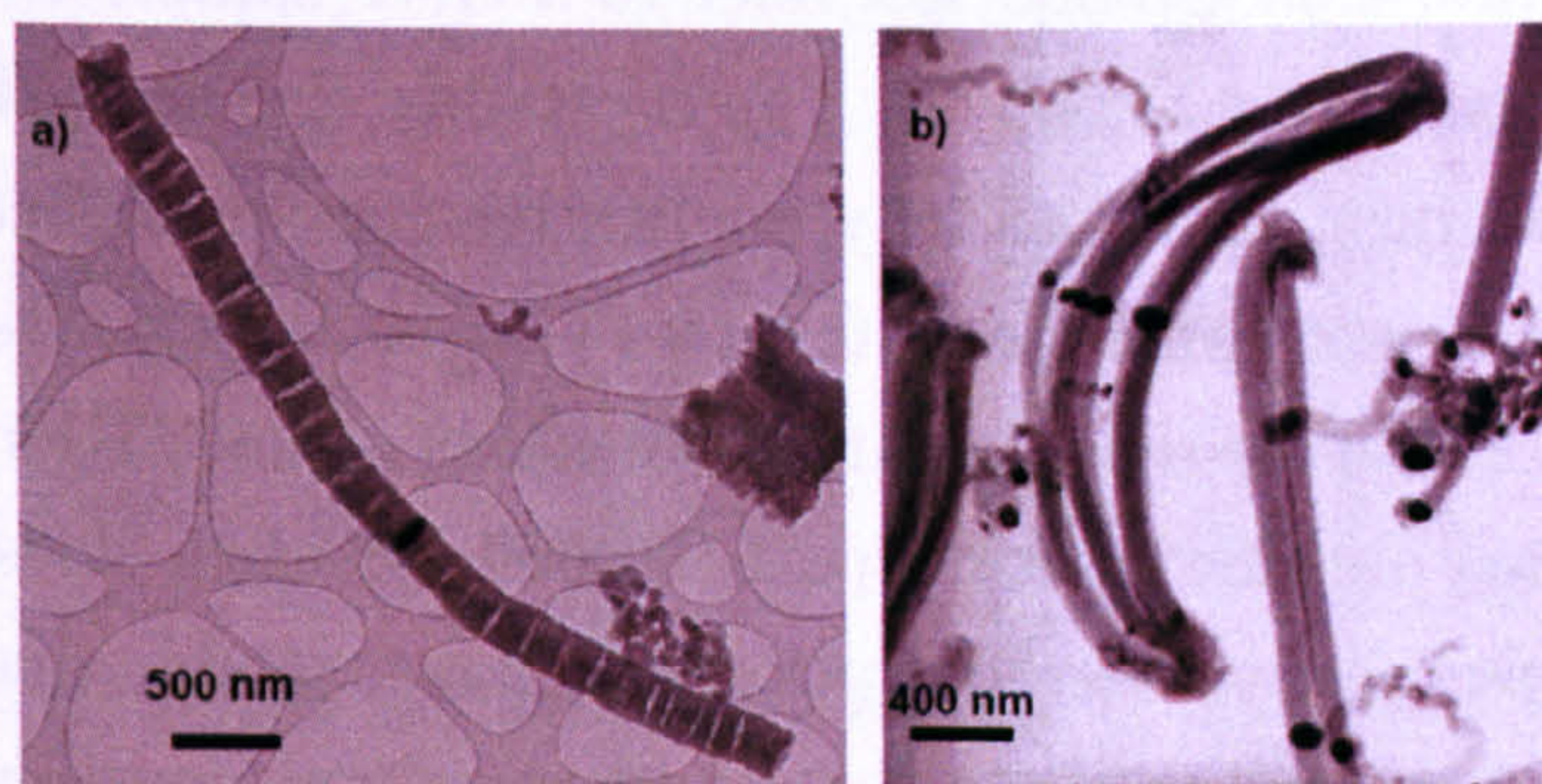


Figure 4.4: TEM images of as prepared platelet GNFs: a) Ni-550 and b) Co-550.

Figures 500 °C, 550 °C, and 600 °C. In both cases, the main peak was found at 26.0 ° which corresponds to the graphitic (002) plane, with a 3.354 Å d-spacing. The other peaks at 44.53 °, 51.93 °, 76.41 °, and at 44.17 °, 51.46 °, 75.82 ° respectively confirm the presence of Ni and Co metal catalysts in the final product. (004) can also be observed at 43 °.

4. CARBON NANOSTRUCTURES FOR HYDROGEN STORAGE

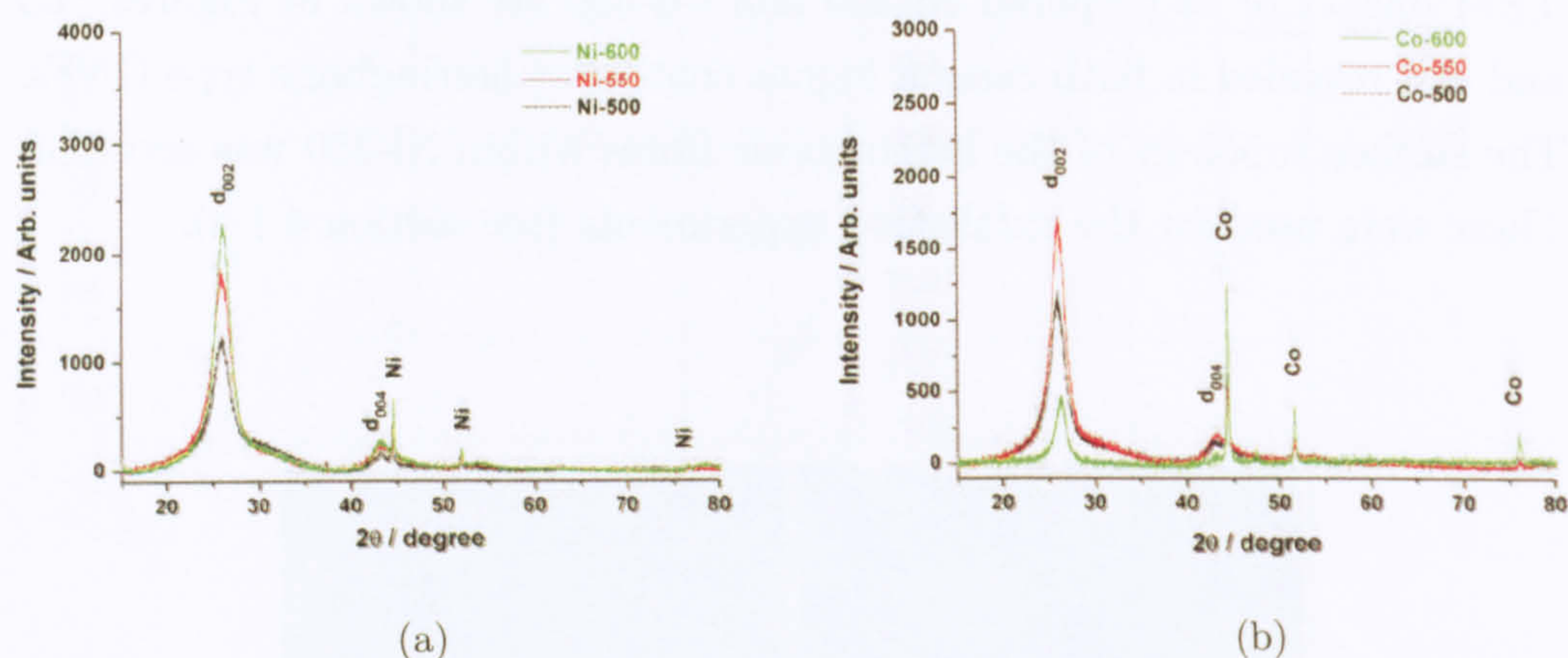
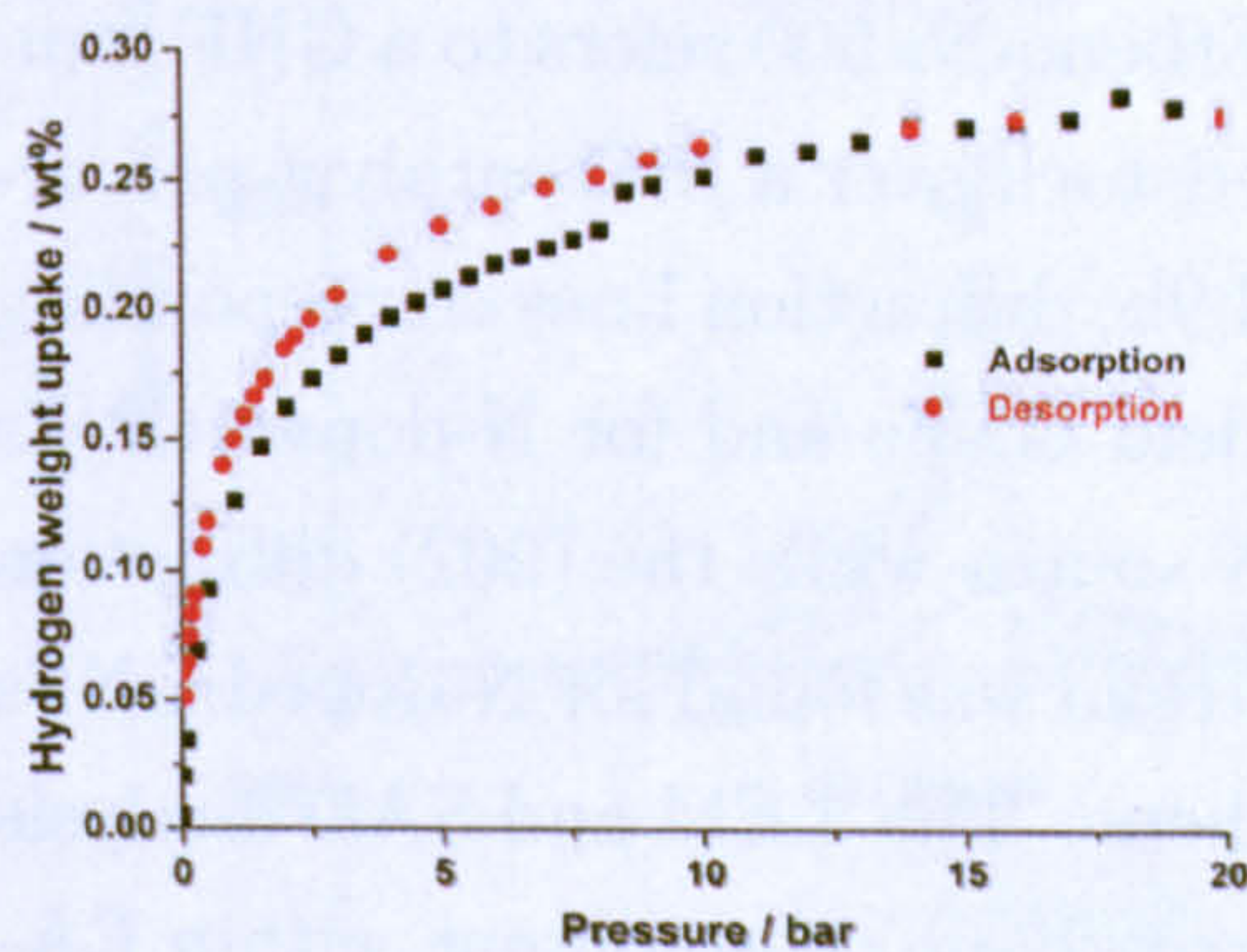


Figure 4.5: a) XRPD of Ni-500, Ni-550 and Ni-600. b) XRPD of Co-500, Co-550, Co-600. The data were collected at room temperature. Baselines were subtracted.

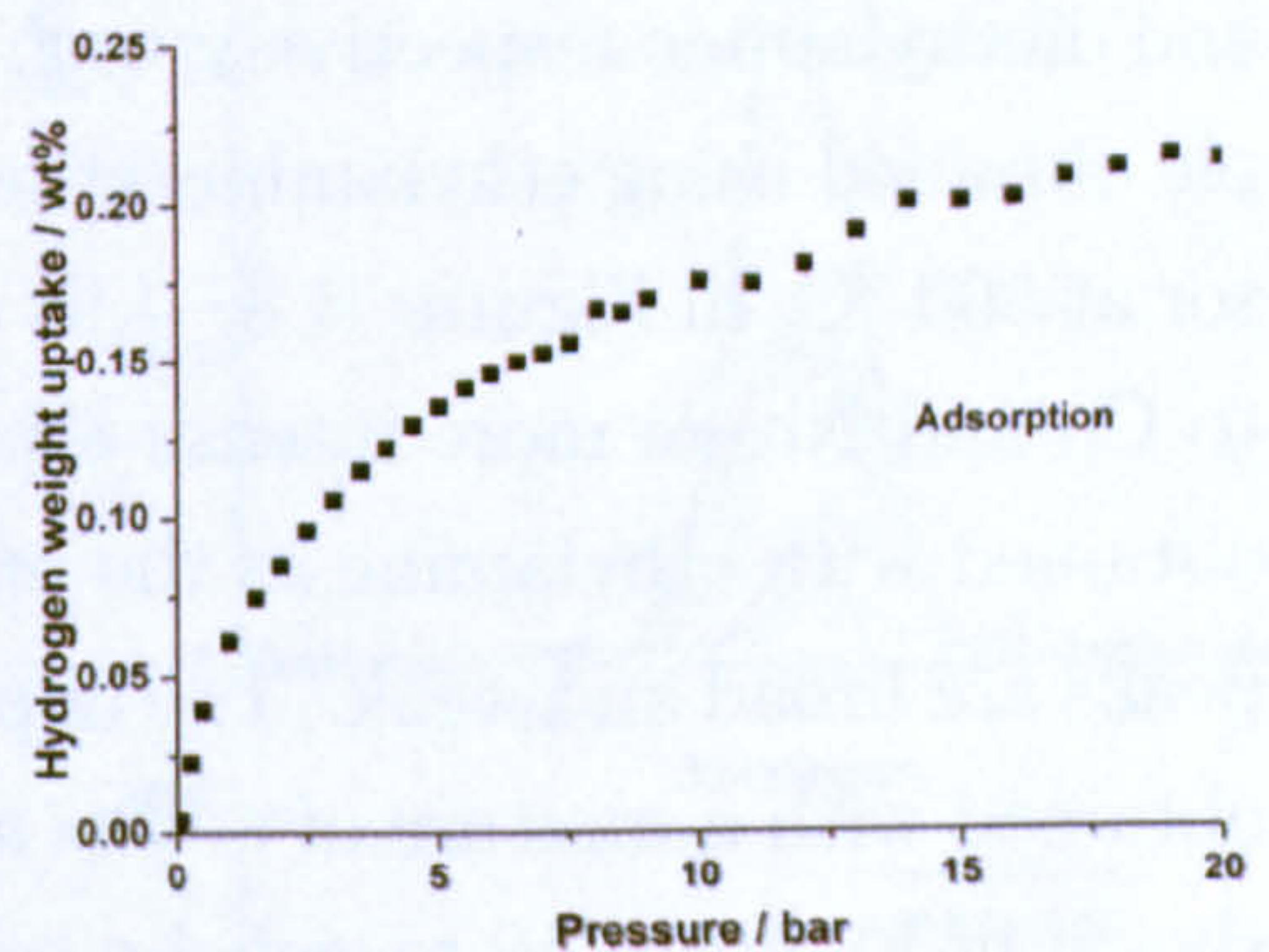
The CVD results and sorption properties of each sample are reported in Table 4.1. The highest yields (carbon mass to catalyst precursor mass ratio) were obtained at 550 °C with 3.42 g and 1.90 g respectively for NiO and Co₃O₄ using approximately a constant weight of 50 mg of catalyst precursors. Sample nomenclature will be reported as catalyst and followed by CVD temperature, *e.g.*: Co-550 will refer to a GNF sample obtained using Co₃O₄ catalyst precursor at 550 °C. The crystallite size analysis were made over 4 GNFs samples, therefore only qualitative conclusions can be drawn from it. Hydrogen isotherms for Ni-600 and Co-550 are reported in Figures 4.6a and 4.6b. These are representative isotherms of the GNFs synthesized. All the isotherms obtained were type I. Ni-600 isotherm does not recover the initial sample weight after desorption which is probably due to a kinetic effect. Therefore, we will suppose that the hydrogen adsorption/desorption mechanism is fully reversible. The step during the adsorption phase in Figure 4.6b is an experimental artefact. Both GNF samples exhibit low excess hydrogen gravimetric uptakes *ca.* 0.28 and 0.20 *wt. %* with low BET surface areas *ca.* 56.56 m².g⁻¹ and 45 m².g⁻¹ respectively within the 0.08–0.32 $\frac{p}{p_0}$ linear region with 6 multi-points BET (Figure 4.7). The BET plot is also representative for the general trend of the GNFs synthesized. For Ni-600, the average pore size was found smaller than 13.5 Å. The average pore volume was 2.8.10² cm³.g⁻¹.

Table 4.1: Non-doped GNF growth parameters. BET surface area measurements and H₂ uptakes at 77 K and 20 bar are reported.

Sample	Catalyst precursor	Temperature (°C)	Catalyst weight (g)	Carbon yield (g)	BET SSA (m ² .g ⁻¹)	H ₂ uptake (wt.%)
Ni-500	NiO	500	0.0507	2.19	-	0.28
Ni-550	NiO	550	0.0580	3.42	-	0.27
Ni-600	NiO	600	0.0512	2.82	57.56	0.27
Co-500	Co ₃ O ₄	500	0.0516	1.20	-	0.21
Co-550	Co ₃ O ₄	550	0.0517	1.90	45.10	0.20
Co-600	Co ₃ O ₄	600	0.0538	0.14	-	-



(a)



(b)

Figure 4.6: a) Hydrogen isotherm of Ni-600 and b) Hydrogen adsorption curve of Co-550 measured at 77 K and 20 bar.

4.1.3 Nitrogen Doped GNFs

Nitrogen doping experiments were carried out using mixtures of ethylamine or diethylamine, as a carbon-nitrogen (CN) source, with and without ethene in the feedstock at CVD temperatures of 500 °C and 550 °C. Sample nomenclature includes the feedstock gases where EA and DEA refer to ethylamine

4. CARBON NANOSTRUCTURES FOR HYDROGEN STORAGE

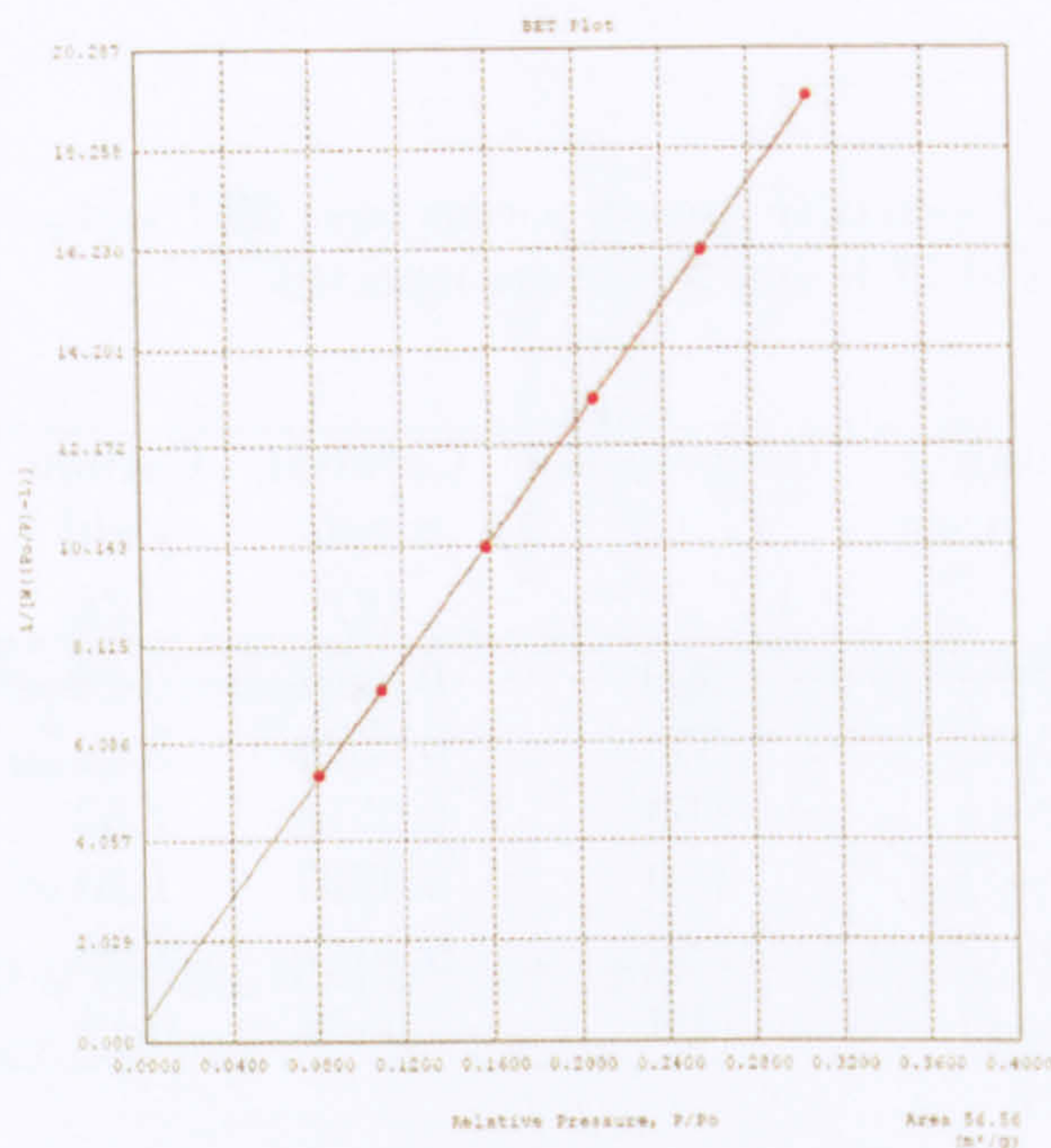


Figure 4.7: BET plot of Ni-600 within the 0.08-0.32 $\frac{P}{P_0}$ linear region.

and diethylamine respectively, *e.g.*: EA-Ethene-Ni-500 refers to a GNF sample obtained using ethylamine/ethene feedstock over a NiO catalyst precursor at 500 °C. In Figures 4.8, 4.9a and 4.9b, diffraction lines corresponding to Co and Ni are more intense for low yield GNFs and for N-doped GNFs obtained with ethylamine as the only CN source while the (002) diffraction peaks are broad and weak. The opposite trend was found for N-doped GNFs obtained with a mixture of amine and ethene. The TEM and SAD analysis shown in Figure 4.10 revealed a high herringbone type content within EA-Ethene-Ni-500, and DEA-Ethene-Ni-550, while more platelet GNFs were found within EA-Ethene-Co-550 sample with a topology different from the platelets found earlier with the undoped GNFs Ni-550 and Co-550 samples.

In Table 4.2 N-doping levels, BET surface areas and hydrogen uptakes are reported. The N atomic contents obtained by CHN analysis were between 0.95 % and 3.32 % with the high N contents corresponding to low yield samples. Hydrogen isotherms of representative N-doped GNFs are shown in Figures 4.11a and 4.11b. These type I isotherms showed full reversibility with respect to the hydrogen adsorption with no hysteresis as the initial gas free sample weight is retrieved at the end of the desorption phase.

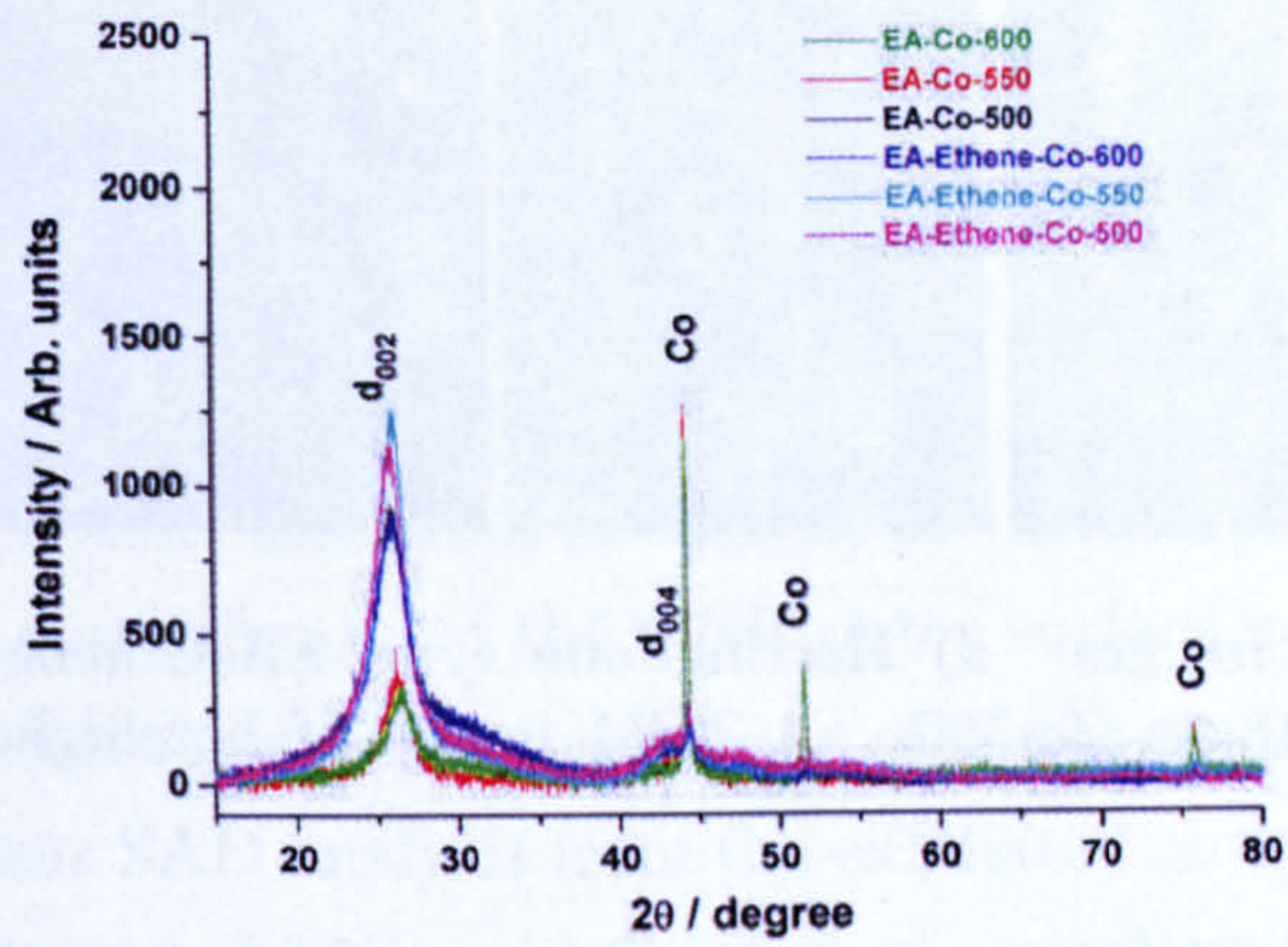


Figure 4.8: XRPD of the as prepared EA-(Ethene)-Co- samples. The data were collected at room temperature. Baselines were subtracted.

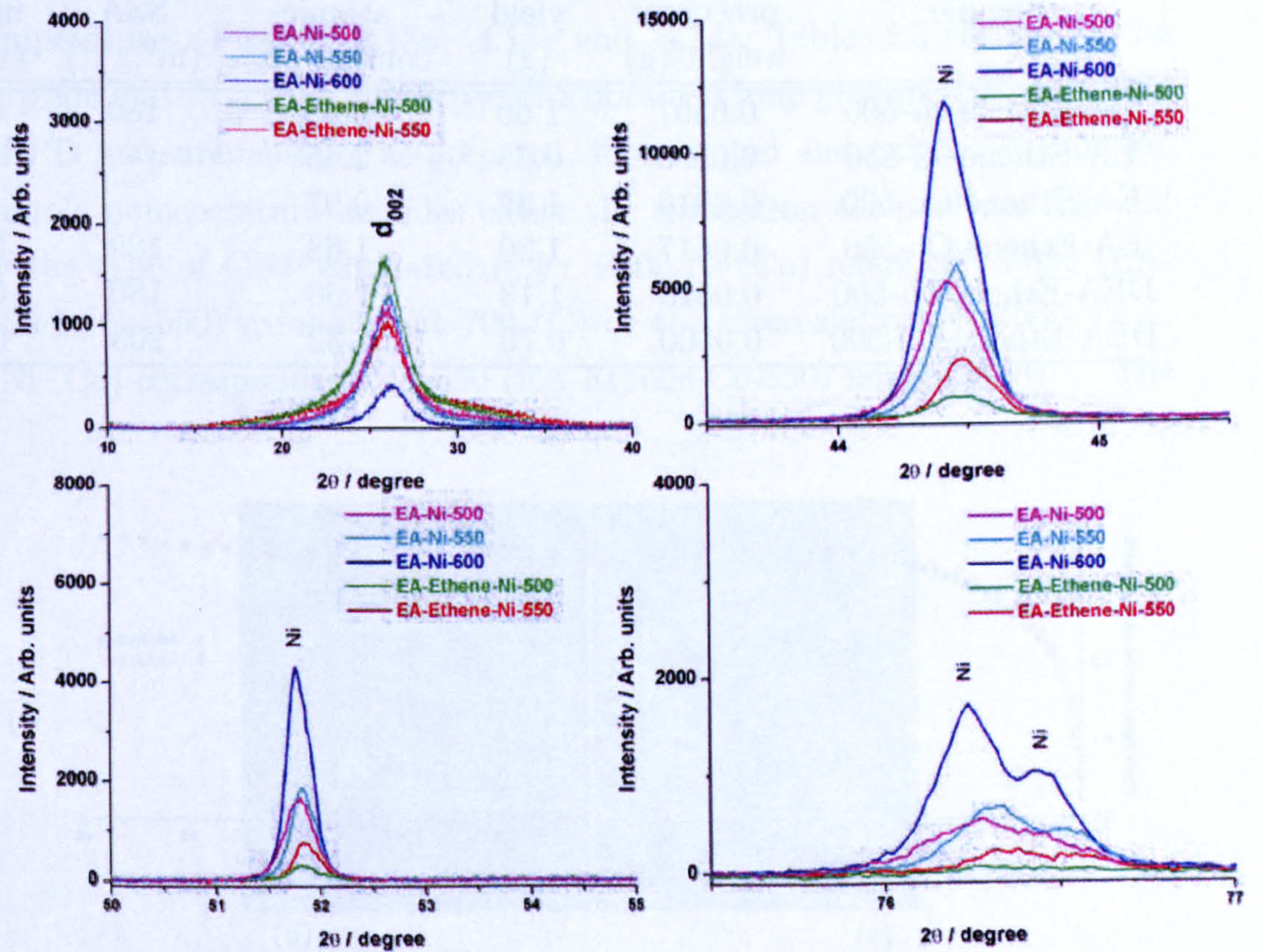


Figure 4.9: XRPD of the as prepared EA-Ni- and EA-Ethene-Ni- samples. The data were collected at room temperature. Baselines were subtracted.

4. CARBON NANOSTRUCTURES FOR HYDROGEN STORAGE

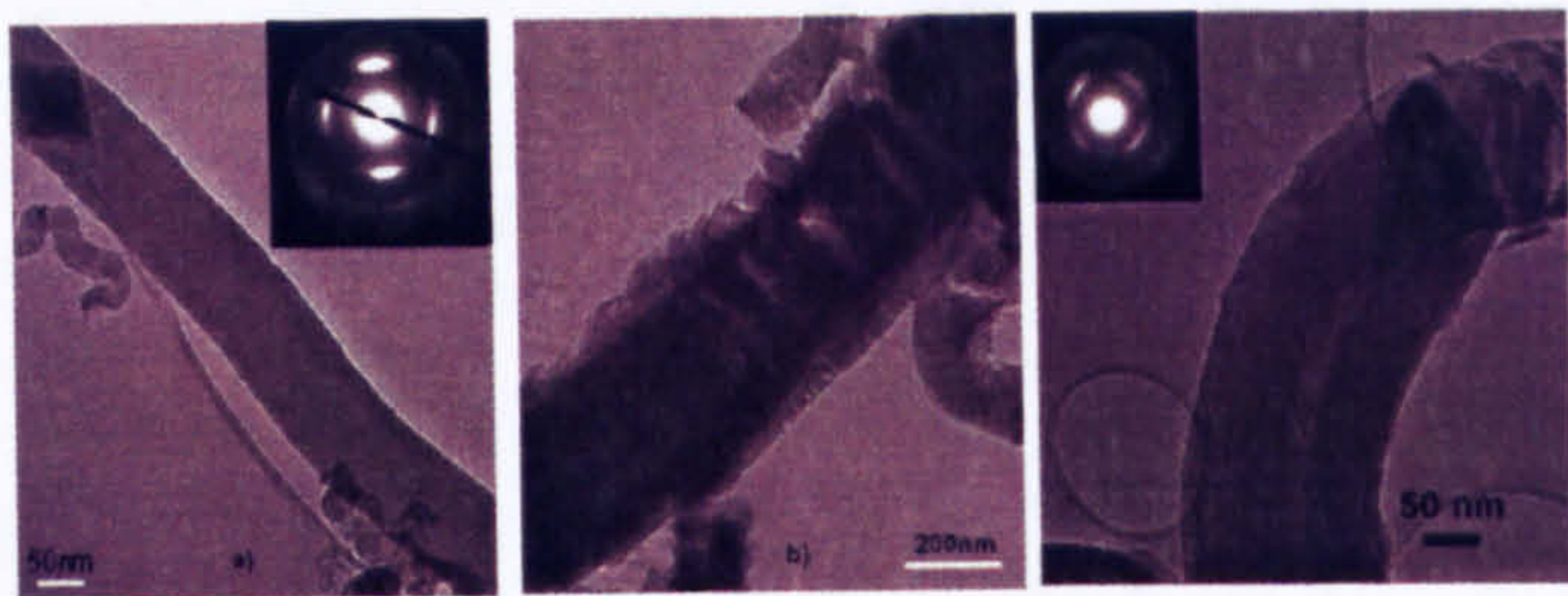


Figure 4.10: TEM images: a) Herringbone type EA-Ethene-Ni-500 and b) Platelet type EA-Ethene-Co-550. c) TEM image of herringbone type DEA-Ethene-Ni-550.

Table 4.2: N-doped GNF growth parameters using a mixture of ethylamine, ethene and hydrogen. BET surface area H₂ weight uptakes and N level measurements are also reported.

Sample	Catalyst precursor weight (g)	Sample yield (g)	N atomic content (%)	BET SSA (m ² .g ⁻¹)	H ₂ uptake (wt.%)
EA-Ethene-Ni-500	0.0507	1.60	0.95	180	0.35
EA-Ethene-Ni-550	0.0580	0.35	2.45	-	-
EA-Ethene-Co-500	0.0516	1.37	0.97	-	-
EA-Ethene-Co-550	0.0517	1.30	1.68	189	0.38
DEA-Ethene-Ni-500	0.0510	1.13	1.60	180	0.38
DEA-Ethene-Co-500	0.0500	0.70	3.32	203	0.41

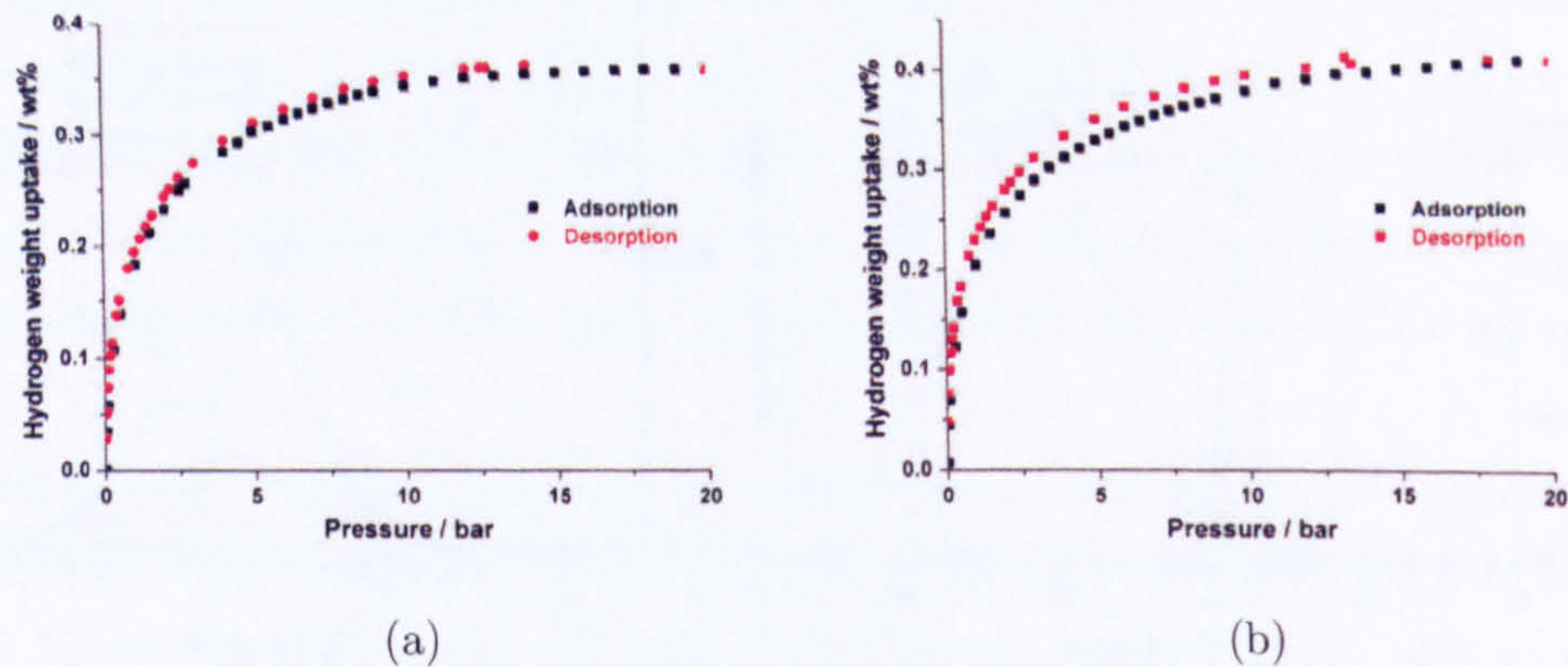


Figure 4.11: a) Hydrogen isotherm of EA-Ethene-Co-550 measured at 77 K and 20 bar. b) Hydrogen isotherm of DEA-Ethene-Ni-550 measured at 77 K and 20 bar.

4.1.4 Exfoliation of Intercalated GNFs

Intercalated compounds of graphite flakes (*University of Salford*) Ni-550 and EA-Ethene-Co-550 were exfoliated via thermal shock at different temperatures. Ni-550 and EA-Ethene-Co-550 were chosen because of their serrated surfaces. TEM images in Figure 4.12 shows the general effect of the intercalation and exfoliation process upon the morphology of the GNFs treated with a clear change of the GNF outer surface compared to the as-prepared material. A general consequence of it was that it was not possible to perform a clear SAD analysis from the exfoliated and intercalated GNFs. The XRPD patterns of I-Ni and I-Co showed a small shift of the (002) peak from 26.02° to 24.40° and 25.57° respectively corresponding to changes in the d-spacing from 3.42 \AA to 3.64 \AA and 3.48 \AA . Both (002) peaks showed a loss of intensity compared to the starting materials. After exfoliation their intensity increased but also shifted back to 26° , for all the exfoliation temperatures (Figures 4.13a, 4.13b and 4.14). Table 4.3 reports on the sorption and structural characteristics obtained from gravimetric, BET, and XRPD measurements of as-prepared, intercalated and exfoliated samples. Sample nomenclature includes either the exfoliation temperature followed by the type of GNF exfoliated (*e.g.*: E700-Ni (Co) refers to Ni-550 (EA-Ethene-Co-550) exfoliated at 700°C) or the intercalation of GNFs (*e.g.*: I-Ni (Co) corresponds to Ni-550 (EA-Ethene-Co-550) intercalated). The

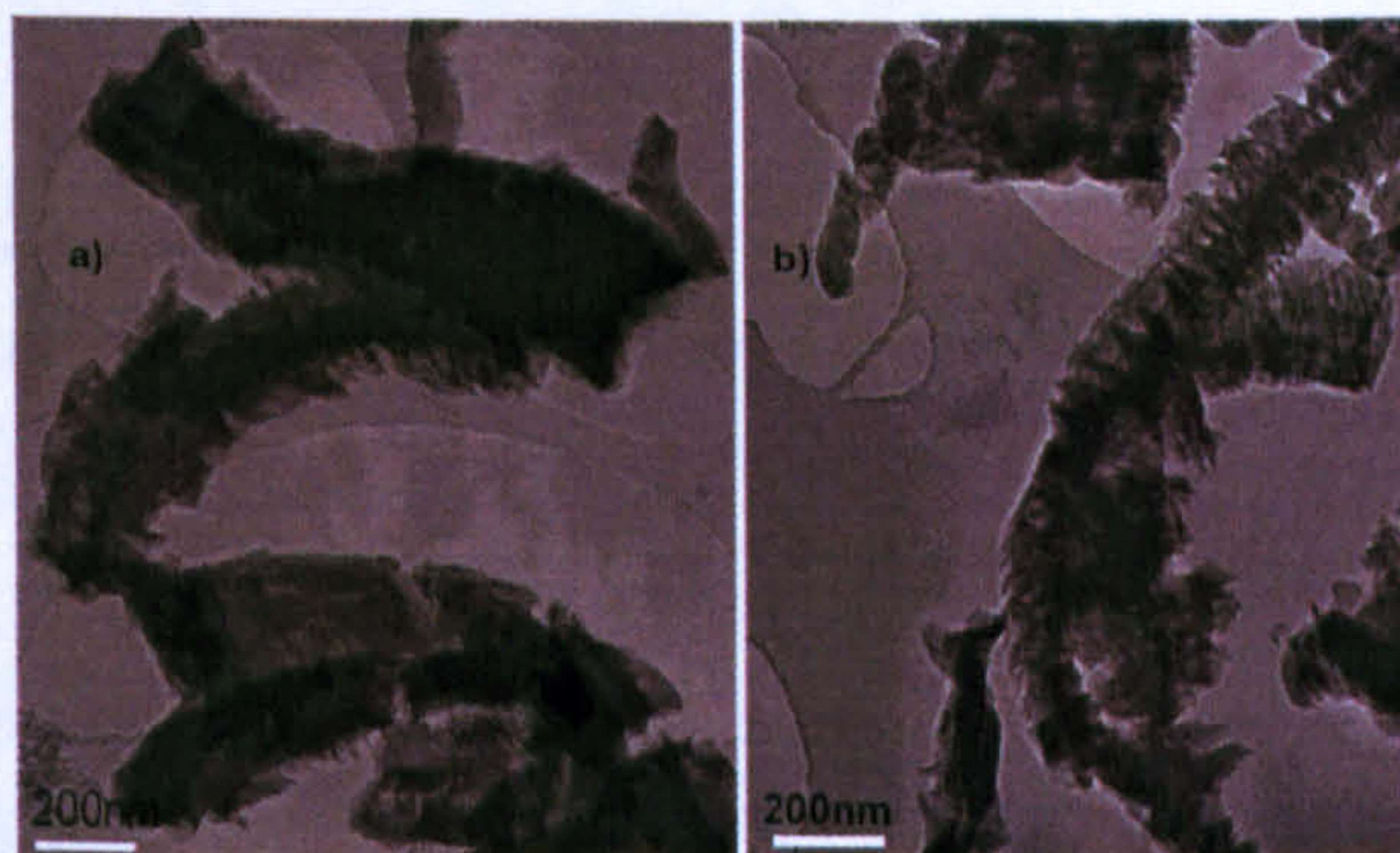


Figure 4.12: TEM images: a) As prepared I-Ni and b) herringbone type E1000-Ni.

BET SSA and the hydrogen sorption properties (Figure 4.15) of the intercalated and exfoliated GNFs were higher than that for the starting GNFs,

4. CARBON NANOSTRUCTURES FOR HYDROGEN STORAGE

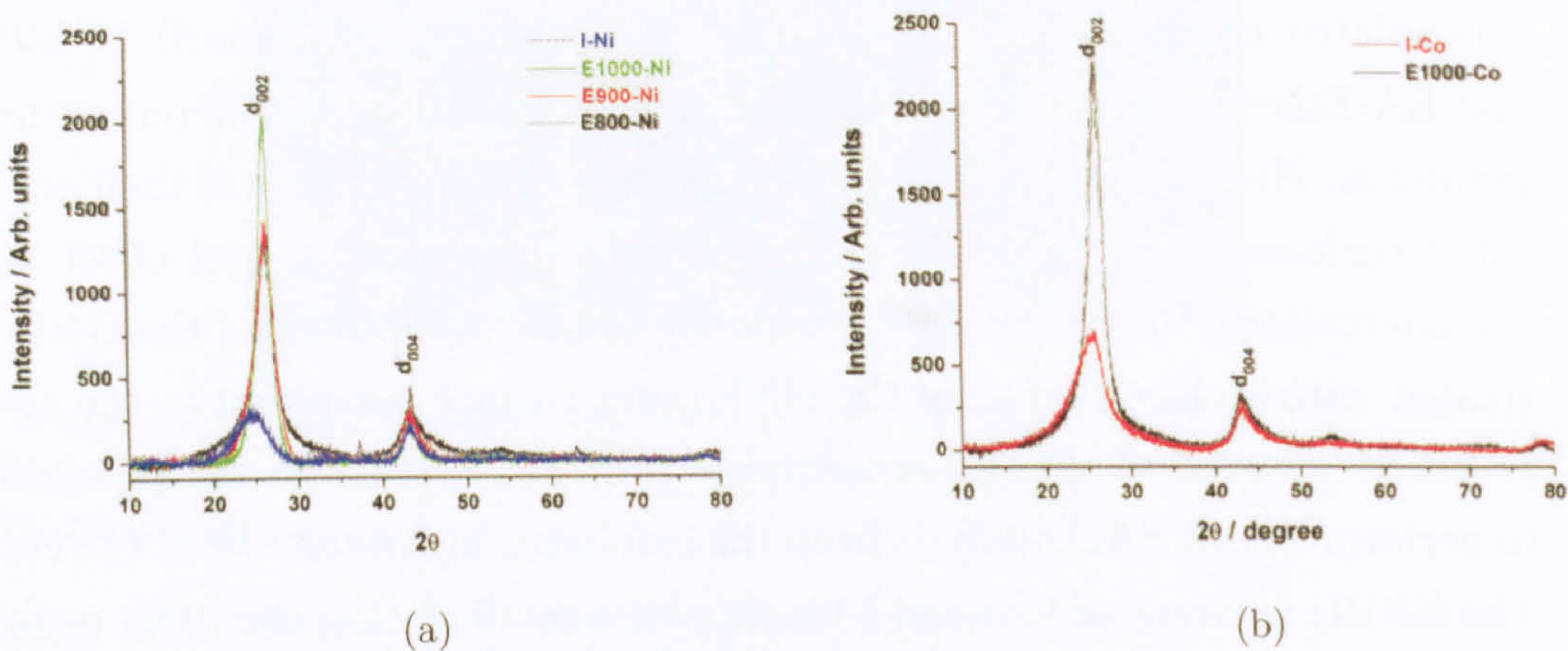


Figure 4.13: a) XRPD of E700-Ni, E800-Ni, E900-Ni, E1000-Ni and I-Ni. b) XRPD of I-Co and E1000-Co. The data were collected at room temperature. Baselines were subtracted.

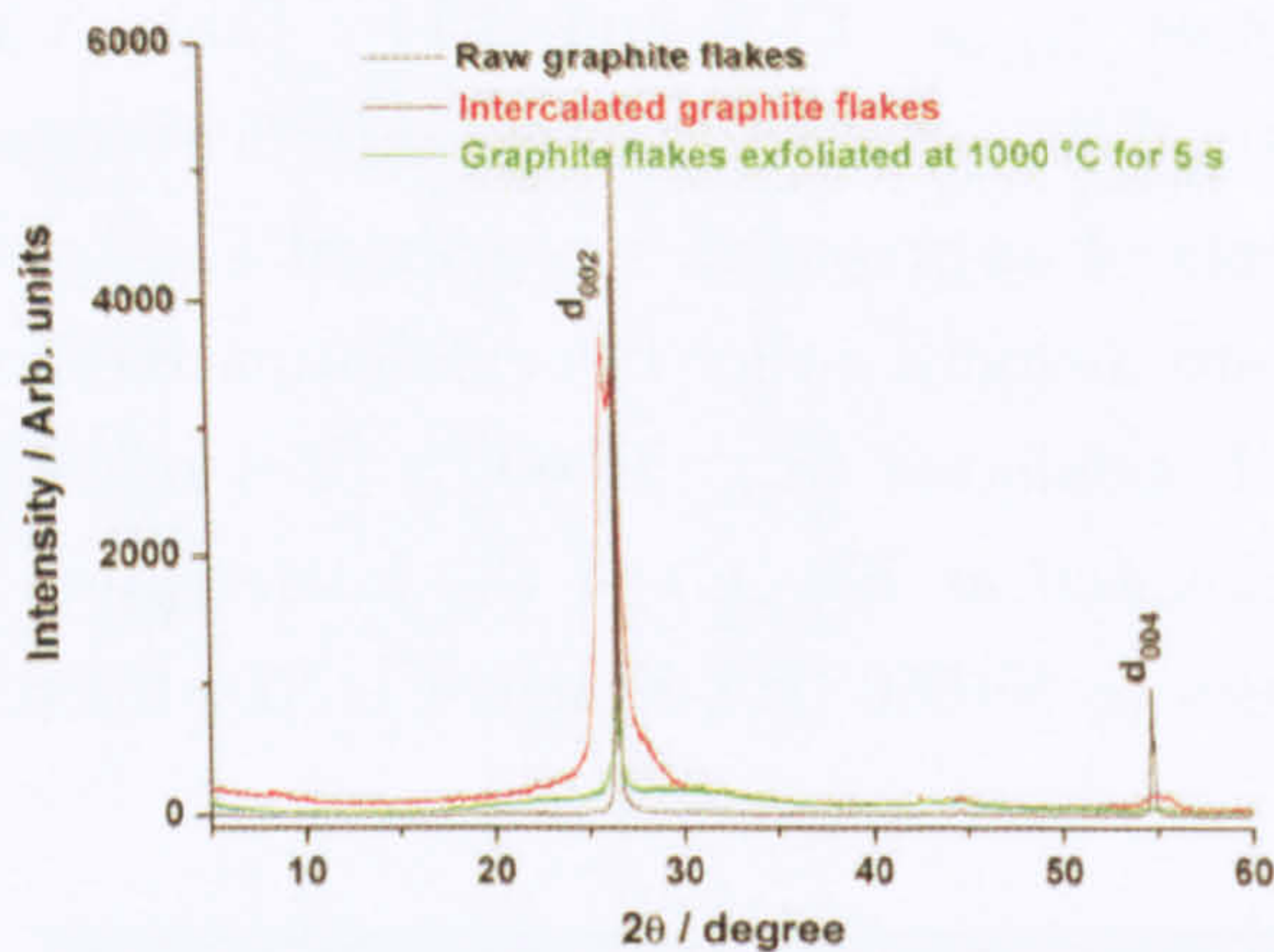


Figure 4.14: XRPD of as-prepared, intercalated, and exfoliated graphite flakes. The data were collected at room temperature. The intensity for the raw graphite flakes was reduced by one order of magnitude for comparison. Baselines were subtracted.

the SSAs being an order of magnitude higher. This general trend seems also to be independent of the GNFs used and the exfoliation temperature.

Table 4.3: Sorption and structural properties of as prepared, intercalated, and exfoliated carbon compounds.

Sample	BET SSA (m ² .g ⁻¹)	H ₂ uptake (wt.%)	d ₍₀₀₂₎ (Å)
E700-Ni	314	0.48	3.39
E800-Ni	353	0.49	3.39
E900-Ni	-	-	3.39
E1000-Ni	355	0.48	3.40
E1000-Co	244	-	3.40
I-Ni	130	0.29	3.64
I-Co	120	-	3.48
Graphite	45	-	3.36
E-graphite	250	-	3.38
I-graphite	55	-	3.36

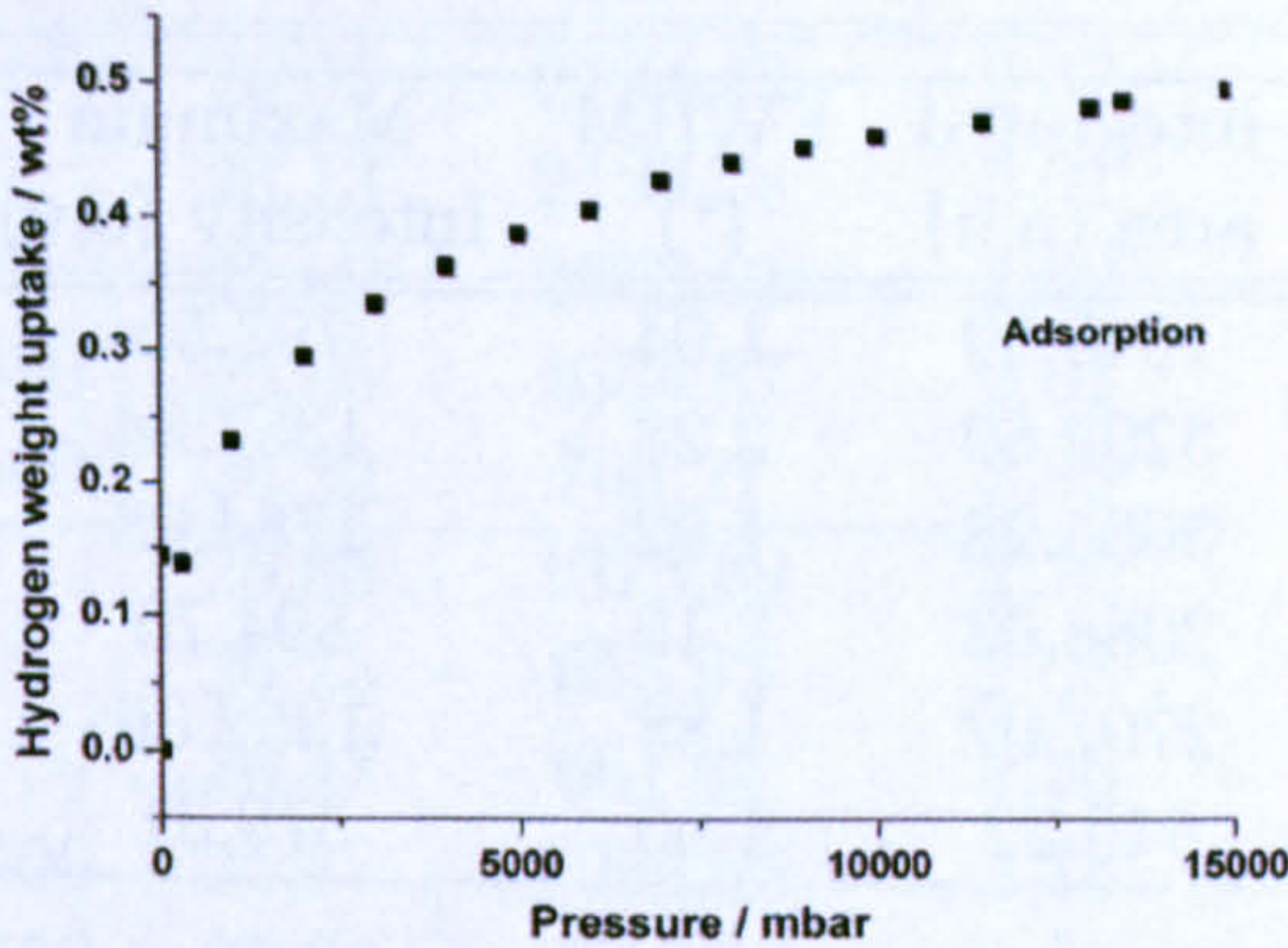


Figure 4.15: Hydrogen adsorption curve of as prepared E1000-Co. The data were collected at 77 K and 20 bar.

4.2 Discussion

For all GNFs synthesized, the crystallinity and the surface topology are key parameters as hydrogen adsorbents. The crystallinity of the graphitic planes is directly related to the shape, intensity, integrated area and position of the (002) peak which is often the main peak detected. Similar conclusions can be drawn from (004) peak. For instance the crystallite size analysis reported in Table 4.4 shows that Ni-500 and Ni-600 exhibit higher crystallinity than Ni-550. The trend is easier to follow with Co-GNF series as

4. CARBON NANOSTRUCTURES FOR HYDROGEN STORAGE

their crystallinity increases with the temperature. This would either suggest a different catalytic behaviour of the carbon source with the metal catalyst (De Jong and Geus, 2000). One can also notice a different behaviour for peaks related to Ni and Co metal catalysts. At a given temperature the carbon source decomposes faster (or slower) on one side of the metal catalyst than the carbon forms into graphitic layers on the other side of the metal catalyst which leads to smaller crystalline domains. This highly depends on the carbon-source and the metal catalyst used. For instance in order to improve the crystallinity of undoped GNFs, one would avoid temperatures close to 550 °C for Ni and higher than 600 °C for Co. However, such crystalline domains are still very small compared to highly crystalline materials.

Table 4.4: Crystallite size analysis for undoped GNFs from XRPD data using gaussian profiles of the (002) reflection.

Sample	Center (°)	Integrated area (a.u)	FWHM (°)	Maximum Intensity (a.u)	Crystallite size Laue (nm)
Ni-500	26.07	1649.59	1.94	797.55	0.76
Ni-550	25.99	3292.60	2.28	1357.84	0.65
Ni-600	26.08	3655.28	1.92	1784.08	0.77
Co-500	25.94	2088.03	2.19	894.70	0.68
Co-550	25.96	2707.02	1.88	1352.06	0.79
Co-600	26.10	645.32	1.60	379.31	0.93

Similar conclusions can be drawn for the N-doping experiments. The N-doped GNFs synthesized using a mixture of amines and ethene with Ni and Co catalysts have bigger crystalline domains at temperatures close to 550 °C, although the use of the amine and ethene mixture does not affect the crystallinity of the N-doped GNFs using a Co catalyst. In general, the use of amine as the only CN source was not sufficient to yield decent amount of samples even though the crystallinity was similar to N-doped GNFs obtained with the amine/ethene mixture. This might be due to a higher local presence of N during the CVD process hindering the formation of more regular graphene layer. The TEM analysis also confirmed a very close surface topology between the sets of samples with mainly a serrated

surface. The N-doped GNFs did not exhibit any significant improvement of the hydrogen storage capacity but only an increase of the BET surface area compared to the as-prepared GNFs. In the first instance this could be due to their serrated surface. However, the role of the N species is not entirely clear. It is, therefore, essential to be able to locate the interstitial and/or substituted N species in the carbon structure (Nevidomskyy et al., 2003, Terrones et al., 2004) in order to identify their role upon the sorption properties. The mixture ethene with different amines has not been successful.

Table 4.5: Crystallite size analysis for N-doped GNFs from XRPD data using Gaussian profiles.

Sample	Center (°)	Integrated area (a.u)	FWHM (°)	Maximum Intensity (a.u)	Crystallite Size Laue (nm)
EA-Ni-500	26.05	2194.43	2.37	1036.97	0.67
EA-Ni-550	26.13	2199.28	2.01	925.51	0.75
EA-Ni-500	25.89	2873.81	2.32	1163.32	0.64
EA-(ethene)-Ni-550	25.95	1354.87	2.01	632.19	0.74
EA-(ethene)-Ni-600	26.22	709.27	2.35	283.13	0.63
EA-Co-500	25.85	1373.09	2.15	598.75	0.69
EA-Co-550	26.25	655.92	2.08	296.81	0.72
EA-Co-600	26.47	661.65	2.38	261.49	0.62
EA-(ethene)-Co-500	25.87	1964.93	2.18	845.94	0.68
EA-(ethene)-Co-550	25.96	2316.17	2.21	983.61	0.67
EA-(ethene)-Co-600	26.03	1607.92	2.35	642.57	0.67

The CHN analysis revealed relatively high N-doping contents *ca.* 10 % using the amines as the only carbon-nitrogen. This was also characterized by poor yields. The amount of N-doped GNFs synthesized significantly improved when using a mixture of ethene with amines but also with a lower N-doping level and a maximum of 3 %. The N-doping method used in this work relied on the decomposition of different organic precursors. Earlier work by Yang *et al.* and Xia *et al.*, successfully reported on N-doping carbon zeolite template using CVD procedure with acetonitrile (Xia and Mokaya, 2004, Xia et al., 2005, Yang et al., 2005b). They managed to incorporate N

4. CARBON NANOSTRUCTURES FOR HYDROGEN STORAGE

species with up to 8 % and keeping the surface area of the zeolite template around $1900 \text{ m}^2.\text{g}^{-1}$. The N-doping levels achieved in our work are comparable with those reported in the literature and using a similar method. Shalagina *et al.* also synthesized GNF using $\text{C}_2\text{H}_4:\text{NH}_3$ mixture with a N doping level up to 7 % (Shalagina *et al.*, 2007). The thermal decomposition of an organic precursor during CVD or a post-treatment of carbon materials under N_2 atmosphere requires relatively high temperatures usually above 500°C to allow catalytic activity or breaking of nitrogen molecules (ca.280 kJ) (Badzian *et al.*, 2001). Choi *et al.* and Tang *et al.* suggested that the N species were not stable at these temperatures on a graphene and proposed instead a new N-doping method at lower temperatures using a two step condensation reaction and a glassware reactor achieving up to 50 % of N content (Tang *et al.*, 2004, Choi *et al.*, 2005). In general, a lot of work has been reported on N-doping on carbon based materials for hydrogen storage, although to our knowledge there was no systematic theoretical work showing the real effect of the N atomic position within the carbon network and the best C:H ratio required to enhance H interactions.

Intercalation experiments were performed on undoped and N-doped GNFs using a mixture of nitric and sulfuric acids. No peak at low angle on the XRPD patterns was observed which suggests that no obvious ordered intercalation staging occurred (Dresselhaus and Dresselhaus, 2002). However, this was also true for the graphite flake sample, which visually showed a very large volume expansion upon thermal shock, evidence that intercalation had occurred. The success of the exfoliation method highly depends on the degree of intercalation prior to thermal shock. The thermal treatment aimed at very rapid degassing of the intercalated species in the hope to leave a stable expanded host structure. Table 4.6 shows very small crystalline domains for exfoliated GNFs similar to as-prepared GNFs and smaller in the cases of intercalated GNFs. The change in crystallinity is evidence for some intercalation disrupting the ordered stacking of the graphene layers. The heat treatment after intercalation helps with the graphitization of the GNFs. This is observed as the crystallite size increases with temperature.

The intercalation process was not obvious because of the heterogeneous

Table 4.6: Crystallite size analysis for exfoliated and intercalated GNFs from XRPD data using Gaussian profiles.

Sample	Center (°)	Integrated area (a.u)	FWHM (°)	Maximum Intensity (a.u)	Crystallite Size Laue (nm)
E800-Ni	26.21	2231.85	2.19	956.29	0.68
E900-Ni	26.35	3088.92	2.44	1188.67	0.61
E1000-Ni	26.14	3214.26	1.71	1757.10	0.86
I-Ni	26.60	1137.93	4.29	248.99	0.34
E1000-Co	25.47	2052.74	3.65	528.96	0.80
I-Co	26.08	3475.07	1.87	1749.10	0.41

GNFs obtained by CVD. The GNFs used for exfoliation mainly contained mixtures of platelets and herringbones fibres with different length, diameter, and topology. The intercalation/exfoliation conditions were verified as being effective, as demonstrated using crystalline graphite flakes which showed a large volume expansion open after thermal shock. Using these very same conditions, there was less obvious volume expansion observed. Investigating the morphology of the GNFs after thermal shock showed that the nanofibres had lost their characteristic shapes. This indicates that some exfoliation occurred, although it is reasonable to assume that this was limited to the surface of the GNFs. Hence it would appear that the intercalation was limited to only the surface. An obvious difference between the GNFs and the graphite flakes are the degree of crystallinity. It is very likely that the less planar graphene sheets found for the GNFs create a higher energy barrier to the diffusion of ions in between the layers. The defects within the layers may form stronger interactions with adjacent layers making it harder for the interlayer spacing to be increased. Or these defects may affect the delocalised π -system, affecting the charge transfer from the ions to the layers. The sorption properties of the exfoliated GNFs showed a little improvement compared to N-doped and undoped GNFs, and an increase of the BET surface area. However these values are still significantly lower than that for Maxsorb reported earlier. AC compounds are microporous materials with high surface area which allows them to have exceptional sorption properties (Hirscher and Panella, 2005, Yang et al., 2005b, 2007). From a

4. CARBON NANOSTRUCTURES FOR HYDROGEN STORAGE

topological point of view, GNFs are inert materials, with little porosity and low surface area where H_2 molecules are only physically adsorbed onto the surface rather than chemically reacting with it. Pradhan *et al.* determined the location of adsorption sites onto a bundle of CNTs with preferential adsorption starting with the channel, the groove, the pore and the surface depending on the surface area available (Pradhan *et al.*, 2002). From a geometric point of view, this adsorption site distribution is also valid for a bundle of GNFs except with the hollow centre. In practice inelastic neutron scattering experiments showed that the binding energies between a carbon host and a H_2 molecule were rather weak (Brown *et al.*, 2000, Georgiev *et al.*, 2004, Mitchell *et al.*, 2004). It is clear that the increase of the surface area and the number of micropores will be a very difficult route to reach sorption properties equivalent to AC compounds. Instead another possibility would be the creation of specific adsorption sites with metal catalysts usually transition metals such as Pd, Pt or Ti. These hetero-atomic species would either increase the binding energies for H_2 molecules (strong physisorption) or dissociate H_2 (Brown *et al.*, 2000, Georgiev *et al.*, 2004, Mitchell *et al.*, 2004, Yildirim and Hartman, 2005).

4.3 Conclusions

Undoped GNFs were successfully produced by CVD using two different metal catalysts and show similar sorption properties as reported in the literature. The integration of hetero-species via N-doping gave N-doping content also comparable to data from similar experiments already reported but with a change of the surface topology compared to the as-prepared GNFs. The sorption investigation of the N-doped GNFs showed low hydrogen capacities and of the same order as the as-prepared GNFs. In order to increase the surface area and increase the number of adsorption sites, GNFs were intercalated and exfoliated. The study of their sorption and structural properties, revealed an increase of the surface area while no significant improvement of the hydrogen uptakes compared to the starting materials. This was explained by the mixture of less ordered platelet and herringbone types GNFs. In practice, it was found difficult through these strategies to narrow the micropore size distribution and to increase the BET surface area

for the GNFs. Highly crystalline carbon based nanostructures would undeniably allow an easier hetero-species enrichment and ion diffusion through the graphitic interlayer and a more homogenous thermal behaviour.

Chapter 5

Metal-Organic Frameworks

This chapter will present and discuss the results from the investigation of Cu (II) – frameworks. The work will help to better understand sorption properties of a series of highly crystalline and homogenous MOF samples with exceptional sorption properties. Combining traditional and more sophisticated techniques, new insights of the hydrogen interactions with the host structure will be given.

5.1 Introduction

MOF compounds exhibit high crystallinity and great flexibility in pore design which is a great advantage compared to activated carbons and carbon nanotubes (see section 2.5). This chapter reports on the investigation of molecular hydrogen interactions with three copper (II) - frameworks: NOTT-100, NOTT-101, and NOTT-102 (Figure 5.1) provided by the research group of Prof. Martin Schröder from the School of Chemistry at the University of Nottingham. The samples are part of a series of MOF compounds based on copper paddle-wheel units connected by different organic ligands (Lin et al., 2006b, Lin, 2008, Lin et al., 2009). In these investigations, Lin *et al.* showed the nature of the linker could significantly affect the sorption properties using volumetric and gravimetric measurements. The present work aimed at providing a detailed map of the adsorption site distribution and a better understanding of hydrogen behaviour within the first three samples of the MOF series combining neutron techniques. X-ray

5. METAL-ORGANIC FRAMEWORKS

power diffraction (XRPD) experiments were performed prior to the neutron experiments in order to confirm the quality and integrity of the solvent free samples. The neutron data were collected at two neutron facilities the National Institute of Standards and Technology - Center for Neutron Research (NIST-CNR, Gaithersburg) and ISIS-Rutherford Appleton Laboratory (Oxford, UK) combining neutron powder diffraction (NPD) and inelastic neutron scattering (INS) techniques.

5.2 Materials

Three Cu (II) – frameworks MOF-505 (NOTT-100), NOTT-101, and NOTT-12 were investigated. These samples exhibit the same cage structure with a spherical and an elliptical cage as shown in Figure 5.1. Each spherical cage is surrounded by eight elliptical cages. Each elliptical cage shares the two axial and six equatorial windows of the spherical cage. An ellipsoidal cage is surrounded by eight spherical cages sharing the two axial windows and three elongated windows in the upper half and three in the lower half of the cage. HKUST-1 is also introduced for comparison purposes. HKUST-1 is a very similar Cu (II) – framework which is a phenyl-1, 3, 5-tricarboxylate or Cu-BTC (Chui et al., 1999). It also exhibits a spherical cage and a secondary cage connected by similar triangular windows as in the NOTT-100 series (Figure 5.2), although there are significant differences in the structure of these cages because of the organic linker in HKUST-1. A spherical cage is surrounded by eight secondary cages connected by a triangular window and six other spherical cages connected by a square window formed by four paddle wheel units. Its secondary cages are formed by six paddle-wheels connected by phenyl rings and four carboxylate groups.

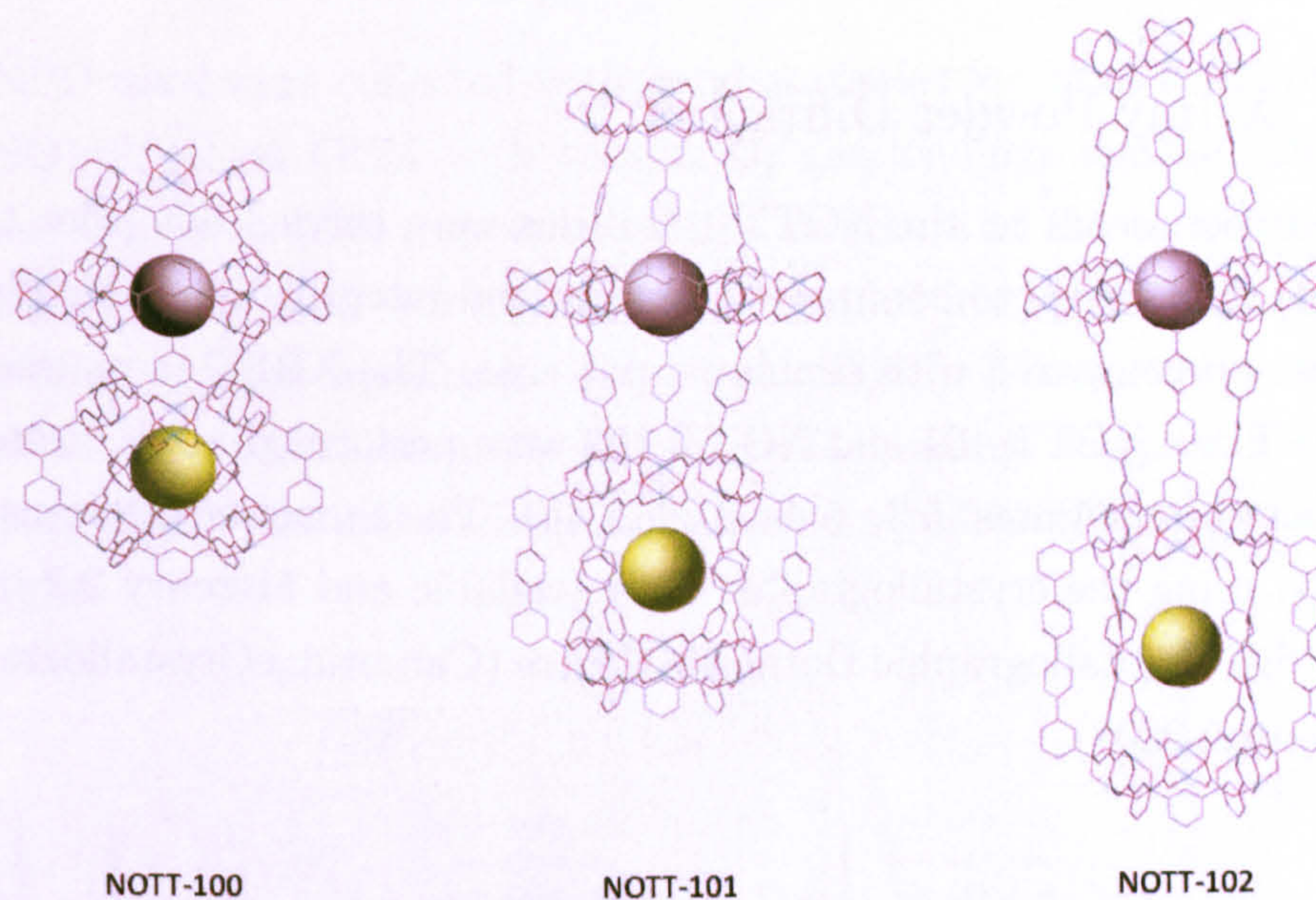


Figure 5.1: From the left MOF-505 (NOTT-100), NOTT-101, and NOTT-102 cage structures with elliptical (grey sphere) and spherical (yellow sphere) cages. Bond colour code: Blue: Copper, Grey: Carbon, Red: Oxygen. No hydrogen for clarity. Crystal structures were obtained from (Lin et al., 2006b). Image generated using DIAMOND software.

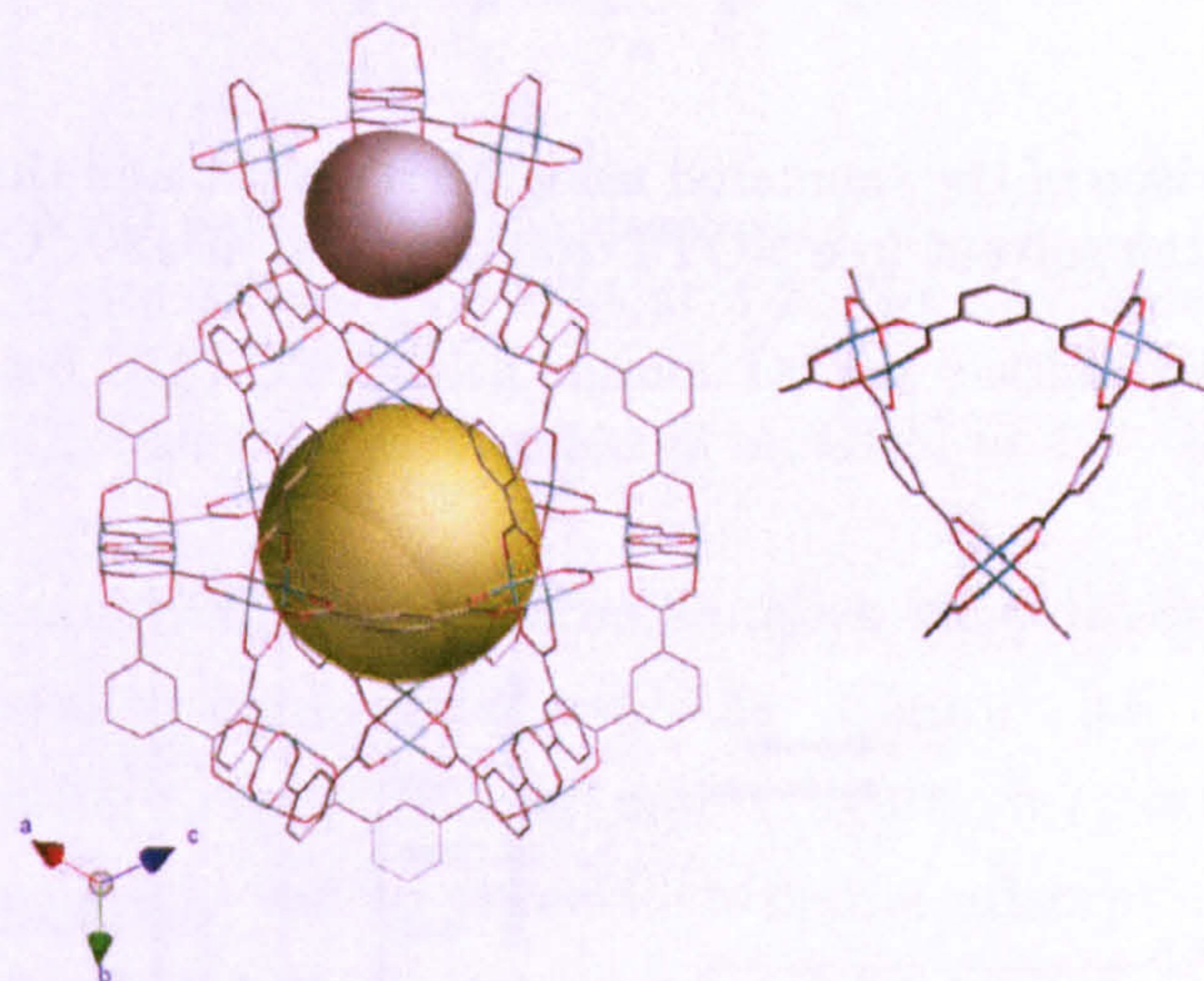


Figure 5.2: On the right: HKUST-1 cage structure with spherical (grey sphere) and secondary (kaki sphere) cages. On the left: triangular windows common to HKUST-1 and NOTT-100 series. Bond colour code: Blue: Cu, Red: O, Grey: C. No hydrogen bonds for clarity. Crystal structure obtained from (Chui et al., 1999). Image generated using DIAMOND software.

5.3 Results

5.3.1 X-Ray Powder Diffraction

XRPD experiments on the NOTT-100 series were carried out prior to the neutron experiments to confirm the quality and integrity of the desolvated samples and compared with simulated patterns. The XRPD measurements on NOTT100, NOTT-101 and NOTT-102 were performed and repeated by Dr. Xiang Lin (Figures 5.3, 5.4a, and 5.4b). The simulated patterns were obtained using the crystallographic data available and Mercury 2.2 by the Cambridge Crystallographic Database Centre (CambridgeCrystallographic-DataCentre, 2008).

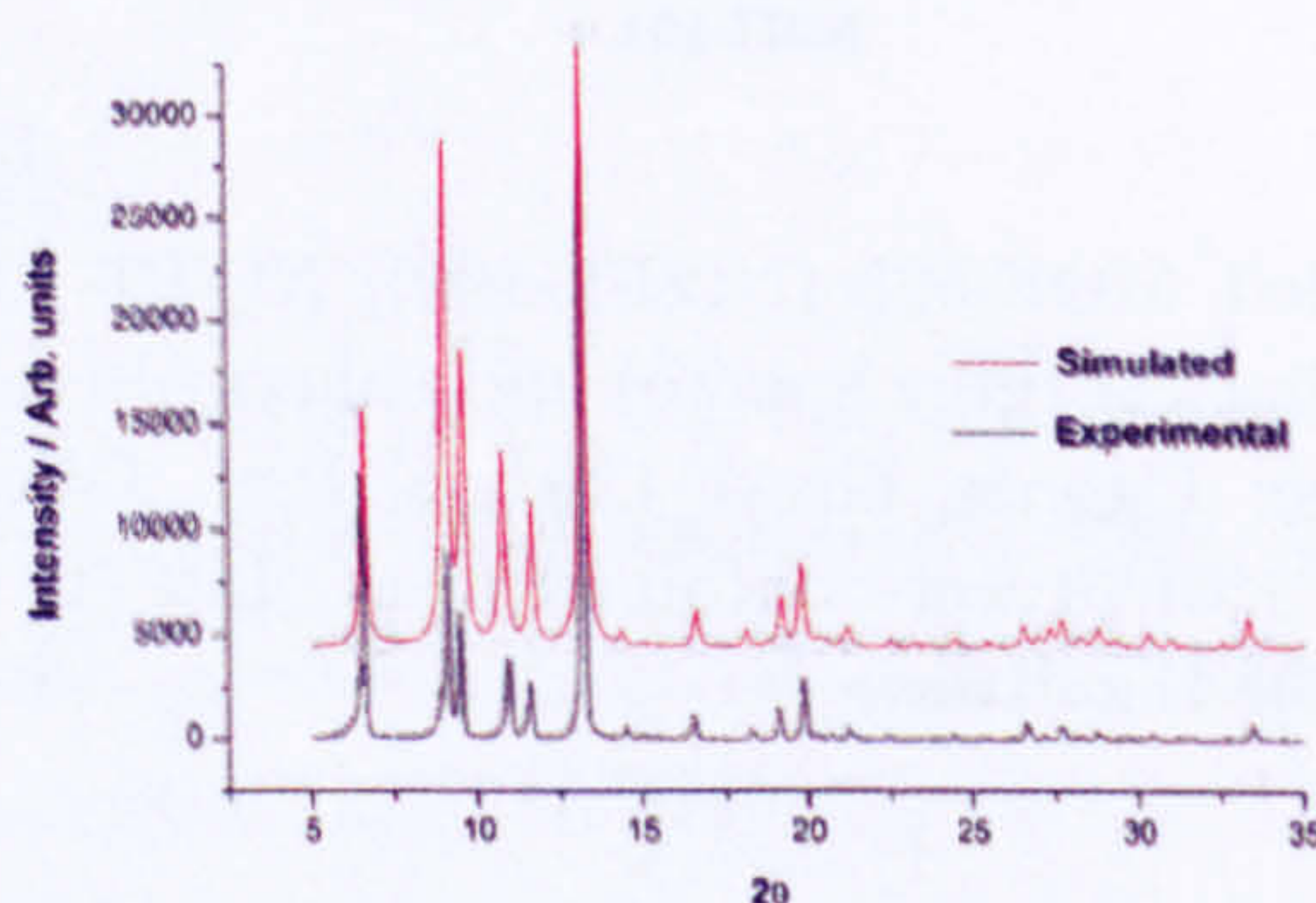


Figure 5.3: Comparison of the simulated using Mercury 2.2 and the experimental XRPD patterns of the solvent free NOTT-100 degassed at 130 °C.

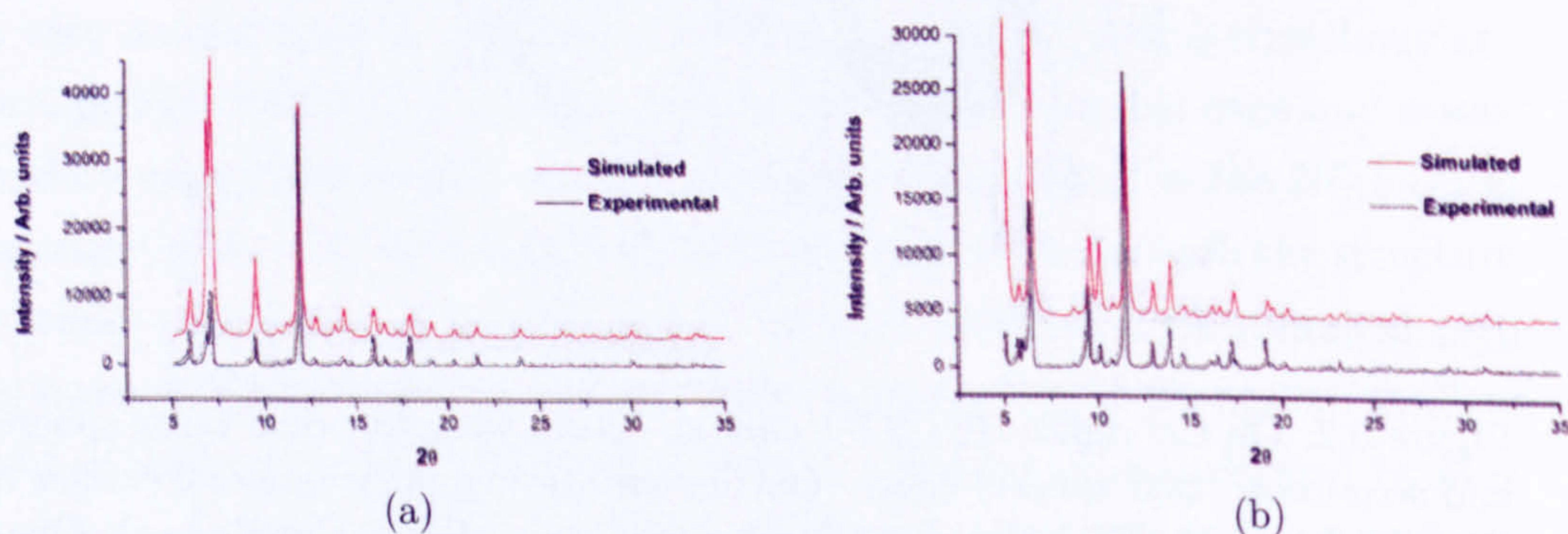


Figure 5.4: Comparison of the simulated using Mercury 2.2 and experimental XRPD patterns of the solvent free NOTT-101 (a) and NOTT-102 (b) degassed at 140 °C.

5.3.2 Neutron Powder Diffraction

The NPD data were collected with good statistics for NOTT-101 on BT1 and NOTT-102 on GEM with various D_2 gas loadings and are shown in Figures 5.5a and 5.5b respectively. The structure of the host framework material of each Cu (II) - framework was obtained from previously reported X-ray single crystal experiments (Lin et al., 2006b). There were neither extra features nor significant peak shifts with D_2 loadings suggesting that the structure of the host material was not affected significantly after adsorption of D_2 gas.

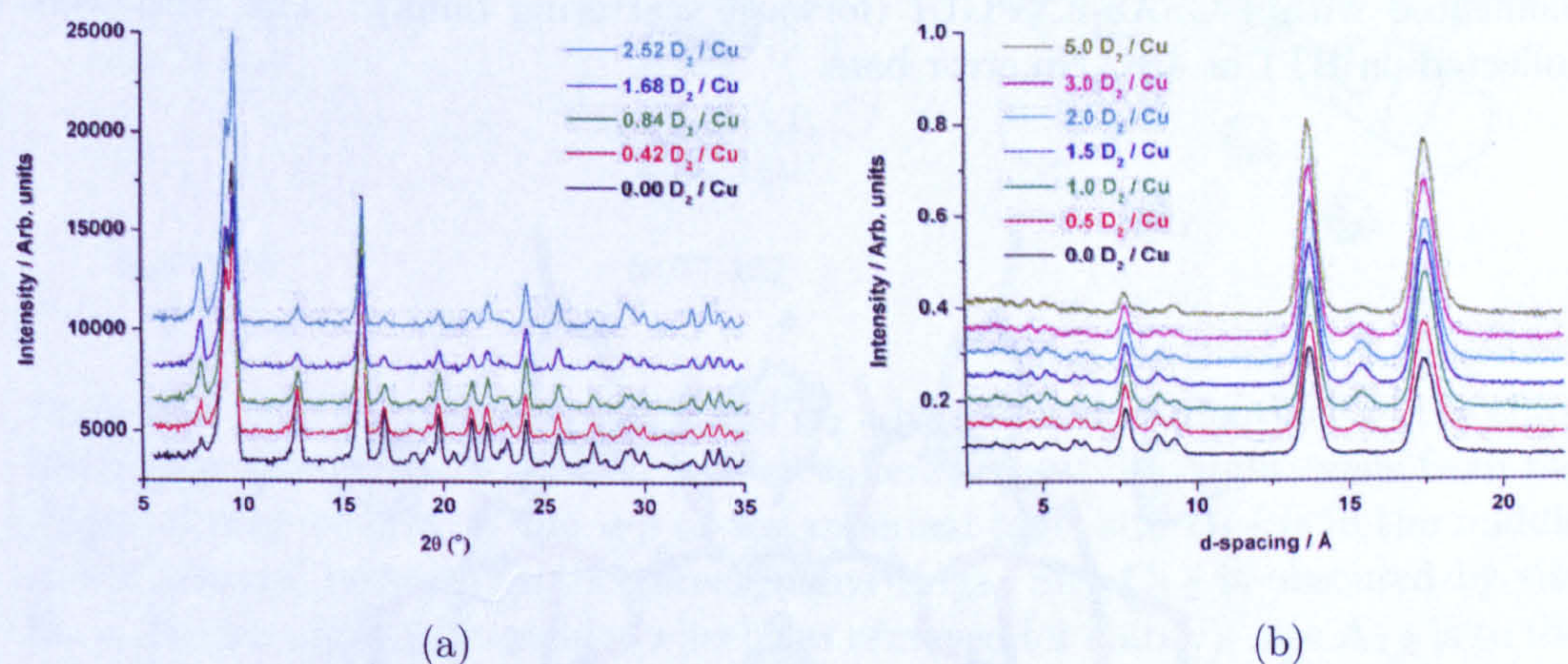


Figure 5.5: a) NPD patterns of the desolvated NOTT-101 with various D_2 gas loadings per Cu site collected on BT1 at 4 K. No error bars. b) NPD patterns of the desolvated NOTT-102 with various D_2 gas loadings per Cu site (forward scattering bank). The data were collected on GEM at 4 K. No error bars.

The refinements of the gas free samples were in excellent agreement with the crystallographic data available (Figure 5.6). The differential nuclear scattering density Fourier map (Figure 5.7) extracted from each NPD pattern clearly led to three identifiable adsorption sites populated on NOTT-101 while NOTT-102 revealed four preferential adsorption sites (Figure 5.8).

5. METAL-ORGANIC FRAMEWORKS

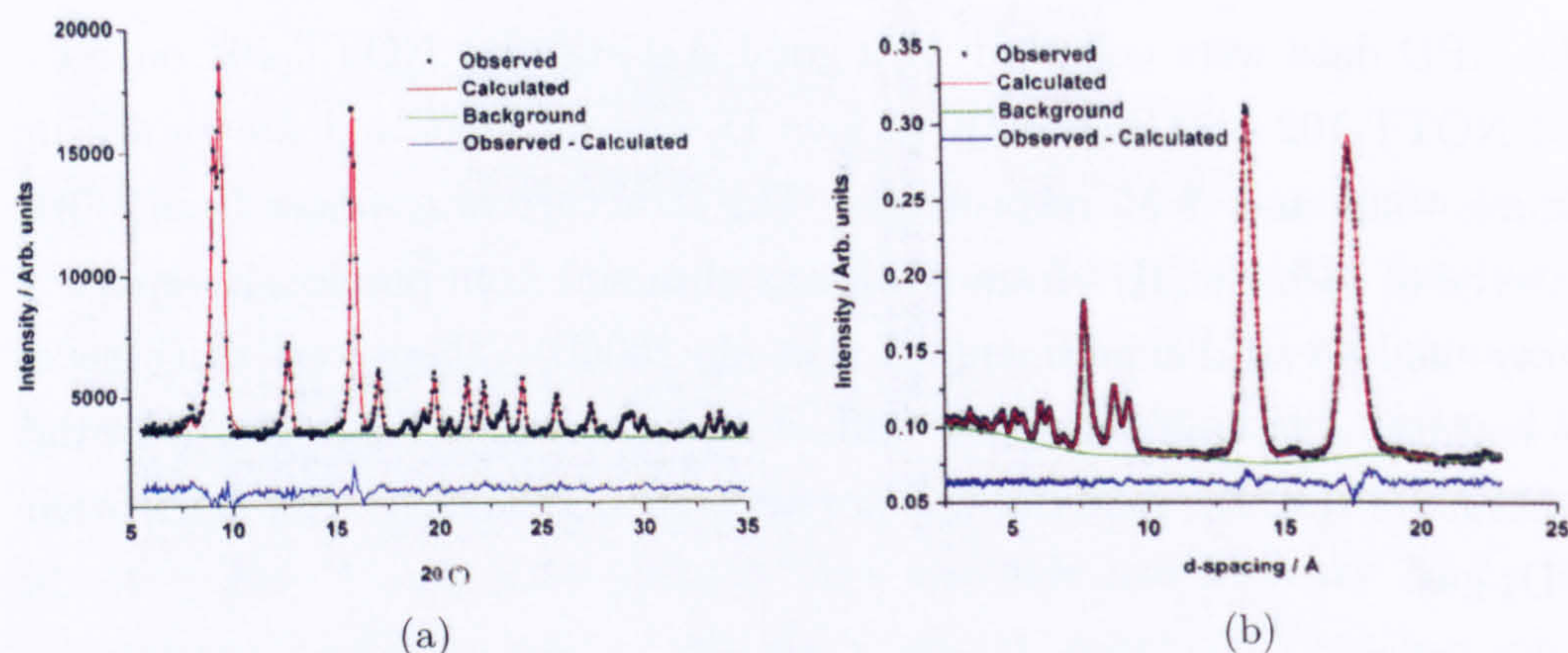


Figure 5.6: a) Bare NOTT-101 and b) NOTT-102 Rietveld refinement as implemented within GSAS-EXPGUI (forward scattering bank). The data were collected on BT1 at 4 K. No error bars.

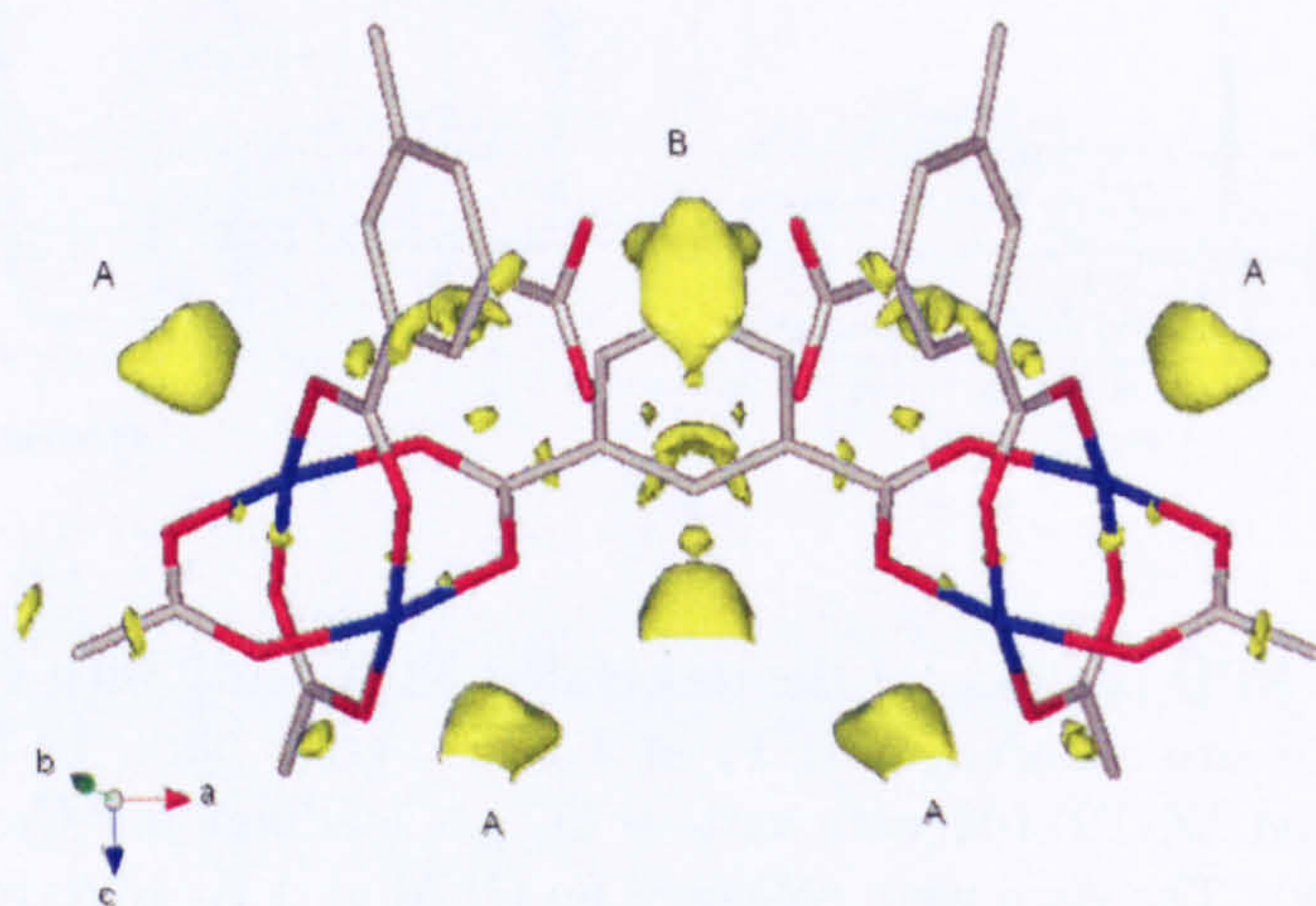


Figure 5.7: Difference nuclear scattering density Fourier map (yellow) showing sites **A** and **B** within the triangular window common to NOTT-101 and NOTT-102. Colour code: Blue: Cu, Red: O, Grey: C. No hydrogen atoms shown for clarity. One copper-paddle wheel was removed. Image was obtained using the visualization program VESTA (Momma and Izumi, 2008).

Tables 5.1 and 5.2 summarize the results from the Rietveld refinements with general good agreement between the simulated patterns and observed data. Tables 5.3 and 5.4 also show that at similar surface coverage the adsorption site distribution found within each NOTT compounds is very close. Site $A_{1,2}$, $B_{1,2}$ and $C_{1,2}$ will be referred to site **A**, **B** and **C** respectively for NOTT-101 and NOTT-102. The Cu (II) centre (sites $A_{1,2}$

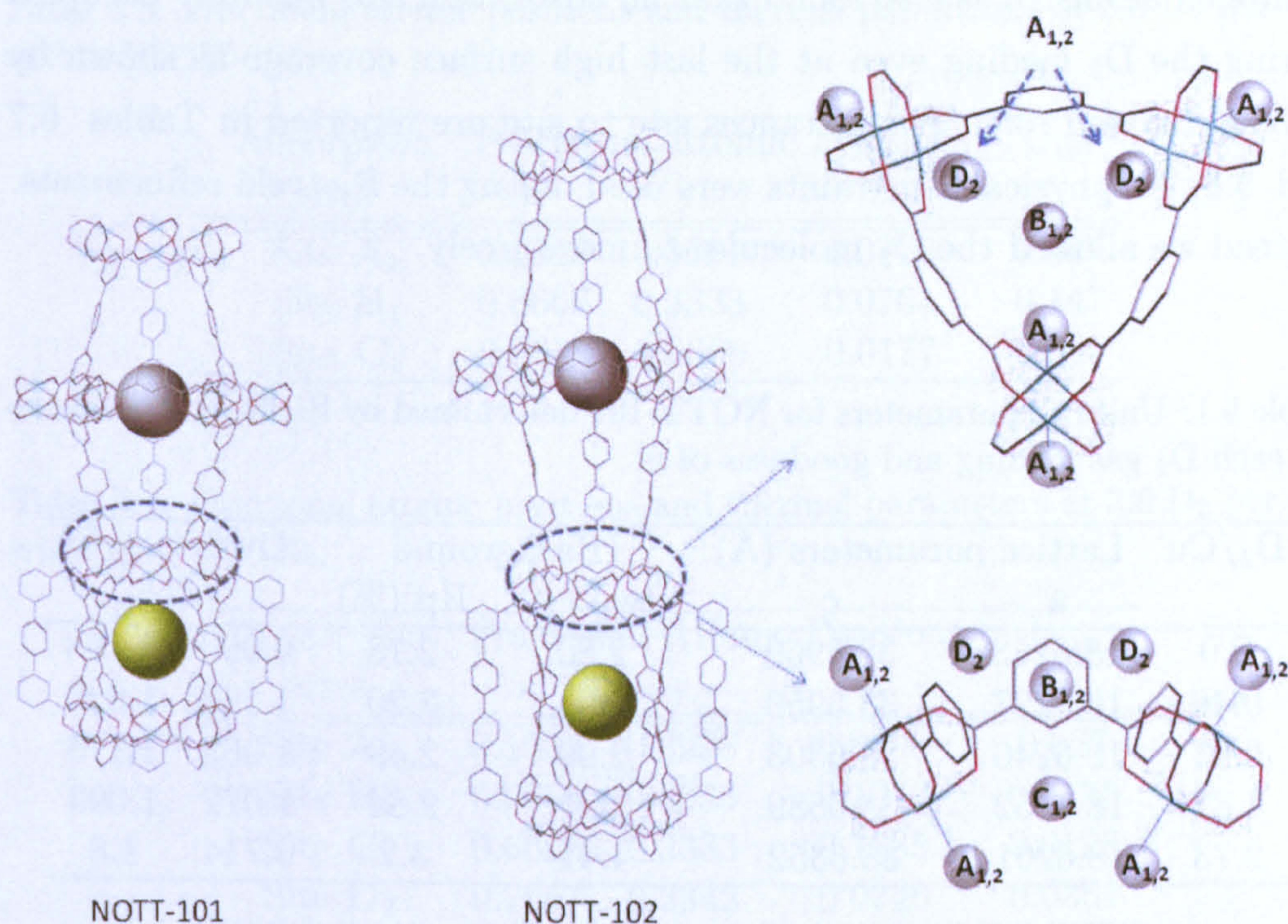


Figure 5.8: NOTT-101 and NOTT-102 D_2 adsorption sites identified in the elliptical (grey sphere) and spherical (yellow sphere) cages. Top right: view from the elliptical cage looking at the top of the spherical cage, site $B_{1,2}$ is in the middle of the window between to the three phenyl rings. Site $C_{1,2}$ is obscured by site $B_{1,2}$. Bottom right (one paddle-wheel was removed for clarity): site $A_{1,2}$ is to the copper centre inside the spherical cage, site $B_{1,2}$ is at the bottom of the elliptical cage close to the phenyl rings and site $C_{1,2}$ is on the same 3-fold axis of site B_1 within the spherical cage. There was an extra site D_2 just above site $A_{1,2}$ (top right one site D_2 was removed to reveal site $A_{1,2}$). Bond colour code: Blue: Cu, Red: O, Grey: C. No hydrogen atoms shown for clarity.

within NOTT-101 and NOTT-102 respectively) was found to be the first site populated with a Cu- D_2 (centroid) distance 2.5 Å and 2.4 Å, the D_2 being located at the apex of a distorted square base pyramid (Figure 5.8). The second adsorption site (sites $B_{1,2}$) is located at either end of the elliptical cage co-ordinating to the three phenyl rings which, along with the copper paddle wheel units, form a 3-fold symmetrical window between the spherical and elliptical cages. The third adsorption site (sites $C_{1,2}$) is on the same three-fold symmetry axis as sites $B_{1,2}$, but within the spherical cage and close to the six oxygen atoms on the copper paddle wheel units. For NOTT-102, a fourth site, D_2 , was shown to be above site B_2 close to the

5. METAL-ORGANIC FRAMEWORKS

hydrogen atoms. It is also found that no adsorption site was fully occupied during the D₂ loading even at the last high surface coverage as shown by Tables 5.5 and 5.6. The distances site to site are reported in Tables 5.7 and 5.8. No physical constraints were used during the Rietveld refinements. Instead we allowed the D₂ molecules to move freely.

Table 5.1: Unit cell parameters for NOTT-101 determined by Rietveld refinement for each D₂ gas loading and goodness of fit.

D ₂ /Cu	Lattice parameters (Å)		-Background		Dwd	χ^2
	a	c	Rwp (%)	Rp (%)		
0.0	18.6263	38.5969	2.80	2.13	0.990	1.198
0.46	18.6227	38.5950	2.94	2.20	1.183	1.020
0.91	18.6240	38.6303	2.99	2.49	1.063	1.175
1.82	18.6152	38.6589	3.6	2.84	1.072	1.093
2.73	18.6201	38.6352	4.41	3.2	0.714	1.8

Table 5.2: Unit cell parameters for NOTT-102 determined by Rietveld refinement for each D₂ gas loading and goodness of fit.

D ₂ /Cu	Lattice parameters (Å)		-Background		Dwd	χ^2
	a	c	Rwp (%)	Rp (%)		
0.0	18.5698	52.3011	0.99	1.07	0.696	3.547
0.5	18.5630	52.3380	1.13	1.22	0.577	3.648
1.0	18.5585	52.3823	1.42	1.46	0.506	5.055
2.0	18.5482	52.4190	1.72	1.81	0.376	6.904
3.0	18.5472	52.4060	2.27	2.38	0.277	9.449
5.0	18.3650	51.9151	2.60	2.80	0.272	5.870

Table 5.3: Fractional atomic positions and thermal parameters at 3.0 D₂ per Cu within NOTT-101.

Adsorption sites	Fractional Atomic Positions			U_{iso}
	x	y	z	
Site A ₁	0.1383	0.5691	0.0776	0.027
Site B ₁	0.6666	0.3333	0.0763	0.147
Site C ₁	0.3333	0.6666	0.0177	0.085

Table 5.4: Fractional atomic positions and thermal parameters at 3.0 D₂ per Cu within NOTT-102.

Adsorption sites	Fractional Atomic Positions			U_{iso}
	x	y	z	
Site A ₂	0.1003	0.8998	0.8906	0.027
Site B ₂	0.6666	0.3333	0.1040	0.0135
Site C ₂	0.6666	0.3333	0.1785	0.0128
Site D ₂	0.7657	0.2342	0.0746	0.0351

Table 5.5: Fractional occupancies for NOTT-101 adsorption sites at 3.0 D₂ per Cu within NOTT-101.

Adsorption sites	Fractional Occupancies			
	0.46D ₂ /Cu	0.91D ₂ /Cu	1.82D ₂ /Cu	2.73D ₂ /Cu
Site A ₁	0.3223	0.5446	0.7206	0.806
Site B ₁	0	0.1104	0.1802	0.3331
Site C ₁	0	0	0.2486	0.3233

Table 5.6: Fractional occupancies for NOTT-102 adsorption sites at 3.0 D₂ per Cu within NOTT-102.

Adsorption sites	Fractional Occupancies				
	0.5 D ₂ /Cu	1.0 D ₂ /Cu	2.0 D ₂ /Cu	3.0 D ₂ /Cu	5.0 D ₂ /Cu
Site A ₂	0.39	0.68	0.72	0.72	0.72
Site B ₂	0.08	0.20	0.22	0.27	0.29
Site C ₂	0.00	0.09	0.20	0.24	0.31
Site D ₂	0.00	0.00	0.18	0.40	0.65

5. METAL-ORGANIC FRAMEWORKS

Table 5.7: Shortest distance site-site within NOTT-101.

Distance site-site (Å)	Site A ₁	Site B ₁	Site C ₁
Site A ₁	0.00	3.98	6.78
Site B ₁	-	0.00	3.63
Site C ₁	-	-	0.00

Table 5.8: Shortest distance site-site within NOTT-102.

Distance site-site (Å)	Site A ₂	Site B ₂	Site C ₂	Site D ₂
Site A ₂	0.00	3.61	6.42	7.41
Site B ₂	-	0.00	3.69	6.31
Site C ₂	-	-	0.00	3.63
Site D ₂	-	-	-	0.00

5.3.3 Inelastic Neutron Scattering

INS data were collected for NOTT-101 using the constant wavelength spectrometer FANS and for NOTT-102 using the time of flight spectrometer TOSCA. The as collected INS spectra of NOTT-101 with various para-H₂ gas loadings are shown in Figure 5.9. Apparent peaks at low energy *ca.* 6 meV and 7 meV were assigned to the pyrolytic graphite monochromator and, therefore, were not considered further. The first loading was made with normal-H₂ gas due to para-H₂ not available. Higher loadings were made with para-H₂ gas. No shift in the position of the INS peaks was observed as the para-H₂ gas loading was increased. The bare material spectrum revealed two features at 7.84 meV and 11.71 meV overlapping with the INS features coming from the H₂ dynamics as the surface coverage increases. The TOSCA spectra for NOTT-102 with various para-H₂ gas loadings are reported with respect to the back and forward scattering detector banks with $S(Q, \omega)_{back}$ and $S(Q, \omega)_{forward}$ in Figures 5.10 and 5.11 respectively where the gas free spectrum showed two distinct features at 4.78 meV and 8.90 meV. As for NOTT-101 INS spectra, these peaks overlapped with those from the adsorbed H₂.

The INS spectra reported in Figures 5.12 and 5.13 are from a similar INS experiment on NOTT-102 with different HD gas loadings. Various amounts of HD gas were aliquoted from a calibrated volume to reach 0.5, 1.0,

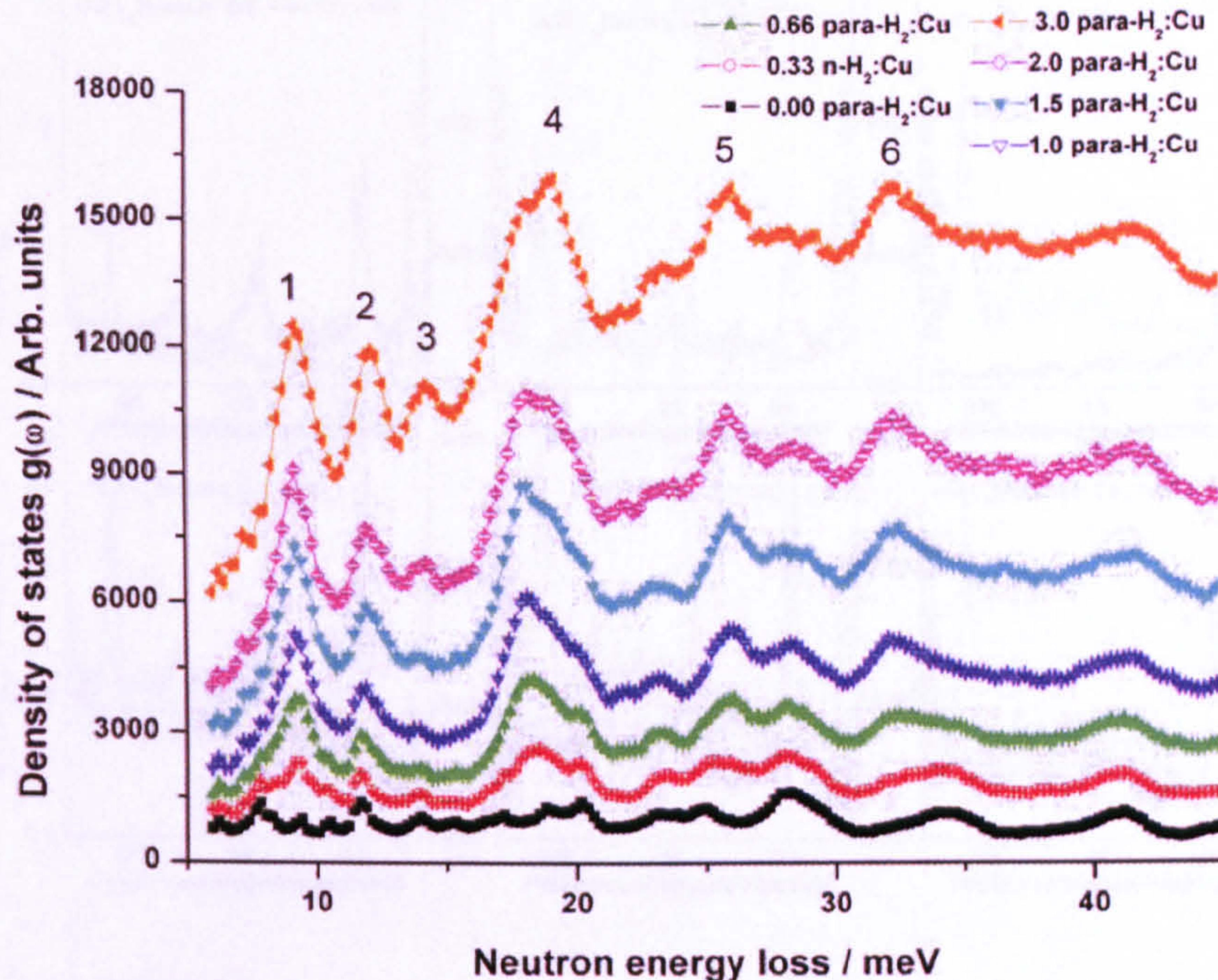


Figure 5.9: As collected INS spectra of NOTT-101 with various para-H₂ loadings per Cu site. The data were collected on FANS at 4 K. Error bars are smaller than the symbols. The first loading was made with normal-H₂ gas.

1.5, 2.0, 2.5, and 3.0 HD molecules per Cu. For this experiment additional amount of sample was loaded into the vanadium can to reach a final sample mass of 1.940 g with a similar total beam current of 1000 μ A. As for NOTT-101 INS spectra, no shift in the position of the INS peaks was observed as the para-H₂ and HD gas loading were increased. Figure 5.14 shows the bare material spectrum before the para-H₂ and the HD loadings normalized to the same amount and confirming the integrity of both samples prior to HD loadings.

5. METAL-ORGANIC FRAMEWORKS

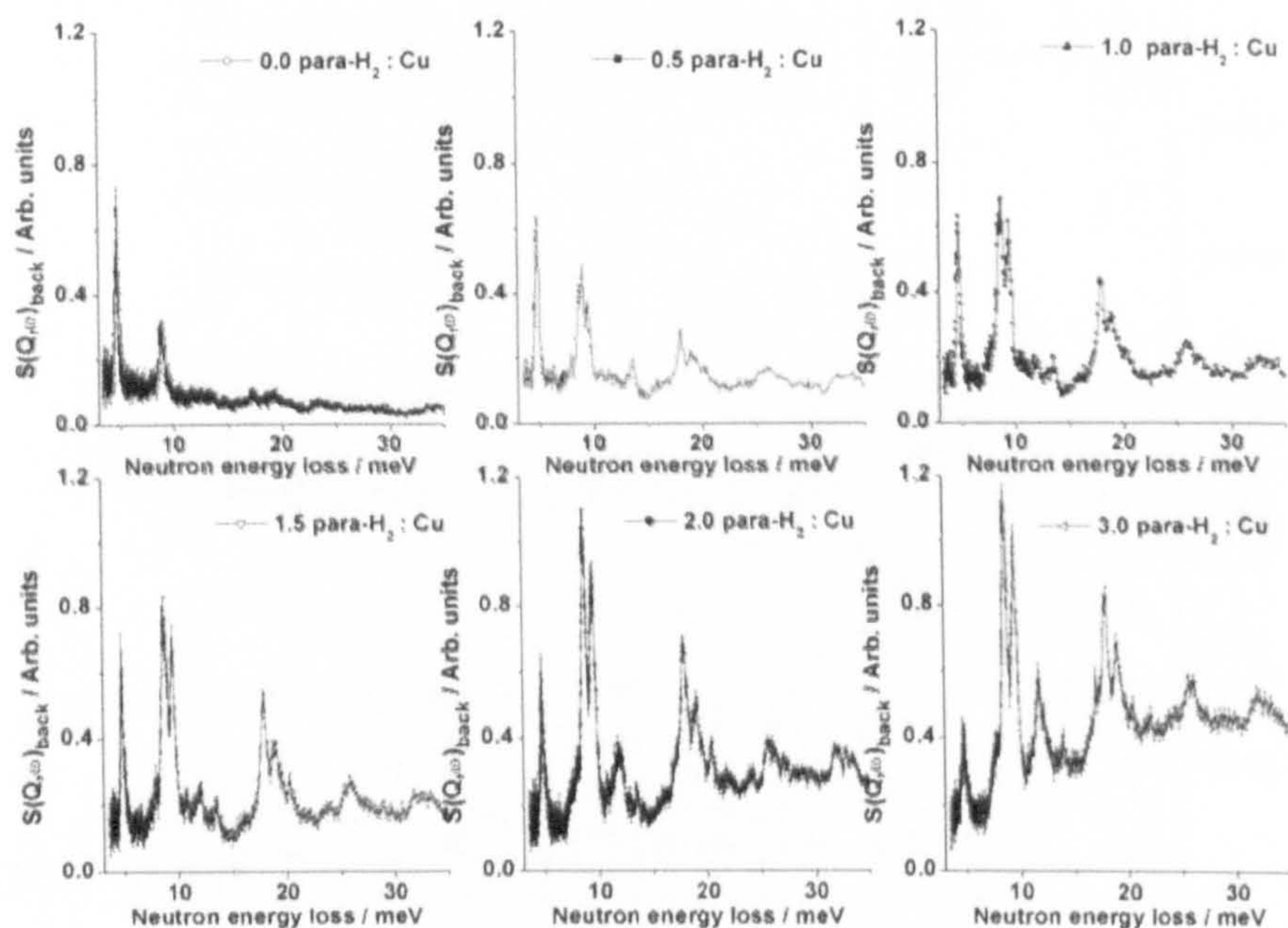


Figure 5.10: As collected $S(Q, \omega)_{back}$ and $S(Q, \omega)_{forward}$ for NOTT-102 with various para- H_2 gas loadings per Cu site collected at 4 K on TOSCA Error bars are represented.

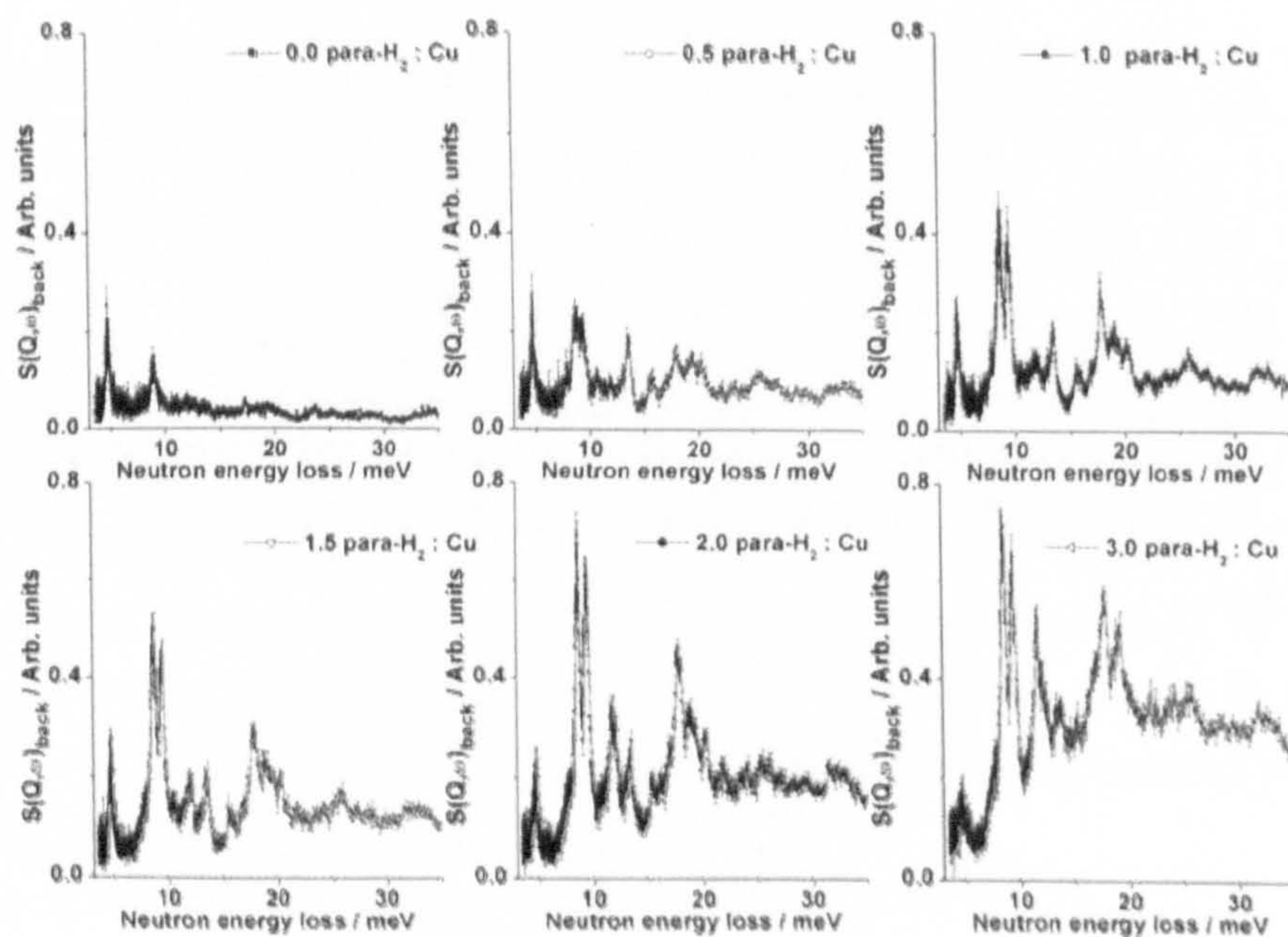


Figure 5.11: As collected $S(Q, \omega)_{forward}$ for NOTT-102 with various para- H_2 gas loadings per Cu site collected at 4 K on TOSCA Error bars are represented.

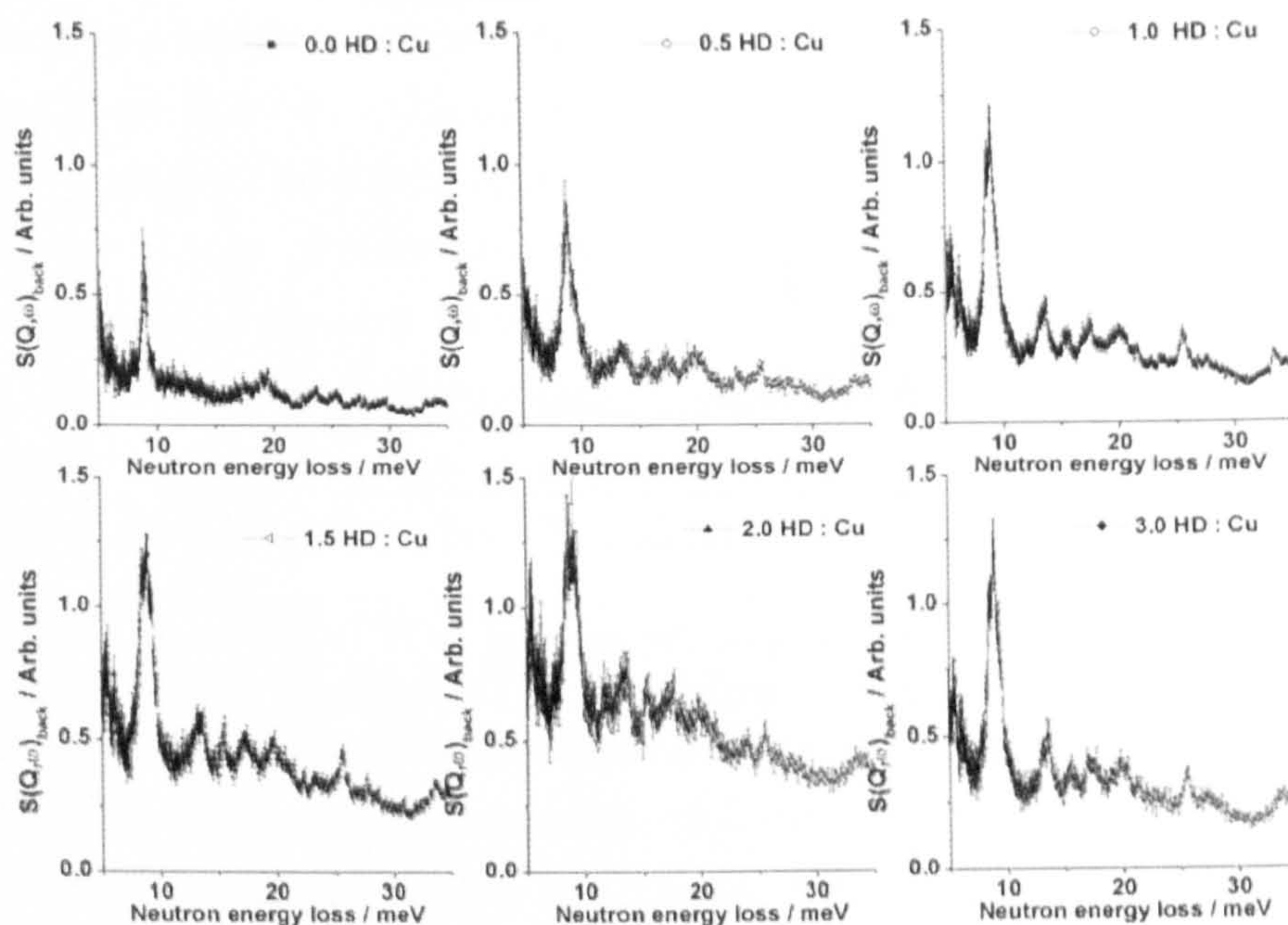


Figure 5.12: As collected $S(Q, \omega)_{back}$ and $S(Q, \omega)_{forward}$ for NOTT-102 with various HD gas loadings per Cu site collected at 4 K on TOSCA Error bars are represented.

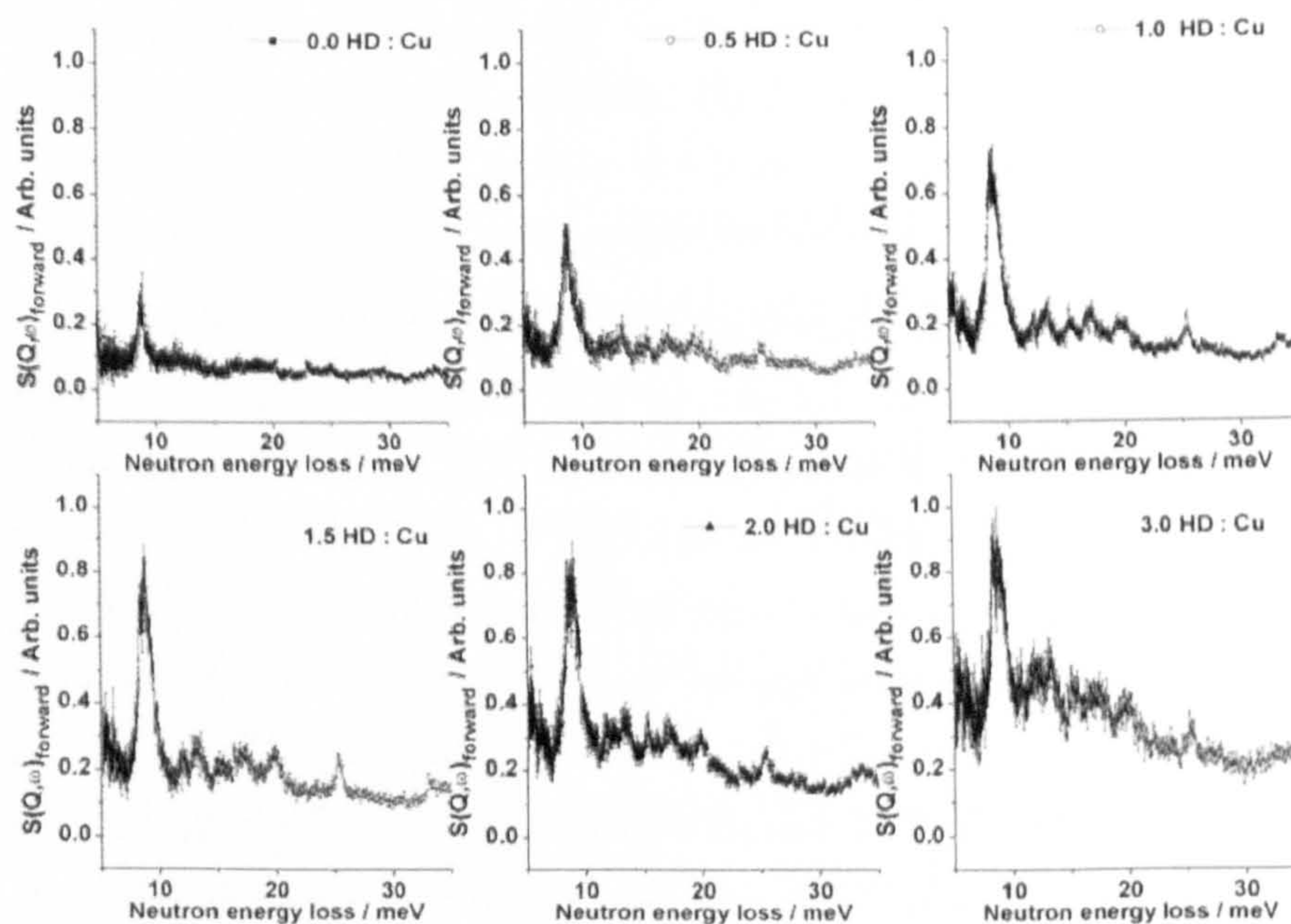


Figure 5.13: As collected $S(Q, \omega)_{forward}$ for NOTT-102 with various HD gas loadings per Cu site collected at 4 K on TOSCA Error bars are represented.

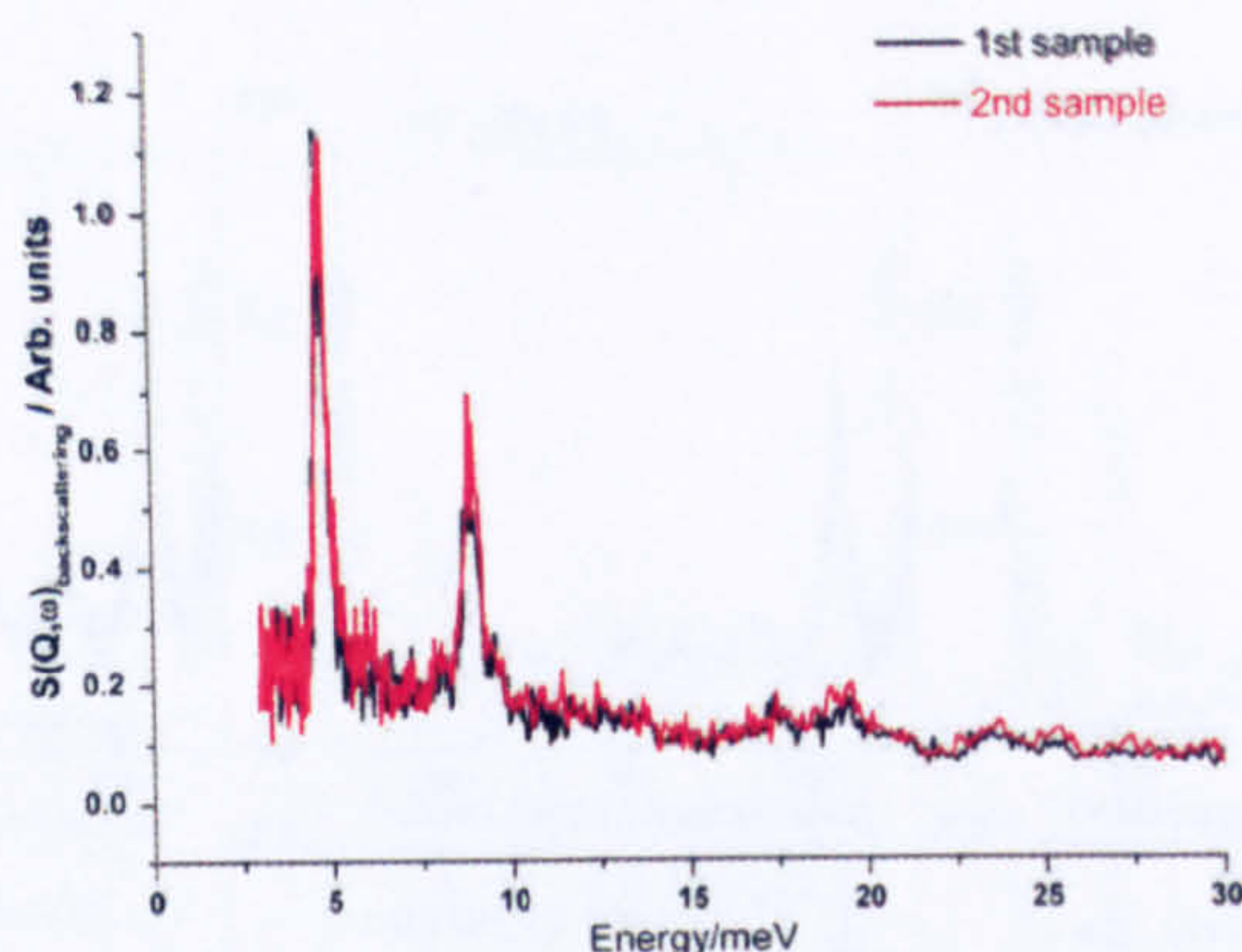


Figure 5.14: As collected $S(Q, \omega)_{back}$ of the gas free NOTT-102 before the para- H_2 (black line) and the HD (red line) experiments. The intensity of the 1st sample has been normalized to the same amount as for the 2nd sample. No error bars for clarity.

5.4 Discussions

This section will discuss the neutron results obtained from NPD and INS experiments for NOTT-101 and NOTT-102. This will help to identify the effect of a different organic linker upon the physisorption mechanism. A comparison will be given with those obtained on HKUST-1 (Peterson et al., 2006, Liu et al., 2007a).

5.4.1 Neutron Powder Diffraction

Three adsorption sites were identified within NOTT-101 (Figure 5.8) and four within NOTT-102 with the copper site the first to be populated on both samples. The Cu-D₂ distance found was 2.51 and 2.39 Å respectively which are similar to that found for HKUST-1, *ca.* 2.39 (1) Å (Peterson et al., 2006). It is highly probable that for a similar surface coverage, a similar adsorption site distribution applies to NOTT-100 although this has yet to be proved using neutron techniques. From a topological point of view, the NPD results for the NOTT samples show preferential adsorption within the spherical cages at low surface coverage *ca.* 0.5 D₂ per Cu (sites **A**_{1,2}). The elliptical cages are also populated with sites **B**_{1,2} but with smaller occupancies than site **A**_{1,2} respectively. At higher coverage third sites **C**_{1,2} are occupied. One might think that the **C**_{1,2} sites will be blocked because

of occupancy of the $\mathbf{A}_{1,2}$ and $\mathbf{B}_{1,2}$ sites, but this ignores the fact that on dosing to a higher level the sample was heated up to 50 K, at which temperature there will be significant diffusion of D_2 gas, hence enabling the filling of $\mathbf{C}_{1,2}$ sites. The filling order of smaller, then larger, pores is consistent with the theory of micropore filling (Rouquerol et al., 1998). Also it was not possible to account for all the D_2 loaded onto the NOTT samples during the experiments. Although the adsorption site distribution was clearly identified on both compounds, nearly 20 % of D_2 gas was not accounted for even at high surface coverage. This is different behaviour for HKUST-1 where for instance the copper site is occupied at 90 % at 0.5 D_2 per Cu compared to 60 % for NOTT samples. A simple explanation will be given later with the INS discussion (see section 5.4.2). The site to site distances appear to be physically consistent with the intermolecular distances within solid H_2 (D_2) *ca.* 3.8 Å (3.6 Å) (Silvera, 1980). This was not the case with HKUST-1 where some site to site distances were found to be around 3.20 (1) Å (Peterson et al., 2006). In our case the presence of coordinated unsaturated metal centres did not affect the inter-molecular D_2 - D_2 distance. This was recently suggested by Liu *et al.* who showed that the presence of coordinated unsaturated metal centres in some MOFs could increase the hydrogen packing density higher than that of the solid phase *ca.* $3.5 \cdot 10^{-5} \text{ g.m}^2$ against $2.8 \cdot 10^{-5} \text{ g.m}^2$ for solid H_2 (Liu et al., 2008). It was assumed that the copper sites $\mathbf{A}_{1,2}$ within the paddle wheel are equivalent. The environment of the copper sites seems to be the same. This could be seen with the Cu-Cu axis which is aligned with the hydrogen molecule, always pointing towards two spherical cages. This means that the environment of the site $\mathbf{A}_{1,2}$ on either side of the paddle wheel remains the same (Figure 5.15.a). This is not always the case especially with samples containing more than two cages (Yan et al., 2009).

It is also important to notice that all the D_2 gas seems to be “trapped” within the triangular windows which act like a funnel between the cages. The other type of windows connecting two spherical cages do not seem to participate in the adsorption process. Hence, to improve the adsorption properties for such MOF structures, a possible option would be to increase the number of these triangular windows within the structure at which there are the strongest sorption interactions (Figure 5.15.b).

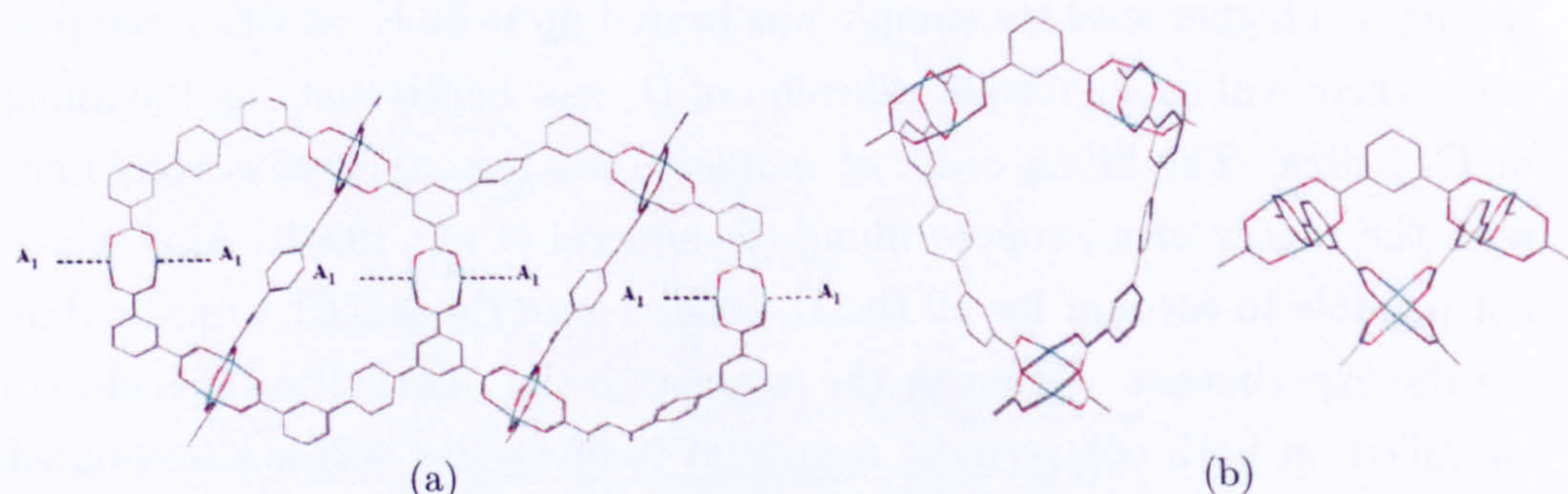


Figure 5.15: a) Equivalence of the sites A_1 on both side of the paddle-wheel for NOTT-101. b) Triangular windows connecting a spherical and elliptical cage. Colour bond: Red O; Blue: Cu; Grey: Carbon. No hydrogen atoms shown for clarity.

5.4.2 Inelastic Neutron Scattering

For NOTT-101, difference INS spectra for two subsequent para- H_2 loadings are shown in Figure 5.17 allowing the identification of the molecular hydrogen spectra with respect to that of the bare material. It also reveals the contribution of the newly adsorbed para- H_2 with respect to the para- H_2 from the previous loading (*i.e.*: spectrum obtained at 1.0 para- H_2 was subtracted from the spectrum collected at 2.0 para- H_2 and so on.). As the number of hydrogen species increases, the amount of neutrons interacting with the sample also decreases. Therefore, the difference of INS spectra minimizes this effect from one loading to the next one so that each INS feature can be assigned to the dynamics of molecular H_2 with the associated adsorption site being occupied.

INS peaks for the first loading were found at 9.11 meV, 12.21 meV, 18.22 meV, 23.42 meV, 25.91 meV, 29.17 meV and 32.73 meV (peaks 1, 2, 4b, 4c, 5, 6, 7 and 8). At higher loadings three further peaks appeared at 14.22 meV, 16.82 meV and 21.88 meV (peaks 3, 4a and 4d). Peaks 6, 7, and 8 seem to form a sequence of equally spaced peaks, which suggests a similar physical origin. As the para- H_2 loading was increased, there were no shifts in the position of any of the INS peaks. Each INS feature was fitted using Gaussian functions (Figure 5.17.a). The difference INS spectra allow us to deconvolute peak 4 into a clear sequence of four peaks 4a, 4b, 4c and

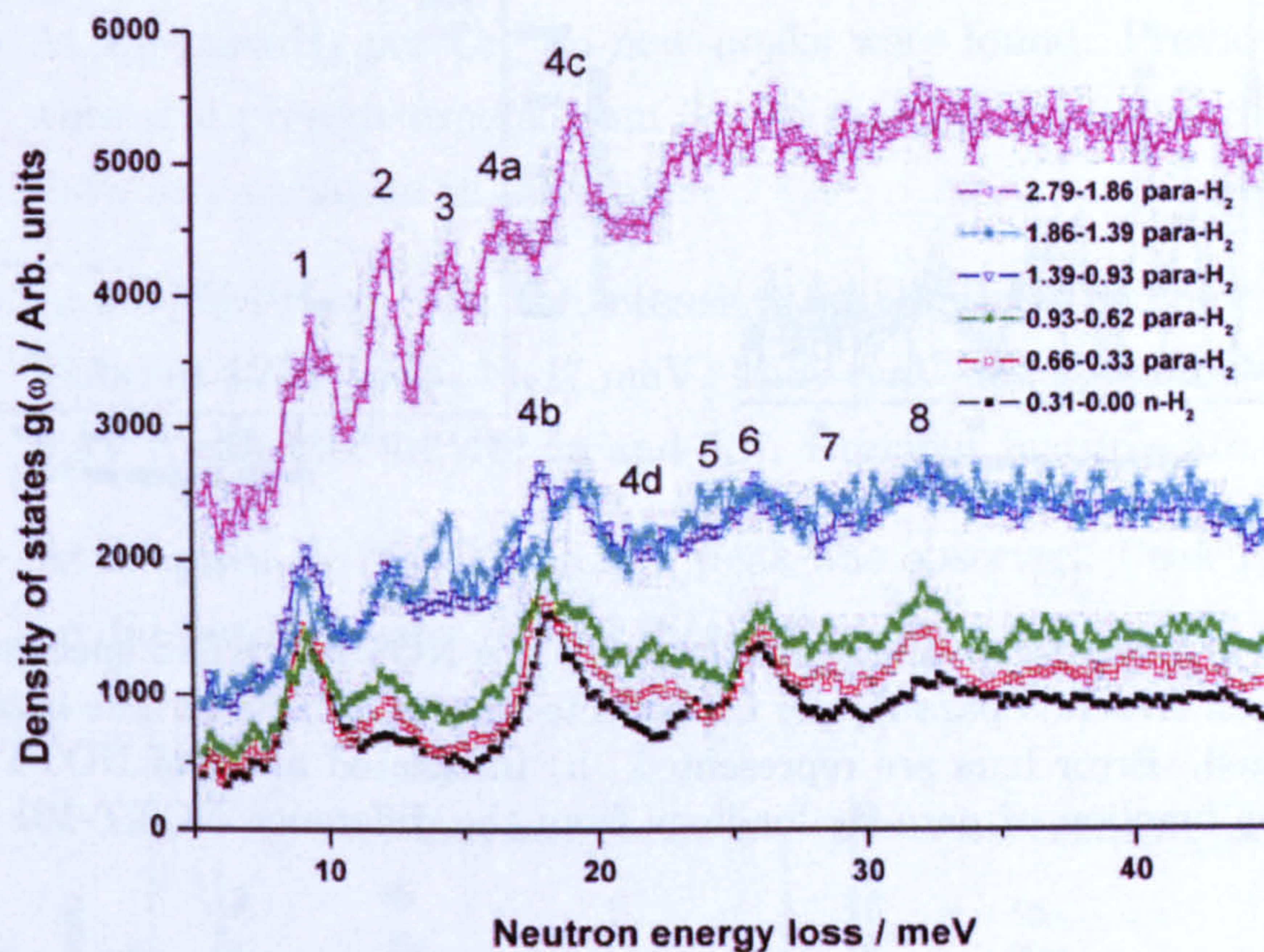


Figure 5.16: Difference INS spectra for NOTT-101 between two subsequent para- H_2 loadings; collected on FANS. The baselines were not subtracted. Error bars are smaller than the symbols.

4d which was not obvious from the as collected INS data in Figure 5.10. Given the instrument resolution of FANS for this energy, *ca.* 1.3 meV this is the simplest approximation for the deconvolution. Peak 1, 2 and 3 were simply fitted with only one Gaussian function as they were symmetrical although significantly broader than the corresponding energy resolution *ca.* 1.2, 1.2 and 1.3 meV respectively. The integrated area of each INS peak was plotted as a function of para- H_2 loadings in Figure 5.17.b. It was found that the integrated areas were still increasing which means that no site had been fully occupied even at the highest loading of 2.79 para- H_2 molecules, in agreement with the NPD data.

We can combine the NPD results with the INS peak deconvolution. Therefore:

- Peak 1, 4b, 4c, 5, 6, 7 and 8 can be assigned to para- H_2 adsorbed onto A_1 .

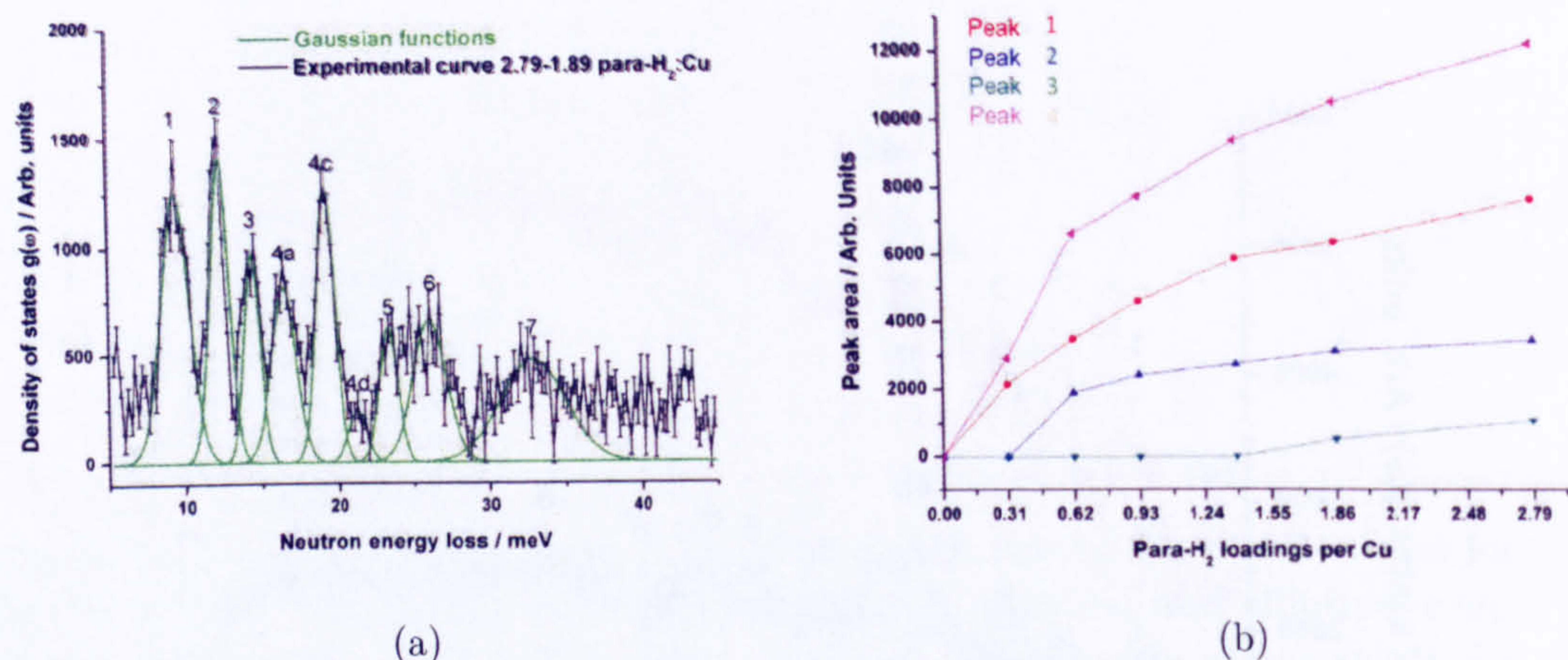


Figure 5.17: a) Peak deconvolution of the difference NOTT-101 INS spectra obtained between 2.79-1.89 para-H₂ per Cu collected on FANS at 4 K. The baseline was subtracted. Error bars are represented. b) Integrated areas of NOTT-101 INS peaks as function of para-H₂ loadings from the difference NOTT-101 INS spectra.

- Peak 2 can be related to para-H₂ on **B**₁.
- Peak 3, 4a and 4d can be related to para-H₂ on **C**₁.

The Figure 5.17b shows the evolution of the integrated area of the main peaks *i.e.*: 1, 2, 3, 4a, 4b, 4c, and 4d. It is found that the integrated areas are still increasing and that there is no site saturation even at the last loading, which is consistent with NPD results found earlier. Difference INS spectra for NOTT-102 obtained from two subsequent para-H₂ gas dosings (*i.e.*: showing the spectra for only the extra para-H₂ adsorbed with each loading) are reported respectively for the back and forward scattering detector banks (Figures 5.18 and 5.19). INS features were revealed as the para-H₂ gas loading increases. For both detector banks, and using the difference INS spectra:

- At 0.5 para-H₂ per Cu, peaks were found at 8.55 meV, 9.45 meV, 13.51 meV, 15.73 meV, 16.96 meV, 17.95 meV, 19.07 meV, 20.42 meV, 26.09 meV, and 33.12 meV (peaks 1, 2, 3c, 3d, 3e, 5b, 5c, 5d, 6, 7 and 8).
- At 1.0 para-H₂ per Cu, a new peak was observed at 11.59 meV (peak 3a). Previous features were still present. Peak 3c, 3d and 3e were not

present any longer in the difference INS spectrum meaning that no change in intensity was observed in the as-collected data.

- At 1.5 para-H₂ per Cu, no new peaks were found. Previous features were still present except from 3c, 3d and 3e. 3c, 3d, and 3e did not show any variation in intensity.
- At 2.0 para-H₂ per Cu, the intensity was recovered and new peaks were found at 12.50 meV, 14.47 meV, 14.87 meV and 17.06 meV and 19.30 meV (peaks 3b, 4a, 4b, 5a and 5d). Previous features are present.
- At 3.0 para-H₂ per Cu, no new peak was observed. Peak 1, 2, 5b, and 5c did not show any further increase in intensity.

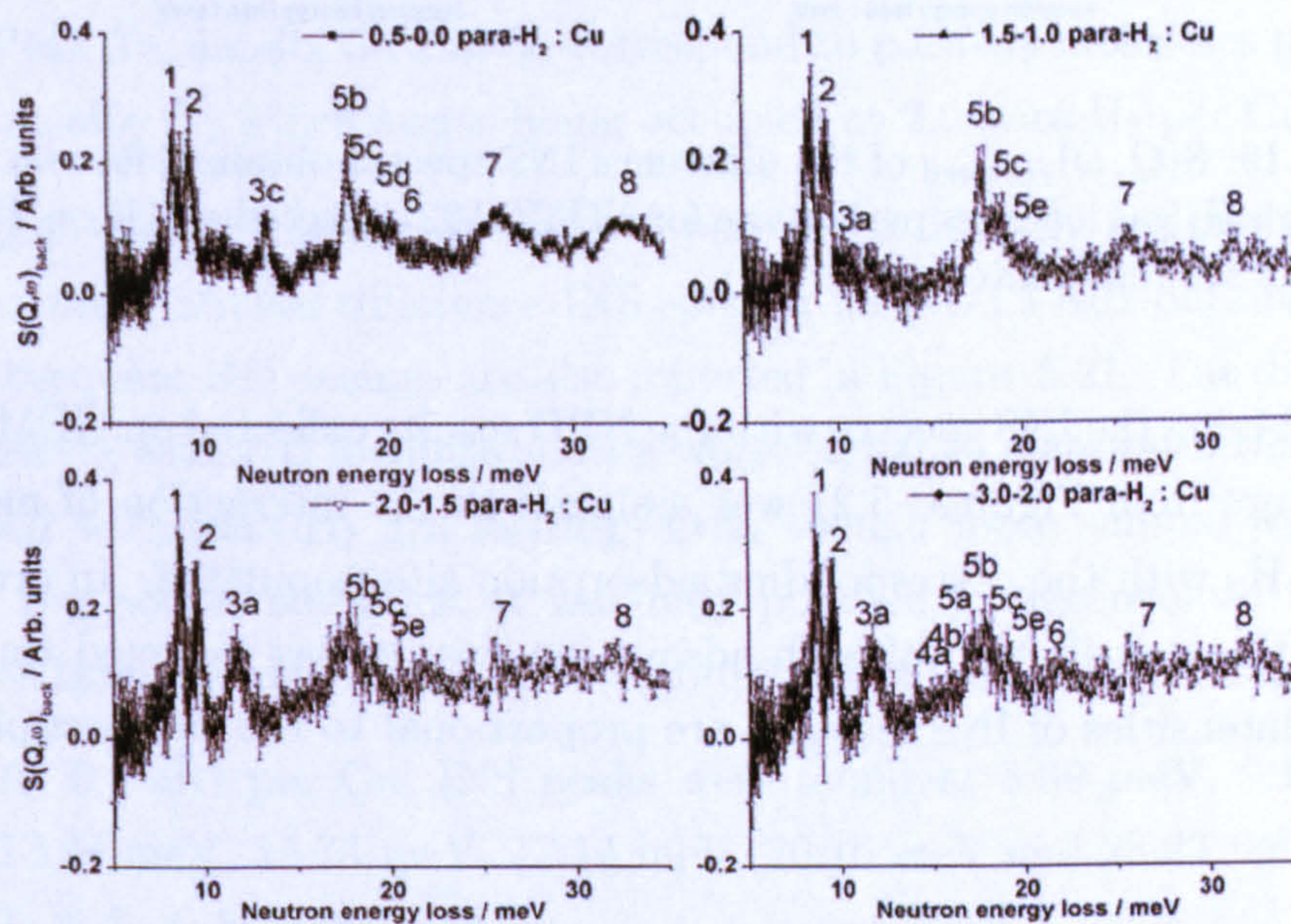


Figure 5.18: $S(Q, \omega)_{back}$ of the difference INS spectra obtained for two subsequent para-H₂ gas loadings per Cu site for NOTT-102 collected at 4 K on TOSCA Error bars are represented.

In general, TOSCA spectra are richer than those obtained on FANS. Figure 5.20 show the deconvolution of INS peaks at 0.5-0.0 and 3.0-2.0 para-H₂ loadings per Cu respectively for the backscattering detector bank. The downside is that TOSCA runs normally require long collection times to achieve good statistics.

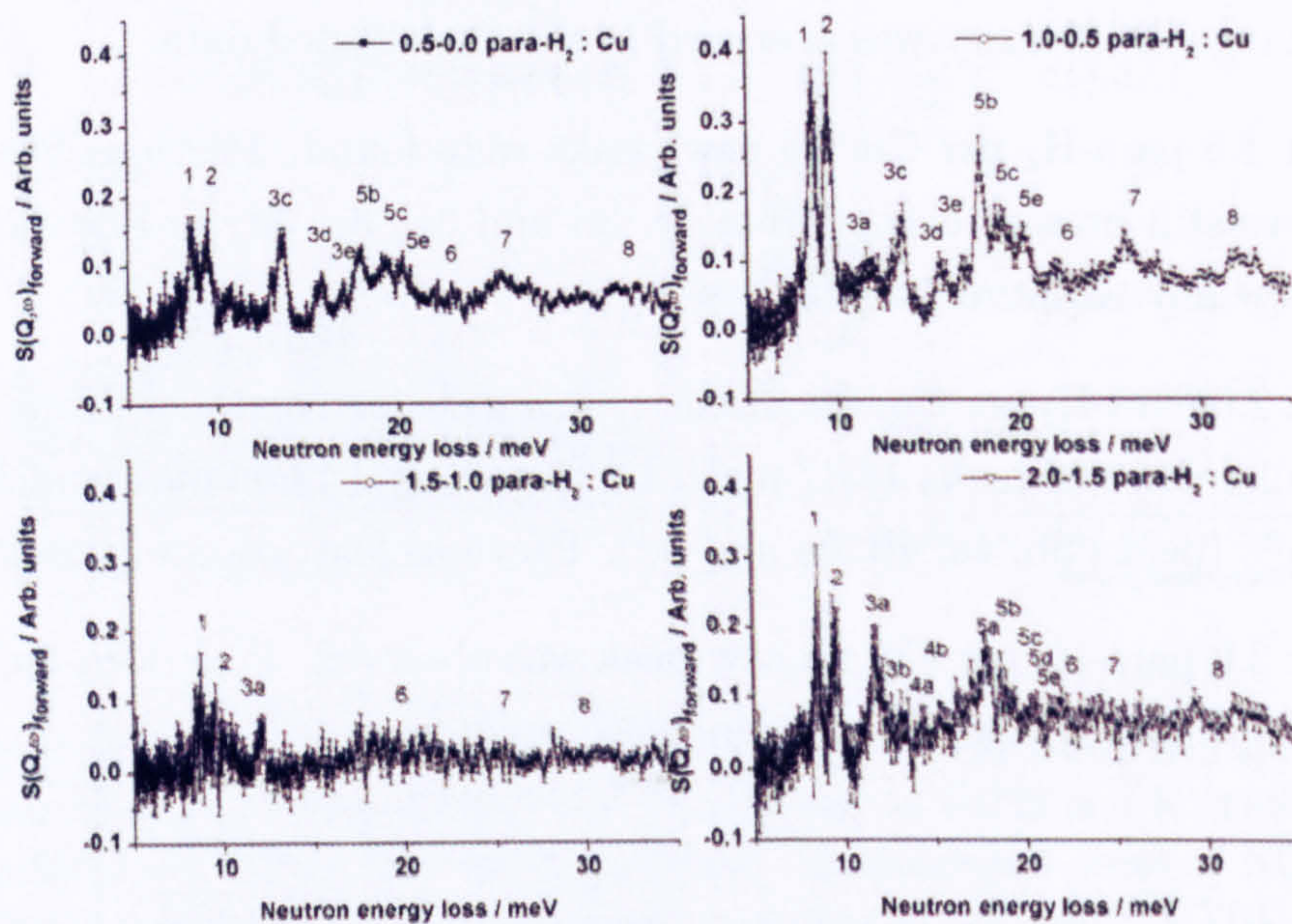


Figure 5.19: $S(Q, \omega)_{forward}$ of the difference INS spectra obtained for two subsequent para- H_2 gas loadings per Cu site for NOTT-102 collected at 4 K on TOSCA. Error bars are represented.

Combining the INS spectra with the NPD results collected on GEM, each INS feature from Figures 5.21 was assigned to the interaction of molecular para- H_2 with the corresponding adsorption site populated. In order to identify the contribution of each adsorption site, it was assumed that the relative intensities of INS features are proportional to the site occupancies so that:

- Peak 1, 2, 5b, 5c, 5e, 6, and 7 are related to the para- H_2 molecules adsorbed onto the copper site A_2 as their intensities seem to follow the occupancy of site A_2 .
- Peak 3c, 3d and 3e seem to only appear at 0.5 and 1.0 para- H_2 per Cu and therefore, could not be assigned to any particular site since the NPD work did not reveal any site following the same behaviour.
- Peak 3a corresponds to para- H_2 molecules populating site B_2 which start being populated at 1.0 para- H_2 per Cu.

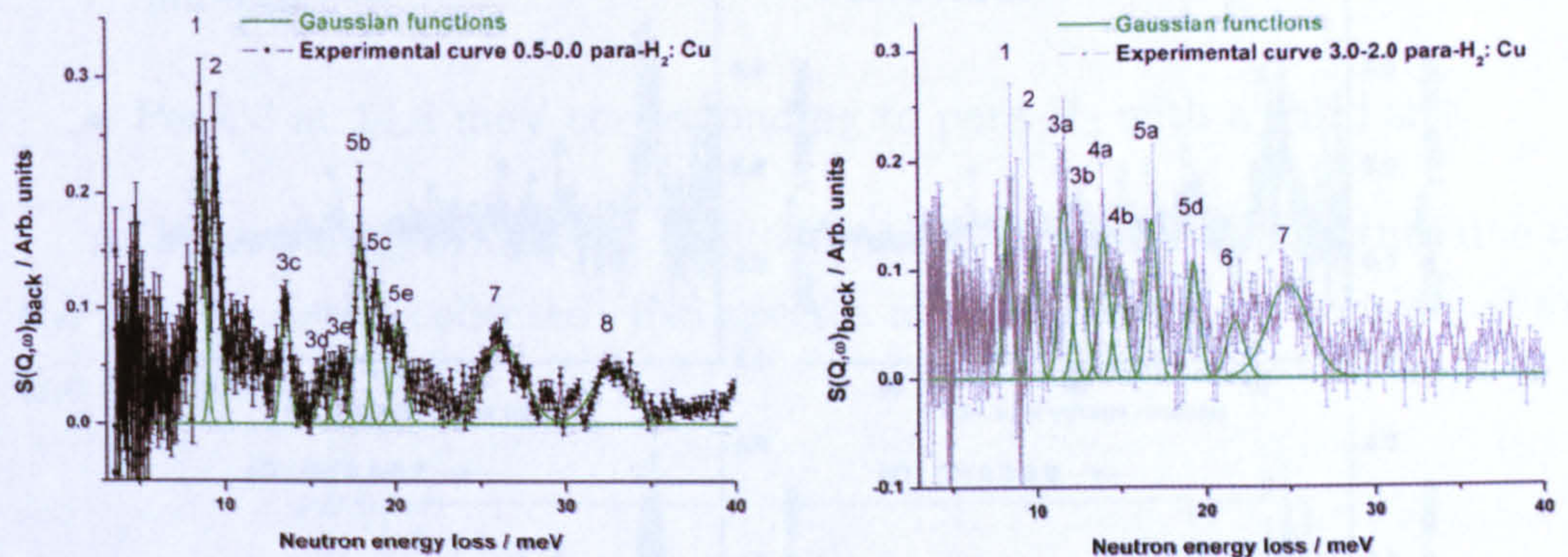


Figure 5.20: Peak deconvolution for NOTT-102 spectrum from the $S(Q, \omega)_{back}$ of 0.5-0.0 and 3.0-2.0 para- H_2 loadings collected on TOSCA at 4 K. Baseline was subtracted. Error bars are represented.

- Peak 3b, 4a, 4b, 5a and 5d correspond to para- H_2 molecules populating site C_2 which starts being occupied at 2.0 para- H_2 per Cu.

At higher energy transfer, it was not possible to identify and assign more INS features. Similar difference INS spectra for NOTT-102 obtained from two subsequent HD dosings are also reported in Figure 5.21. The difference INS spectra with HD loadings show a worse signal to noise ratio than those obtained with para- H_2 gas loadings even though more sample was used. Given the poorer statistics, it was only possible to deconvolute the INS features from the difference spectra 0.5-0.0 and 1.0-0.5 HD per Cu:

- At 0.5 HD per Cu, INS peaks were found at 8.39 meV, 9.10 meV, 13.24 meV, 15.73 meV, 17.14 meV, 20.16 meV and 28.23 meV (peak 1, 2, 3, 4, 5, 6, 7 and 8).
- At 1.0 HD per Cu, new peaks occurred at 33.31 meV and 35.42 meV (peak 9 and 10).

The difference between the spectrum collected at 0.5 HD and the gas free spectrum reveals INS features corresponding to HD molecules adsorbed onto the copper site A_2 as suggested by the NPD work (Figure 5.22) *i.e.*: peak 1, 2, 3, 4, 5, 6, 7, 8. The difference INS spectra 1.0 – 0.5 also showed the two extra peaks at 33.31 meV (peak 9) and 35.42 meV (peak 10) which can be assigned to HD molecules adsorbed on B_2 .

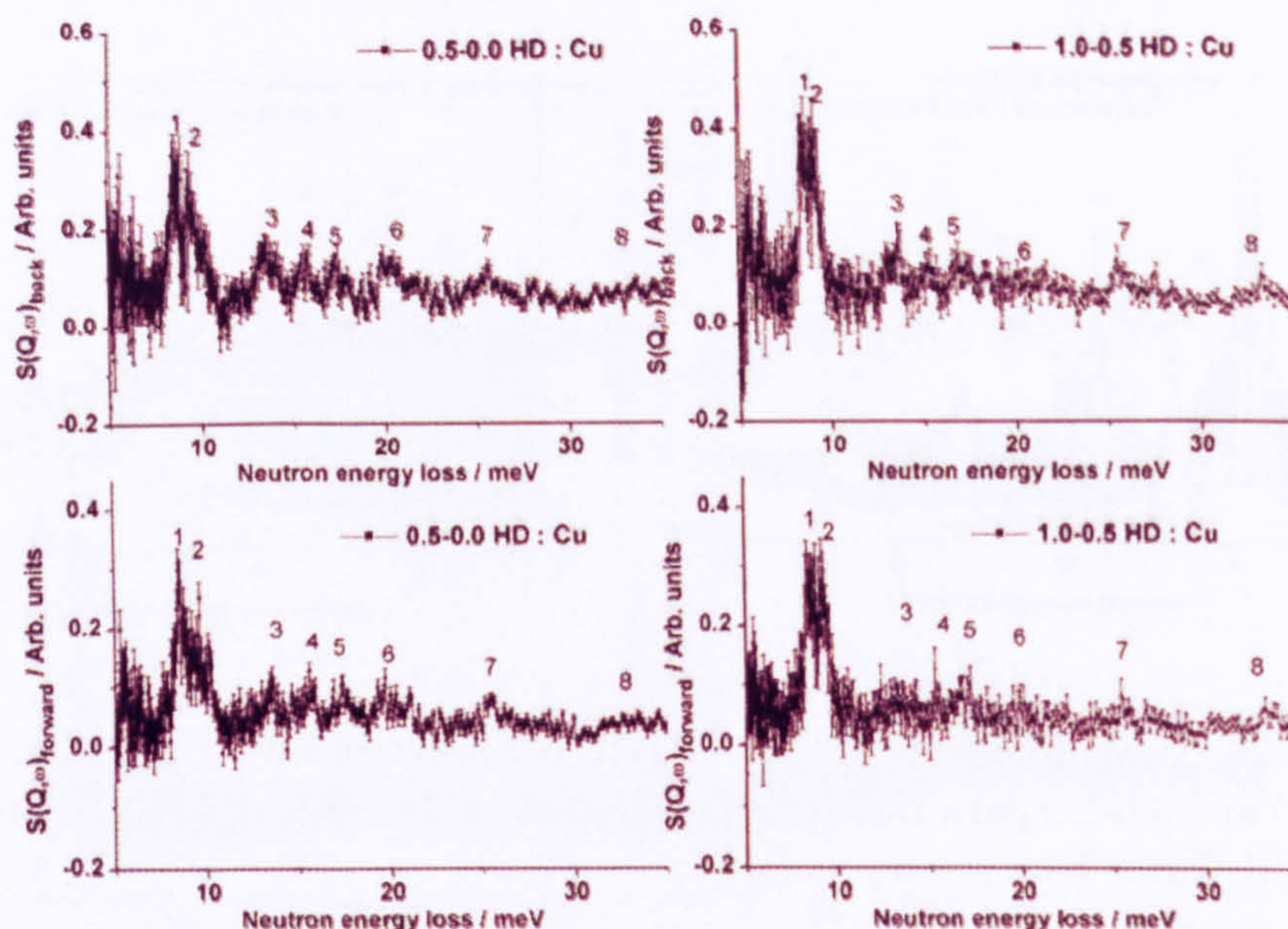


Figure 5.21: $S(Q, \omega)_{back}$ and $S(Q, \omega)_{forward}$ of the difference INS spectra between two subsequent HD gas loadings per Cu site for NOTT-102 collected at 4 K on TOSCA. Error bars also represented.

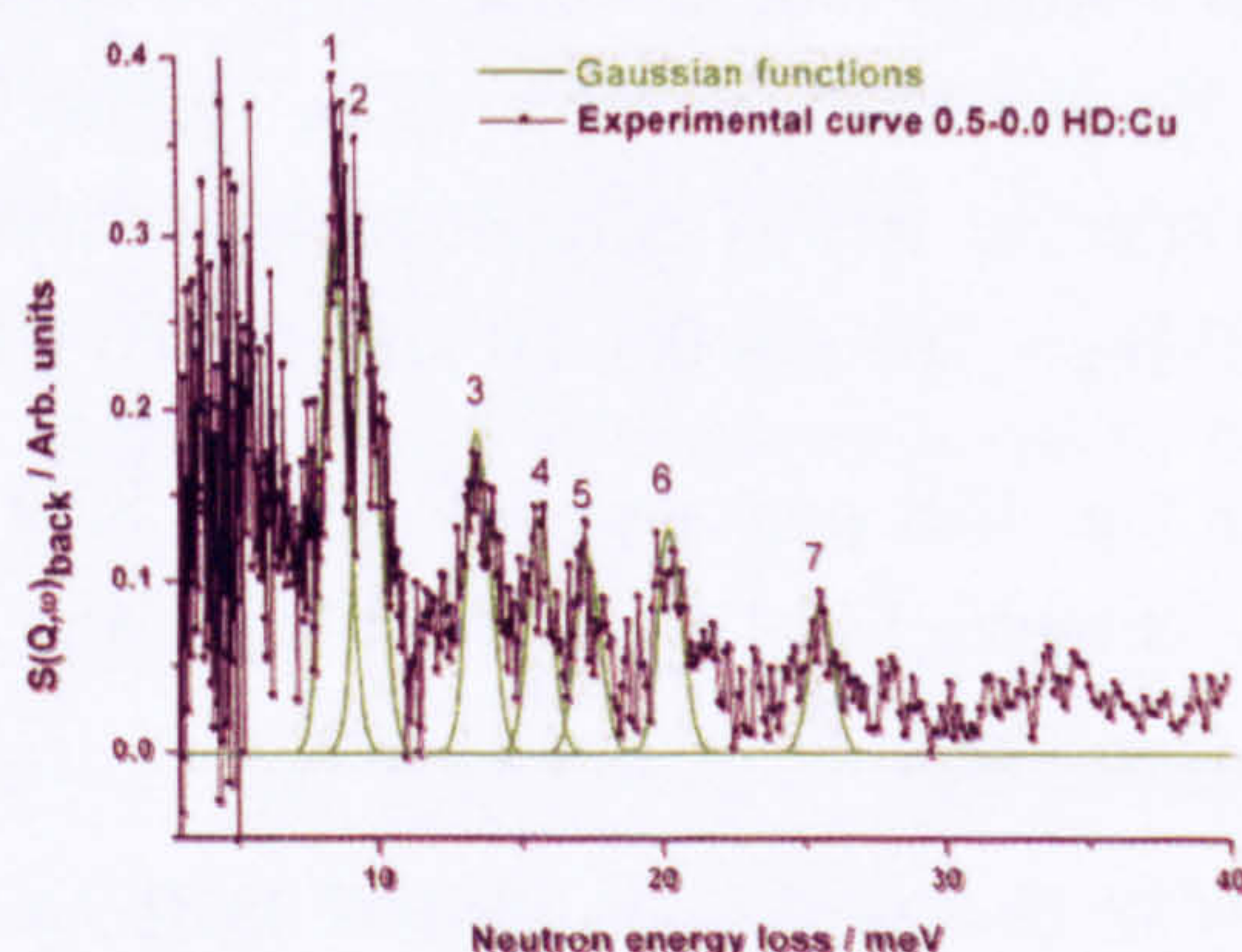


Figure 5.22: Peak deconvolution of NOTT-102 spectrum from the $S(Q, \omega)_{back}$ of 0.5-0.0 HD loadings collected on TOSCA at 4 K. Error bars are represented.

Figure 5.23 shows the INS spectra for HKUST-1 collected on FANS at 4 K. The sequence of peaks is similar to that obtained for NOTT-101 with:

- Peak 1 at 9.2 meV assigned to para- H_2 interacting with the site A_2 .

- Peak 2 at 12.9 meV corresponding to para-H₂ interacting with a second site.
- Peak 3 at 14.8 meV corresponding to para-H₂ with a third site.

At lower energy transfer it is difficult to identify any INS feature due to the poor statistics collected. INS spectra at 1.5 HD were not considered for the analysis.

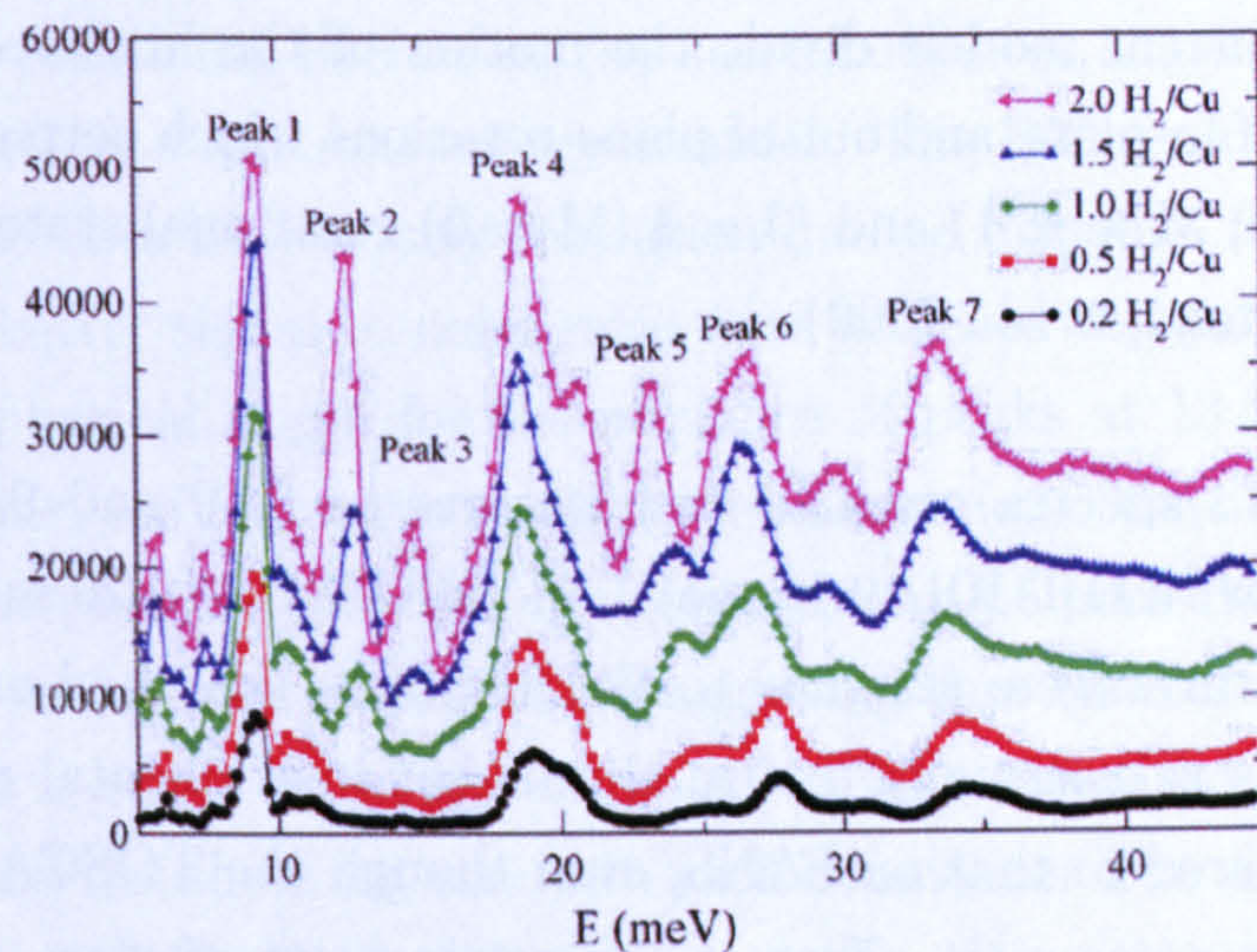


Figure 5.23: INS spectra for HKUST-1 on FANS with various amount of para-H₂ gas. Data were collected at 4 K. The bare material spectrum was subtracted from each spectrum. Error bars are smaller than the symbols (Liu et al., 2007b).

The hydrogen molecule was treated according to the Young and Koppel model and considered as a rigid rotor (Young and Koppel, 1964). This means that the H-H (D-D / H-D) distance is constant which is consistent with IR results reported by Bordiga *et al.* showing a small shift of the H-H bond stretch (Bordiga et al., 2007). Early neutron work on MOF-5 suggested yet a variation of the rotational constant B although this has not been proved so far (Rosi et al., 2003). More recent work also suggests similar variation of the rotational constant B (Ramirez-Cuesta et al., 2007a,b). In solid hydrogen, H₂ molecules are free to rotate due to weak intermolecular interactions. The anisotropy and the symmetry of the external potential corresponding to an adsorption site can lift the degeneracy of unperturbed J rotational energy levels. In the present case, for a para-H₂ manifold, the J level of interest is $J=1$ which would lead to two energy levels $M = 0$ and

5. METAL-ORGANIC FRAMEWORKS

$M = \pm 1$. For example, for a rotational transition, one would expect a peak shifted at lower energy transfer and its complementary peak at higher energy transfer. The split between these new energy levels depends on the nature of the adsorption potential. In an isotropic potential the rotational J energy levels are also perturbed, but the original degeneracy is preserved which implies a shift of the corresponding INS peak on the left side of the 14.7 meV free rotor line. Physically, an adsorption site simply hinders the rotations of the H_2 molecule either in or out-of plane rotation in the simplest case. Current models divide the motion of the hindered rotor as a combination of in-plane and out-of plane rotations which correspond to the H_2 in a ($J = 1, M = \pm 1$) and ($J = 1, M = 0$) rotational states (Brunauer et al., 1938, Brown et al., 2000).

NOTT-102 INS spectra revealed two features at 8.55 and 9.45 meV instead of one for NOTT-101 (9.11 meV) and HKUST-1 (9.20 meV) spectra. These INS features were assigned to the hydrogen adsorbed onto the copper sites. This is essentially due to the higher instrumental resolution of TOSCA compared to that on FANS, even though the TOSCA data had a worse signal to noise ratio. From a geometric point of view, site A_1 and A_2 are equivalent and should therefore, lead to a similar sequence of INS peaks. This is consistent with the FWHM of the NOTT-101 peak 1 which was significantly larger than HKUST-1 peak 1 (*ca.* 2.1 meV and 1.4 meV respectively) and than the actual instrument resolution achievable on FANS (*ca.* 1.2 meV). Sites B_1 and B_2 also offer a very similar environment for H_2 molecules therefore, one would expect very close INS features. This is also consistent with the INS spectra as site B_1 was related to a single peak at 12.21 meV while two peaks were accounted for the B_2 site, at 11.94 meV and 13.32 meV. The FWHM of NOTT-101 peak at 12.21 meV is close to the instrumental resolution achievable on FANS *ca.* 1.5 meV and 1.3 meV respectively suggesting that it can be deconvoluted as a single feature. The third sites were assigned to two peaks at 14.22 meV and 16.82 meV for site C_1 and to three peaks at 12.51 meV, 13.95 meV, 16.93 meV and 19.32 meV for site C_2 . NOTT-101 peak at 14.22 meV shows a FWHM slightly higher than the instrumental resolution (*ca.* 1.9 meV and 1.4 meV respectively). This is consistent with the INS work as there was no NOTT-101 INS peak

decreasing in intensity. In essence, the adsorption site distributions and the filling order for NOTT-101 and NOTT-102 were found to be nearly identical. Moreover, the position of the rotational lines for each samples were different suggesting that the interaction potentials experienced by hydrogen molecules were also different. The ligands used for NOTT-101 and NOTT-102 were found to have little effect upon the adsorption site distribution and the filling order. Also this work showed that the H_2 interaction with the copper site remained unchanged. Instead the length of the ligand only affected the rotational barrier of the secondary sites since the rotational lines appeared at a different energy transfer. The INS peak deconvolution for the FANS data is obviously resolution limited although faster data collection and better signal to noise ratio were achieved compared to TOSCA data. The physical origin for the sequence of peaks at 13.51 meV, 15.73 meV and 16.96 meV remains unclear. It was assumed that these were not related to the para- H_2 adsorbed onto site A_2 . At 1.5 para- H_2 per Cu, these peaks seem to saturate in intensity suggesting that the corresponding adsorption site is either no longer occupied or fully saturated. However, the NPD work did not show any site with such behaviour. The as-collected INS spectra (Figure 5.13) showed that these peaks do not disappear and were not present on the gas free spectrum.

According to the current model, an INS feature at low energy transfer associated to a second peak at higher energy transfer can be treated as $(J = 1, M = \pm 1) \leftarrow (J = 0, M = 0)$ and $(J = 1, M = 0) \leftarrow (J = 0, M = 0)$ rotational transitions. In the case of lift of degeneracy of the $(J = 1, M = \pm 1)$ energy level, this can lead to a doublet and could be a possible explanation for the doublet centred around 10 meV observed on the TOSCA data although this has not been proved, and only observed with zeolites samples (Ramirez-Cuesta et al., 2007b). Given the present data, this model is the simplest explanation without introducing a zero-point energy argument (Mitchell *et al.*, 2004) as used by FitzGerald *et al.* (FitzGerald et al., 1999). A recent neutron investigation on HKUST-1 combined with DFT calculations assigned the INS peak corresponding to the copper site at low energy transfer to $(J = 1, M = \pm 1) \leftarrow (J = 0, M = 0)$ rotational transition suggesting also that it was not possible to witness its complementary fea-

5. METAL-ORGANIC FRAMEWORKS

ture corresponding to the rotational transition ($J = 1, M = 0$) \leftarrow ($J = 0, M = 0$) given the range of energy transfer available on FANS (Brown et al., 2009). For all samples, the sequence of peaks at higher energy transfer *ca.* 25 meV is not well resolved and was not considered any further. This is a real challenge to find ways to allowing higher rotational transitions. For comparison, Georgiev *et al.* found one INS feature very close to that for free rotor at 14.7 meV from para- H_2 manifold adsorbed onto an activated carbon sample. They concluded on a 2D planar rotor behaviour of the H_2 molecule although a complete mixing of the $J = 1$ rotational states. An earlier study reported on SWCNTs also showed a similar INS feature observed at 14.5 meV using para- H_2 loadings and concluding on weak hindrance of the hydrogen molecule (Georgiev et al., 2004, 2005, 2006a,b). This shows that MOFs in general do not exhibit the same interaction potential as activated carbon samples and SWCNTs / MWCNTs since the NOTT-100 INS rotational lines have been shifted from 14.7 meV.

Intriguingly one can notice the increase of the overall background with the para- H_2 gas loading which is more obvious for NOTT-101 and NOTT-102 spectra than for those obtained for HKUST-1. This is due to the non-site specific adsorption of para- H_2 i.e.: where para- H_2 molecules are randomly adsorbed through the pores. This is in agreement with the NPD results shown earlier (i.e.: the occupancy of specific sites did not account for all the D_2) and corresponds to the increased molecular recoil with dosing in the INS data. This could be explained by the BET SSA of the NOTT series around $2900 \text{ m}^2.\text{g}^{-1}$ higher than that for HKUST-1 *ca.* $1532 \text{ m}^2.\text{g}^{-1}$ which offers more non-site specific adsorption. The peak at 14.74 meV accounts for the freely rotating para- H_2 molecules. As the strong sites were already populated the remaining H_2 molecules were adsorbed onto non-sites specific locations.

The second series of experiments with HD gas loadings were more complicated than expected. HD molecule is an asymmetric molecule with a rotational constant different from that of the hydrogen molecule depending on whether the centre of the bond or the centre of gravity of the molecule is considered. Therefore, a pure rotational line is expected to occur at 75%

and 66% respectively of the energy loss value for the free rotor. At 0.5 para-H₂ per Cu we assumed that the NOTT-102 INS doublet around 9 meV was due to the rotational transitions. However, at similar HD coverage, the strongest peak was a similar doublet centred at 9 meV which did not correspond to any of the peaks found in the para-H₂ study. Also there was a doublet or singlet peak observed around 6 meV. At higher loading the quality of the data was rather poor to undertake the analysis. A second series of experiments with longer collection time is needed. Only a few investigations successfully reported on the shift of the pure rotational line using para-H₂ and HD gas (Ulivi et al., 2007).

Let us now compare NOTT-100 series and HKUST-1 sorption properties. D₂ gas loadings on NOTT-101 and NOTT-102 were done up to 2.52 and 5 molecules of D₂ per Cu site at 50 K respectively which is equivalent to a pressure up to 0.94 bar and 2.28 bar respectively (for the 77 K isotherm). Each spherical cage within HKUST-1 contains twelve Cu sites, a greater concentration of these Cu sites than for the NOTT samples with only six similar Cu sites within a spherical cage. This could explain the higher hydrogen uptake of HKUST-1 compared to NOTT-101 and NOTT-102 at low coverage (respectively below 0.23 and 0.46 bar, as shown in Figures 5.31 and 5.32). NOTT-100 hydrogen uptakes are always higher than HKUST-1 although the cage structure is similar to NOTT-101 and NOTT-102. This may imply different behaviour for the same active site distributions due to a smaller cage topology. A successful NPD experiment on NOTT-100 would allow a direct comparison of the site occupancies between NOTT-100 and HKUST-1 at various coverage of the surface. NPD and INS results for NOTT samples showed different sorption behaviour from HKUST-1 in which the Cu (II) sorption sites were fully occupied at a loading of 2.0 D₂ per Cu site. In NOTT-101 however at 1.68 D₂ and 2.52 D₂ per Cu site, the fractional occupancy was respectively 72% and 80% with sites B₁ and C₁ starting to be populated. The same filling order was observed with NOTT-102 and site B₂ and C₂ occupied without saturating the copper sites. This suggests that the secondary sites in HKUST-1 do not compete with the Cu (II) sites as effectively as sites B_{1,2} and C_{1,2} in NOTT-101 and NOTT-102. The Cu-D₂ distance on all the samples was similar which also suggests a

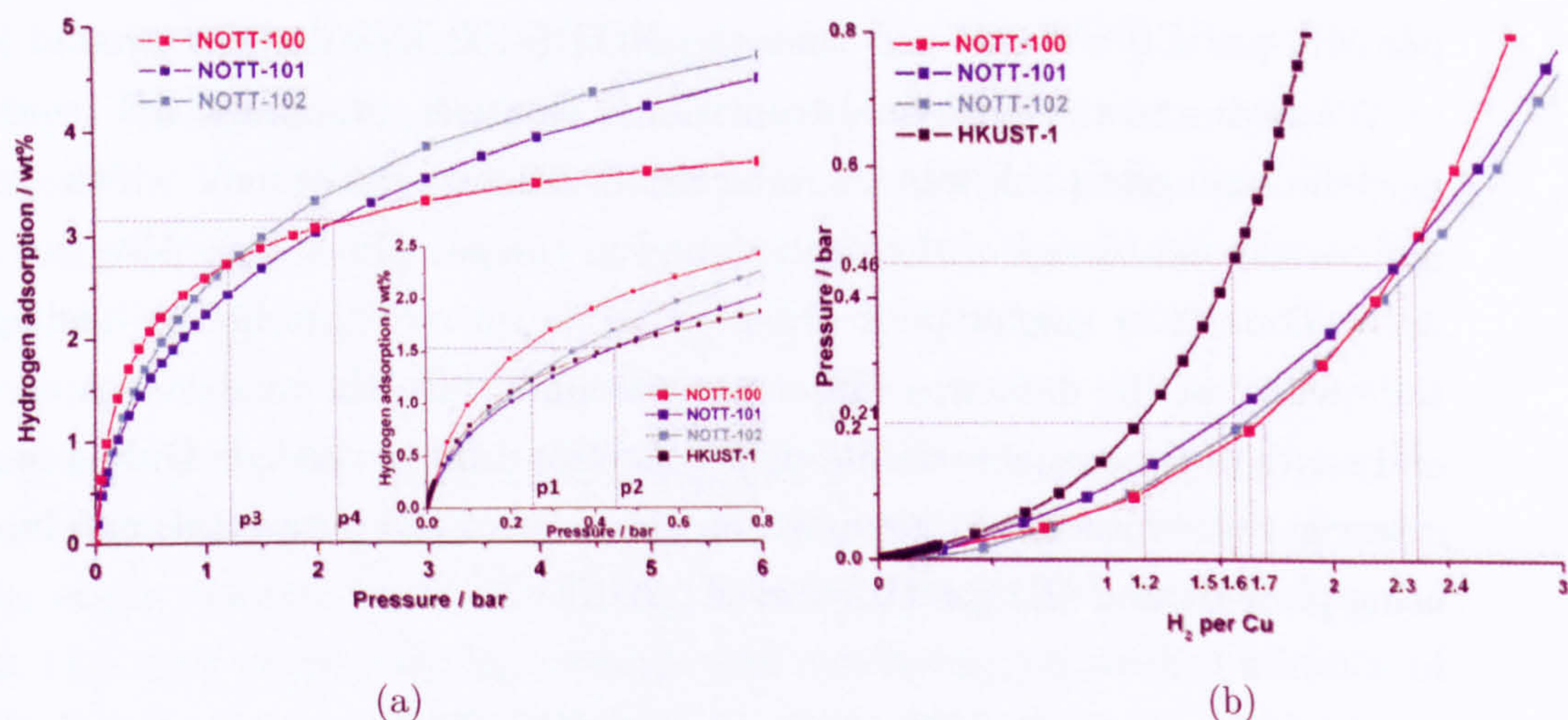


Figure 5.24: a) NOTT-100, NOTT-101, NOTT-102 isotherms at 77 K using the IGA-003. Inset represents the lower pressure region of the isotherm ($p < 0.8$ bar). b) Conversion curves pressure / hydrogen weight uptake for NOTT-100, NOTT-101, and NOTT-102 within the low pressure region ($p < 0.8$ bar). HKUST-1 data reproduced from (Peterson et al., 2006). NOTT data reproduced from (Lin et al., 2006b).

similar strength of adsorption interaction to Cu (II) in the NOTT-100 series and HKUST-1. The Figure 5.24.a represents the isotherms of each Cu (II) - frameworks identifying 4 pressures of interest. Figure 5.24.b shows the same data but displaying the hydrogen uptake per mole of Cu sites.

- For $p < p_1$ excess hydrogen weight uptakes are as follows: NOTT-101 < NOTT-102 < HKUST-1 < NOTT-100. This region limited by initial loadings between 0 and 1.5 H₂ per Cu for NOTT-101 and 0 and 1.2 H₂ per Cu for HKUST-1. At $p = p_1$ for the NOTT-100 series, sites **A**_{1,2}, **B**_{1,2}, and **C**_{1,2} are already populated but not fully occupied. At this coverage, NOTT-100 store more hydrogen molecules than HKUST-1, NOTT-101, and NOTT-102. In other words, this also means that above 1.5 H₂ per Cu, NOTT-101 will store more H₂ than HKUST-1.
- For $p_1 < p < p_2$ the order of hydrogen capacity is NOTT-102 < HKUST-1 < NOTT-101 < NOTT-100. NOTT-101 and NOTT-100 have higher excess hydrogen uptake than HKUST-1 while NOTT-102 capacity is still lower. This region covers loadings from 1.6 to 2.4 H₂

per Cu for NOTT-102 and from 1.2 to 1.6 H₂ per Cu for HKUST-1. At $p = p_2$ or 2.4 and 1.6 H₂ per Cu for NOTT-102 and HKUST-1, NOTT-102 will store more H₂ than HKUST-1.

- For $p_2 < p < p_3$ the order of hydrogen capacity is HKUST-1 < NOTT-102 < NOTT-101 < NOTT-100. Now HKUST-1 capacity is lower than for the NOTT-100 series. At $p = p_3$ or 3.7 H₂ per Cu, NOTT-101 will store more H₂ than NOTT-100.
- For $p_3 < p < p_4$ the order of hydrogen capacity is HKUST-1 < NOTT-102 < NOTT-100 < NOTT-101. NOTT-100 shows less than NOTT-101 but it is still higher than NOTT-102. At $p = p_4$ or 4.9 H₂ per Cu, NOTT-102 will store more H₂ than NOTT-100. For $p_4 < p$ the order of hydrogen capacity is HKUST-1 < NOTT-100 < NOTT-102 < NOTT-101. NOTT-101 and NOTT-102 are now higher than NOTT-100.

Essentially for $p_4 < p$ the sorption dynamic of the Cu (II) - frameworks is ruled by the distribution of specific adsorption sites **A**_{1,2}, **B**_{1,2}, and **C**_{1,2} but also by the cage topology. At higher coverage, it is mainly the specific surface area that is responsible for the hydrogen uptakes with a linear effect upon the hydrogen capacity. However, it would be interesting to optimize the elliptical cage into smaller pockets where randomly distributed H₂ molecules could be adsorbed onto the surface. The second type of cage within HKUST-1 is probably a too small volume leading to a low BET surface area available *ca.* 1532 m².g⁻¹ which is significantly less than that of NOTT-101.

Being able to identify and characterize hydrogen adsorption sites is essential for hydrogen storage applications as this will help to design compounds with the desired structure to maximise the hydrogen capacities. This study has identified the site distribution within Cu (II) – framework materials. The dynamics of the H₂ molecule with its local environment is still not clearly defined and the theory need to be further refined. This study has also compared earlier neutron studies on a similar Cu (II) - framework which helped to understand the importance of the distribution of sorption sites for such

compounds, the importance of specific adsorption sites at low loadings and non-specific site sorption on the general pore walls at higher loadings. This information will help aid the design of MOFs for hydrogen storage applications. For example, at low pressures ($p < 0.04$ bar at 77K) (Figure 5.24.b), H_2 molecules directly interacted with the coordinatively unsaturated copper sites. It was also found that the secondary adsorption sites within NOTT-101, and NOTT-102 were occupied earlier than within HKUST-1 as the Rietveld analysis of the two studies concluded. One can notice that the secondary sites are all located within triangular windows formed by copper paddle-wheel units and connecting the two types of cages. It would still be interesting to minimize the pore size within the NOTT-101 and NOTT-102 elliptical cage to 7 Å in an attempt to achieve a smaller pore size, but with similar surface area and create more favourable sorption properties.

5.5 Conclusions

NPD and INS techniques were combined in order to understand interactions of H_2 molecules adsorbed on NOTT-101 and NOTT-102. For both samples, a similar adsorption site distribution was found with up to four adsorption sites identified: the Cu (II) co-ordination site was the first one populated hindering the rotations of H_2 molecules. The Cu- D_2 distances were found around 2.5 Å which is consistent with the literature. Two other sites $B_{1,2}$ and $C_{1,2}$ were identified. Although $B_{1,2}$ were very close, they did not have the same effect on H_2 molecules as corresponding rotational lines were observed at different energy transfer suggesting different rotational barriers. Similar conclusion can be drawn for sites $C_{1,2}$. The ligand was found to have little effect upon the adsorption site distribution and the filling order. Also this work showed that the H_2 interaction with the copper site was remained unchanged. Instead the length of the ligand only affected the rotational barrier of the secondary sites.

Chapter 6

Summary and Conclusions

This last chapter summarizes strengths and weaknesses of GNFs and MOFs investigated in this work as solid state hydrogen storage media. It highlights main results from engineering options tested on GNF samples to enhance hydrogen interactions and the neutron work on Cu (II) - MOF. The future work to be done for each type of material will be suggested in order to achieve the hydrogen economy.

6.1 Pore Size

GNF samples were successfully synthesized using CVD method but revealed a very broad pore size distribution and a low crystallinity as shown by BET, TEM and XRPD analysis. The CVD technique using a floating catalyst does not allow any flexibility regarding the design pore size distribution around 7 Å. Instead, we observed an unusual serrated surface with smaller slit pores along the surface. It was not possible to identify the origin of the slits created. Therefore, being able to tune the GNF pore size remains a very difficult task. Carbon templates using CVD method have proved to be successful (Yang et al., 2005b) and could be an interesting option which would overcome this problem, as they can reproduce the framework structure of the initial host. MOFs are highly crystalline compounds and offer a more flexible range of structures thanks to the wide variety of metal clusters and organic ligands that can be combined. This represents an easier option compared to a post-synthesis treatment. The topology of the cage

6. SUMMARY AND CONCLUSIONS

is important as small cages are expected to be populated first and interact more with hydrogen molecules. In fact, our neutron investigation confirmed that only a fraction of the elliptical cage was used during physisorption and that the connection between the spherical and elliptical cages was essential. It was shown that the hydrogen was preferentially adsorbed within triangular windows formed by three copper paddle-wheels units connected by the carboxylate groups. This raises the issue of the hydrogen diffusion path through the pores. It is important to identify and understand hydrogen diffusion paths in order to improve the hydrogen dynamics within the pores to access adsorption sites.

6.2 Specific Surface Area

Exfoliation experiments on GNFs did not show any significant improvement of the surface area. The expansion of the graphitic interlayer after thermal shock relied on a successful intercalation of hetero-species within the graphitic layers. This method required highly crystalline and homogeneous samples which was not the case for the as-prepared GNFs. However, the newly created slit pores within the serrated surface of the GNFs could be exploited if one can control the parameters responsible for the surface topology. Earlier work showed that the surface area available played a significant role only at high coverage of the surface. This was often shown as a linear relationship between the surface area and the sorption properties. In particular, earlier neutron work showed that on a type I isotherm, the plateau of the adsorption/desorption curve at high coverage of the surface was driven by the physisorption on the surface area available. Our neutron work on NOTT samples showed that the surface area available favours the presence of non-specific adsorption sites where weak physisorption occurs. The specific surface area is also correlated to the apparent density of the material in that high surface area materials have lower apparent densities. This is a clear advantage in terms of gravimetric capacity although it would lower the volumetric capacity.

6.3 Adsorption Site Distribution

N-doping experiments on GNFs aimed at changing the local electronic structure of the carbon network in order to enhance the hydrogen interactions. However, the N-doped GNFs did not show any significant improvements of the sorption properties. This was probably due to the nature of the organic precursor. Our neutron work combining neutron powder diffraction and inelastic neutron scattering techniques confirmed the existence of specific adsorption sites within NOTT-101 and NOTT-102. In particular the presence coordinatively unsaturated copper centres explained the adsorption mechanism at low coverage of the surface. It was also shown that for these NOTT samples, secondary sites close to the organic ligand were also able to compete with the copper sites. In fact it is the distribution of specific sites within the cage that rules the H_2 adsorption/desorption process. Once the specific sites are being occupied, the surface area allows the hydrogen molecule to be physisorbed via non-site specific adsorption.

6.4 Conclusions

Herein, we reported on the successful preparation of a series of GNFs using the CVD method combined with two catalyst precursors. The sorption investigation of the as-prepared materials revealed low hydrogen capacity which is consistent with the reported value. TEM images showed the presence of GNF with unusual serrated surfaces although the BET surface area was still low typically of the order of $50 \text{ m}^2.\text{g}^{-1}$. The N-doping growth using an organic precursor composed of ethene and / or amines successfully produced N-doped GNFs which were composed of a heterogeneous mixture of platelet and herringbone type GNFs with up to 4 % N doping level. Gravimetric sorption investigations did not report any significant improvement of the hydrogen capacity compared to the as-prepared GNFs. The second experimental option was to increase the surface area by expanding the graphitic interlayer after rapid thermal degas. The exfoliation of the GNFs relied on the ionic intercalation of the graphitic planes and on the stability of the ion free carbon structure after heat treatment. The presence of different types of less ordered GNFs for the starting material

6. SUMMARY AND CONCLUSIONS

most likely hindered the ionic intercalation. The surface area of the intercalated/exfoliated GNFs increased by one order of magnitude compared to the as-prepared GNFs. However, these improvements only correlated with modest improvements in the hydrogen capacity *ca.* 0.6 wt.% at 77 K and 20 bar. The engineering routes attempted for this research project to enhance the hydrogen capacity of carbon nanostructures did not lead to any significant improvement compared to as-prepared samples, although exfoliated compounds exhibited higher BET surface areas.

A series of MOF materials were successfully investigated combining NPD and INS techniques. In order to improve these potential candidates for solid state hydrogen storage, it was essential to locate hydrogen adsorption sites and characterise the behaviour of adsorbed molecular hydrogen. The NPD work showed adsorption on specific sites with a similar filling order for NOTT-101 (A_1 , B_1 , and C_1) and NOTT-102 (A_2 , B_2 , and C_2) with the Cu site as the first site populated with a Cu-D₂ distance close to 2.5 Å. During the refinement, the fractional occupancy of each site showed that part of the hydrogen molecules was adsorbed onto non-specific sites as opposed to sites $A_{1,2}$, $B_{1,2}$, and $C_{1,2}$ but also that sites $B_{1,2}$, and $C_{1,2}$ before sites $A_{1,2}$, were fully occupied. We showed the importance of the coordinatively unsaturated metal centres but also the existence of other specific sites close to the organic ligand and capable of competing with the metal centres which is in agreement with the molecular recoil witnessed by INS study. The NPD work showed that the adsorption site distribution and the filling order were independent of the organic ligand. This was not reflected by the INS analysis which showed that similar secondary sites (*e.g.*: B_1 and B_2) exhibited different rotational barriers. It suggested that similar rotational barriers were only found for the Cu sites which is consistent with their isosteric heat of adsorption in the zero-pressure limit as reported in the literature. The NPD and INS work confirmed that the adsorption mechanism is not uniform with the existence of discrete adsorption site. It also showed that hydrogen molecules adsorbed onto non-specific sites were different from free hydrogen molecules in the solid phase. Neutron data were successfully collected at low coverage of the surface, highlighting the role of the strongest sites. It was not possible to apply similar methods to investigate the role

of the surface area upon the sorption properties although most of the work reported on the subject in the literature assumed a uniform behaviour of the hydrogen molecule on the surface.

In this work, we emphasized the importance of highly crystalline and homogenous materials for solid state hydrogen storage. The distribution of specific adsorption sites combined with the pore size are two key parameters responsible for favourable sorption properties. MOFs exhibit these primary characteristics. This work also confirmed that MOFs with coordinatively unsaturated metal centres are very promising materials for hydrogen storage applications.

6.5 Future Work

From an adsorbent point of view, carbon based materials reported in this work were cost efficient and relatively easy to synthesize. Although high yields were obtained, GNFs produced showed low crystallinity and were heterogeneous which dramatically affected the behaviour of the sample required during doping and exfoliation/intercalation experiments. Carbon templates are exciting candidates for solid state hydrogen storage as they combine the host-structure framework of the zeolites template and the low gravimetric density of the carbon materials (Yang et al., 2005a). One of the main advantages of these materials is the flexibility of the size and the shape of the pore replicated.

The neutron investigation on NOTT-101 and NOTT-102 confirmed the co-existence of site specific (strong) and non-site specific (weak) adsorption sites for molecular hydrogen, showing that the adsorption site distribution is not necessarily uniform like a homogeneous surface but can be discrete with preferential adsorption sites such as coordinatively unsaturated metal centres. In fact, it was seen that it is the combination of the site distribution, the high surface area and the pore size that improved the physisorption properties. Lately, another Cu (II) - framework NOTT-112 showed exceptional sorption properties at 77 K and 20 bar (Yan et al., 2009) with asymmetric Cu sites. It combined the high surface area of the NOTT-100

6. SUMMARY AND CONCLUSIONS

samples and the Cu site distribution of HKUST-1. From a characterisation point of view, we saw throughout our INS work that current models do not provide a general scattering law for adsorbed H_2 molecule. Therefore, theoretical work is required to fully understand the behaviour of adsorbed hydrogen molecules. For instance, one will have to generalize the scattering law from the well known Young and Koppel's model for any interaction potential including rotation-vibration coupling close to an adsorption site. Density functional theory calculations and semi-empirical methods are currently being combined to test and validate different models (Brown et al., 2009, Colognesi et al., 2009).

Bibliography

I. Alstrup. A new model explaining carbon-filament growth on nickel, iron, and ni-cu alloy catalysts. *Journal of Catalysis*, 109(2):241–251, 1988.

Gary Attard and Colin Barnes. *Surfaces*. Oxford chemistry primers. Oxford University Press, Oxford, 1998.

A. Badzian, T. Badzian, E. Breval, and A. Piotrowski. Nanostructured, nitrogen-doped carbon materials for hydrogen storage. *Thin Solid Films*, 398:170–174, 2001.

P. Benard and R. Chahine. Storage of hydrogen by physisorption on carbon and nanostructured materials. *Scripta Materialia*, 56(10):803–808, 2007.

M. J. Benham and D. K. Ross. Experimental-determination of absorption-desorption isotherms by computer-controlled gravimetric analysis. *Zeitschrift Fur Physikalische Chemie Neue Folge*, 163:25–32, 1989.

Alexander J. Blake, Neil R. Champness, Peter Hubberstey, Wan-Sheung Li, Matthew A. Withersby, and Martin Schröder. Inorganic crystal engineering using self-assembly of tailored building-blocks. *Coordination Chemistry Reviews*, 183(1):117–138, 1999.

F. Donald Bloss. *Crystallography and crystal chemistry*. Holt, Rinehart and Winston, New York, 1971.

S. Bordiga, L. Regli, F. Bonino, E. Groppo, C. Lamberti, B. Xiao, P. S. Wheatley, R. E. Morris, and A. Zecchina. Adsorption properties of hkust-1 toward hydrogen and other small molecules monitored by ir. *Physical Chemistry Chemical Physics*, 9(21):2676–2685, 2007.

BIBLIOGRAPHY

- M. Bououdina, D. M. Grant, and G. S. Walker. Synthesis and H_2 adsorption on graphitic nanofibres. *Journal of Alloys and Compounds*, 404:634–636, 2005.
- M. Bououdina, D. Grant, and G. Walker. Review on hydrogen absorbing materials - structure, microstructure, and thermodynamic properties. *International Journal of Hydrogen Energy*, 31(2):177–182, 2006.
- D. P. Broom and P. Moretto. Accuracy in hydrogen sorption measurements. *Journal of Alloys and Compounds*, 446:687–691, 2007.
- E. L. Brosha, J. Davey, F. H. Garzon, and S. Gottesfeld. Irreversible hydrogenation of solid C_{60} with and without catalytic metals. *Journal of Materials Research*, 14(5):2138–2146, 1999.
- C. M. Brown, T. Yildirim, D. A. Neumann, M. J. Heben, T. Gennett, A. C. Dillon, J. L. Alleman, and J. E. Fischer. Quantum rotation of hydrogen in single-wall carbon nanotubes. *Chemical Physics Letters*, 329(3-4):311–316, 2000.
- C. M. Brown, Y. Liu, T. Yildirim, V. K. Peterson, and C. J. Kepert. Hydrogen adsorption in hkust-1: a combined inelastic neutron scattering and first-principles study. *Nanotechnology*, 20(20), 2009.
- S. Brunauer, P. H. Emmett, and E. Teller. Adsorption of gases in multimolecular layers. *Journal of the American Chemical Society*, 60:309–319, 1938.
- S. Brunauer, L. S. Deming, W. E. Deming, and E. Teller. On a theory of the van der waals adsorption of gases. *Journal of the American Chemical Society*, 62:1723–1732, 1940.
- CambridgeCrystallographicDataCentre. Mercury - crystal structure visualisation and exploration made easy, 2008.
- R. Chahine and T.K. Bose. Low pressure adsorption storage of hydrogen. *International Journal of Hydrogen Energy*, 19:3, 1994.
- A. Chambers, C. Park, R. T. K. Baker, and N. M. Rodriguez. Hydrogen storage in graphite nanofibers. *Journal of Physical Chemistry B*, 102(22):4253–4256, 1998.

- J. S. Chang, J. S. Hwang, S. H. Jhung, S. E. Park, G. Ferey, and A. K. Cheetham. Nanoporous metal-containing nickel phosphates: A class of shape-selective catalyst. *Angewandte Chemie-International Edition*, 43(21):2819–2822, 2004.
- B. Chen, D. S. Contreras, N. Ockwig, and O. M. Yaghi. High h_2 adsorption in a microporous metal-organic framework with open-metal sites. *Angew. Chem. Int. Ed.*, 44:4745, 2005.
- P. Chen, X. Wu, J. Lin, and K. L. Tan. High h_2 uptake by alkali-doped carbon nanotubes under ambient pressure and moderate temperatures. *Science*, 285(5424):91–93, 1999.
- H. S. Cheng, A. C. Cooper, G. P. Pez, M. K. Kostov, P. Piotrowski, and S. J. Stuart. Molecular dynamics simulations on the effects of diameter and chirality on hydrogen adsorption in single walled carbon nanotubes. *Journal of Physical Chemistry B*, 109(9):3780–3786, 2005.
- H. C. Choi, J. Park, and B. Kim. Distribution and structure of n atoms in multiwalled carbon nanotubes using variable-energy x-ray photoelectron spectroscopy. *Journal of Physical Chemistry B*, 109(10):4333–4340, 2005.
- Stephen S. Y. Chui, Samuel M. F. Lo, Jonathan P. Charmant, A. Guy Orpen, and Ian D. Williams. A chemically functionalizable nanoporous material $[\text{Cu}_3(\text{tma})_2(\text{H}_2\text{O})_3]_n$. *Science*, 283(5405):1148–1150, 1999.
- Claude Cohen-Tannoudji, Bernard Diu, Franck Laloë, Susan Reid Hemley, Nicole Ostrowsky, and D. B. Ostrowsky. *Quantum mechanics*. Wiley, New York ; London, 1977.
- D. Colognesi, M. Celli, F. Cilloco, R. J. Newport, S. R. Parker, V. Rossi-Albertini, F. Sacchetti, J. Tomkinson, and M. Zoppi. Tosca neutron spectrometer: The final configuration. *Applied Physics a-Materials Science & Processing*, 74:S64–S66, 2002.
- D. Colognesi, F. Formisano, A. J. Ramirez-Cuesta, and L. Ulivi. Lattice dynamics and molecular rotations in solid hydrogen deuteride: Inelastic neutron scattering study. *Physical Review B*, 79(14):–, 2009.

BIBLIOGRAPHY

- D. E. Cox and R. J. Papoular. Structure refinement with synchrotron data: R-factors, errors and significance tests. *European Powder Diffraction: Epdic Iv, Pts 1 and 2*, 228:233–238, 1996.
- CUTE. Cute hydrogen supply infrastructure and fuel cell bus technology. *EvoBus*, Brochure, 2004.
- Krijn P. De Jong and John W. Geus. Carbon nanofibers: catalytic synthesis and applications. *Catalysis Reviews: Science and Engineering*, 42(4):481 – 510, 2000.
- A. C. Dillon and M. J. Heben. Hydrogen storage using carbon adsorbents: past, present and future. *Applied Physics a-Materials Science & Processing*, 72(2):133–142, 2001.
- A. C. Dillon, K. M. Jones, T. A. Bekkedahl, C. H. Kiang, D. S. Bethune, and M. J. Heben. Storage of hydrogen in single-walled carbon nanotubes. *Nature*, 386(6623):377–379, 1997.
- M. Dinca, A. Dailly, Y. Liu, C. M. Brown, D. A. Neumann, and J. R. Long. Hydrogen storage in a microporous metal-organic framework with exposed mn^{2+} coordination sites. *J. Am. Chem. Soc.*, 128(51):16876–16883, 2006.
- Robert E. Dinnebier and Simon J. L. Billinge. *Powder diffraction: theory and practice*. Royal Society of Chemistry, Cambridge, 2008.
- M. Dresselhaus, G. Dresselhaus, P. Eklund, and R. Saito. Carbon nanotubes. *Physics World*, 11(1):33–38, 1998.
- M. S. Dresselhaus. Carbon nanotubes: Discovery, structure, and properties. *Abstracts of Papers of the American Chemical Society*, 218:U249–U249, 1999.
- M. S. Dresselhaus. Nanotubes - a step in synthesis. *Nature Materials*, 3(10):665–666, 2004.
- M. S. Dresselhaus and P. Avouris. Introduction to carbon materials research. *Carbon Nanotubes*, 80:1–9, 2001.

- M. S. Dresselhaus and G. Dresselhaus. Intercalation compounds of graphite. *Advances in Physics*, 51(1), 2002. doi: DOI: 10.1016/0379-6779(82)90047-9.
- M. S. Dresselhaus and M. Endo. Relation of carbon nanotubes to other carbon materials. *Carbon Nanotubes*, 80:11–28, 2001.
- M. S. Dresselhaus, G. Dresselhaus, and R. Saito. C₆₀-related tubules. *Solid State Communications*, 84(1-2):201–205, 1992.
- M. S. Dresselhaus, G. Dresselhaus, and R. Saito. Physics of carbon nanotubes. *Carbon*, 33(7):883–891, 1995.
- M. S. Dresselhaus, K. A. Williams, and P. C. Eklund. Hydrogen adsorption in carbon materials. *Mrs Bulletin*, 24(11):45–50, 1999.
- I. A. S. Edwards. Structure in carbons and carbon forms. In H. Marsh, editor, *Introduction to Carbon Science*. Butterworths, London, 1989.
- EPSRC. Epsrc engineering and physical sciences research council. <http://www.epsrc.ac.uk/default.htm>.
- G. Ferey. Building units design and scale chemistry. *Journal of Solid State Chemistry*, 152(1):37–48, 2000.
- G. Ferey. Microporous solids: From organically templated inorganic skeletons to hybrid frameworks ... ecumenism in chemistry. *Chemistry of Materials*, 13(10):3084–3098, 2001.
- S. A. FitzGerald, T. Yildirim, L. J. Santodonato, D. A. Neumann, J. R. D. Copley, J. J. Rush, and F. Trouw. *Quantum dynamics of interstitial H₂ in solid C₆₀*. PhD thesis, American Physical Society, 1999.
- Anthony Harolde Foderaro. *The elements of neutron interaction theory*. MIT Press, Cambridge, 1971.
- P. A. Georgiev, D. K. Ross, A. De Monte, U. Montaretto-Marullo, R. A. H. Edwards, A. J. Ramirez-Cuesta, and D. Colognesi. Hydrogen site occupancies in single-walled carbon nanotubes studied by inelastic neutron scattering. *Journal of Physics-Condensed Matter*, 16(8):L73–L78, 2004.

BIBLIOGRAPHY

- P. A. Georgiev, D. K. Ross, A. De Monte, U. Montaretto-Marullo, R. A. H. Edwards, A. J. Ramirez-Cuesta, M. A. Adams, and D. Colognesi. *In-situ inelastic neutron scattering studies of the rotational and translational dynamics of molecular hydrogen adsorbed in single-wall carbon nanotubes (SWNTs)*. PhD thesis, 2005.
- P. A. Georgiev, A. Giannasi, D. K. Ross, M. Zoppi, J. L. Sauvajol, and J. Stride. Experimental q-dependence of the rotational $j=0$ -to-1 transition of molecular hydrogen adsorbed in single-wall carbon nanotube bundles. *Chemical Physics*, 328(1-3):318–323, 2006a.
- P. A. Georgiev, D. K. Ross, P. Albers, and A. J. Ramirez-Cuesta. The rotational and translational dynamics of molecular hydrogen physisorbed in activated carbon: A direct probe of microporosity and hydrogen storage performance. *Carbon*, 44(13):2724–2738, 2006b.
- M. Glerup, M. Castignolles, M. Holzinger, G. Hug, A. Loiseau, and P. Bernier. Synthesis of highly nitrogen-doped multi-walled carbon nanotubes. *Chemical Communications*, (20):2542–2543, 2003.
- J. Hafizovic, M. Bjorgen, U. Olsbye, P. D. C. Dietzel, S. Bordiga, C. Prestipino, C. Lamberti, and K. P. Lillerud. The inconsistency in adsorption properties and powder xrd data of mof-5 is rationalized by framework interpenetration and the presence of organic and inorganic species in the nanocavities. *Journal of the American Chemical Society*, 129(12):3612–3620, 2007.
- A. C. Hannon. Results on disordered materials from the general materials diffractometer, gem, at isis. *Nuclear Instruments & Methods in Physics Research Section a-Accelerators Spectrometers Detectors and Associated Equipment*, 551(1):88–107, 2005.
- C. N. He, N. Q. Zhao, C. S. Shi, X. W. Du, H. J. Li, L. Cui, and F. He. Carbon onion growth enhanced by nitrogen incorporation. *Scripta Materialia*, 54(10):1739–1743, 2006.
- M. Hirscher and B. Panella. Nanostructures with high surface area for hydrogen storage. *Journal of Alloys and Compounds*, 404-406:399–401, 2005.

- M. S. Hoogenraad. *PhD thesis*. PhD thesis, Utrecht University, 1995.
- HyFLEET:CUTE, 2004. <http://www.global-hydrogen-bus-platform.com/>.
- HyTRAIN. Hytrain hydrogen research training network, 2005. <http://www.imr.salford.ac.uk/hytrain/index.html>.
- S. Iijima. Helical microtubules of graphitic carbon. *Nature*, 354(6348): 56–58, 1991.
- J. H. Jia, X. Lin, A. J. Blake, N. R. Champness, P. Hubberstey, L. M. Shao, G. Walker, C. Wilson, and M. Schröder. Triggered ligand release coupled to framework rearrangement: Generating crystalline porous coordination materials. *Inorganic Chemistry*, 45(22):8838–8840, 2006.
- A. J. Kidnay and M. J. Hiza. Low temperature removal of small quantities of nitrogen or methane from hydrogen gas by physical adsorption on a synthetic zeolite. *Aiche Journal*, 12(1):58, 1966.
- R. Kitaura, K. Seki, G. Akiyama, and S. Kitagawa. Porous coordination-polymer crystals with gated channels specific for supercritical gases. *Angewandte Chemie-International Edition*, 42(4):428, 2003.
- H. W. Kroto, J. R. Heath, S. C. O'Brien, R. F. Curl, and R. E. Smalley. C₆₀ - buckminsterfullerene. *Nature*, 318(6042):162–163, 1985.
- G. J. Kubas, R. R. Ryan, B. I. Swanson, P. J. Vergamini, and H. J. Wasserman. Characterization of the 1st examples of isolable molecular-hydrogen complexes, $\text{Mo}(\text{CO})_3(\text{pcy}3)_2(\text{H}_2)$, $\text{W}(\text{CO})_3(\text{pcy}3)_2(\text{H}_2)$, $\text{Mo}(\text{CO})_3(\text{pi-pr}3)_2(\text{H}_2)$, $\text{W}(\text{CO})_3(\text{pi-pr}3)_2(\text{H}_2)$ - evidence for a side-on bonded H_2 ligand. *Journal of the American Chemical Society*, 106(2):451–452, 1984.
- Gregory J. Kubas. *Metal-dihydrogen and [s]-bond coordination: the consummate extension of the Dewar-Chatt-Duncanson model for metal-olefin [p] bonding*. 2001.
- Max von Laue, Georg Menzer, Clara von Simson, E. Verständig, and Richard Von Mises. *Stereoskopbilder von Kristallgittern = Stereoscopic drawings of crystal structures*. Springer, 1926.

BIBLIOGRAPHY

- J. E. Lennard-Jones and A. F. Devonshire. The interaction of atoms and molecules with solid surfaces. iii. the condensation and evaporation of atoms and molecules. In *Proceedings of the Royal Society of London. Series A, Mathematical and Physical Sciences (1934-1990)*, volume 156, pages 6–28, 1936.
- X. Lin. Metal-organic framework materials for hydrogen storage. In G. Walker, editor, *Solid Hydrogen Storage: Materials and Chemistry*. Woodhead Publishing, 2008.
- X. Lin, D. M. J. Doble, A. J. Blake, A. Harrison, C. Wilson, and M. Schröder. Cationic assembly of metal complex aggregates: Structural diversity, solution stability, and magnetic properties. *Journal of the American Chemical Society*, 125(31):9476–9483, 2003.
- X. Lin, A. J. Blake, C. Wilson, X. Z. Sun, N. R. Champness, M. W. George, P. Hubberstey, R. Mokaya, and M. Schröder. A porous framework polymer based on a zinc(ii) 4,4'-bipyridine-2,6,2',6'-tetracarboxylate: Synthesis, structure, and zeolite-like behaviors. *Journal of the American Chemical Society*, 128(33):10745–10753, 2006a.
- X. Lin, J. Jia, X. Xuebo Zhao, M. Thomas, K., J. Blake, A., S. Walker, G., R. Champness, N., P. Hubberstey, and M. Schröder. High h₂ adsorption by coordination-framework materials. *Angewandte Chemie*, 118(44):7518–7524, 2006b.
- X. Lin, I. Telepeni, A. J. Blake, A. Dailly, C. M. Brown, J. M. Simmons, M. Zoppi, G. S. Walker, K. M. Thomas, T. J. Mays, P. Hubberstey, N. R. Champness, and M. Schröder. High capacity hydrogen adsorption in cu (ii) tetracarboxylate framework materials: The role of pore size, ligand functionalization, and exposed metal sites. *Journal of the American Chemical Society*, 131(6):2159–2171, 2009.
- Y. Liu, C. M. Brown, J. L. Blackburn, D. A. Neumann, T. Gennett, L. Simpson, P. Parilla, A. C. Dillon, and M. Heben. Inelastic neutron scattering of h₂ adsorbed on boron substituted single walled carbon nanotubes. *Journal of Alloys and Compounds*, 446:368–372, 2007a.

- Y. Liu, C. M. Brown, D. A. Neumann, V. K. Peterson, and C. J. Kepert. Inelastic neutron scattering of H_2 adsorbed in HKUST-1. *Journal of Alloys and Compounds*, 446:385–388, 2007b.
- Y. Liu, J. H. Her, A. Dailly, A. J. Ramirez-Cuesta, D. A. Neumann, and C. M. Brown. Reversible structural transition in MIL-53 with large temperature hysteresis. *Journal of the American Chemical Society*, 130(35):11813–11818, 2008.
- T. Loiseau, C. Serre, C. Huguenard, G. Fink, F. Taulelle, M. Henry, T. Bataille, and G. Férey. A rationale for the large breathing of the porous aluminum terephthalate (MIL-53) upon hydration. *Chemistry-a European Journal*, 10(6):1373–1382, 2004.
- S. G. Louie. Electronic properties, junctions, and defects of carbon nanotubes. *Carbon Nanotubes*, 80:113–145, 2001.
- S.W. Lovesey. *Theory of neutron scattering from condensed matter*. 1984.
- A. D. Lueking, H. R. Gutierrez, D. A. Fonseca, and E. Dickey. Structural characterization of exfoliated graphite nanofibers. *Carbon*, 45(4):751–759, 2007.
- S. McCaldin, M. Bououdina, D. M. Grant, and G. S. Walker. The effect of processing conditions on carbon nanostructures formed on an iron-based catalyst. *Carbon*, 44(11):2273–2280, 2006.
- Richard B. McClurg, Richard C. Flagan, and William A. Goddard III. The hindered rotor density-of-states interpolation function. *The Journal of Chemical Physics*, 106(16):6675–6680, 1997.
- E. Melancon and P. Benard. Theoretical study of the contribution of physisorption to the low-pressure adsorption of hydrogen on carbon nanotubes. *Langmuir*, 20(18):7852–7859, 2004.
- P. C. H. Mitchell, S. F. Parker, A. J. Ramirez-Cuesta, and J. Tomkinson. *Vibrational spectroscopy with neutrons with applications in chemistry biology materials science and catalysis*. World Scientific. 2004.

BIBLIOGRAPHY

- Koichi Momma and Fujio Izumi. Vesta: a three-dimensional visualization system for electronic and structural analysis. *Journal of Applied Crystallography*, 41(3):653–658, 2008.
- NESSHY. Nesshy novel efficient solid storage for H_2 , 2006. <http://www.nesshy.net/>.
- Andriy H. Nevidomskyy, Gábor Csányi, and Michael C. Payne. Chemically active substitutional nitrogen impurity in carbon nanotubes. *Physical Review Letters*, 91(10):105502, 2003.
- Roger G. Newton. *Scattering theory of waves and particles*. Texts and monographs in physics. Springer-Verlag, New York, 2nd ed edition, 1982.
- NIST. National institute of standards and technology, 2006. <http://www.nist.gov/index.html>.
- P. E. Nolan, D. C. Lynch, and A. H. Cutler. Carbon deposition and hydrocarbon formation on group viii metal catalysts. *Journal of Physical Chemistry B*, 102(21):4165–4175, 1998.
- T. Oku, H. Kitahara, M. Kuno, I. Narita, and K. Suganuma. Synthesis, atomic structures and arrangement of carbon and boron nitride nanocage materials. *Scripta Materialia*, 44(8-9):1557–1560, 2001a.
- T. Oku, M. Kuno, H. Kitahara, and I. Narita. Formation, atomic structures and properties of boron nitride and carbon nanocage fullerene materials. *International Journal of Inorganic Materials*, 3(7):597–612, 2001b.
- T. Oku, I. Narita, and A. Nishiwaki. Atomic structures of bamboo-type boron nitride nanotubes with cup-stacked structures. *Journal of the European Ceramic Society*, 26(4-5):443–448, 2006.
- V. K. Peterson, Y. Liu, C. M. Brown, and C. J. Kepert. Neutron powder diffraction study of D_2 in $\text{Cu}_3(1,3,5\text{-benzenetricarboxylate})_2$. *Journal of the American Chemical Society*, 128(49):15578–15579, 2006.
- E. Poirier, R. Chahine, P. Bénard, L. Lafi, G. Dorval-Douville, and P. A. Chandonia. Hydrogen adsorption measurements and modeling on metal-organic frameworks and single-walled carbon nanotubes. *Langmuir : the ACS journal of surfaces and colloids*, 22(21):8784–8789, 2006.

- B. K. Pradhan, G. U. Sumanasekera, K. W. Adu, H. E. Romero, K. A. Williams, and P. C. Eklund. Experimental probes of the molecular hydrogen-carbon nanotube interaction. *Physica B-Condensed Matter*, 323(1-4):115–121, 2002.
- C. Prestipino, L. Regli, J. G. Vitillo, F. Bonino, A. Damin, C. Lamberti, A. Zecchina, P. L. Solari, K. O. Kongshaug, and S. Bordiga. Local structure of framework cu(ii) in hkust-1 metallorganic framework: Spectroscopic characterization upon activation and interaction with adsorbates. *Chemistry of Materials*, 18(5):1337–1346, 2006.
- J. J. Purewal, H. Kabbour, J. J. Vajo, C. C. Ahn, and B. Fultz. Pore size distribution and supercritical hydrogen adsorption in activated carbon fibers. *Nanotechnology*, 20(20), 2009.
- A. J. Ramirez-Cuesta, P. C. H. Mitchell, D. K. Ross, P. A. Georgiev, P. A. Anderson, H. W. Langmi, and D. Book. Dihydrogen in cation-substituted zeolites x - an inelastic neutron scattering study. *Journal of Materials Chemistry*, 17(24):2533–2539, 2007a.
- A. J. Ramirez-Cuesta, P. C. H. Mitchell, D. K. Ross, P. A. Georgiev, P. A. Anderson, H. W. Langmi, and D. Book. Dihydrogen in zeolite cax—an inelastic neutron scattering study. *Journal of Alloys and Compounds*, 446-447:393–396, 2007b.
- Hugo Rietveld. A profile refinement method for nuclear and magnetic structures. *J. Appl. Cryst.*, 2:65–71, 1969.
- N. M. Rodriguez. A review of catalytically grown carbon nanofibers. *Journal of Materials Research*, 8:3233–3250, 1993.
- F Rodriguez-Reinoso. Production and applications of activated carbons. In F. Schüth, K. S. W. Sing, and J. Weitkamp, editors, *Handbook of porous solids*. Wiley-VCH, Weinheim, 2002.
- Nathaniel L. Rosi, Juergen Eckert, Mohamed Eddaoudi, David T. Vodak, Jaheon Kim, Michael O’Keeffe, and Omar M. Yaghi. Hydrogen storage in microporous metal-organic frameworks. *Science*, 300(5622):1127–1129, 2003.

BIBLIOGRAPHY

- F. Rouquerol, J. Rouquerol, G. Dellagatta, and C. Letoquart. Use of isothermal micro-calorimetry data for the determination of integral molar entropies of adsorption at the gas-solid interface by a quasi-equilibrium procedure. *Thermochimica Acta*, 39(2):151–158, 1980.
- F. Rouquerol, J. Rouquerol, and K. Sing. Adsorption by powders & porous solids. *Academic press*, 1998.
- J. Rowsell and O. M. Yaghi. Strategies for hydrogen storage in metal-organic frameworks. *Angew. Chem. Int. Ed.*, 44:4670, 2005.
- J. L. C. Rowsell, J. Eckert, and O. M. Yaghi. Characterization of H_2 binding sites in prototypical metal-organic frameworks by inelastic neutron scattering. *J. Am. Chem. Soc.*, 127(42):14904–14910, 2005.
- M. Rzepka, P. Lamp, and M. A. de la Casa-Lillo. Physisorption of hydrogen on microporous carbon and carbon nanotubes. *Journal of Physical Chemistry B*, 102(52):10894–10898, 1998.
- M. Sankaran and B. Viswanathan. Nitrogen-containing carbon nanotubes as a possible hydrogen storage medium. *Indian Journal of Chemistry Section a-Inorganic Bio-Inorganic Physical Theoretical & Analytical Chemistry*, 47(6):808–814, 2008.
- M. Sankaran, B. Viswanathan, and S. S. Murthy. Boron substituted carbon nanotubes - how appropriate are they for hydrogen storage? *International Journal of Hydrogen Energy*, 33(1):393–403, 2008.
- P. Schaffautl. *J. prakt Chem.*, 21, 155., 21:155, 1841.
- P. Scherrer. *Göttinger Nachrichten Gesell.*, 2:98, 1918.
- Louis Schlapbach and Andreas Züttel. Hydrogen-storage materials for mobile applications. *Nature*, 414(6861):353–358, 2001.
- F. C. Schouten, E. W. Kaleveld, and G. A. Bootsma. Aes-leed-ellipsometry study of kinetics of interaction of methane with ni(110). *Surface Science*, 63(1):460–474, 1977.

- F. C. Schouten, O. L. J. Gijzeman, and G. A. Bootsma. Interaction of methane with ni(111) and ni(100) - diffusion of carbon into nickel through the (100) surface - aes-leed study. *Surface Science*, 87(1):1–12, 1979.
- C. Serre, F. Millange, C. Thouvenot, M. Nogues, G. Marsolier, D. Louer, and G. Ferey. Very large breathing effect in the first nanoporous chromium (iii) - based solids: Mil-53 or cr-iii (oh) center dot o₂c-c₆h₄-co₂ center dot ho₂c-c₆h₄-co₂h (x) center dot h₂O_y. *Journal of the American Chemical Society*, 124(45):13519–13526, 2002.
- A. E. Shalagina, Z. R. Ismagilov, O. Y. Podyacheva, R. I. Kvon, and V. A. Ushakov. Synthesis of nitrogen-containing carbon nanofibers by catalytic decomposition of ethylene/ammonia mixture. *Carbon*, 45(9):1808–1820, 2007.
- Isaac F. Silvera. The solid molecular hydrogens in the condensed phase: Fundamentals and static properties. *Reviews of Modern Physics*, 52(2):393, 1980.
- Isaac F. Silvera, A. Driessen, and J. A. de Waal. The equation of state of solid molecular hydrogen and deuterium. *Physics Letters A*, 68(2):207–210, 1978.
- R. Strobel, L. Jorissen, T. Schliermann, V. Trapp, W. Schutz, K. Bohmhammel, G. Wolf, and J. Garche. Hydrogen adsorption on carbon materials. *Journal of Power Sources*, 84(2):221–224, 1999.
- R. Strobel, J. Garche, P. T. Moseley, L. Jorissen, and G. Wolf. Hydrogen storage by carbon materials. *Journal of Power Sources*, 159(2):781–801, 2006.
- C. C. Tang, Y. Bando, D. Golberg, and F. F. Xu. Structure and nitrogen incorporation of carbon nanotubes synthesized by catalytic pyrolysis of dimethylformamide. *Carbon*, 42(12-13):2625–2633, 2004.
- Teo, Kenneth B. K., Charanjeet. Singh, Manish. Chhowalla, Milne, and William. I. Catalytic synthesis of carbon nanotubes and nanofibers, 2003.
- M. Terrones, H. Terrones, N. Grobert, W. K. Hsu, Y. Q. Zhu, J. P. Hare, H. W. Kroto, D. R. M. Walton, P. Kohler-Redlich, M. Ruhle, J. P. Zhang,

BIBLIOGRAPHY

- and A. K. Cheetham. Efficient route to large arrays of cn_x nanofibers by pyrolysis of ferrocene/melamine mixtures. *Applied Physics Letters*, 75 (25):3932–3934, 1999.
- M. Terrones, A. Jorio, M. Endo, A. M. Rao, A. Kim, T. Hayashi, J.-C. Terrones, H. Charlier, G. Dresselhaus, and M. Dresselhaus. New direction in nanotube science. *materialstoday*, 2004.
- B. H. Toby. Expgui, a graphical user interface for gsas. *J. Appl. Cryst.*, 34: 210–213, 2001.
- M. Toyoda, H. Katoh, and M. Inagaki. Intercalation of nitric acid into carbon fibers. *Carbon*, 39(14):2231–2234, 2001a.
- M. Toyoda, A. Shimizu, H. Iwata, and M. Inagaki. Exfoliation of carbon fibers through intercalation compounds synthesized electrochemically. *Carbon*, 39(11):1697–1707, 2001b.
- M. Toyoda, H. Katoh, A. Shimizu, and M. Inagaki. Preparation of intercalation compounds of carbon fibers and their exfoliation. *New Carbon Materials*, 17(1):1–3, 2002a.
- M. Toyoda, J. Sedlacik, and M. Inagaki. Intercalation of formic acid into carbon fibers and their exfoliation. *Synthetic Metals*, 130(1):39–43, 2002b.
- M. Toyoda, H. Katoh, A. Shimizu, and M. Inagaki. Exfoliation of nitric acid intercalated carbon fibers: effects of heat-treatment temperature of pristine carbon fibers and electrolyte concentration on the exfoliation behavior. *Carbon*, 41(4):731–738, 2003.
- T. J. Udovic, D. A. Neumann, J. Leão, and C. M. Brown. Origin and removal of spurious background peaks in vibrational spectra measured by filter-analyzer neutron spectrometers. *Nuclear Instruments and Methods in Physics Research Section A: Accelerators, Spectrometers, Detectors and Associated Equipment*, 517(1-3):189–201, 2004.
- UK-SHEC. Uk sustainable hydrogen energy consortium, 2007. <http://www.uk-shec.org.uk/>.

- L. Ulivi, M. Celli, A. Giannasi, A. J. Ramirez-Cuesta, D. J. Bull, and M. Zoppi. Quantum rattling of molecular hydrogen in clathrate hydrate nanocavities. *Physical Review B (Condensed Matter and Materials Physics)*, 76(16):161401–4, 2007.
- U.S. Department of Energy. Hydrogen posture plan: An integrated research, development and demonstration plan, 2006. <http://www.hydrogen.energy.gov/>.
- U.S. Department of Energy. Hydrogen posture plan: An integrated research, development, 2009a. <http://www.hydrogen.energy.gov/>.
- U.S. Department of Energy. Hydrogen, fuel cells and infrastructure technologies program, 2009b. <http://www1.eere.energy.gov/hydrogenandfuelcells/mypp/>.
- U.S. Department of Energy. Multi-year research, development and demonstration plan: Production, 2009c. <http://www.hydrogen.energy.gov/>.
- U.S. Department of Energy, 2009d. <http://www.ne.doe.gov/>.
- U.S. Department of Energy. Multi-year research, development and demonstration plan: Storage, 2009e. <http://www.hydrogen.energy.gov/>.
- U.S. Department of Energy. Multi-year research, development and demonstration plan: Delivery, 2009f. <http://www.hydrogen.energy.gov/>.
- J. G. Vitillo, L. Regli, S. Chavan, G. Ricchiardi, G. Spoto, P. D. C. Dietzel, S. Bordiga, and A. Zecchina. Role of exposed metal sites in hydrogen storage in mofs. *Journal of the American Chemical Society*, 130(26): 8386–8396, 2008.
- R. B. Von Dreele, J. D. Jorgensen, and C. G. Windsor. Rietveld refinement with spallation neutron powder diffraction data. *Journal of Applied Crystallography*, 15(6):581–589, 1982.
- Gavin S Walker. *Solid hydrogen storage: Materials and chemistry*. Woodhead Publishing, 2008.

BIBLIOGRAPHY

- Q. Y. Wang and J. K. Johnson. Molecular simulation of hydrogen adsorption in single-walled carbon nanotubes and idealized carbon slit pores. *Journal of Chemical Physics*, 110(1):577–586, 1999.
- David White and Edwin N. Lassettre. Theory of ortho-para hydrogen separation by adsorption at low temperatures, isotope separation. *The Journal of Chemical Physics*, 32(1):72–84, 1960.
- Y. Xia and R. Mokaya. Synthesis of ordered mesoporous carbon and nitrogen-doped carbon materials with graphitic pore walls via a simple chemical vapor deposition method. *Advanced Materials*, 16(17):1553–1558, 2004.
- Yongde Xia, Zhuxian Yang, Robert Mokaya, Sayari Abdelhamid, and Jaroniec Mietek. Synthesis of hollow spherical mesoporous n-doped carbon materials with graphitic framework. In *Studies in Surface Science and Catalysis*, volume Volume 156, pages 565–572. Elsevier, 2005.
- O. M. Yaghi, M. O’Keeffe, N. W. Ockwig, H. K. Chae, M. Eddaoudi, and J. Kim. Reticular synthesis and the design of new materials. *Nature*, 423(6941):705–714, 2003.
- Y. Yan, X. Lin, S. H. Yang, A. J. Blake, A. Dailly, N. R. Champness, P. Hubberstey, and M. Schröder. Exceptionally high h_2 storage by a metal-organic polyhedral framework. *Chemical Communications*, (9):1025–1027, 2009.
- W. Yang, X. Lin, J. Jia, A. J. Blake, C. Wilson, P. Hubberstey, N. R. Champness, and M. Schröder. A biporous coordination framework with high h_2 storage density. *Chemical Communications*, (3):359–361, 2008.
- Zhuxian Yang, Yongde Xia, and Robert Mokaya. Hollow shells of high surface area graphitic n-doped carbon composites nanocast using zeolite templates. *Microporous and Mesoporous Materials*, 86(1-3):69–80, 2005a.
- Zhuxian Yang, Yongde Xia, Robert Mokaya, Sayari Abdelhamid, and Jaroniec Mietek. Porous n-doped carbon with various hollow-cored morphologies nanocast using zeolite templates via chemical vapour deposi-

- tion. In *Studies in Surface Science and Catalysis*, volume Volume 156, pages 573–580. Elsevier, 2005b.
- Zhuxian Yang, Yongde Xia, Xuezhong Sun, and Robert Mokaya. Preparation and hydrogen storage properties of zeolite-templated carbon materials nanocast via chemical vapor deposition: effect of the zeolite template and nitrogen doping. *The journal of physical chemistry. B*, 110(37):18424–18431, 2006.
- Zhuxian Yang, Yongde Xia, and Robert Mokaya. Enhanced hydrogen storage capacity of high surface area zeolite-like carbon materials. *Journal of the American Chemical Society*, 129(6):1673–1679, 2007.
- Y. Ye, C. C. Ahn, B. Fultz, J. J. Vajo, and J. J. Zinck. Hydrogen adsorption and phase transitions in fullerite. *Applied Physics Letters*, 77(14):2171–2173, 2000.
- T. Yildirim and M. R. Hartman. Direct observation of hydrogen adsorption sites and nanocage formation in metal-organic frameworks. *Physical Review Letters*, 95(21):215504, 2005.
- T. Yildirim, J. Iniguez, and S. Ciraci. Molecular and dissociative absorption of multiple hydrogens on transition metal decorated c_{60} , 2005.
- James A. Young and Juan U. Koppel. Slow neutron scattering by molecular hydrogen and deuterium. *Physical Review*, 135(3A):A603, 1964.
- D. J. Zhang, H. Sun, J. Q. Liu, and C. B. Liut. A new family of heterofullerenes: Stoichiometric tio_2 nanoclusters. *Journal of Physical Chemistry C*, 113(1):21–25, 2009.
- B. Zheng, W. T. Zheng, K. Zhang, Q. B. Wen, J. Q. Zhu, S. H. Meng, X. D. He, and J. C. Han. First-principle study of nitrogen incorporation in amorphous carbon. *Carbon*, 44(5):962–968, 2006.
-